

Electronic Thesis and Dissertation Repository

---

7-23-2021 3:00 PM

## Seismic Imaging in Crystalline Terrains of the Superior Province, Canada

Brian Villamizar, *The University of Western Ontario*

Supervisor: Gerhard Pratt, *The University of Western Ontario*

A thesis submitted in partial fulfillment of the requirements for the Doctor of Philosophy degree  
in Geophysics

© Brian Villamizar 2021

Follow this and additional works at: <https://ir.lib.uwo.ca/etd>



Part of the [Geophysics and Seismology Commons](#)

---

### Recommended Citation

Villamizar, Brian, "Seismic Imaging in Crystalline Terrains of the Superior Province, Canada" (2021).  
*Electronic Thesis and Dissertation Repository*. 8088.  
<https://ir.lib.uwo.ca/etd/8088>

This Dissertation/Thesis is brought to you for free and open access by Scholarship@Western. It has been accepted for inclusion in Electronic Thesis and Dissertation Repository by an authorized administrator of Scholarship@Western. For more information, please contact [wlsadmin@uwo.ca](mailto:wlsadmin@uwo.ca).

# Summary for Lay Audience

The Earth has finite resources, including mining commodities such as gold, copper and nickel that we use to build the world's infrastructure including roads, hospitals, electrical grids, and telecommunications. For many decades, the mining industry has been successfully able to mine shallow mineral deposits. However, these near-surface deposits are becoming increasingly difficult to find. There is a pressing need for exploration methods that can find deeper mining prospects more reliably. This requires mapping the distribution of ore deposits at depth. Subsurface imaging methods can provide solutions for these exploration campaigns. In this work, I employed seismic techniques to image both the structural near-surface configuration of the subsurface and the architecture of potential mineralized structural pathways at depth. I used full-waveform inversion to retrieve high-quality geophysical images of the first few kilometers of the subsurface. Full-waveform inversion is a highly accurate iterative tomographic technique that makes optimal use of the seismic wave information. I investigated the effect of crooked geometries in waveform inversion by not only considering a two-dimensional (2D) modeling and inversion approach, but also a two-and-one-half-dimensional (2.5D) approach. In addition, I performed advanced reflection processing by implementing geologically driven techniques in which "bins" used to group traces are re-orientated along geological strike, improving energy focusing. The final result is an optimal reflectivity image. Combining near-surface velocity images with reflectivity images at depth, I was able to fill the gap between surface geology and crustal-scale structures in two different hard rock environments in Canada: in the Larder Lake and Sudbury mining district.

# Abstract

The imaging of structures in sedimentary basins has typically been carried out using conventional seismic reflection techniques. In complex geological architectures, such as those within the Superior Province in Canada, conventional seismic imaging yields suboptimal results due to factors stemming from complex energy scattering and crooked seismic geometries. Full-waveform inversion (FWI) is a nonlinear inverse technique capable of retrieving quantitative images of velocity structures. Judicious data preconditioning, and multiscale inversion strategies allow FWI to effectively estimate velocity variations in the first few kilometers of the subsurface. Non-conventional seismic reflection processing, based on azimuthal binning and enhanced migration velocity models, improves energy focusing and imaging quality of structures at depth.

I demonstrate that the serious nonlinearity of FWI in crystalline zones (in Larder Lake and in the northeastern portion of the Sudbury Structure), is alleviated by implementing a “multiscale layer-stripping” strategy. The strategy uses a i) combination of explosive and vibroseis sources to retrieve low-wavenumber features of the velocity background, ii) hierarchical minimization of logarithmic phase-only and conventional phase-amplitude residuals to mitigate large dynamic variations within the data, and iii) progressive inclusion of higher frequencies and late arrivals to obtain a natural transition between low- and high- wavenumber features. I illustrate that the implementation of optimum binning strategies effectively enhances signal alignment, generating in-phase stacked sections. The use of near-surface FWI P-wave velocity estimations in the construction of migration velocity models, improves the strength and continuity of reflections at depth.

With the application of these imaging techniques, I unravel the geometry of prominent structures in structurally-controlled mineralized zones. In Larder Lake, the Larder Lake-Cadillac Deformation Zone (LLCDZ), and the Lincoln-Nipissing Shear Zone (LNSZ), are imaged. The LNSZ is retrieved as a north-dipping fault, extending to depths not previously identified of 8 km. The Sudbury velocity model reveals the internal character of the structure, agreeing with known geology and borehole information. New estimates of thicknesses and dips are given for the northeastern portion of the Sudbury Structure.

**Keywords:** Full-waveform inversion, Finite-difference modeling, Seismic imaging, Azimuthal binning, Energy focusing, Reflection processing, Crystalline environments, Larder Lake, Sudbury.

# Statement of Co-Authorship

The work presented in this thesis (Chapters 2 to 5) has either been or will be submitted to a peer-reviewed journal. The co-authors of Chapters 2 to 5 are Dr. Gerhard Pratt, professor at the University of Western Ontario, and Dr. Mostafa Naghizadeh, professor at Laurentian University, both institutions in Ontario, Canada. Dr. Gerhard Pratt and Dr. Mostafa Naghizadeh provided geophysical and geological guidance, research instructions, and written revisions and editing to Chapters 1 to 6.

In addition, Dr. Gerhard Pratt facilitated the source code for the implementation of 2D and 2.5D visco-acoustic full-waveform inversion in the frequency domain. Instructions on modeling and inversion methodologies, as well as the fundamentals of inverse theory were also provided by Dr. Gerhard Pratt.

The data processing, forward modeling, and seismic inversion related to all the experiments presented from Chapter 2 to 5, were designed and implemented entirely by myself, with the support and mentorship of my co-authors.

# Acknowledgments

I would like to express my sincerest gratitude to Dr. Gerhard Pratt, and Dr. Mostafa Naghizadeh for the incredible life opportunity that this doctorate has come to be. I will always be deeply indebted to Dr. Mostafa Naghizadeh, who went through an ordeal to secure funding for this project, which ultimately led to its materialization. My appreciation also extends to Dr. Gerhard Pratt, who expertly guided me through the full-waveform inversion journey, and whose enjoyable academic lectures are always an exciting learning opportunity. Without a doubt, one of the most knowledgeable lecturers I have ever known. There are no words to express my gratitude towards Dr. Pratt's unwavering support and understanding.

To my friends at Western University, Carolina Rodriguez, Sameer Ladak, Shannon Hibbard, Mayling Aviles, Jahnavi Shah, and Josh Hedgepeth. Thank you for all the fun moments, long conversations, BBQs, and game nights we had **B.C.**, (i.e., before Covid-19). Special thanks to Bernie Dunn, who not only was a dear friend during my time at Western, but who also assisted with the success of my Ph.D. by providing expert IT support. Many thanks to my fellow geoscientists with whom I had fruitful conversations; Sameer Ladak, Chris Boucher, Hema Sharma, Kate Rubingh, and Benjamin Consolvo.

I owe my deepest gratitude to my beautiful wife, Chantal Montgomery, who supported me in more than one way throughout this journey. I also wish to thank Joanne Montgomery (a.k.a., *Jobobin*), for receiving me as a member of her family, and for being a wonderful human being. Thanks to Randy Montgomery for putting up with my shenanigans, and for all his delicious meals. Last but certainly not least, I would like to thank my mom, Maria Villamizar, dad, Oscar Urbaneja, and sisters, Oskarlys and Gennessee, as well as the rest of my family in Venezuela, who also helped me achieved this milestone.

# Table of Contents

<b>Summary for Lay Audience</b>	<b>i</b>
<b>Abstract</b>	<b>ii</b>
<b>Statement of Co-Authorship</b>	<b>iii</b>
<b>Acknowledgements</b>	<b>iv</b>
<b>Table of Contents</b>	<b>v</b>
<b>List of Tables</b>	<b>ix</b>
<b>List of Figures</b>	<b>x</b>
<b>1 Introduction</b>	<b>1</b>
1.1 Seismic methods . . . . .	2
1.1.1 Seismic refraction method . . . . .	3
1.1.2 Seismic reflection method . . . . .	5
1.2 Seismic imaging . . . . .	8
1.2.1 Traveltime Tomography . . . . .	9
1.2.2 Forward modeling . . . . .	14
1.2.3 Laplace-Fourier Domain . . . . .	16
1.2.4 Waveform Inversion . . . . .	17
1.2.4.1 Source signature . . . . .	23
1.3 Project background and geological overview . . . . .	23
1.3.1 Larder lake mining district . . . . .	25
1.3.2 Sudbury mining district . . . . .	26
1.4 Objectives of thesis . . . . .	28
1.5 Thesis outline . . . . .	29

<b>2</b>	<b>Full-waveform inversion in a crystalline terrain using combined explosive and vibroseis sources</b>	<b>31</b>
2.1	Introduction . . . . .	31
2.2	Method . . . . .	33
2.2.1	Forward modeling . . . . .	33
2.2.2	Inverse problem and optimization . . . . .	34
2.3	Data . . . . .	35
2.3.1	Survey acquisition . . . . .	35
2.3.2	Explosive and vibroseis sources . . . . .	38
2.3.3	Data preconditioning . . . . .	39
2.4	Inversion . . . . .	42
2.4.1	First-arrival travelttime tomography . . . . .	42
2.4.2	Full-waveform inversion . . . . .	44
2.4.3	Validation . . . . .	49
2.4.4	FWI on explosive/vibroseis vs. vibroseis-only data . . . . .	52
2.5	Results and discussion . . . . .	56
2.5.1	Representative sensitivity kernels . . . . .	56
2.5.2	Full-waveform inversion results . . . . .	57
2.5.3	Geological discussion . . . . .	58
2.6	Conclusions . . . . .	61
<b>3</b>	<b>Seismic imaging of crystalline structures: 2D and 2.5D visco-acoustic full-waveform inversion</b>	<b>63</b>
3.1	Introduction . . . . .	63
3.2	Method . . . . .	65
3.2.1	Forward problem . . . . .	65
3.2.2	Inverse problem . . . . .	68
3.3	Case study in 2D and 2.5D FWI - Larder Lake . . . . .	69
3.3.1	Local geology . . . . .	69
3.3.2	Acquisition geometry . . . . .	69
3.3.3	Data preconditioning . . . . .	71
3.3.4	Full-waveform inversion . . . . .	73
3.3.5	Interpretation . . . . .	82
3.4	Conclusions . . . . .	85
<b>4</b>	<b>Seismic imaging of crystalline structures: improving energy focusing and signal alignment with azimuthal binning</b>	<b>86</b>

4.1	Introduction . . . . .	86
4.2	Energy focusing and signal alignment . . . . .	88
4.2.1	Standard binning . . . . .	88
4.2.2	Cross-profile dip effects . . . . .	89
4.2.3	Azimuthal binning . . . . .	89
4.3	Seismic reflection processing in Larder Lake . . . . .	90
4.3.1	Enhanced binning . . . . .	93
4.3.2	Azimuthal v. standard stacked sections . . . . .	96
4.3.3	Azimuthal v. standard migrated sections . . . . .	101
4.4	CMP gathering on slalom lines . . . . .	104
4.5	Structural interpretation of migrated reflections . . . . .	104
4.5.1	Southern domain . . . . .	105
4.5.2	Northern domain . . . . .	107
4.5.3	Surface geology and structures at depth . . . . .	108
4.6	Conclusions . . . . .	108
<b>5</b>	<b>Imaging the northeast lobe of the Sudbury Structure through 2D and 2.5D visco-acoustic full-waveform inversion</b>	<b>110</b>
5.1	Introduction . . . . .	110
5.2	Method . . . . .	112
5.2.1	Forward modeling . . . . .	112
5.2.2	Inversion . . . . .	113
5.3	Geological background . . . . .	114
5.4	Seismic reflection survey . . . . .	116
5.5	Laplace-Fourier-domain FWI . . . . .	118
5.5.1	Data preconditioning . . . . .	119
5.5.2	Starting velocity model . . . . .	120
5.5.3	Modeling . . . . .	125
5.5.4	Full-waveform inversion . . . . .	126
5.6	Discussion . . . . .	136
5.6.1	Whitewater Group . . . . .	137
5.6.2	Sudbury Igneous Complex . . . . .	139
5.7	Conclusions . . . . .	140
<b>6</b>	<b>General conclusions</b>	<b>141</b>
6.1	Seismic imaging of hard rock environments . . . . .	141
6.1.1	Low-frequency components of explosive sources . . . . .	141

6.1.2	Dynamic variations in the observed wavefield . . . . .	142
6.1.3	Progressive strategy on offsets and later seismic phases . . . . .	143
6.1.4	2D v. 2.5D full-waveform inversion . . . . .	144
6.1.5	Advanced seismic reflection processing . . . . .	145
6.1.6	Geological significance of seismic imaging . . . . .	146
6.2	Future considerations . . . . .	147
6.2.1	FWI developments on the horizon . . . . .	149

<b>Bibliography</b>		<b>152</b>
---------------------	--	------------

# List of Tables

2.1	Acquisition parameters . . . . .	38
2.2	Finite-diference forward modeling parameters . . . . .	45
2.3	Schedule of frequencies and offset tapering used in each inversion group. . . . .	47
3.1	Transverse wavenumber components per inversion group. See Table 3.2 for further details on the stages of FWI we use. . . . .	75
3.2	Multiscale inversion strategy. . . . .	76
4.1	Processing sequence of Larder Lake. . . . .	92
4.2	Standard (std) v. optimized (opt) binning azimuths for Larder Lake. Bin direction in the standard CMP method is perpendicular to the processing line. In the optimized method, bin direction is determined according to local geological strike. . . . .	94
5.1	Multiscale inversion strategy. . . . .	127

# List of Figures

1.1	Schematic diagram of onshore seismic data acquisition. Examples of wave paths are shown in black for reflected seismic waves, and in white for refracted seismic waves. The source is a truck-mounted vibroseis that introduces vibratory perturbations into the subsurface. Notice that both types of waves are recorded by the receivers (i.e., geophones) located on the surface. . . . .	4
1.2	Geological map of the Superior Province portraying seismic transects acquired by the Metal Earth R&D project (black), and by the Lithoprobe project (blue). The black rectangles indicate the study areas in this thesis, the Larder Lake and Sudbury mining districts. Modified after Naghizadeh (2019) . . . . .	24
2.1	Relevant geological units in the Larder Lake area, displaying the acquisition geometry. The original (crooked) geometry is shown by the blue (receivers) and light orange (vibroseis sources) solid lines. Explosive sources are indicated by red dots. Only the southernmost three explosive sources are used in this study. The 22-km long 2D projected geometry used for FWI is represented by the straight line in brown. Key structural features are depicted by the two dashed yellow lines: the Larder Lake-Cadillac Deformation Zone (to the north) and the Lincoln-Nipissing Shear Zone (to the south). Black lines on the projected geometry indicate 4 km intervals, which correlate with the horizontal axis of the models shown here. Grey line indicates the Ontario and Quebec border. Modified after the Metal Earth - Geology map of Larder Lake area (2019). . . . .	36
2.2	Normalized Fourier spectra of co-incident raw shot gathers for both explosive and vibroseis sources. . . . .	38

2.3	Trace-normalized shot gathers corresponding to co-incident (a) explosive and (b) vibroseis sources located at a distance of 11.8 km along the projected 2D geometry.	40
2.4	Frequency-wavenumber spectrum of a gather located at 11.8 km along the line with (a) no residual statics applied and (b) with residual statics applied. White arrows highlight events associated with secondary arrivals that we wish to suppress. . . . .	41
2.5	Vibroseis gather at 11.8 km along the projected geometry. The data are presented (a) prior to preconditioning, with no windowing or muting; (b) with windowing, muting, F-K filtering, and with surface-consistent and shot-to-shot amplitude balancing; (c) with all preconditioning, including low pass filtering and time-damping (with $\tau = 0.3$ s). . . . .	43
2.6	Initial velocity model from FATT to be used in the subsequent FWI. The grey-shaded region indicates areas in which no raypaths are observed. . . . .	44

2.7	Final FWI P-wave FWI results, showing a) the velocity model, b) the velocity model with a preliminary structural interpretation (according to different velocity domains and geological map), and c) the de-trended velocity model. Grey-shaded regions indicate areas with little to no energy penetration. The thin solid black line in b) and c) indicates the sub-horizontal separation of sediments and less competent volcanic units, from the folded and faulted Larder Lake Group (north of the LNSZ, indicated by dashed black lines) and the McElroy assemblage (south of the LNSZ). Principal faults are indicated by thick solid black lines. . . . .	48
2.8	Comparison of a) observed waveforms of a shot gather located at approximately 15 km along the projected line, b) visco-acoustic synthetic waveforms using the FATT velocity model, and c) visco-acoustic synthetic waveforms using the final FWI velocity model. The red line in all panels represents the manually picked first-arrival times on the observed data. The white arrows indicate areas of good agreement between observed and final predicted waveforms. The white rectangles represent a zoomed-in area to be discussed in the next figure. Waveforms discarded due to noise or out-of-plane errors are indicated by the black regions. . . . .	51
2.9	Zoom-in on the rectangles displayed in Figure 5.12 showing a) the original observed waveforms, b) observed waveforms after bandpass filtering, re-sampling, and trace decimation, c) synthetic waveforms from the FATT velocity model, and d) synthetic waveforms from the final FWI velocity model. Colored lines in (b) and (d) are indicative of the same seismic phases. . . . .	52
2.10	Time-domain source signature for each shot in our dataset. These signatures are estimated using (a) the initial FATT model, and (b) the final FWI model. . . . .	53
2.11	Resolution analysis by checkerboard tests, with +/- 5 per cent velocity anomalies superimposed on the starting FATT model. Checkered pattern dimensions are a) 1000x500 m and b) 500x250 m. . . . .	54
2.12	Explosive/vibroiseis FWI results vs. vibroseis-only results, showing results after the 13th inversion stage (see Table 5.1). Velocity models obtained by starting the FWI at a) starting at 7 Hz (without explosive sources), and b) 4 Hz (with explosive sources). Grey-shaded regions indicate areas with little to no energy penetration. The blue outline identifies the shape of the low velocity anomaly referred to in the text. Source signature inversions are depicted c) using the velocity model in a), and d) using the velocity model in b). Key features are identified in c) that suggest a more reliable velocity reconstruction (e.g. orange and red arrows showing flatter events and enhanced continuity/coherency, respectively). . . . .	55
2.13	Wavepath images, depicting the model update response for a monofrequency source-receiver pair at a) the minimum frequency of 7 Hz and b) the maximum frequency of 15 Hz. The source is located at 11.8 km along the projected line and the receiver is located at 19 km. . . . .	57
2.14	Synthetic FWI experiment for a steeply dipping slap inserted into the FATT veloc-	

3.2	Monochromatic data images showing the real part of frequency-domain wavefields at 7 Hz (a) before and (b, c) after data preconditioning. Data in (b) is used for 2D FWI (includes rejection of traces due to offset errors), whereas data in (c) is used for 2.5D FWI. A more coherent and continuous pattern is observed after the removal of contaminating phases in (b, c) (e.g., elastic modes, surface waves, etc.). Blank areas indicate seismograms without traveltimes because of (b) rejection due to offset errors and noise, and (c) noise. Notice that under a 2.5D scheme, no data rejection due to offset errors is required. . . . .	72
3.3	Full-waveform inversion results. (a) initial velocity model from traveltimes tomography, (b) 2D and (c) 2.5D final FWI model, velocity difference of initial velocity model from (d) 2D (i.e., Figure 3.3b minus 3.3a) and (e) 2.5D (i.e., Figure 3.3c minus 3.3a) FWI model. Dashed black lines represent a preliminary structural interpretation, which is associated with several interpreted fault planes as indicated at the bottom of (b, c). The solid black line in (c) represents an interpreted separation between sedimentary material/deformed volcanic rocks, and more competent volcanic successions at depth. . . . .	78
3.4	Resolution analysis by checkerboard tests, with +/- 5 per cent velocity anomalies superimposed on the initial FATT model. Checkered pattern dimensions are a) 1000x500 m and b) 500x250 m. . . . .	79
3.5	Observed (a, d, g) and synthetic waveforms generated with 2D approach (b, e, h) and the 2.5D approach (c, f, i), and using the respective FWI velocity models. The red line in all panels represents the manually picked first-arrival times on the observed data. The blue arrows indicate severe mismatch areas on the 2D modeled waveforms as well; this same area exhibits a good match on the 2.5D modeled waveforms. . . . .	80
3.6	Source inversion using the a) initial, b) 2D FWI, and c) 2.5D FWI velocity models, respectively. . . . .	83
3.7	Final 2.D FWI velocity model overlaid by a portion of the local geological map of Larder Lake. . . . .	84
4.1	Three different processing line geometries considered for reflection processing. Note, in spite of the apparent width of this cloud, the maximum cross-line dimension was limited to 0.2 km. . . . .	91
4.2	Southern portion of the Larder Lake transect around the LNSZ. Locally optimized bins are shown in red at three different positions along the slalom line. . . . .	93

4.3	CMP gathers using (a, c) the standard binning method, and the (b, d) azimuthal binning method. CMP gathers are located (a, b) north of the LNSZ, and (c, d) north of the LLCDDZ. The horizontal axis indicates the distance along the slalom line, and the alternating red-blue bands indicate CMP fold (i.e., the limits of each color-coded band indicates the amount of traces within that specific bin). Red arrows indicate enhanced signal alignment in (b, d). Blue arrows indicate strong defocusing in (c), caused by reflection time delays from out-of-plane events. . . . .	97
4.4	Stacked CMP traces under the (a) standard (Figure 4.3c), and (b) azimuthal (Figure 4.3d) approaches. There are 5 CMP traces in (a) and (b), corresponding to the 5 CMP bins depicted in Figures 4.3c and 4.3d. Arrows highlight most prominent reflections, blue arrows indicate reflections stacked in-phase by both binning approaches, whereas red arrows indicate reflections preserved only by the azimuthal method. The improvements in (b) indicate the merits of this approach in spite of the slight decrease in fold. . . . .	98
4.5	A portion of the Larder Lake dataset after stacking using the (a) commercially processed stacked section, (b) standard, and (c) azimuthal binning method. The blue arrows indicate a dipping reflector imaged by the in-house processing (b, c), but not by the commercial processing (a). The smaller image at the bottom of each section represents the zoomed-in of the black rectangle. Within the rectangle, cross-dip effects are mitigated by the optimized binning azimuthal binning, as highlighted by the green arrows. . . . .	99
4.6	Stacked sections with varying azimuths (top blue/green header) near the southern domain of the LLCDDZ. Stacks with (a) arbitrary binning, (b) standard binning, (c) binning according to surface geology information, and (d) optimum binning. The binning of (a) and (b) is not geologically-driven. . . . .	100
4.7	(a) Final post-stack migrated section from azimuthal binning. A zoomed-in window of the migrated section near the LLCDDZ is shown from using the (b) commercial processing, (c) CVA model, (d) FATT+CVA model, and (e) FWI+CVA model. The blue and green arrows highlight reflections appearing in the in-house section, but lost in the commercial section. The solid black line in (b) and (e) indicates the vertical extent of the reflection package. Letter F - faults, letter T - truncation surface, SP - splay fault, MLF - Mulven fault, MMF - Misema-Mist fault. . . . .	102
4.8	P-wave velocity model overlying the final migrated seismic section. Remarkable correlation between the different velocity domains in the FWI model and the spatial position of the main breaks on the reflectivity section is observed. . . . .	107

5.1	Geologic map of the Sudbury Structure. Dashed yellow lines indicate the position of Lithoprobe seismic transects; the dashed red line towards the northeast represents the LN182. The receiver and shot geometries of LN182 are shown by the dashed red line and the dashed blue line, respectively. Modified after Ames et al. (2008). . . . .	115
5.2	Source-receiver pairs of data. Black regions indicate available data, whereas white regions indicate unavailable data. (a) after removing non-compliant traces not meeting the offset error criteria (required for a 2D approach), and (b) before removing non-compliant waveforms (ideal for a 2.5D approach). . . . .	118
5.3	Amplitude versus offset bins of (a) forward modeled data, (b) observed data, (c) forward modeled, and observed data after amplitude correction. The observed data are scaled to the synthetic data, mitigating the minimization of large data residuals during the inversion. . . . .	121
5.4	Vibroseis gather at approximately 2 km along the survey geometry. The data are presented (a) prior to preconditioning, with no time windowing or muting; (b) with windowing, muting, F-K filtering, surface-consistent and shot-to-shot amplitude balancing, and with observed-to-synthetic amplitude scaling; (c) with all preconditioning, including low pass filtering and time-damping (with $\tau = 0.1$ s). . . . .	122
5.5	Traveltime residuals mapped onto source and receiver indices, computed using the velocity model (a) before, and (b) after 3D traveltime tomography. . . . .	123
5.6	Final traveltime misfit observed in a (a) common shot array, and (b) common receiver array. The red line represents a Savitzky–Golay smoothing filter, indicating the RMS misfit trend of the full array. . . . .	124
5.7	Final traveltime tomography (starting velocity model for FWI). The grey-shaded region indicates areas in which no raypaths are observed. . . . .	125

5.8	Full-waveform tomography results after stage 17 using the (a) 2D and (b) 2.5D modeling approach. (c) the velocity differences between the model in panel (a) and the model in panel (b). . . . .	130
5.9	Observed (a, d, located at approximately 1.5, and 7.5 km along the model, respectively), and synthetic waveforms generated with the (b, e) 2D and (c, f) 2.5D FWI velocity model. Manually picked first-arrival times are represented by the red line in all panels. The blue arrows indicate a near-offset zone where 2.5D modeling slightly outperforms the 2D modeling in terms of first arrival misfit. . . . .	131
5.10	Final FWI P-wave results, showing a) the velocity model, and b) the detrended velocity model. Both models depict a structural overlay, which correlates with the known geology of the area. Grey-shaded regions indicate areas with little to no energy penetration. . . . .	132
5.11	Time-domain wavelets recovered for each source. These signatures are estimated using (a) the starting FATT model, and (b) the final 2D FWI model. . . . .	133
5.12	(a) observed shot gather located at 2 km along the model. Forward-modeled gather using the (b) starting velocity model, and (c) final FWI velocity model. The red line in all panels indicates the manually picked refracted arrivals. The white rectangle represent a zoomed-in area described below. Black zones highlight waveforms discarded due to low signal-to-noise ratio and/or offset errors. . . . .	134
5.13	Zoom-in on the rectangles displayed in Figure 5.12 showing a) original observed waveforms with no preconditioning, b) observed waveforms after bandpass filtering, re-sampling, and trace decimation, c) synthetic waveforms from the FATT velocity model, and d) synthetic waveforms from the final FWI velocity model. Colored lines in (b) and (d) are indicative of the same seismic phases. . . . .	135
5.14	Recovery of 335x165 m checkerboard patterns, with +/- 5 per cent velocity anomalies superimposed on the starting FATT model. . . . .	137
5.15	Migrated seismic section along the LN182 overlying the final FWI P-wave velocity model. Dashed black lines delineate the trace of transition zones. Blue arrows indicate potential reflection termination patterns. . . . .	138

# Chapter 1

## Introduction

The Earth is a finite entity with finite resources. The Canadian mining industry has been dealing with this reality in the last few decades since the supply from shallow ore endowments of mineral commodities, such as gold copper and nickle, has been declining (Goodfellow et al., 2003). Mining activities are imperative in our modern society as they provide the materials necessary to build the world infrastructure, such as roads, hospitals, electrical grids, and telecommunications. Therefore, deeper exploration of mineral resources appears to be the most feasible option since near-surface deposits are steadily been depleted.

The geological configuration of the first few kilometers of the subsurface is of particular interest for exploration operations. Research shows that in some of the economically significant Canadian mining districts, such as in the Timmins and the Larder Lake area, potential ore bodies may have been placed within 3 km from the Earth surface as a result of post-orogenic tectonic activity (Bleeker, 2015). Therefore, the understanding of the geological architecture of the near surface is crucial to map the structural pathways associated with the migration of mineralized fluids. Traditionally, the mining industry has relied on indirect geophysical methods such as gravity, electric, and magnetic methods to characterize and delineate the mineralized conduits and their relationship with emplacement areas (Olasunkanmi et al., 2017; Gobashy et al., 2020). However, these geophysical methods have strong limitations in spatial resolution, especially at depth, which limits their applicability for deep exploration (Duff et al., 2012). The limitation for targeting mineral deposits at depth has led to the acquisition of surface seismic in crystalline environments across several regions in Canada, Australia, Europe, and Africa, with the hope of overcoming the inherent challenges of hardrock settings (Wright et al., 1994; Malehmir et al., 2012). Some of these challenges relate to the heterogeneity of the medium hosting mineral deposits, the complex geological settings, steeply dipping interfaces causing seismic energy to be scattered in all directions and masking the response from targets, complicated near-surface conditions due to the strong contrast between shallow material and igneous/metamorphic bodies, low intrinsic signal-to-noise

ratio, among others factors. In spite of these obstacles, seismic methods have demonstrated to be highly valuable in crystalline rocks (Adamczyk et al., 2014; Kennett and Saygin, 2015; Malehmir et al., 2017c).

## 1.1 Seismic methods

Controlled source seismic methods have long been used for imaging the structural and stratigraphic configuration of the subsurface. The theoretical development behind the modern methods started almost 300 years ago. Gillin (2020), cites Whewell (1840) as being one of the pioneers in acoustic sciences. However, modern seismology goes further back to the mid-18<sup>th</sup> century when Bevis (1757) and Michell (1761) published their accounts on the Lisbon earthquake of 1755. Shortly after, Mallet (1846) dabbled into seismic wave velocity measurements by means of “artificial earthquakes” and later, in 1857, Mallet studied an earthquake that occurred in Italy in December of that year by implementing principles of physics to describe the origin of earthquake forces. Mallet published his findings in 1862. By the end of the 19<sup>th</sup> century, in 1899, Knott introduced the theory of reflection and refraction of plane elastic waves at interfaces. Readers are referred to by Ari Ben-Menahem (1995) for a thorough chronological sequence of the development of seismic methods.

Seismic methods are designed to study the architecture of the subsurface by analyzing the propagation of acoustic and elastic waves. There are different approaches to generate seismic waves, all of them based on the introduction of a mechanical perturbation into the Earth. This perturbation represents a change in the stress state of the medium, which is measured by recording devices - geophones - located away from the source. In active seismic methods, the source of the perturbation is generally artificially generated by implementing weight drop, hammer, explosives, vibroseis (truck-mounted seismic vibrator), etc., (Hubbard and Linde, 2011). Seismic sources produce different types of waves, the major two classes being body waves and surface waves. Surface waves receive their name because they propagate along, or very near, the surface of the earth. The main type of surface waves are Rayleigh waves, Stoneley waves, and Love waves. The propagation of these waves is confined along or near one of the surfaces that bound the medium, and are quickly attenuated with distance from that surface. Rayleigh waves involves a combination of longitudinal and transverse motion, where particles move along the vertical plane in an elliptical retrograde fashion along the direction of propagation. Stoneley waves are confined to a plane interface of two elastic media, typically a solid-fluid interface but can also exist at a solid-solid boundary provided shear wave velocities are nearly equal in the two media (Aki and Richards, 2002). Love waves involve transverse motion parallel to the surface, which means particles support shear movements in the direction of propagation. A more comprehensive discussion on surface

waves can be found in Sheriff and Geldart (1982).

Body waves are significantly more important in this study due to the type of seismic methods employed to accomplish this thesis's objectives. There are two major classes of body waves. The first type is known as primary, longitudinal, compressional, dilatational, or P-wave. This type of wave is the fastest traveling wave, it propagates through any media that supports seismic waves, and has a particle motion in the same direction along which the wave propagates. The second type of body waves is called secondary, transverse, shear, or S-wave. In contrast to the P-wave, the particle motion of the shear wave is confined within the plane perpendicular to that along which they propagate. Shear waves can only propagate through materials that support shear deformation, hence, they are not observed in fluids. Unlike shear waves, longitudinal waves can effectively propagate through fluids due to their finite compressibility, which allows energy to be transported in space (Dukhin and Goetz, 2010).

Two major seismic methods are employed to acquire and process seismic data: the refraction method and the reflection method. Figure 1.1 displays the ray paths of refracted and reflected seismic waves, and the basic acquisition layout when collecting seismic data in an onshore configuration. The ultimate goal of these methods is to retrieve information about the underlying structure and stratigraphy seismic waves travel through within the subsurface.

### 1.1.1 Seismic refraction method

Geophysical prospecting using a form of the refraction method dates back to the first quarter of the 20<sup>th</sup> century with the discovery of the Orchard salt dome deposit in the Gulf of Mexico by the Texas Gulf Sulfur Company (Green, 1974). The refraction method measures the arrival times of the critically refracted energy that returns to the surface after traveling in the subsurface. The refraction method is mainly focused on first arriving energy, known as the *onset* of seismic energy. These early arrival times are always related to direct arrivals or refracted arrivals. The basic scheme is to register the time it takes the propagating pulse to travel from source to receiver, and then analyze time-distance diagrams to derive information on velocities and depths of different seismically-sensitive subsurface layers. The method is successful when seismic velocity increases with depth, but fails when an inversion in the velocity field is encountered. This is because the rays associated with the wavefield bend away from the horizontal at such an interface. In general, refraction surveys are designed to cover sufficiently long areas to ensure the recording of first arrivals from desired target layers. Most refraction profiles are five to ten times as long as the estimated target depth, which means wide-angle data are vital (i.e., offsets in the range of tens of meters to hundreds of kilometers). Commonly, the velocity structures retrieved by the refraction method are limited in depth, not only due to this offset requirement but also due to limitations on the available

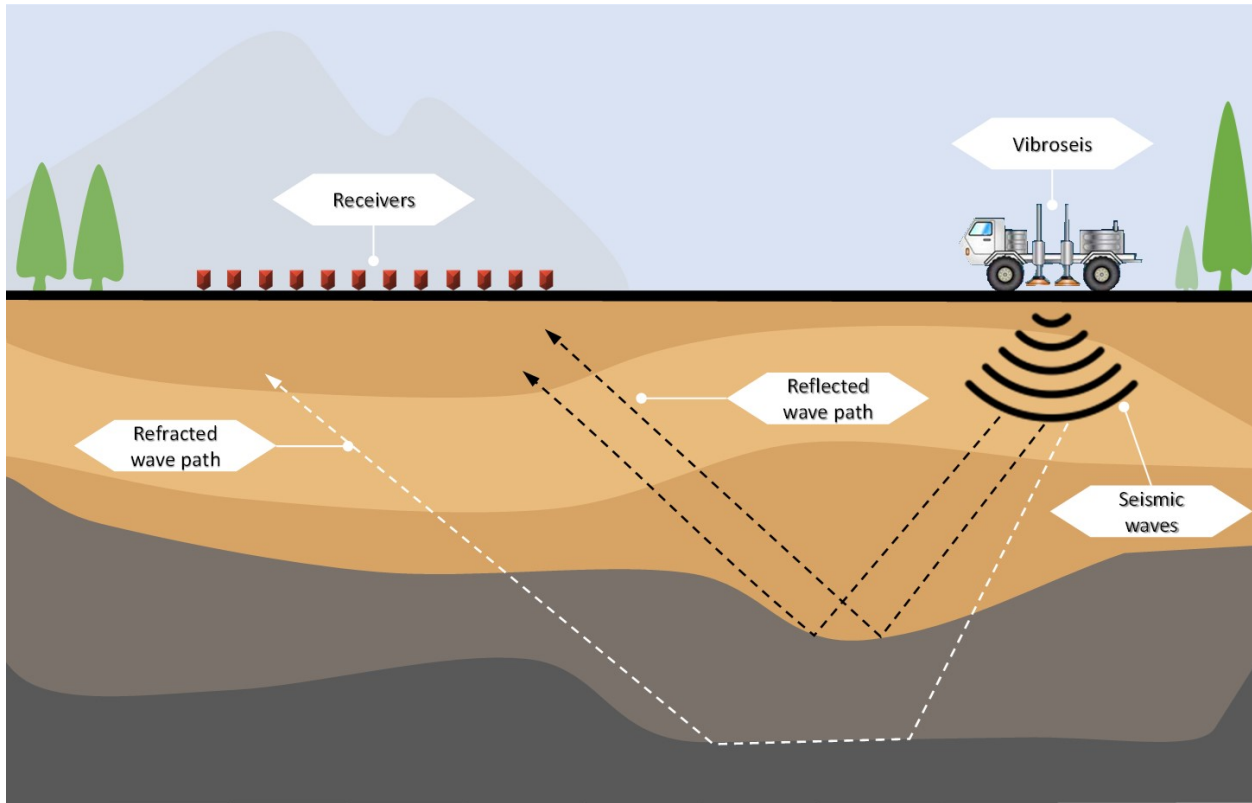


Figure 1.1: Schematic diagram of onshore seismic data acquisition. Examples of wave paths are shown in black for reflected seismic waves, and in white for refracted seismic waves. The source is a truck-mounted vibroseis that introduces vibratory perturbations into the subsurface. Notice that both types of waves are recorded by the receivers (i.e., geophones) located on the surface.

energy necessary to carry out the survey. This is because a large amount of energy is required to transmit seismic waves over long ranges for the reception of deep refracted phases. The availability of these long offset ranges, needed to conduct the seismic experiment is usually limited by environmental concerns, anthropogenic obstacles, etc. The seismic refraction method has a wide range of applications that goes from engineering-related areas (Ma and Qian, 2020), to the geoscience field on crustal-scale (Makris et al., 1983; Clowes et al., 2005) or soil-scale (Flinchum et al., 2018) studies, to onshore (Ebeniro et al., 2018) and offshore (Watremez et al., 2018) projects.

The imaging of subsurface elastic parameters can be achieved by acquiring and processing refraction datasets. The most common parameter model estimated from refraction methods is the long-wavelength component of the near-surface velocity field. This velocity field contains the large- and medium- scale wavelength components of the medium. Therefore, large-scale structural features are successfully retrieved from refraction datasets due to the large source-receiver offsets and the sparsity of station distribution. The inversion of source-receiver traveltimes of seismic refracted phases is the most popular method to recover the low- to medium- wavenumber components of the velocity background (Huang et al., 1986; Zelt and Smith, 1992; Zhang and Tok-

söz, 1998). Low-wavenumbers indicate a smooth velocity behavior (coarse patterns are present), whereas high-wavenumbers indicate a rougher and discontinuous velocity behavior (finer details are present).

### **1.1.2 Seismic reflection method**

The seismic reflection method is similar to its cousin, the seismic refraction method, in that both techniques use similar technology to collect information of the subsurface by using seismic waves. However, seismic reflection profiling is the most widely implemented and well-known geophysical method (Sheriff and Geldart, 1995). This is partly due to the gigantic investment of the oil and gas industry in the development of the method as a subsurface mapping technique. The advancement of computational technology has also played a crucial role in today's state-of-the-art seismic reflection method. Some of the most important breakthroughs in unraveling the secrets of our planet's architecture, such as its structure, composition, and behavior, are due to the use of seismic reflection profiling. Seismic reflection surveying generates high-quality reflectivity images with resolution scales of meters to hundreds of meters depending on the imaging goal (for example, top tens of meters of the subsurface to the entire lithosphere). The general goal of seismic reflection is to map layer boundaries and the structural configuration of the rocks illuminated by the propagation of seismic waves. Seismic profiling relies on the elastic/acoustic contrasts of different materials in the subsurface to generate reflected and back-scattered events that carry information about the architecture of the medium. In surface reflection profiling, these reflected and back-scattered waves are captured by recording systems located along the surface of the Earth. Geophysicists use the information captured by these recording systems to produce migrated seismic images, which is the main end product of the seismic reflection method. Seismic migrated images portrays detailed structural information of the subsurface. The basic characteristics of the seismic experiment are described below.

#### **Seismic reflection surveying and processing in crystalline environments**

Unlike the refraction method, reflection profiling utilizes near-normal incidence elastic energy reflected from subsurface layers. This characteristic indicates the reflection method contains the high-wavenumber components of the subsurface reflectivity, but does not contain the long-wavelength components. In general, seismic surveys are designed to capture either reflected or refracted arrivals and it is rare to use both types of arrivals. However, both types of waves carry important information for the success of seismic processing in generating accurate and high-quality reflectivity images. Seismic waves are recorded by geophones positioned on the ground and their output are called seismic traces. A seismic trace is the representation of time-series containing the

amplitude variations associated with ground motion. These variations stems from the reflections between rock units of different physical properties, controlled by the density and the velocity of the medium, and by the angle of incidence of the incoming wavefront. The differences in physical properties (seismic impedance) are observed in seismic traces by a compressional or dilational initial response of the recorded P-wave. The polarity of the seismic waveform is designated by considering the compression or dilatation of the perceived P-wave. Evaluating the characteristics of a seismic waveform (shape, amplitude, phase) is not enough to directly image or quantify the physical properties that shaped such a waveform. This is because more sophisticated processes must be applied to unlock the information within seismic traces. However, such processes are of little help when the acquired data is of poor quality. Therefore, careful seismic design is a vital step in the reflection technique that aims to collect data with high signal-to-noise ratio while minimizing operational costs and environmental impact.

Much work goes into preserving good signal-to-noise ratio when designing acquisition surveys. Because seismic amplitudes span large ranges, weaker reflection signals might be masked by poor signal-to-noise ratio and/or limitations in instrumentation. This poses a challenge to data acquisition as equipment must have a sufficiently large dynamic range to successfully capture attenuated reflections from deep targets. Up until the 1950s, the primary method for seismic reflection data collection was based on single-fold techniques. Single-fold geometries are designed to probe each point in the subsurface by a single geometric arrangement of a source and receiver, which does not offer redundant data for noise reduction. The single-fold method consists in exciting a source and simultaneously recording the ground perturbation at a number of receiver positions, then moving the source and receivers to a new position for the next source point. Seismic data from single-fold techniques are usually very noisy, which led to the implementation of large seismic arrays using geometric patterns of shots or receivers. Due to the higher costs of sources, receivers are used for designing optimum arrays with sensors wired together to sum their signals and reduce random noise. Only when Mayne (1962) introduced the common midpoint (CMP) acquisition approach, effective noise reduction became possible without requiring large acquisition arrays. Mayne (1962) proposed a method in which each subsurface point has multiple coverage with different source and receiver positions (i.e., different source-receiver offsets). Under this acquisition approach, data may be organized using different configurations. The set of seismic traces excited by the same source is called a common source gather (CSG), the set of traces corresponding to a single receiver group for all excited sources is called a common receiver gather (CRG), and the set of traces where source-receiver distance is constant is called a common offset gather (COG).

The CMP method established the foundations of today's seismic processing approach. As highlighted above, in the CMP approach, the distance between shots and receivers is varied in a systematic fashion to illuminate the same point at depth several times with different offsets.

After collecting the data, traces are sorted into CMP gathers and a time correction is applied to account for the offset variability. This correction is called normal moveout (NMO) correction and the purpose is to align reflection events. Once the seismic traces within a CMP gather are aligned, trace summation is used to increase signal-to-noise ratio. The summation is performed along a hyperbolic trajectory and it is called seismic stacking. The improvement in signal-to-noise ratio occurs because random and coherent noise will not be aligned by the time shifts applied to reflection events. Therefore, the stacking process suppresses the presence of coherent and random noise. The factor by which the signal-to-noise ratio is enhanced is  $\sqrt{N}$ , where  $N$  is the number of stacked traces.

In crystalline settings (or indeed any settings where geographical conditions pose access limitations), the CMP method faces challenges. Seismic acquisition in hard rock terrains, such as those in the Canadian Shield, is often limited by accessibility and environmental restrictions. This also makes full 3D operations prohibitively expensive. Seismic operations rely on existing roads and bush tracks, resulting in severely crooked seismic transects. This crookedness deviates from the ideal straight-line path of the CMP method, which requires near-horizontal sedimentary “layer cake” stratigraphy to succeed. Because reflection points do not lie beneath a crooked acquisition line, a cloud of CMPs is recorded instead (i.e., CMP scattering). This cloud contains reflections that originate from interfaces lying in the offline direction of the survey, increasing the contribution of out-of-plane energy within a CMP gather. This, in turn, degrades energy focusing and causes signal ill-alignment, producing suboptimal reflectivity images. Coupled with the acquisition difficulties, most crystalline terrains are characterized by complex geological structures that further complicate the scenario. For instance, complicated geometry of igneous and metamorphic bodies produces complicated energy scattering. Such energy scattering destructively interacts with reflected energy from continuous or more regular shaped reflectors, further entangling the observed seismic phases. Seismic data acquired in areas with steeply dipping faults and thrust-fold belts, typical in hard rock, are challenging for seismic imaging. These data have intrinsic low signal-to-noise ratio, highly irregular spatial distribution of CMPs and reflection points at depth, non-uniform fold and offset distribution in CMP bins, strong contribution of cross-profile energy that misrepresents or masks reflections from structures beneath the transect, etc. Nonetheless, resolving crystalline structures through seismic imaging has been successful in the past (Nedimović and West, 2003; Milkereit, 2015; Malehmir et al., 2017c; Beckel and Juhlin, 2019). I discuss the foundations of seismic imaging next.

## 1.2 Seismic imaging

We should make a distinction between “reflection imaging” (i.e., migration) and “tomographic imaging”. Tomography is a word borrowed from the Ancient Greek word “*tomos*”, which means section or slice. In medical imaging, “tomography” has come to mean the science of reconstructing targets from their projections (i.e., X-Ray, ultrasound, etc.). Seismic tomography is an imaging method that consists of the projection (using seismic waves) of some physical quantity in order to reconstruct a model of such quantity. This reconstruction requires *modeled* measurements, which are found by simulating *true* observations. In order to recreate *true* observations, a relationship between data space and model space must be established. This relationship is based on mathematical approximations representing the physics controlling the seismic experiment. The main role of such approximations is to generate synthetic data by using a model related to the underlying subsurface parameter of interest (e.g., velocity, density, seismic attenuation, etc.). The tomographic process involves the iterative optimization of the underlying parameter models by minimizing the differences between observed and modeled data. The selection of the appropriate modeling/inversion strategy depends on the characteristics of the seismic experiment itself, which often involves a trade-off between computational efficiency, accuracy and resolution.

The process described above encompasses, in a nutshell, two intertwined concepts in seismic imaging, the forward problem and the inverse problem. The former involves *a priori* knowledge of the physical system and its constitutive properties to describe or predict observables (i.e., measured data). In seismic imaging, the forward problem seeks to evaluate how aspects observed in the measured data, such as traveltimes, amplitudes, attenuation, dispersion, etc., depend on the underlying model parameters describing the physical properties of the subsurface. The inverse problem involves moving backwards. We start by considering the end result (i.e., the measured waveforms), and then applying mathematical methods to characterize the medium the seismic waves passed through. In general, the inverse problem is more difficult to solve than the forward problem. When we work backwards, in the specific case of seismic imaging where we aim to describe the intrinsic physical properties of the medium, the solution is likely non-unique. The non-uniqueness of the inverse approach means that different representations of the model parameter can equally map to the observed data due to the ill-posedness and underdetermined nature of the inverse problem. Although the ill-posedness of the inverse problem may be mitigated by introducing *a priori* information, it is still an intricate process because the available information is often not enough to formulate a properly posed problem. For instance, observed seismic data are waveforms resulting from the combined interaction between the properties of the medium and the source signature. Neither of these elements are usually known, contributing to the non-uniqueness of the inverse problem.

We can classify seismic imaging techniques based on their objectives as suggested by Wapeenaar (1996). In a broad sense, we can consider two categories, reflectivity imaging and subsurface parameter imaging. The former refers to the long-standing reflection processing technique that aims to reconstruct the high-wavenumber components of the data by solving for the reflection/transmission coefficients. The end goal of reflectivity imaging is the generation of seismic migrated sections as described in Section 1.1.2 and exemplified in the works of Hagedoorn (1954); Claerbout (1971); Schneider (1978); Sava and Fomel (2006); Zhou et al. (2018). Subsurface parameter imaging, on the other hand, aims to reconstruct both the low- and high- wavenumber components in the dataset by explicitly solving an inverse problem (Lailly, 1983; Tarantola, 1984a; Wu and Toksöz, 1987; Pratt et al., 1998; Pratt, 1999). The most common inverted parameter model historically is that of seismic velocity, which is a prerequisite to perform conventional seismic processing. Two common methods for the reconstruction of the velocity field from seismic data are traveltime tomography and full waveform tomography. In this study, these two methods are combined to render near-surface velocity structures containing the low- and high- wavenumber features of the wavefield.

### 1.2.1 Traveltime Tomography

Conventionally, seismic tomography has used the traveltimes of the first-arrival waves to estimate the velocity structure of the subsurface (Ivansson, 1985; Phillips and Fehler, 1991; Moser, 1991; Zelt, 1999). The determination of such traveltimes in laterally and vertically varying media has traditionally required some sort of ray tracing technique (Vidale, 1988). The basic equation to calculate traveltimes and rays is the Eikonal equation, that may be derived by applying high-frequency asymptotic methods to the acoustic wave equation. Cerveny (2001) showed that considering an acoustic wave equation for pressure,  $P$ , with a variable velocity,  $c = c(\mathbf{x})$ , a constant density, and no source term,

$$\nabla^2 P(\mathbf{x}, t) = \frac{1}{c^2(\mathbf{x})} \ddot{P}(\mathbf{x}, t), \quad (1.1)$$

an approximate time-harmonic high-frequency solution could be found in the form,

$$P(\mathbf{x}, t) = A(\mathbf{x}) e^{[-i\omega(t-T(\mathbf{x}))]}, \quad (1.2)$$

which, in turn, represents a plane-wave solution for  $A(\mathbf{x}) = \text{const.}$ , and  $T(\mathbf{x}) = P\mathbf{x}$ , where  $T(\mathbf{x})$  is the time delay (traveltime) at a particular position  $\mathbf{x}$ . The key assumption is that the frequency,  $\omega$ , is high,  $\omega \gg 0$ .

Now, using the vector identity  $\nabla \cdot a\mathbf{b} = \mathbf{b} \cdot \nabla a + a\nabla \cdot \mathbf{b}$ , it can be demonstrated that

$$\nabla^2 P(\mathbf{x}, t) = \left\{ i\omega (\nabla A + i\omega A \nabla T) \cdot \nabla T + \left( \nabla^2 A + i\omega \nabla T \cdot \nabla A + i\omega A \nabla^2 T \right) \right\} e^{[-i\omega(t-T(\mathbf{x}))]}.$$

Therefore, equation (1.1) can be expressed as follow,

$$-\omega^2 A \left[ (\nabla T)^2 - 1/c^2 \right] + i\omega \left[ 2\nabla A \cdot \nabla T + A \nabla^2 T \right] + \nabla^2 A = 0. \quad (1.3)$$

For frequencies approaching infinity,  $\omega \gg 0$ , the key terms are the first (with  $\omega^2$ ), and the second (with  $\omega$ ), and because high-frequency solutions are been sought, these two terms should vanish. The Eikonal equation is then defined,

$$(\nabla T)^2 = \frac{1}{c^2}. \quad (1.4)$$

Equation (1.4) plays an vital role in the ray method, representing a nonlinear partial differential equation of the first order for traveltimes,  $T(\mathbf{x})$ . This equation is often solved by ray tracing, where traveltimes and rays are calculated. Rays can be defined as characteristics of the Eikonal equation that represent the normal to the wavefront, pointing in the direction of propagation (Cerveny, 2001).

The ray method is applicable both in isotropic and anisotropic media, and it is based on the concept that seismic data with very high frequencies follows a certain trajectory according to the ray tracing equations (Vidale, 1988). Traveltime tomography by means of the ray method faces significant limitations. One of the main weaknesses of the ray method is the asymptotic high-frequency assumption (i.e.,  $\omega \gg 0$ ), as invoked above, because it is only valid for the high-frequency components of the wavefield, which results in an incomplete approach. Rays, as used in ray theory, behave much like rays of light propagating through materials with different refraction indices. If variations in these refraction indices are discontinuous, high-frequency asymptotic ray theory fails (or needs special treatments). The ray method implies the medium should vary smoothly compared to the wavelength. This limits ray theory to retrieve low wavenumber information only. Additionally, there are natural limits for how high frequencies can be as they have finite values. Thus, the assumption for asymptotic expansion causes a decrease in the reliability and accuracy of the method. In reality, seismic waves with finite frequencies do not travel along infinitely thin ray paths between source and receiver locations, they rather propagate through different geometric configurations along a wavepath, which interrogates a larger part of the subsurface. Therefore, the structure of the propagating wavefront is changed and so are the traveltimes, causing them to deviate from their ray-theoretical values.

Another weakness inherent to the ray method is the fact that the magnitudes of the underlying parameter models should vary smoothly with respect to the size of the minimum wavelength in the

data. This does not mean the ray approximation is not applicable in complex settings; however, one must meet the “smoothness” requirement. As highlighted by Vidale (1988), if the models change rapidly with respect to the wavelength, there may be many different paths that connect two points of interest. Consequently, when many paths are available, the one with the minimum traveltime may be easily missed, reducing the accuracy of the result. This implies that asymptotic ray theory is suitable for relatively thick layered models, and breaks down for fine layering and rapid model parameter changes within those layers. In addition, ray-based methods tend to fail in certain singular regions such as shadow zones and at or around caustic points (where the amplitude of the ray is predicted to be infinite).

There are additional approaches that attempt to overcome the limitations of ray tracing for the estimation of first-arrival traveltimes, such as wavefront tracking schemes in which finite-difference solutions of the Eikonal equation are introduced (Vidale, 1990; Podvin and Lecomte, 1991; Cao and Greenhalgh, 1994; Qian and Symes, 2002). Finite-difference techniques offer a more attractive alternative to estimating traveltimes on a regular grid as they are less computationally expensive than ray-based methods (Mo and Harris, 2002). Although the finite-difference approach goes a step forward and considers the propagation of wavefronts rather than rays, the method faces significant difficulties. For instance, the finite-difference method is prompt to fail when applied to models containing strong first-order velocity contrasts (Podvin and Lecomte, 1991). Both approaches described above are only appropriate for computing first-arrival traveltimes, which is accomplished by finding solutions to the Eikonal equation through either the modeling of the propagation of geometric rays (i.e., the ray method), or wavefronts (i.e. the finite-difference/finite-element methods). Both approaches share a dependence on the asymptotic high-frequency approximation used to obtain the Eikonal equation.

### **Nonlinear traveltime tomography**

Here I briefly present the theoretical basis of the nonlinear traveltime tomography method introduced by Zhang and Toksöz (1998). The velocity field represents one of many model parameters,  $\mathbf{m}$  (i.e., slowness), that can be used to predict a set of data,  $\mathbf{d}$  (i.e., traveltimes), for a given source-receiver array by means of integration through the model, as shown by equation (1.4). Any tomographic problem can be represented as the combination of data and model parameters (more often than not, this combination is non-linear),

$$\mathbf{d} = \mathbf{G}(\mathbf{m}), \quad (1.5)$$

where  $\mathbf{G}$  is the scientific theory connecting the data parameters to the model parameters, representing the physical laws used to establish the relationship between  $\mathbf{d}$  (traveltimes) and  $\mathbf{m}$ . If  $\mathbf{G}$



The objective function used for data optimization is,

$$\begin{aligned}\Phi(\mathbf{m}) &= (1 - \bar{\omega}) \|\zeta_{\Psi}(\mathbf{d} - \mathbf{G}(\mathbf{m}))\|^2 + \bar{\omega} \|D_x(\mathbf{d} - \mathbf{G}(\mathbf{m}))\|^2 + \tau \|\mathbf{Rm}\|^2 \\ &= (1 - \bar{\omega}) \|\bar{\mathbf{d}} - \bar{\mathbf{G}}(\mathbf{m})\|^2 + \bar{\omega} \|\hat{\mathbf{d}} - \hat{\mathbf{G}}(\mathbf{m})\|^2 + \tau \|\mathbf{Rm}\|^2,\end{aligned}\quad (1.7)$$

where  $\bar{\omega}$  is a weighting factor between average and apparent slowness's misfit norm,  $\mathbf{G}(\mathbf{m})$  is the predicted traveltimes data,  $\mathbf{m}$  represents the model parameter set,  $\zeta_{\Psi}$  is a traveltimes scaling operator,  $\Psi$  is the ray length,  $D_x$  is a differential operator for traveltimes with respect to distance,  $\mathbf{R}$  is a regularization operator acting on the model parameters,  $\tau$  is a smoothing parameter,  $\bar{d} \equiv \frac{d}{\Psi}$  is the average-slowness data,  $\hat{d} \equiv \frac{\partial d}{\partial \Psi}$  is the apparent-slowness data (gradient of traveltimes-distance curves). The minimization of the objective function in equation (1.7) constrains the model space considering the integrated traveltimes, the gradient of the traveltimes curves, and a regularization term controlling the roughness of the solution.

The minimization of equation (1.7) is accomplished by implementing the Gauss-Newton method, and then solving the inverse problem by applying a conjugate gradient technique. This avoids the explicit construction of the sensitivity matrix (the Fréchet derivatives matrix). The inversion of the refraction traveltimes data is performed by considering the following expression,

$$\begin{aligned}& \left( (1 - \bar{\omega}) \Upsilon_k' \Upsilon_k + \bar{\omega} \Lambda_k' \Lambda_k + \tau \mathbf{R}' \mathbf{R} + \epsilon_k \mathbf{I} \right) \Delta \mathbf{m}_k \\ &= (1 - \bar{\omega}) \Upsilon_k' (\bar{\mathbf{d}} - \bar{\mathbf{G}}(\mathbf{m})) + \bar{\omega} \mathbf{B}_k' (\hat{\mathbf{d}} - \hat{\mathbf{G}}(\mathbf{m})) - \tau \mathbf{R}' \mathbf{R} \mathbf{m}_k,\end{aligned}\quad (1.8)$$

where

$$\Upsilon \equiv \frac{\partial \bar{\mathbf{G}}}{\partial \mathbf{m}} = \frac{1}{\Psi} \cdot \frac{\partial \mathbf{G}}{\partial \mathbf{m}}, \quad (1.9)$$

$$\Lambda \equiv \frac{\partial \hat{\mathbf{G}}}{\partial \mathbf{m}} = \frac{\partial^2 \mathbf{G}}{\partial \mathbf{m} \partial x}, \quad (1.10)$$

$$m_{k+1} = m_k + \Delta m_k, \quad (1.11)$$

$$k = 1, 2, 3, \dots, N;$$

$k$  represents the iteration number,  $\Delta \mathbf{m}$  is the velocity model update, and  $\Upsilon$  and  $\Lambda$  are the average-slowness and the apparent-slowness sensitivity matrix, respectively (Zhang and Toksöz, 1998). Each non-zero term in  $\Upsilon$  is the division of the local ray length across a cell by the entire ray length, whereas each non-zero term in  $\Lambda$  represents the differences of the ray lengths in a cell divided by the receiver spacing.

The nonlinear traveltime tomography method introduced by Zhang and Toksöz (1998) produces low-wavenumber models where sufficient ray coverage is present, successfully describing the long-wavelengths components of the velocity background, which makes the technique suitable for addressing the half-cycle phenomenon crucial to the full waveform inversion technique. This phenomenon occurs when predicted vs observed data (traveltimes in this case) residuals have errors higher than half a period (Virieux and Operto, 2009).

### 1.2.2 Forward modeling

Before continuing into the discussion on waveform inversion, let us formulate the forward problem. Accurate modeling of wavefield propagation is vital when attempting waveform inversion because one of the two primary data inputs are predicted seismograms (synthetic data). One of the most accurate forms of forward modeling is the implementation of the visco-elastic wave equation in anisotropic media (Saenger and Bohlen, 2004; Angus et al. 2004). However, even today, solving for the visco-elastic wave equation in three dimensions represents a huge computational burden. Hence, solving the acoustic or visco-acoustic wave equation (Kosloff and Baysal, 1982; Yan and Liu (2013); Kamei and Pratt, 2013), has proved to render optimum results despite the fact that elastic effects and anisotropy are neglected.

In this work, it is assumed that the simulation of wave propagation is adequately described by solving the acoustic wave equation in two dimensions (2D) by means of finite-difference methods, which avoid the use of the asymptotic high-frequency ray approximation (Pratt, 1999). The 2D isotropic, visco-acoustic wave equation in the frequency domain is

$$\nabla \cdot \left( \frac{1}{\rho(x, z)} \nabla u(x, z; \omega) \right) + \frac{\omega^2}{\kappa(x, z)} u(x, z; \omega) = f(x, z; \omega), \quad (1.12)$$

where  $\rho$  is the bulk density,  $\kappa$  is the bulk modulus,  $\omega$  is the angular frequency,  $u$  is the pressure field,  $f$  is a generalized source term,  $x$  and  $z$  represent planes along which wave propagate. The acoustic assumption is frequently used in exploration seismics as we are primarily interested in P-waves. The viscous terms are easily incorporated by using a complex-valued modulus in order to better include attenuation effects. The 2D wave equation assumes there is no variation in the properties of the medium along the  $y$  plane (i.e.,  $y = 0$ ). This implies that the source extends infinitely in the direction perpendicular to the shooting line, effectively forming a line source in 3D space.

In order to abandon the assumption that the physics extend to infinity in the out-of-plane direction, and hence wavefronts propagate cylindrically from a line source, a 2.5D modeling approach can be introduced. As described by Song and Williamson (1995); Song et al. (1995); Zhou and Greenhalgh (2006), among others, the propagation of visco-acoustic wavefields, assuming a (3D) point source, can be better illustrated by the 2.5D wave equation,

$$\left( \nabla \cdot \left( \frac{1}{\rho(x, z)} \nabla \right) + \frac{\omega^2}{\kappa(x, z)} - \frac{k_y^2}{\rho(x, z)} \right) u(x, k_y, z; \omega) = f(x, k_y, z; \omega), \quad (1.13)$$

where  $k_y$  is the transverse wavenumber component. The 3D wavefield response,  $u(x, y, z)$ , in the frequency domain is calculated by the inverse spatial Fourier transform with respect to  $k_y$ ,

$$u(x, y, z; \omega) = \int_{-\infty}^{\infty} u(x, k_y, z; \omega) e^{(-ik_y y)} dk_y, \quad (1.14)$$

for a range of out-of-plane wavenumbers determined by a maximum wavenumber value called *critical value of the medium*,  $k_c$ . This *critical value of the medium* highlights the separation between wave propagation and evanescent fields (Zhou and Greenhalgh, 2006). The out-of-plane wavenumber range over which the wave equation is solved can be expressed as,

$$k_{y\text{range}} = [0, \min(k_c)]. \quad (1.15)$$

Once the range of transverse wavenumbers is established, the next key step is to define the sampling,  $\Delta k_y$ , required for the reconstruction of the cross-profile component. We follow the efficient sampling strategy introduced by Zhou and Greenhalgh (2006) based on the maximum available source-receiver distance, the medium velocity, and the temporal frequency being inverted.

Seismic attenuation is responsible for energy dissipation of propagating waves. As a result, seismic waves experience exponential amplitude decay as they travel through the subsurface due to different effects including geometrical spreading, absorption, and scattering. Because full-waveform inversion relies on the computation of synthetic waveforms, the mathematical modeling approach must account for attenuative effects. The introduction of a complex-valued velocity field,  $c$ , readily allows attenuation,  $Q^{-1}$ , to be implemented in the frequency domain using the imaginary part (Song et al., 1995),

$$Q^{-1}(x, z) = -\frac{\Im[c(x, z; \omega)]}{2\Re[c(x, z; \omega)]}, \quad (1.16)$$

where  $Q^{-1}$  is the inverse of the seismic quality factor,  $c$  represents a complex-valued quantity,  $\Im[c(x, z; \omega)]$ , and  $\Re[c(x, z; \omega)]$  indicate the imaginary and real part of the complex-valued velocity field. The velocity,  $c$  is obtained from bulk modulus and density using  $c = \sqrt{k/\rho}$ . Because we are considering attenuative media, a dispersion relationship (i.e., a relationship describing velocity changes as a function of frequency), such as the one presented by Aki and Richards (1980), is introduced.

The numerical system implicit in equation (1.12) and equation (1.13), defined in the Fourier space for each source, can be expressed in its discrete form as in Pratt et al. (1998), where dependency on model parameters and frequency has been dropped for notation simplicity,

$$\mathbf{S}\mathbf{u} = \mathbf{f}, \quad (1.17)$$

where  $\mathbf{u}$  represents the pressure wavefield, and  $\mathbf{f}$  the source wavefield, both usually act at every node point of the regularly spaced finite-difference grid ( $\Delta = \Delta x = \Delta z$ ) with dimensions  $N_x \times N_z$ .  $\mathbf{S}$  is the complex-valued impedance matrix that represents the physics of wavefield propagation, and only depends on the frequency and on the model parameters (Pratt and Worthington, 1990). Note that the notation used here is different from the notation used in Section 1.2.1. This is done to emphasize the difference in methods, in Section 1.2.1 I describe the theoretical background of ray methods, used for travelttime tomography; in contrast, here I describe the theoretical background of wave methods as preamble for full-waveform inversion.

Re-arranging equation (1.17),

$$\mathbf{u} = \mathbf{S}^{-1}\mathbf{f}, \quad (1.18)$$

which represents the solution to the forward problem, not to be mistaken with the inverse problem. The pressure field,  $\mathbf{u}$ , can be obtained by solving the system of equations in (1.17) and (1.18) without explicitly computing  $\mathbf{S}^{-1}$ . A direct-solver approach based on a lower-triangular upper-triangular (LU) decomposition of  $\mathbf{S}$  is used by means of nested dissection (George et al., 1994), and a mixed-grid finite-difference approach developed by Pratt and Worthington (1988) and Jo et al. (1996). Absorbing boundary conditions are the conditions applied at the artificial boundaries of a numerical model to mitigate the generation of undesired reflections due to its finite dimensions. The absorbing boundary condition used in this work is based on the perfectly matched layer method (Chen et al., 1995; Hastings et al., 1996).

### 1.2.3 Laplace-Fourier Domain

So far I have described the forward problem in terms of a matrix formalism in the frequency domain where the frequency itself,  $\omega$ , is real-valued. Brenders and Pratt (2007b) introduced the concept that the nonlinearity of the inverse problem can be reduced by focusing the inversion on early arriving waveforms, while damping the amplitudes of later arrivals. The relevance of such approach lies in the time damping functionality, which is not possible in the Fourier domain. Shin and Ho Cha (2009) further developed this concept by introducing the ‘‘Laplace-Fourier domain’’, in which the frequency components implicit in equation (1.17),  $\omega$ , are replaced with complex-valued frequency components,  $\Omega$ . Following the formalism in Shin and Ho Cha (2009); Kamei and Pratt (2013); Kamei et al. (2015); consider the Laplace transform for a time domain wavefield as,

$$u(\sigma) = \int_{-\infty}^{\infty} u(t) e^{-i\sigma t} dt, \quad (1.19)$$

where  $\sigma$  is a real-valued Laplace parameter,  $t$  is time, and  $u(t)$  is the pressure wavefield. The Fourier transform of the time-domain wavefield can be written as,

$$u(\Omega) = \int_{-\infty}^{\infty} u(t) e^{-i\Omega t} dt, \quad (1.20)$$

where  $\Omega = \omega - i\sigma$  is a complex frequency. Rewriting the Fourier transform in (1.20),

$$u(\Omega) = \int_{-\infty}^{\infty} u(t) e^{-\sigma t} e^{-i\omega t} dt, \quad (1.21)$$

and further considering  $\sigma = \frac{1}{\tau}$  as a real-valued Laplace constant, equation (1.21) can be written as,

$$u(\Omega) = \int_{-\infty}^{\infty} u(t) e^{-\frac{t}{\tau}} e^{-i\omega t} dt. \quad (1.22)$$

Equation (1.19) and equation (1.22) show that, by using complex-valued frequencies, we can obtain the Fourier transform of the original time-domain wavefield, multiplied by a time damping factor,  $e^{-\frac{t}{\tau}}$ . This damping factor serves as a preconditioning operator as highlighted by Brenders and Pratt (2007b), in the sense that the nonlinearity of the problem can be mitigated by only allowing the early part of the waveforms into the reconstruction, which results in the fitting of the very low-wavenumber components of the velocity field. This is because refracted arrivals represent the most linear components of the wavefield, and are more sensitive to low wavenumbers than other seismic phases. Fitting this portion of the data reduces the risk of cycle skipping. This is possible in the Laplace-Fourier space due to the introduction of complex-valued frequencies. Progressive relaxation of the characteristic decay time factor,  $\tau$ , in the Laplace-Fourier domain, enables the inclusion of different types of arrivals with different resolution power.

## 1.2.4 Waveform Inversion

Although not strictly correct, the terminology full-waveform inversion and waveform inversion are used interchangeably throughout this work. Mostly, I use full-waveform inversion, or simply “FWI”. Mora (1987) stated that the vast amount of the information contained within a seismic waveform, such as diffractions, ground roll, refractions, multiples, and mode conversions, is ignored in the traveltime tomography technique described in Section 1.2.1. A more comprehensive approach for subsurface imaging, based on the complete description of the wave equation, was introduced by Lailly (1983) and Tarantola (1984a). This technique is known as FWI, and can be described as a generalized inverse process that requires only a forward modeling code, its adjoint, and an iterative numerical-solver (Margrave et al., 2011). Full-waveform inversion involves the optimization of a subsurface parameter model by minimizing an objective function. This function measures the differences between observed and synthetic waveforms predicted from an estimated

model (Kamei et al., 2015).

### **State-of-the-art of FWI**

In principle, full-waveform inversion is capable of reconstructing any subsurface parameter model to which seismic waves are sensitive, provided the physics used for wavefield simulations are appropriate. The most comprehensive approach to this end is based on 3D anisotropic visco-elastic finite approximation models. Anisotropic elastic FWI have been successfully performed using borehole and surface seismic data. For instance, Owusu et al. (2015) implemented high-frequency FWI to a walkaway vertical seismic profile, retrieving a layered geological model in the Arabian Gulf. Wang et al. (2021) retrieved P-wave velocity, P-impedance, and Vp/Vs ratio using a 3D dataset from deepwater West Africa by implementing anisotropic 3D elastic FWI up to 50 Hz.

Bergslid et al. (2015) studied the influence of anisotropy on elastic FWI. They found that not considering anisotropy may drive the inversion towards erroneous results, and the use of a simple anisotropic model is enough to perform elastic FWI in anisotropic media. Trinh et al. (2019) simultaneously inverted for P- and S-wave velocity fields using a 3D elastic and visco-elastic FWI approach, where the anisotropic characteristics of the medium were constrained by a nonstationary Bessel filter (Trinh et al., 2017a). They showed that S-wave velocity fields are better constrained by properly modeling surface waves. Trinh et al. (2019) used the SEAM II Foothill dataset, which is a synthetic dataset aimed at illustrating the imaging challenges of mountainous regions. Similarly, Teodor et al. (2021) used a 3D anisotropic and nonstationary Bessel filter during their implementation of 3D elastic FWI. In their study, Teodor et al. (2021) integrated surface waves analysis techniques with 3D elastic full-waveform inversion to enhance the imaging of geologically complex near-surface targets.

However, due to the high computational costs associated with three-dimensional FWI, its application is still prohibitive across many academic and industrial programs. Therefore, many studies involving elastic approximations are still restricted to 2D modeling such as Köhn et al. (2012); Groos et al. (2017); Borisov et al. (2020); Djeflal et al. (2021); Plessix and Krupovnickas (2021). Studies accounting for anisotropy often use an acoustic approximation as a way to optimize computational resources, such as Warner et al. (2013); Shin et al. (2019). Warner et al. (2013) solved for the 3D anisotropic acoustic wave equation, and implemented FWI to a 3D dataset with significant P-wave anisotropy over the Tommeliten Alpha field in the North Sea. Their results revealed a low-velocity region associated with a gas cloud closely correlating with available borehole information and reflectivity images. Shin et al. (2019) performed monocomponent multiparamter FWI in VTI media by properly simulating PP radiation patterns for anisotropic parameters.

Important advancements in terms of imaging deeper portions of the subsurface, still within a full-waveform inversion framework, have been proposed. Conventional FWI relies on very long

offsets and uses refraction information from diving and turning waves to update the underlying model parameter. However, these updates are limited to the portion of the earth interrogated by such refracted arrivals. In contrast, reflection-based FWI not only attempts to perform deep model updates by using the reflection component of the dataset, but also may be a more suitable approach than conventional FWI when the dataset is dominated by reflected seismic phases. This is because, under such circumstances, the gradient updates of conventional FWI may be dominated by the high-wavenumber components of reflections, even after performing judicious data preprocessing and gradient preconditioning.

Sun et al. (2016) and Sun et al. (2017) proposed a decomposition of a subsurface model into its tomographic and reflectivity components to build the background macro velocity field of conventional FWI. Wang et al. (2019a) addressed potential contamination of the gradient image from the contribution of the reflectivity component (i.e., high-wavenumber migration artifacts) by explicitly generating the tomographic component using Born modeling, minimizing the contribution of migration-like updates when reconstructing the low-wavenumber velocity background. Martin et al. (2021) illustrated a similar approach where the cross-talk between high- and low-wavenumber features is mitigated by implementing a cascade of two different solutions to the acoustic wave equation based on the wavefield decomposition of background (low wavenumber) and perturbation (high wavenumber) components. They showed that with this approach, no *a priori* density information is required as they converted the variable density acoustic wave equation to a vector-reflectivity one (evoking the inevitable coupling of velocity and density at high frequencies).

## Theory

Because FWI is a computational-intensive technique, Lailly and Tarantola were not successful in implementing it to retrieve the low-wavenumber components of the velocity background. Full-waveform inversion only became practical when Pratt and his collaborators established FWI in the frequency domain in the early 1990s (Pratt, 1989, 1990; Pratt et al., 1996, 1998; Pratt, 1999). They investigated the feasibility of early-arrival FWI in updating the long-wavelength components of the velocity field. While Lailly and Tarantola initially proposed the use of the full set of seismic phases available within a seismic experiment for velocity reconstructions, Pratt and his collaborators focused on refracted arrivals, which are more sensitive to the low wavenumbers than, for instance, reflected phases. The technique can be implemented either in the time or in the frequency domain. Sirgue and Pratt (2004), showed that frequency-domain inversion, using a reduced set of frequencies, yields equivalent results to those from time-domain inversion, at a much smaller computational cost. I implement full-waveform inversion in the Laplace-Fourier domain, as explained in Section 1.2.3.

Full-waveform inversion is an inverse problem in which we try to find a model parameter (rep-

representing, for instance, a physical quantity like velocity) that minimizes the differences between predicted (synthetic) and observed (measured) seismic waveforms in a least-squares manner. Such minimization aims to reconstruct the “true” variations of a particular model parameter in a quantitative sense. To address the inverse problem, we need to define a set of model parameters,  $\mathbf{m}$ , at every node point of the finite-difference grid, and use equation (1.18) to generate modeled waveforms with which estimate data residuals,  $\delta\mathbf{d}$ . The difference between predicted and observed waveforms (i.e. data residuals) is described in the Laplace-Fourier domain as,

$$\delta\mathbf{d} = \mathbf{u}(\mathbf{m}) - \mathbf{d}, \quad (1.23)$$

where  $\delta\mathbf{d}$ ,  $\mathbf{u}$ , and  $\mathbf{d}$  are complex-valued and depend on  $\Omega$  (omitted in the equations for notational simplicity). These data errors are defined at each source-receiver pair where the observed data are available at  $n$  receiver locations, and any given parameter model can be estimated at each of those locations. Thus,  $\mathbf{u}$ , and  $\mathbf{d}$  can be represented in vector form as (Pratt et al., 1998),

$$\mathbf{d} = \begin{pmatrix} d_1 \\ d_2 \\ \vdots \\ d_n \end{pmatrix}; \mathbf{u} = \begin{pmatrix} u_1 \\ u_2 \\ \vdots \\ u_n \end{pmatrix}. \quad (1.24)$$

Data residuals as described by equation (1.23) are a generic form of representing residuals, called “conventional phase-amplitude” residuals. This conventional approach for calculating the differences between waveforms is simply defined as,

$$\delta d_j = u_j - d_j \quad (1.25)$$

where  $j = (1, 2, \dots, n)$ . In this work, we use a combination of conventional phase-amplitude data residuals as in equation (1.25), and “logarithmic phase-only” data residuals as indicated below.

Logarithmic phase-only residuals are defined following Shin and Min (2006). The estimated and observed wavefield (i.e.  $\mathbf{u}$ , and  $\mathbf{d}$ , respectively) can be written as plane waves,

$$u_j = A_{u_j} e^{(i\theta_{u_j})}, \quad (1.26)$$

and

$$d_j = A_{d_j} e^{(i\theta_{d_j})}. \quad (1.27)$$

Substituting equation (1.26) and equation (1.27) into equation (1.25),

$$\delta d_j = A_{u_j} e^{(i\theta_{u_j})} - A_{d_j} e^{(i\theta_{d_j})}, \quad (1.28)$$

we obtain data residuals that depend on data amplitude errors, whose magnitudes act as weighting

factors during the inversion.

Equation (1.28) can be separated into its amplitude and phase components,

$$\delta d_j = \ln\left(\frac{A_{uj}}{A_{dj}}\right) + i(\theta_{uj} - \theta_{dj}). \quad (1.29)$$

Further separating the data residuals in equation (1.29) in terms of its imaginary part, the expression for logarithmic phase-only residuals is found,

$$\delta d_j^\dagger = \Im\left[\ln\left(\frac{A_{uj}}{A_{dj}}\right) + i(\theta_{uj} - \theta_{dj})\right] = (\theta_{uj} - \theta_{dj}). \quad (1.30)$$

The dynamic and kinematic components of data residuals can be effectively separated into the real and imaginary parts of equation (1.29). The logarithmic phase-only wavefield residuals allow the inversion to focus on the kinematics (i.e. phase component) of the data, which is helpful during early stages of full-waveform inversion. This is because the inversion is sensitive to the magnitude of amplitudes in the observed waveforms.

To minimize data residuals, we establish a least-squares norm,  $L_2$  norm, of the misfit vector,  $\delta \mathbf{d}$ , in equation (1.23),

$$E(\mathbf{m}) = \frac{1}{2} \delta \mathbf{d}^t \delta \mathbf{d}^*, \quad (1.31)$$

where  $E(\mathbf{m})$  is the objective function,  $t$  represents the transpose of the data residuals, and  $*$  is its complex conjugate, which ensures the objective function is real-valued (recall that wavefields  $\mathbf{u}$ , and  $\mathbf{d}$  are complex-valued). Equation (1.31) ignores any *a priori* statistical information on data or model co-variance,  $\mathbf{C}_d$  and  $\mathbf{C}_m$ , which are used to weight the relative contributions of data residuals and model perturbations. This effectively assumes uncorrelated data and uniform variances, setting  $\mathbf{C}_d$  and  $\mathbf{C}_m$  equal to identity matrices, implying both data and model parameters are equally important.

Different numerical optimization methods have been developed to minimize the misfit function,  $E(\mathbf{m})$ , with two main groups being global and local inverse search methods. Both categories seek the global solution by exploring the topography of the objective function. In most instances, global searches of the optimal parameter set are not feasible due to the size of the problem. This is because global methods attempt to find the best-fitting model by exploring the full range of the model space, resulting in high computational costs. In contrast, local search methods rely on the accuracy of the starting point. Therefore, local searches must be within the basin of attraction of the global minimum to succeed. The optimization employed in this study is based on a steepest descent local minimization method, the conjugate gradient method,

$$\mathbf{m}_{(k+1)} = \mathbf{m}_{(k)} - \alpha_k \nabla_{\mathbf{m}} E_k, \quad (1.32)$$

where  $k$  is the iteration number,  $\alpha$  is the step length, and  $\nabla_{\mathbf{m}}E$  represents the gradient of the objective function with respect to every model parameter. Following Pratt et al. (1998), the gradient of the misfit function can be written as,

$$\nabla_{\mathbf{m}}E(\mathbf{m}) = \Re \{ \mathbf{J}' \delta \mathbf{d}^* \} \quad (1.33)$$

where  $\mathbf{J}$  is the sensitivity or Fréchet matrix, which represents the partial derivatives of the wavefield,  $\mathbf{u}$  in equation (1.17), with respect to the model parameters,  $\mathbf{m}$ .  $\mathbf{J}$  is defined as  $\mathbf{J} = \frac{\partial \mathbf{u}}{\partial \mathbf{m}}$ . The gradient is defined as the real part of equation (1.33) to ensure the resulting gradient is real-valued. This is because elements of the Fréchet derivative matrix, and data errors are complex-valued. However, the expensive computation of the Fréchet matrix is avoided by using the adjoint method (Lailly, 1983; Tarantola, 1984a; Pratt et al., 1998; Plessix, 2006),

$$\nabla_{\mathbf{m}}E(\mathbf{m}) = \Re \left\{ \mathbf{F}' \left[ \mathbf{S}^{-1} \right]' \delta \mathbf{d}^* \right\}, \quad (1.34)$$

where  $\mathbf{F}$  contains the “virtual sources” for each model parameter. These sources relate to the interaction of the original wavefield with perturbations in the model space, as highlighted by Pratt et al. (1998),

$$\mathbf{F} = -\frac{\partial \mathbf{S}}{\partial \mathbf{m}} \mathbf{u}. \quad (1.35)$$

Considering  $\mathbf{S}$  is approximately symmetric, then  $[\mathbf{S}^{-1}]' = \mathbf{S}^{-1}$ , and if  $\mathbf{v} = \mathbf{S}^{-1} \delta \mathbf{d}^*$  represents the “back-propagated” wavefield, then equation (1.34) can be written as,

$$\nabla_{\mathbf{m}}E(\mathbf{m}) = \Re \{ \mathbf{F}' \mathbf{v} \}, \quad (1.36)$$

which shows the model gradient can be recast in the frequency domain as the zero-lag correlation between the forward propagated wavefield, and the back-propagated data residuals using the virtual sources. This approach effectively avoids the explicit calculation of the partial-derivative wavefields for each model parameter at every node point of the finite-difference grid. This formulation can be seen more clearly if we expand equation (1.36) as,

$$\nabla_{\mathbf{m}}E(\mathbf{m}) = -\Re \left\{ \mathbf{u}' \frac{\partial \mathbf{S}'}{\partial \mathbf{m}} \mathbf{S}^{-1} \delta \mathbf{d}^* \right\}. \quad (1.37)$$

The gradient in equation (1.37) depends on the definition of the data residuals,  $\delta \mathbf{d}$ . Recall that in this study I consider two different residuals, namely conventional phase-amplitude, and logarithmic phase-only data residuals.

The last requirement in the implementation of the conjugate gradient method in equation (1.32) is the computation of the step length,  $\alpha$ , which for linear forward problems can be described as

(Pratt et al., 1998),

$$\alpha = \frac{|\nabla_{\mathbf{m}} E(\mathbf{m})|^2}{|\mathbf{J}\nabla_{\mathbf{m}} E(\mathbf{m})|^2} \quad (1.38)$$

where  $\|\cdot\|$  depicts the Euclidean length of the vectors. Line search techniques may be used to compute the step length when the nonlinearity of the problem is severe.

#### 1.2.4.1 Source signature

In order to solve for the predicted wavefield in equation (1.17), we need the source component, which is assumed to be known and identical to the source signature embedded in the observed wavefields. However, such information (i.e. the amplitude and phase of the source term) is not known *a priori*. This implies we need to correct the modeled data by computing a reliable source signature. Pratt (1999) introduced a linear approach for calculating an optimum source wavelet, which assumes the velocity model is approximately correct. The method is based on the cross-correlation of modeled and observed seismic waveforms, normalized by the auto-correlation of modeled waveforms in the frequency domain,

$$s = \frac{\mathbf{u}' \mathbf{d}^*}{\mathbf{u}' \mathbf{u}^*}, \quad (1.39)$$

where  $s$  is a complex-valued scalar used to define the physical properties of the source signature at each frequency in the survey.

### 1.3 Project background and geological overview

The project described in this thesis is part of the Metal Earth R&D project (Naghizadeh, 2019). The Metal Earth R&D project is a research effort led by Laurentian University within the semi-autonomous Mineral Exploration Research Center (MERC), funded by the Canada First Research Excellence Fund and federal/provincial/industry partners. The Metal Earth group aims to better understand the origin, evolution, and distribution mechanisms related to the emplacement of base and precious metal deposits, focused on the Precambrian Era. New geophysical data has been acquired under the direction of the Metal Earth project, accounting for over 900 line-km of high-resolution seismic reflection profiles, extending from western Ontario (Wabigoon geological subprovince) to western Quebec (Abitibi geological subprovince). Passive seismic, magnetotelluric, and gravity surveys have also been acquired (Naghizadeh, 2019). These data are currently being processed and analyzed by faculty, research scientists, and graduate students in a Canada-wide, and international effort at different institutions, including Western University, University of Toronto, University of

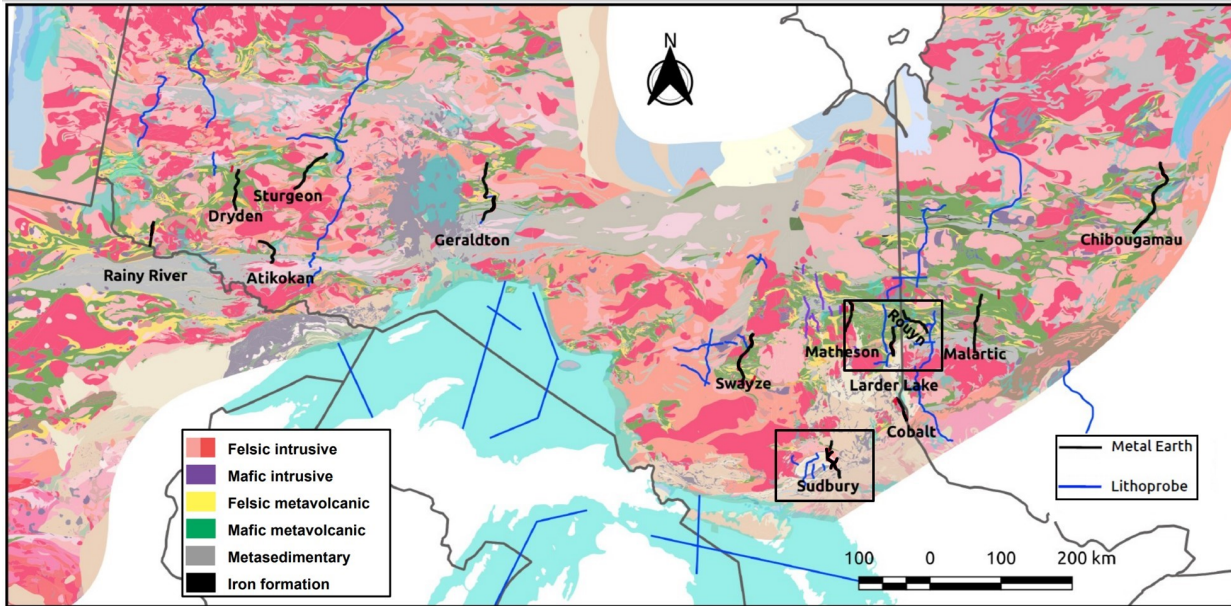


Figure 1.2: Geological map of the Superior Province portraying seismic transects acquired by the Metal Earth R&D project (black), and by the Lithoprobe project (blue). The black rectangles indicate the study areas in this thesis, the Larder Lake and Sudbury mining districts. Modified after Naghizadeh (2019)

Ottawa, University of Alberta, University of South Wales. The various government and company partners also support research activities, such as the Center for Excellence in Mining Innovation, the Geological Survey of Canada (GSC), the Government of Northwest Territories, the Kirkland Lake Gold company, and the Goldspot company.

The Metal Earth project follows in some ways the multidisciplinary national Earth science research project in Canada known as Lithoprobe, which was initiated in the early 1980s and lasted for several decades (Hammer et al., 2010). Some of the seismic profiles surveyed by Metal Earth overlap with the transects from Lithoprobe. This was a carefully designed strategy to maximize the success in unraveling the fundamental questions about the configuration of the lithosphere by complementing the new research findings with those from Lithoprobe's. The Lithoprobe project was a multi-institutional endeavor involving the Natural Sciences and Engineering Research Council of Canada (NSERC), the GSC, and major Canadian mining companies. The project aimed to describe the evolution of the northern half of North America to answer questions related to the geological processes involved in shaping its current structural architecture and tectonic history. This crustal-scale study was supported by the acquisition, processing, and interpretation of near-vertical incidence seismic reflection data. Figure 1.2 depicts a geological map of the Superior Province with the geometry of seismic transects corresponding to both the Metal Earth and the Lithoprobe project. Readers are referred to Clowes et al. (1999) and references therein, where a comprehensive recollection of the Lithoprobe initiative is presented.

The study areas considered in the realization of this thesis are located within the Superior Province, as depicted by the black rectangles in Figure 1.2. I use high-quality seismic reflection surveys from the Larder Lake and Sudbury mining district to complete my work. A brief account on the geological background of these areas is given below. For a comprehensive geological review, readers are referred to the work of Jolly (1976); Jensen and Barton (2000); Ayer et al. (2005); Thurston et al. (2008); Bleeker (2015) for the Larder Lake area, and the work of Pye et al. (1984); Stöfler et al. (1992); Rousell et al. (1997); Therriault et al. (2002); Zieg and Marsh (2005); Halls (2009) for the Sudbury area.

### **1.3.1 Larder lake mining district**

The Larder Lake mining area is located in the Superior Province within the Archean Abitibi greenstone belt, known to host high-grade and world-class gold deposits. This portion of the Superior Province is part of the immense Canadian Shield, a massive Precambrian rock body occupying more than half of Canada and part of the northern United States of America. The Superior Province was built by Proterozoic tectonic events that shaped this portion of the Canadian Shield with smaller fragments of Archean microcontinents derived from the Paleoproterozoic through the Neoproterozoic (Huang et al., 2014). Hoffman (1991), attributed the origin of the Abitibi greenstone belt to accretion of a series of volcanic island arcs. The Abitibi subprovince is bounded by the metasedimentary Pontiac subprovince to the south, and by the Opatitica plutonic belt to the north. To the east, the greenstone belt is bounded by the Grenville Province, and to the west by the Kapuskasing structural zone. Throughout its evolutionary history, the metavolcanic greenstone belt supported favorable conditions for the formation, accumulation, and preservation of base and precious metal endowments. The gold-producing belt associated with the Kirkland Lake-Larder Lake mining district expands for more than 250 km, from Kirkland Lake in southern Abitibi, across northwestern Quebec, to the Malartic-Cadillac area. Ispolatov et al. (2008) indicated that the Larder Lake belt corresponds to a 3- to 5-km-wide east-trending succession of Late Archean Timiskaming rocks with the Larder Lake-Cadillac deformation zone (LLCDZ) as its southern boundary.

Common structures found in the area comprise felsic to intermediate (2695-2685 Ma), and alkalic (2680-2672 Ma) stocks and dikes (Ayer et al., 2005). The Precambrian volcanic, sedimentary, and intrusive host rocks contain native gold, gold tellurides, and sulphides. The emplacement of the metallic mineral deposits within the igneous and metamorphic units are the product of complex geological processes involving volcanism, sedimentation, plutonism, and deformation in the Precambrian Era. The exploitation of mineral resources in the Larder Lake area came into place when mineral endowments were discovered at Cobalt in 1903. In 1906, shortly after the Cobalt

discovery, great interest poured over the Larder Lake area, especially around what today is owned by Kerr-Addison Gold Mines. However, interest in the area was largely and rapidly discredited due to the failure in finding economic mineral deposits. Only when the Omega mine encountered a large tonnage of ore in 1936, began the Larder Lake district to attract mineral prospectors.

Major gold-bearing ore deposits are concentrated along the LLCDZ, showcasing the long-known fact that ore bodies in the area have a closer relationship to structural domains than to rock types (Zhang et al., 2014). The LLCDZ represents the main controlling structural feature in terms of mineralization pathways in the Larder Lake district. The spatial association between gold-bearing ore bodies and major fault corridors is explained in detailed in Bleeker (2015). The deformation zone is also referred to as the “Main Break”, and it is a brittle to brittle-ductile east-trending structure. This structure is comprised by successions of folded metasedimentary and mafic to ultramafic volcanic rocks as well as intervening domes of intrusive rocks (Monecke et al., 2019). Economic concentrations of gold in the Larder Lake area are presented in deposits classified as quartz-carbonate vein-dominated lode gold deposits, which are structurally controlled. A more detailed description of ore occurrences in Larder Lake is given by Savage (1964). He highlighted that gold deposits in the Larder Lake camp occur as fissure or composite quartz veins, quartz stock work deposits in the carbonate zone, quartz-sulphide deposits in lavas and tuffs, sulphide bodies without much quartz, and in talc-chlorite schists, and mineralized dikes. South of the LLCDZ is the Lincoln-Nipissing shear zone (LNSZ), which is a deformation zone associated with mafic to felsic intrusions along and around its trace. Although this structure is poorly documented and exhibit limited exposure, it has drawn interest in recent years due to the identification of felsic intrusions regionally associated with gold mineralization (Robert, 2001). The LNSZ trends west-northwesterly, and it represents a structural and stratigraphic marker in the area, separating the McElroy assemblage to the south from the Larder Lake assemblage to the north. This shear zone is characterized by a uniform northwest-striking, northeast-younging volcanic succession to the south, and by complex faulted and folded structures of the Larder Lake assemblage to the north, which are overlain by metasedimentary rock units of the Hearst assemblage (Brace and Sherlock, 2017).

### **1.3.2 Sudbury mining district**

The Sudbury Structure is deemed to be the richest nickel-producing structure in the world with a significant amount of copper by-products and precious metals. Because of the abundance and distribution of shock-deformed features, the Sudbury Structure is interpreted by most researchers as a voluminous crustal melt sheet derived from a colossal high-energy impact event 1850 Ma ago (Dressler et al., 1992). However, after over a century of mining activities around the Sudbury

Structure, debate about its origins are still ongoing (Riller, 2005; Ubide et al., 2017; Latypov et al., 2019). The debate on the origins of the Sudbury Structure began with the work of Dietz (1964), who concluded the structure might have been the result of an intense shock only caused by giant events related to meteorite impacts. Grieve et al. (1991) indicated that the controversy over an endogenic versus an exogenic origin have its roots in equivocal features of the Sudbury Structure, which prevent the meteorite impact event from being widely accepted. Some of these features are highlighted in Card and Hutchinson (1972); Muir (1984), such as the geometrical shape of the Sudbury area being elliptical, rather than circular, as well as the lack of a central uplift, and the absence of a negative gravity anomaly. However, Milkereit and Green (1992) highlighted that research on isotopes, geochemistry, and petrography in the late 1980s supported the hypothesis of a meteorite impact. Lightfoot (2016) stated that the non-circular morphology of the Sudbury Structure is due to multiphase deformation associated with a change in structural regime, mostly formed by NW-SE crustal shortening of a once-circular shape. These multidisciplinary research efforts suggested that rocks and ore of the Sudbury Igneous Complex (SIC) were mostly derived from the Archean crust and Early Proterozoic cover rocks, without significant contribution from mantle magmatism. Although still a controversial topic within the geoscience community, the Sudbury Structure is widely deemed to be a deformed multi-ring impact basin with an approximate diameter of 250 km, covering an area of over 15000  $km^2$  (Spray et al., 2004; Zieg and Marsh, 2005).

The Sudbury Structure is bounded to the north by the granitoid and gneissic rocks of the Archean Superior Province, and to the south by the metavolcanic and metasedimentary rocks of the Proterozoic Southern province, which belongs to the Huronian Supergroup (Lenauer and Riller, 2017). The following description of the geological architecture of the Sudbury Structure is extracted from Zieg and Marsh (2005). The Sudbury Structure is composed by four major structural domains. (i) The shocked and brecciated country rocks - the basement rocks around the Sudbury Structure display shock metamorphic features, such as shatter cones and planar deformation features in quartz grains. The brecciation appears in two distinctive forms known as Sudbury Breccia and Footwall Breccia. The former is a pseudotachylite containing wall-rock fragments, and occurs in dikes, pods, and lenses. The latter, Footwall Breccia, lies along the lower contact of the SIC, generally forming thicker bodies and containing igneous to metamorphic clasts. (ii) The Sudbury Igneous Complex - this complex is divided by two main units, norite and granophyre, separated by a continuous thin layer of quartz gabbro. Quartz diorite are found in the SIC in radial or concentric offset dikes. The Sublayer, which is a discontinuous basal unit, contains an assortment of local and exotic mafic to ultramafic xenoliths. Lenauer and Riller (2017), indicates that this Sublayer hosts significant economic concentrations of Cu-Ni-PGE sulphide deposits. (iii) The Whitewater Group. (iii.1) Onaping Formation - during the cratering process, abundant fragmental debris was ejected into the atmosphere and deposited on top of the melt sheet. The Onaping For-

mation contains remnants of this fragmental debris as well as large fragments of quartz arenite and other sedimentary lithologies from the Huronian Supergroup. At its base, the Onaping Formation presents a coarse and clast supported igneous matrix. (iii.2) The Vermilion Formation - consisting of carbonate, siltstone, and chert breccia, with Zn-Pb-Cu mineralization. (iii.3) The Onwatin and Chelmsford Formations - these sedimentary formations consist of a series of mudstones and graywackes, respectively, resulting from the uppermost Onaping Formation grading towards the Onwatin and Chelmsford Formations. The structural configuration at depth of the Sudbury Structure is mostly delineated by interpreting seismic reflection profiles from the Lithoprobe project. The dip of the norite and quartz gabbro contact has been used as a diagnostic structural feature for understanding the geometry of the Sudbury Structure by, among others, Milkereit and Green (1992); Milkereit et al. (2000); Wu et al. (1995).

## 1.4 Objectives of thesis

In this thesis I investigate and apply imaging techniques to the geologically complex crystalline environments of the Larder Lake and Sudbury mining districts. The goal is not only to enhance our understanding on the configuration of deeper structures (more than 3 km deep), but also of near-surface structures (less than 3 km in depth). This is because the depth limit of modern mining technology is approximately 2.5 km, and superficial mineral endowments (with depths of less than 1 km) are already being depleted. Therefore, imaging the mineralization conduits present in the near surface, and their development at depth is vital for the discovery of deeper and high-grade ore deposits. To this end, I employ frequency-domain visco-acoustic full-waveform inversion to generate high-quality, and high-resolution quantitative models of the near surface. I implement an enhanced seismic reflection processing technique, including a surgically designed binning strategy, that account for both survey crookedness and local structural variations. I demonstrate that combining near-surface FWI imaging with seismic reflectivity imaging, a natural transition between shallow and crustal-scale structures is established. This fills the gap between what we know today from surface geology, and our macro-structural understanding of features at depth.

I use two different seismic datasets, a 45-km long profile from Larder Lake, and a 15-km long profile from Sudbury. To the best of my knowledge, this is the first attempt of implementing full-waveform inversion in these hard rock settings in Canada. The Larder Lake reflection profile is severely crooked, having a midpoint-trace cloud scattered up to distances of 4 km perpendicular to the transect direction. In contrast, the Sudbury reflection profile exhibits a much milder deviation from a straight path, displaying midpoint-trace scattering of no more than 0.4 km in the transverse direction of the profile. I explore the effect of survey crookedness on the model updates by performing both the computationally expensive 2.5D FWI approach, and the more affordable

2D FWI approximation. I illustrate that accounting for the out-of-plane wavenumber components contained within severely crooked geometries, such as that of the Larder Lake transect, is essential to accurately retrieve velocity estimations. On the other hand, I prove that moderately crooked geometries, such as that of the Sudbury transect, benefit better from a two-dimensional approach.

I investigate improvements in energy focusing and signal alignment by implementing azimuthal binning methods during seismic reflection processing. Mitigating signal ill-alignment is required in severely crooked profile to ensure seismic reflections are in phase, as well as to diminish amplitude smearing during stacking. I find that correcting cross-profile dip components under the azimuthal binning method, and adopting a post-stack migration strategy, renders equivalent results to those from implementing the more time-consuming and computationally-expensive pre-stack migration method. I study the different imaging quality effects introduced on the seismic migrated image, which stems from the use of different velocity models. Adopting a migration velocity field containing low- and medium- wavenumber components, from the FWI P-wave velocity structure, proved vital. I illustrate that near-surface velocity variations have an important impact on retrieving high-quality migrated images at depth.

## 1.5 Thesis outline

In Chapter I, I have provided a general overview on seismic methods, including the seismic refraction and the seismic reflection method. The fundamentals of seismic imaging are also discussed, briefly reviewing concepts and formulations of the forward and inverse problem (focused on the specifics of my thesis). A geological overview on the study areas is provided, as well as an introduction to the background of my research project.

In Chapter II, I present the implementation of a two-dimensional visco-acoustic full-waveform inversion in the Laplace-Fourier domain to the southern part of the Larder Lake seismic transect. This chapter is part of a paper titled “Full-waveform inversion in a crystalline terrain using combined explosive and vibroseis sources” by Brian J.G. Villamizar, R. G. Pratt, and M. Naghizadeh, submitted to *Geophysics* for revision in April 2021. The research presented in this paper is focused towards the southern 22 km of the Larder Lake transect in order to image the more structurally complex, and poorly documented LNSZ, south of the LLCZ. This work serves as a *stepping stone* for the design of effective processing and data preconditioning techniques for the full Larder Lake geometry. This design is focused on mitigating the nonlinearity and non-uniqueness in waveform inversion. The hierarchical combination of explosive sources and vibroseis sources in the inversion strategy is discussed in this chapter, providing an effective approach to retrieve very low wavenumber components that help mitigating the nonlinear nature of the inverse problem.

In Chapter III, I explore the implementation of two- and two-and-half-dimensional full-waveform

inversion to the entire 45-km long Larder Lake seismic survey. This chapter is part of an article titled “Seismic imaging of crystalline structures: 2D and 2.5D visco-acoustic full-waveform inversion” by Brian J.G. Villamizar, R. G. Pratt, and M. Naghizadeh, submitted to *Geophysics* for revision in June 2021. In this chapter, I investigate the imaging effects of transverse wavefield components on severely crooked profiles. I apply both 2D and 2.5D FWI, combining two different objective functions for residual minimization, namely “logarithmic phase-only” and “conventional phase-amplitude” residuals. I assess the differences of the resulting 2D and 2.5D velocity models in terms of overall imaging quality, coherency of inverted source signatures, and similarities between finite-difference time-domain synthetic and observed seismograms.

In Chapter IV, I perform azimuthal binning to improve signal alignment before stack, and apply seismic reflection processing to retrieve the reflectivity image of the Larder Lake dataset. This chapter is part of a manuscript titled “Seismic imaging of crystalline structures: improving energy focusing and signal alignment with azimuthal binning” by Brian J.G. Villamizar, R. G. Pratt, and M. Naghizadeh, submission to a journal is pending. In Chapter IV, I study the influence of binning strategies on the quality of the resulting stacked image. I carry out binning considering different geometries, including a straight-line binning geometry, three-straight-segment binning geometry, and a slalom line geometry that closely follows the actual crookedness of the survey. Azimuthal binning is then introduced along with an enhanced migration velocity field. I discuss the implications these two approaches have on the overall imaging quality of structures at depth.

In Chapter V, I provide an analysis on a reflection dataset located in the northeast lobe of the Sudbury Structure. This chapter is part of an article titled “Imaging the northeast lobe of the Sudbury Structure through 2D and 2.5D visco-acoustic full-waveform inversion” by Brian J.G. Villamizar, R. G. Pratt, and M. Naghizadeh, submission to a journal is pending. Because the architecture of this portion of the Sudbury Structure is poorly understood, I implement both 2D and 2.5D FWI to retrieve a high-quality near-surface velocity structure. The effect of out-of-plane wavenumbers in the resulting FWI image is evaluated when a mildly crooked seismic survey is used. I briefly analyze the geological relevance of the final P-wave velocity model, connecting different velocity domains with known structures within the Sudbury high-impact area.

General discussion and conclusions are presented in Chapter VI.

## **Chapter 2**

# **Full-waveform inversion in a crystalline terrain using combined explosive and vibroseis sources**

### **2.1 Introduction**

Surface seismic methods have historically been associated with exploration in sedimentary basins, with few examples in hardrock terrains. Nevertheless, attempts to use exploration seismics for mineral exploration have resulted in the acquisition of seismic data across several crystalline settings in Canada, Australia, Europe, and Africa, as highlighted by Wright et al. (1994) and more recently by Malehmir et al. (2017a). The highly complex reflection character of crystalline environments poses intricate challenges in seismic imaging, stemming in part from the difficulty of properly quantifying near-surface velocities. This is especially true with land seismic data in hardrock, where the heterogeneous characteristics of the regolith complicates energy propagation due to strong, shallow velocity variations. Therefore, a reliable reconstruction of the near-surface velocity field is vital in order to produce high-quality images of the subsurface.

Full-waveform inversion (FWI) is a state-of-the-art seismic technique that generates high-resolution images of near-surface velocity structure by minimizing an objective function in an iterative way, updating the model to match observations in an attempt to obtain realistic representations of the subsurface (Lailly, 1983; Tarantola, 1984a; Mora, 1989; Pratt et al., 1998; Pratt, 1999). Unlike conventional ray-based techniques for velocity inversion such as travelttime tomography, FWI uses broadband wavepaths that allow for deeper velocity imaging and higher resolution (Woodward 1992; Consolvo 2018). Many successful FWI studies have been reported in sedimentary terrains (e.g., Kamei et al., 2015; Gray et al., 2019), however, only a handful of examples

are found in crystalline settings typically encountered in mineral resource exploration. What examples exist are often based on synthetic experiments (Butzer, 2015; Bentham et al., 2018), or in shallow settings (with depths less than 500 m) (Zhang and Juhlin, 2013; Dokter et al., 2017), or using vertical geometries (e.g. VSP, crosshole radar data; Ernst et al., 2007; Egorov et al., 2018, respectively).

I use data from both explosive and vibroseis sources from the Larder Lake transect, acquired in the Superior Province by the Metal Earth project in 2017. The Metal Earth project is an industry-academic collaboration which aims to develop a comprehensive understating of the genesis and distribution of mineral endowments in the Superior Craton, Canada (Naghizadeh et al., 2019). The area of interest is located in the economically important Abitibi greenstone belt, specifically in the Larder Lake area. The Larder Lake transect is a 45-km crooked, two-dimensional, single-component (2D-1C), large offset seismic survey that lies within a corridor extending from the St Anthony Lake in the Larder Lake Municipality to the Cripple Lakes in the Timiskaming Municipality, in Ontario.

In this chapter, I implement 2D frequency-domain visco-acoustic FWI to image the architecture of the southern 22 km of the Larder Lake transect, involving the Lincoln-Nipissing Shear Zone (LNSZ). I focus on the LNSZ because of its similarities with the well-known gold-bearing Larder Lake-Cadillac Deformation Zone (LLCDF), located approximately 10 km north of the LNSZ. My objective is to image the velocity structure associated with the LNSZ, and unravel its role as a structural mechanism controlling the distribution of potential metal deposits in the area (Bigot and Jébrak, 2015; Brace and Sherlock, 2017; Brace et al., 2018; St-Jean et al., 2019).

Following Smithyman and Clowes (2012); Kamei and Pratt (2013); Consolvo (2018), I implement a suitable data preconditioning workflow, and apply a multiscale inversion strategy to address the nonlinearity inherent to FWI in strongly heterogeneous environments. A crucial part of the strategy is to mitigate nonlinearity and effectively address cycle-skipping problems (i.e., when synthetic/observed data residuals do not match, with an error higher than half a period, as described by Virieux and Operto, 2009). This involves the incorporation of very low-frequency components available in the dataset from only three widely-spaced explosive (dynamite) sources. To evaluate this, I establish two inversion streams to assess the value of these sources: first, a combined explosive/vibroseis geometry, and second a vibroseis-only geometry. The former stream involves the inversion of frequencies from 4 to 7.5 Hz using the explosive sources, before continuing with the inversion of frequencies between 7 and 15 Hz using the vibroseis geometry; the latter stream uses only the vibroseis sources and, hence, inversion frequencies run only from 7 to 15 Hz. The motivation for introducing very-low-frequency components in my inversion strategy stems from the findings of Hicks and Pratt (2001), who noted that updating the parameter model using the most linear parts of the observed waveforms facilitates the correct fit of seismic phases, avoid-

ing convergence to local minima. Kamei (2013) suggested that in certain cases accurate velocity images can be successfully retrieved by logarithmic phase-only residuals, implying that kinematic information plays a more important role than dynamic information in FWI. I follow a similar approach by using logarithmic phase-only residuals at early stages of the inversion, and continuing with conventional phase-amplitude residuals at later stages.

In the following section of Chapter 2, I briefly present the theoretical background of the FWI method. In the next section, I describe the data acquisition, the data quality, and the data preconditioning required for subsequent FWI. This section includes an assessment of the characteristics of explosive and vibroseis sources. Then, in the fourth section of this chapter, I separately perform FWI on the explosive/vibroseis geometry and on the vibroseis-only geometry, analyzing the outcomes in terms of model accuracy and reliability. I provide a comprehensive appraisal through the evaluation of source signature inversions, checkerboard tests, and detailed comparisons of synthetic and observed seismograms. In the final section, I discuss the velocity results and their geological significance. A numerical experiment simulating a low-velocity sub-vertical structure, is also presented. This experiment assesses the capabilities of the inversion strategy on retrieving a low-velocity zone with similar characteristics of that of the LNSZ (e.g. width, dip, orientation).

## 2.2 Method

Here I review the fundamental theory of frequency-domain (and Laplace-Fourier domain) FWI (after, e.g., Pratt 1990; Pratt et al. 1998; Pratt 1999; Sirgue and Pratt 2004; Kamei and Pratt 2013).

### 2.2.1 Forward modeling

Numerical simulation of the 2D acoustic or visco-acoustic wave equation (Kosloff and Baysal, 1982; Pratt and Worthington, 1990; Kamei and Pratt, 2013), has proven effective despite the fact that elastic effects and anisotropy are neglected. As in these earlier studies, I also assume the physics of wave propagation is properly captured by means of finite-difference methods, which avoid the use of the asymptotic high-frequency ray approximation, and further avoids the computational expense of fully 3D, anisotropic, visco-elastic methods (Pratt, 1999). In my approach, forward modeling is described by the isotropic, 2D, visco-acoustic wave-equation in the frequency domain,

$$\nabla \cdot \left( \frac{1}{\rho(x, z)} \nabla u(x, z; \omega) \right) + \frac{\omega^2}{\kappa(x, z)} u(x, z; \omega) = f(x, z; \omega), \quad (2.1)$$

where  $\rho$  is the bulk density,  $\kappa$  is the bulk modulus,  $\omega$  is the angular frequency,  $u$  is the pressure field, and  $f$  is a generalized source term. To accommodate viscous effects,  $\kappa$  is assumed to be

complex-valued. Density values are computed using the velocity model updates and the Gardner's relationship (Gardner et al., 1974).

The numerical system implicit in equation (2.1), defined in the Fourier space for each source, can be expressed using the discrete form,

$$\mathbf{S}(\mathbf{m}, \omega) \mathbf{u}(\omega) = \mathbf{f}(\omega), \quad (2.2)$$

(Pratt and Worthington, 1990; Pratt et al., 1998), where  $\mathbf{u}(\omega)$  is a vector containing the mono-frequency pressure wavefield at discrete points,  $\mathbf{f}(\omega)$  is a similar vector containing the source wavefield, and  $\mathbf{S}$  is the complex-valued impedance matrix that discretely represents the differential terms in equation (2.1), depending only on the frequency and on the model parameters,  $\mathbf{m}$ . Note that explicit dependency on model parameters and frequency will be dropped henceforward for notational simplicity.

Often the forward problem above is interpreted as a Fourier domain approach where the frequency,  $\omega$ , is real-valued. However, Brenders and Pratt (2007b) noted that the non-linearity of the problem can be mitigated by only allowing the early part of the waveforms into the reconstruction using an exponential time-damping approach. Shin and Ho Cha (2009) refined this concept by noting that the frequency parameter implicit in equation (2.2),  $\omega$ , may be replaced with a complex-valued frequency,

$$\Omega = \omega - i\sigma, \quad (2.3)$$

where  $\sigma$  is a real-valued Laplace constant. This approach was termed a ‘‘Laplace-Fourier’’ domain approach by Shin and Ho Cha (2009). By using complex-valued frequencies, we obtain the Fourier transform of the original time-domain wavefield, multiplied by a time damping factor,  $e^{-t/\tau}$ , where  $\tau = 1/\sigma$  (Shin and Ho Cha, 2009; Kamei and Pratt, 2013). This damping factor serves as a preconditioning operator, in the sense that we may choose to fit only the early part of the waveforms during the reconstruction.

## 2.2.2 Inverse problem and optimization

To address the inverse problem, I define a set of model parameters,  $\mathbf{m}$ , (usually at every node point of the 2D finite-difference grid), and produce synthetic waveforms,  $\mathbf{u}(\mathbf{m}, \omega)$ . The difference between synthetic and observed waveforms (i.e. the data residuals) is described in the Laplace-Fourier domain as,

$$\delta d_j = u_j - d_j, \quad (2.4)$$

where  $j = (1, 2, \dots, n)$ , and the vector components  $\delta d_j$ ,  $u_j$ , and  $d_j$  are complex-valued and depend

on the Laplace-Fourier frequency  $\Omega$  (not used in the notation for simplicity). These data residuals are defined for each source-receiver pair where the observed data are available, i.e., at  $n$  receiver locations.

Data residuals as described by equation (2.4) represent the “conventional phase-amplitude” approach in which simple subtraction of complex quantities is used in the definition. An alternative is to define a logarithmic residual (as in Shin and Min 2006), which allows the separation of phase and amplitude information in the residuals. This approach enables a logarithmic phase-only residual to be defined, i.e.,

$$\delta d_j^P = \Im \left[ \ln \left( \frac{A_{uj}}{A_{dj}} \right) + i(\theta_{uj} - \theta_{dj}) \right] = (\theta_{uj} - \theta_{dj}), \quad (2.5)$$

(after Bednar et al., 2007). Kamei et al. (2014) provided a summary of the advantages and disadvantages of these and other related definitions of the data residuals. The logarithmic phase-only residuals allow the inversion to focus on the kinematics (i.e. the phase spectrum) of the observed wavefields, which is helpful during early FWI stages as the phase-amplitude optimization method is highly sensitive to the non-geological variations in the observed amplitudes. I establish a least-squares norm,  $L_2$  norm, of the residuals (either phase-amplitude, or phase-only), and minimize the chosen form of data residuals using the conjugate gradient method. I implement a multiscale layer-stripping inversion strategy involving the inclusion of longer offsets and higher frequencies as the inversion progresses. The progressive inclusion of longer offsets and higher frequencies effectively results in velocity updates at deeper sections of the model, and the strategy can help mitigate cycle skip nonlinearities. To carry out FWI, the forward problem in equation (2.2) must be solved. This implies that the source term,  $\mathbf{f}$ , must be accounted for. I implement the linear inverse solution introduced by Pratt (1999). Under this approach, an optimal source signature can be estimated for each shot gather, assuming the true velocity structure is known and shot and receiver stations share the same coupling effect. The more accurate the velocity field used in these estimates, the more coherent is the resulting ensemble of inverted source wavelets. Thus the coherency and consistency of the estimated source wavelets are a measure of the validity of the inverted velocity model.

## 2.3 Data

### 2.3.1 Survey acquisition

The Larder Lake 2D seismic survey I use is part of over 900 line-km of deep seismic reflection survey data acquired in crystalline environments by the Metal Earth project in 2017 (Naghizadeh et al., 2019). A location map along with key geological features and the survey geometry is depicted in Figure 2.1.

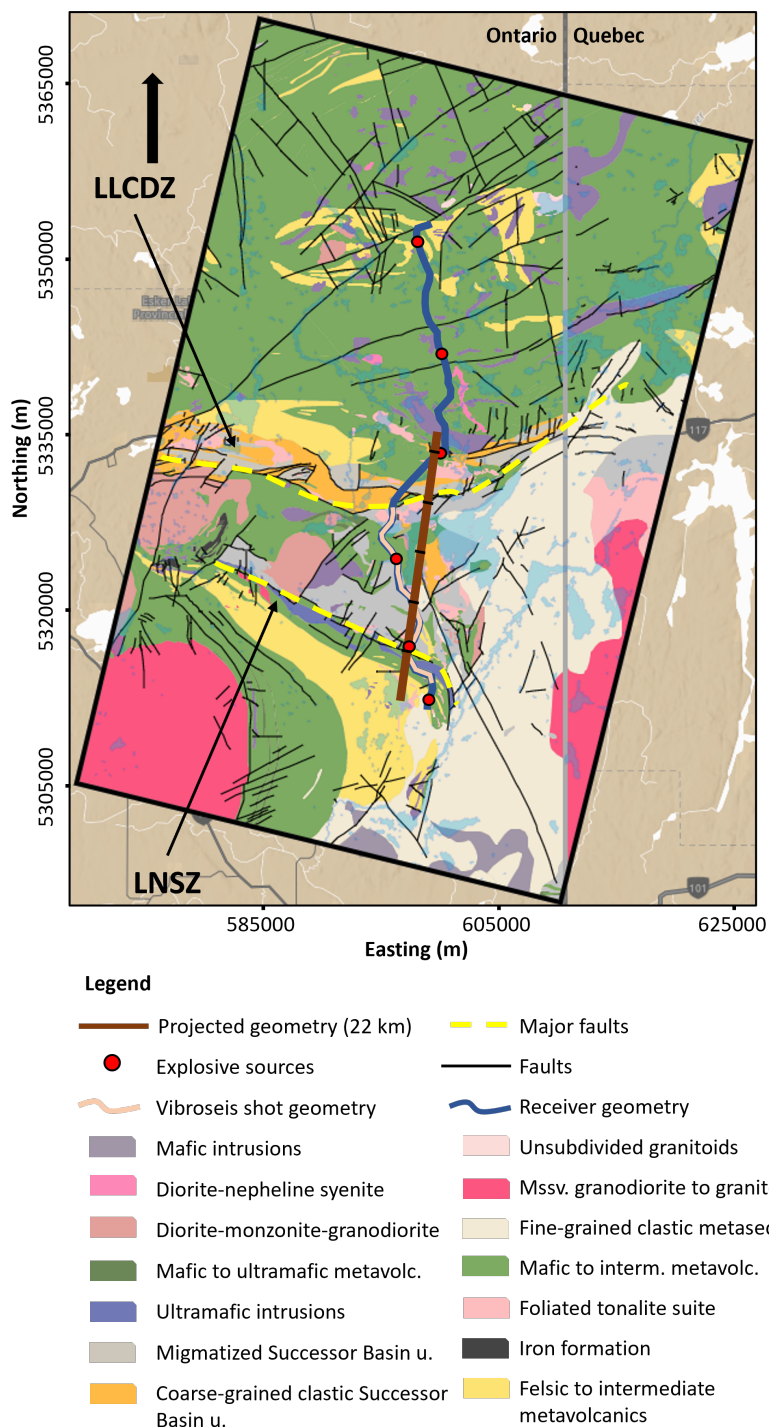


Figure 2.1: Relevant geological units in the Larder Lake area, displaying the acquisition geometry. The original (crooked) geometry is shown by the blue (receivers) and light orange (vibroseis sources) solid lines. Explosive sources are indicated by red dots. Only the southernmost three explosive sources are used in this study. The 22-km long 2D projected geometry used for FWI is represented by the straight line in brown. Key structural features are depicted by the two dashed yellow lines: the Larder Lake-Cadillac Deformation Zone (to the north) and the Lincoln-Nipissing Shear Zone (to the south). Black lines on the projected geometry indicate 4 km intervals, which correlate with the horizontal axis of the models shown here. Grey line indicates the Ontario and Quebec border. Modified after the Metal Earth - Geology map of Larder Lake area (2019).

The seismic line is in northwestern Ontario within the Abitibi subprovince of the Superior Province. The area is dominated by ultramafic to intermediate volcanic units unconformably overlain by metasedimentary and metavolcanic rocks. The metasedimentary rocks in the vicinity of Larder Lake are part of the Cobalt Group, a stratigraphic subset of the Huronian Supergroup (Savage, 1964). Key structural features are present in the area, such as the Larder Lake-Cadillac deformation zone and the Lincoln-Nipissing shear zone (both indicated on Figure 2.1). In this chapter, I focus on the 22-km long 2D line shown on the figure for two main reasons: i) to image the more structurally complex southern part of Larder Lake (involving the poorly documented LNSZ), and ii) to devise an optimum inversion strategy for crystalline settings applicable to the full survey.

The seismic line comprises 2,426 single wireless vertical-component 5-Hz geophones with a spacing of 12.5 m, 295 vibroseis sources with a spacing of approximately 50 m, and 3 explosive sources with spacing between 5 and 7 km. Note that the receivers were not grouped into arrays. Usually, in seismic operations aimed at imaging the subsurface by means of short-offset techniques (such as migration), receiver arrays are implemented to reduce the influence of non-vertical arrivals (they are filtered out through the destructive interference of oblique traveltimes). However, FWI benefits from multi-angle arrivals available when single receiver geometries are used. The vibroseis system used for acquiring the Larder Lake transect was formed by four vibrator trucks generating a linear up-sweep of 5-120 Hz. Explosive sources with a nominal size of 3 kg were deployed in 15 m deep shot holes. Following a similar approach used by Kamei et al. (2015) and Consolvo et al. (2017), I project the 3D survey coordinates into a 2D coordinate plane (the brown line in Figure 2.1), as the FWI algorithm used here assumes a 2D model and geometry. The coordinate projection I use does not preserve source-receiver offsets, since this would require virtual source and/or receiver locations, further complicating the inversion (Kamei et al., 2015). I mitigate the effect of the offset errors by establishing an offset error threshold and rejecting non-compliant waveforms not meeting the error criteria. Non-compliant data are identified as those waveforms with an offset error of over 6 per cent; these are rejected. Other approaches are also possible, such as the projection proposed by Zelt (1999), discussed further by Adamczyk et al. (2015). In their approach, source-receiver offsets are preserved at the expense of performing time shifts to correct for stations projected onto incorrect topographic locations. Time corrections depend on near-surface velocity estimations, which can lead to erroneous corrections if the near-surface layer is highly heterogeneous. Therefore, discarding waveforms is a safer strategy if the dataset is not significantly affected by the trace rejection.

### 2.3.2 Explosive and vibroseis sources

As described above, a combination of explosive and vibroseis sources were used at the Larder Lake survey. The original intent of this design was to take advantage of the different and complementary spectral properties of these sources. Table 2.1 provides some of the acquisition parameters for each source type. Figure 2.2 shows the normalized average Fourier amplitude spectrum of two almost-coincident raw shot gathers, corresponding to an explosive source and a vibroseis source. The availability of low-frequency signals generated by explosive sources is their main advantage compared to vibroseis.

Table 2.1: Acquisition parameters

Parameter	Explosive	Vibroseis
Source spacing	5-7 km	50 m
Source depth	15 m	0 m
Receiver spacing	12.5 m	12.5 m
Maximum offset	30 km	15 km

In Figure 2.2 we see that, for a single, co-incident location, both explosive and vibroseis sources exhibit 4 octaves of useful bandwidth, between 4-64 Hz and 8-128 Hz, respectively.

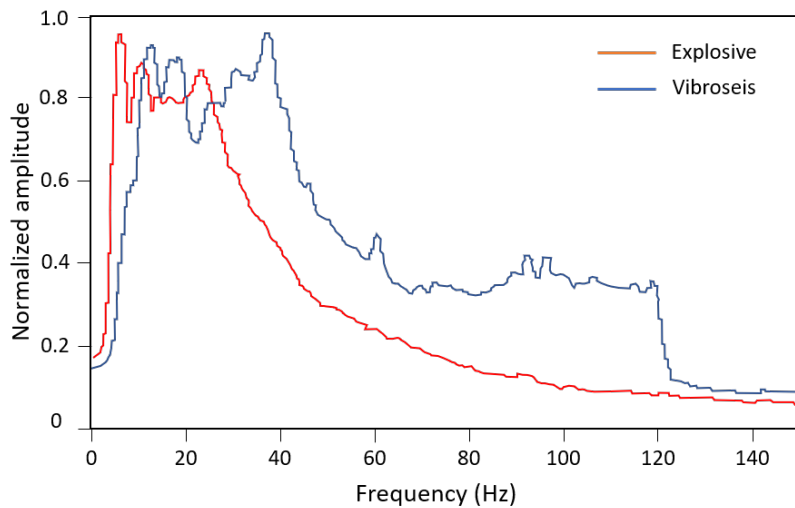


Figure 2.2: Normalized Fourier spectra of co-incident raw shot gathers for both explosive and vibroseis sources.

The explosive source spectrum reveals significant power down to 4 Hz (even with the natural damping effect of 5 Hz geophones). These remarkably low frequencies allow us to consider the inclusion of low-wavenumber information during FWI that would otherwise be difficult to obtain with vibroseis sources alone.

A more data-oriented comparison is depicted in the representative co-incident explosive and vibratory shot gathers (Figure 2.3). The most significant differences between the two gathers are the larger offset extent of the early-arrival (refracted) energy on the explosive shot gather, and the corresponding improvement in signal-to-noise ratio. The vibroseis source shows clear refraction arrivals up to a maximum offset of only 10-15 km, whereas the first arrivals from the explosive source exhibit excellent coherence up to nearly 30 km (the maximum available offset for this gather). In addition to the clarity of the first arrivals, additional seismic events may be identified in both gathers, including surface waves and converted modes. Reflected energy is not readily identified in either shot gather; this difficulty in observing reflected energy is not uncommon in crystalline environments (Nedimović, 2000).

In summary, we see that the waveforms from explosive sources show more consistent and higher amplitude arrivals across the transect, especially at far offsets. This indicates that the penetrative power of these explosive sources is definitely stronger than the vibroseis sources, resulting in an improvement in imaging deeper regions of the subsurface. The explosive sources are also very rich in low-frequency components, which are of interest to avoid cycle-skipping problems. Nevertheless, the lower-energy vibroseis shots were deployed at much closer spacing and they exhibit strong medium-to-high frequency content, which are vital for the reconstruction of high-wavenumber features. Although these vibroseis data are limited by poor signal-to-noise ratios for offsets longer than 10-15 km, they illuminate much of the same structure with a high signal-to-noise ratio at the smaller offsets. It seems critical to exploit the complementary nature of both explosive and vibroseis sources by combining them in frequency-domain FWI.

### 2.3.3 Data preconditioning

A set of processes are applied to observed seismograms in order to improve their quality and prepare the data for inversion. These are summarized as follows:

**Rejection of noise and secondary arrivals in the frequency-wavenumber (F-K) Domain:** as shown in Figure 2.3, strong secondary arrivals are present in the vast majority of shot gathers. In order to ensure the inversion focuses on early-arriving waveforms, I design and apply a set of filters in the frequency-wavenumber domain such that an optimum conservation of the low-frequency and low-wavenumber components of the Fourier-transformed time-distance (T-X) signal is achieved,

while removing the unwanted energy.

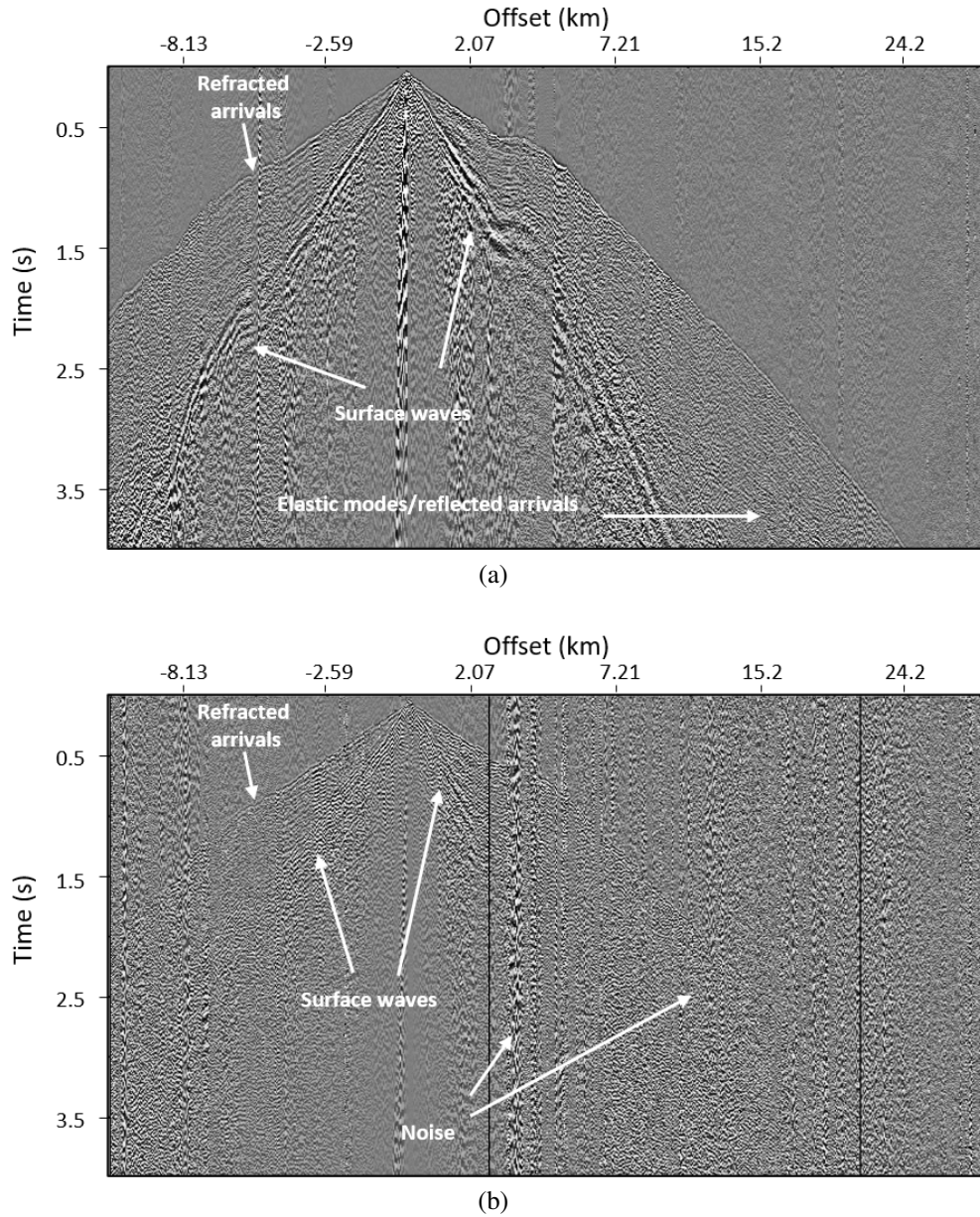


Figure 2.3: Trace-normalized shot gathers corresponding to co-incident (a) explosive and (b) vibroseis sources located at a distance of 11.8 km along the projected 2D geometry.

In order to minimize errors during the Fourier transformation process, I apply residual statics to shot and receivers. Figure 2.4 depicts the frequency-wavenumber spectrum for the vibroseis shot gather depicted in Figure 2.3b. Figure 2.4a is generated using input data with no static corrections, while Figure 2.4b shows the F-K spectrum of the static-corrected waveforms. Noise bands at 45 Hz and 60 Hz may be observed on both figures. Dipping events, consistent with the secondary arrivals observed in the T-X domain, appear to have higher power levels and stronger coherency in

the F-K spectrum of the static-corrected data. This enhances our capability to identify and isolate such signals.

**Amplitude corrections and balancing:** although most shot gathers exhibit similar energy strength, individual source amplitudes are influenced by the local ground conditions. Likewise, receiver instrument responses are influenced by near-geophone ground conditions (e.g. coupling effects, local ambient noise variations, localized lithologic changes, etc.). I detect and compensate for these effects by applying surface-consistent amplitude corrections (after Taner and Koehler 1981; Levin 1989; Cary and Lorentz 1993; van Vossen et al. 2006). I do not use trace-normalization - my workflow preserves amplitude changes with offset, but I do perform shot-to-shot amplitude balancing by normalizing each source gather to its maximum value. Figure 2.5a displays a raw vibroseis gather located at a distance of 11.8 km along the projected line. Figure 2.5b displays the same gather following F-K filtering, amplitude correction, amplitude balancing, and time windowing.

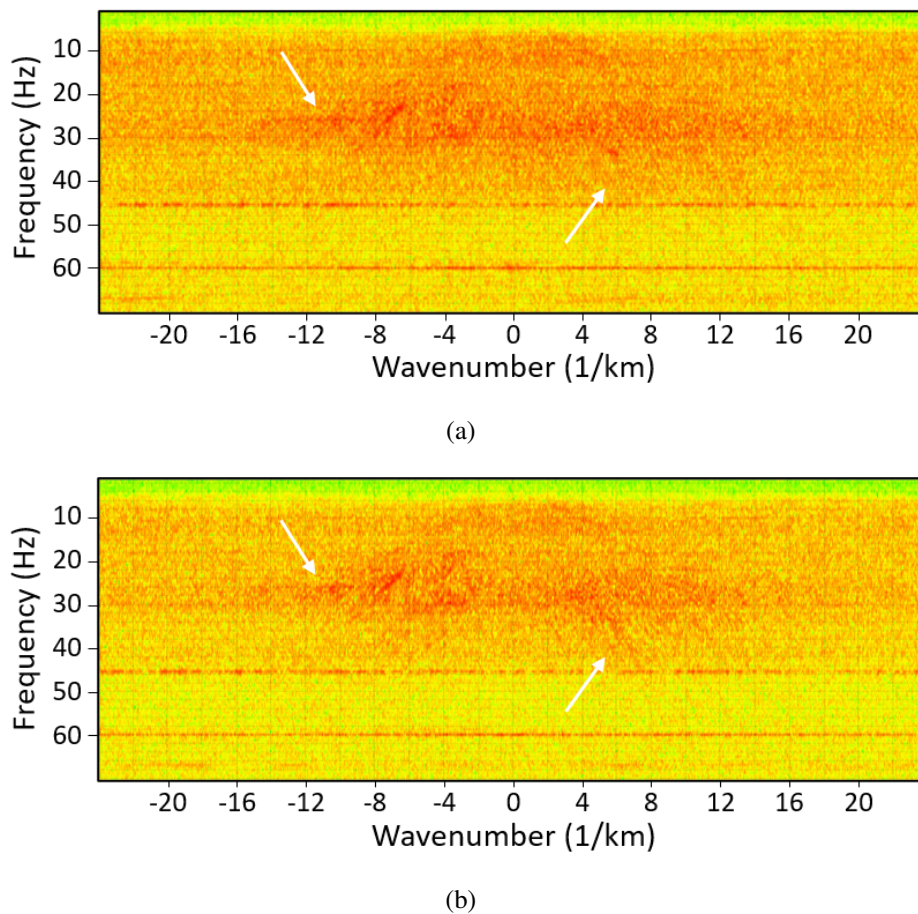


Figure 2.4: Frequency-wavenumber spectrum of a gather located at 11.8 km along the line with (a) no residual statics applied and (b) with residual statics applied. White arrows highlight events associated with secondary arrivals that we wish to suppress.

**Trace editing and muting:** in order for the inversion to succeed, we need to suppress phases in the data that are not consistent with the acoustic approximation. I perform trace editing and muting by removing noisy traces, and by time-windowing waveforms to a maximum of 2 s below first breaks, as highlighted by data gaps in both Figure 2.5b and 2.5c. The rejection of data traces is driven by the manual picking of first arrivals; ambiguous arrivals are not picked and the corresponding data traces are rejected. Differences between the gathers in Figure 2.5 are most noticeable at far offsets, especially at offsets longer than 3 km where a better energy distribution is observed in the amplitude-processed gather (Figure 2.5b). The refracted waveforms are more pronounced in Figure 2.5b compared to other arrivals. Secondary events such as surface waves and elastic modes are mitigated as a result of F-K filtering.

**Low pass filtering and time damping:** additional preconditioning steps include low-pass filtering the data with frequency corners 0-0-15-17 Hz. Finally, discretized Laplace-Fourier components of the preconditioned data are obtained by time-damping the observed waveforms and applying a discrete Fourier transformation (DFT). This is equivalent to using the complex-valued frequency of equation (2.3). For time-damping, I use two characteristic decay times,  $\tau = 0.2$  s and  $\tau = 0.3$  s, equal to 10 and 15 per cent of the maximum time window, respectively. (Figure 2.5c shows the effect of low-pass filtering and time damping on the data just prior to Fourier transformation).

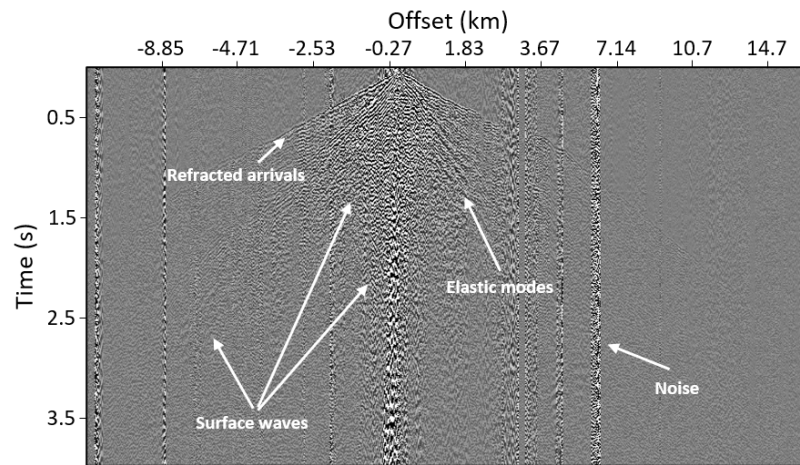
## 2.4 Inversion

My overall inversion approach is based on the combination of ray-based first-arrival traveltome tomography, followed by the construction of a numerical model for subsequent finite-difference modeling, and full-waveform inversion. This is effectively the scheme laid out originally by Brenders and Pratt (2007b). I use the 3D first-arrival traveltome tomography algorithm of Zhang and Toksöz (1998) (TomoPlus suite), and the 2D/2.5D frequency-domain full-waveform inversion algorithm of Pratt (1999).

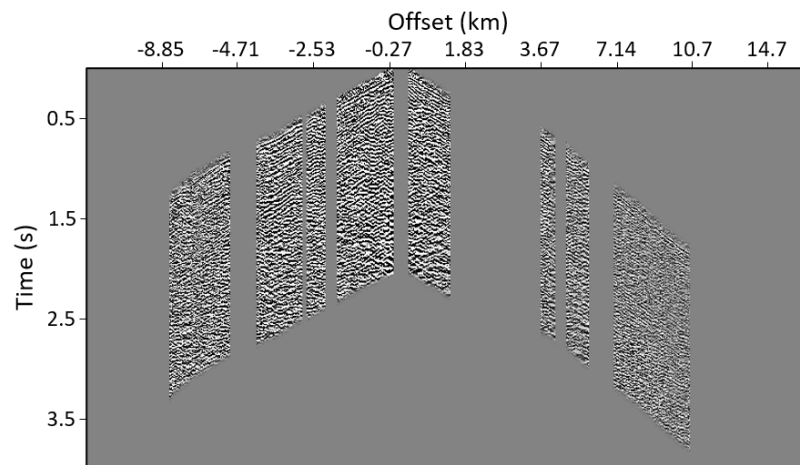
### 2.4.1 First-arrival traveltome tomography

The first step towards the implementation of nonlinear refraction traveltome tomography (after Zhang and Toksöz 1998) is manual picking of first break energy on direct and refracted waves. While automated processes work well up to a maximum offset of 3-4 km, accuracy decreases at longer offsets due to low signal-to-noise ratio. I manually pick arrivals for 298 shot gathers over the full offset range, placing an extra effort into picking as many traveltimes as possible, especially at far offsets.

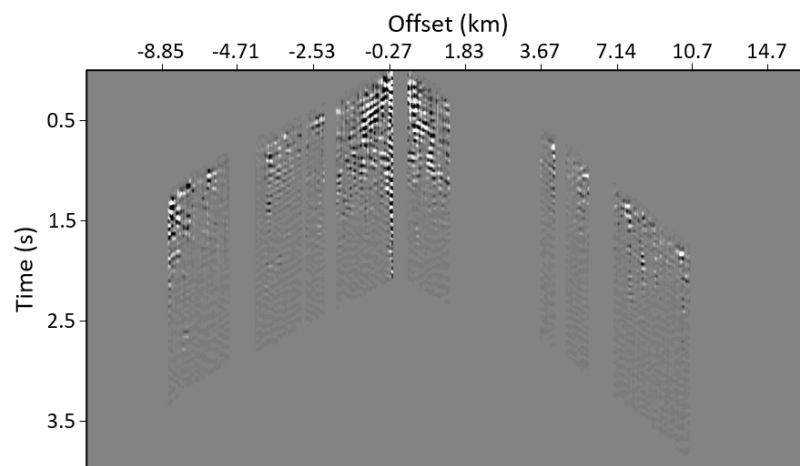
CHAPTER 2. FULL-WAVEFORM INVERSION IN A CRYSTALLINE TERRAIN USING COMBINED EXPLOSIVE AND VIBROSEIS SOURCES



(a)



(b)



(c)

Figure 2.5: Vibroseis gather at 11.8 km along the projected geometry. The data are presented (a) prior to preconditioning, with no windowing or muting; (b) with windowing, muting, F-K filtering, and with surface-consistent and shot-to-shot amplitude balancing; (c) with all preconditioning, including low pass filtering and time-damping (with  $\tau = 0.3$  s).

Note, however, that first arrival energy is obscured by noise in the data at offsets longer than 10 km for most gathers in our data. Therefore, I also implement extensive quality-control measures to ensure the resulting first arrival traveltimes tomography (FATT) is accurate. To this end I use traveltimes similarity, where two nearby shots are projected to each other and the RMS traveltimes difference is assessed; reciprocal errors, I test for reciprocity, by interchanging shot and receiver locations and evaluating their associated traveltimes. I compute FATT velocity models using a regular 50 m grid size to parameterize the velocities in 3D. FATT is executed using a 3D nonlinear refraction implementation, which allows to fully preserve the 3D character of the crooked geometry. I carry out 10 iterations, reducing the RMS misfit between predicted and observed traveltimes to within 16 ms.

## 2.4.2 Full-waveform inversion

### Model description

To proceed to 2D FWI we extract 2D initial velocity estimates from the 3D FATT model along the projected receiver and source path, imposing strong smoothing in the cross-line direction. Figure 2.6 displays the resulting starting model for FWI, with gray shaded regions indicating areas where no raypaths are observed. Note that depth penetration is expected to increase during FWI, because ray backprojection patterns in the high-frequency asymptotic approximation of ray tracing are different from the patterns of backpropagation in the waveform tomography case (Woodward 1992; Consolvo 2018).

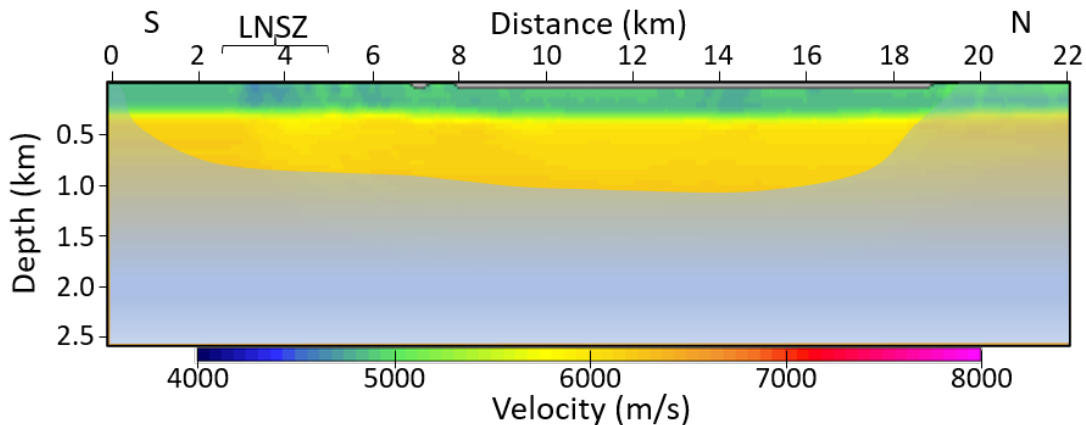


Figure 2.6: Initial velocity model from FATT to be used in the subsequent FWI. The grey-shaded region indicates areas in which no raypaths are observed.

The velocity model I use in FWI is 22 km long and 2.5 km deep. I discretize the model using a 2D finite-difference grid with square elements 50 m on a side. This mitigates numerical disper-

sion, as the smallest propagating wavelength ( $\lambda_{\min}$ ) is sampled with at least four grid points (after Jo et al., 1996). The resulting uniform grid contains  $440 \times 75$  grid points. I add 15 grid points at the corner and edges of the model to properly implement absorbing boundary conditions, resulting in total of  $(15 * 2 + 440) \times (15 * 2 + 75)$ , or  $470 \times 105$  grid points. I assign strong attenuation ( $Q = 1$ ) to the air layer, which helps in suppressing wave propagation above the surface, and I consider the subsurface to have a constant seismic quality factor ( $Q = 500$ ). Gardner’s relationship (Gardner et al., 1974) is implemented to estimate density values at each node, using the updated velocity model after each iteration. Different approaches to better constrain density variations during monoparameter FWI have been proposed (such as Silva et al., 2019; Jiang, 2020), as well as density inversion during multiparameter FWI (Prieux et al., 2013; Pratt and Smithyman, 2018; Li and Gu, 2019). However, strong amplitude variations in the Larder Lake dataset poses a difficult challenge for density inversion, and such an endeavor is beyond the scope of this work. In addition, an acoustic approximation for wave propagation is implemented here, which means the numerical solution of the dynamic components of the wavefields are only partially constrained.

Table 2.2: Finite-difference forward modeling parameters

Parameter	Value
Grid size ( $N_x \times N_z$ )	470 x 105
Maximum frequency ( $f_{\max}$ )	20 Hz
Minimum frequency ( $f_{\min}$ )	0.5 Hz
Number of frequencies $N_f$	40
Frequency interval ( $\Delta f$ )	0.5 Hz
Maximum modeled time ( $T_{\max}$ )	2 s

### Forward modeling

Frequency-domain forward modeling is based on the solution to the visco-acoustic wave equation using discretized Laplace-Fourier frequencies (i.e., equation (2.1)). I set the frequency increment ( $\Delta f$ ) using the sampling theorem,  $\Delta f = 1/T_{\max}$ , where  $T_{\max}$  is the maximum time window used for modeling. Modeling is carried out for all 298 sources, with 2,426 receivers per source. Table 2.2 lists the main modeling parameters. A constant frequency increment of 0.5 Hz for a 2 s time window implies the modeling of 40 discrete frequencies, given  $f_{\max} = 20$  Hz. If time domain results are required, a transformation of the discrete frequency-domain data via inverse Laplace-Fourier

DFT to the time domain can be accomplished. Since the maximum time window does not entirely represent the actual length of the original signal in time, frequency undersampling may corrupt the modeling result once transformed into the time domain. The complex-valued frequencies in the Laplace-Fourier domain effectively damp the resulting time series by multiplication with a decaying exponential function, which favors early-arriving events, while damping late-arriving waveforms (Song and Williamson, 1995; Shin and Ho Cha, 2009; Kamei and Pratt, 2013).

### **Full waveform inversion**

The FWI scheme implemented in this chapter is initiated by transforming the preconditioned time-domain data waveforms into the Laplace-Fourier domain. I then proceed to iteratively update the starting velocity model to reduce data residuals using a schedule of frequency choices. The strategy I implement is shown in Table 2.3, which is designed to address the significant nonlinearity expected due to the complex geological setting of the area. This strategy is a multiscale layer-stripping strategy for two potential streams: a joint explosive/vibroiseis stream (using stages 1 to 23), and a vibroseis-only stream (using only stages 5 to 23). The explosive/vibroiseis stream takes advantage of the lower frequencies available from the three explosive sources, and initiates the FWI from the starting model at 4 Hz, continuing up to 7.5 Hz. Once the velocity model has been updated using frequencies up to 7.5 Hz, the FWI continues from 7 Hz up to a maximum frequency of 15 Hz, using only vibroseis sources. In contrast, the vibroseis-only stream uses only frequencies from 7 Hz to 15 Hz (starting at stage 5). In neither stream do I simultaneously invert for both types of sources, since balancing the two inversion quantities is non-trivial and likely not fruitful. Data are inverted in regular frequency increments of 0.5 Hz. Inversion runs are stopped following two criterion: i) the maximum number of iteration has been achieved and/or ii) the residual reduction has achieved an optimum threshold.

The final inverted velocity model is shown in Figure 2.7. Figure 2.7a depicts the final FWI model, Figure 2.7b introduces a preliminary structural overlay, and Figure 2.7c shows the de-trended velocity structure. Refer to Section 2.5.2 for details on its structural significance.

Both streams are based on the sequential inversion of frequency stages, starting with three frequencies per stage and quickly advancing to a five-frequency approach. To increase inversion stability, low frequency components continue to contribute to the inversions as we move to higher frequencies, as I overlap the previous four frequencies at each stage. A total of 23 frequency stages are listed in Table 2.3, however it should be noted that a higher total number of iterations is actually performed because I perform extra inversion runs every 2-3 stages, applying an inverse taper to the gradient image to force deeper portions of the model to update.

Table 2.3: Schedule of frequencies and offset tapering used in each inversion group.

Inversion Strategy	Stage	Frequencies (Hz)	Iterations	Offset corners (km)	Residuals	Time-damping constant (s)
Explosive sources	1	4 4.5 5	1	1-1-6-8	Log. phase-only	0.2
	2	4.5 5 5.5 6	5			
	3	5 5.5 6 6.5 7				
	4	5.5 6 6.5 7 7.5				
Vibroseis sources	5	7 7.5 8	1	1-1-8-10		
	6	7 7.5 8	5			
	7	7 7.5 8 8.5				
	8	7 7.5 8 8.5 9				
	9	7.5 8 8.5 9 9.5				
	10	8 8.5 9 9.5 10				
	⋮	⋮		1-1-12-15	Conventional phase-amplitude	
	20	13 13.5 14 14.5 15				
	21	8 8.5 9 9.5 10				
	22	9.5 10 10.5 11 11.5				
23	11 11.5 12 12.5 13					

As shown in Table 2.3, I implement an initial inversion strategy using logarithmic phase-only residuals for frequencies 7 to 11 Hz. In tests conducted with these data I found that adding conventional phase-amplitude information after updating the model with the logarithmic phase-only objective function was important. Once a more accurate velocity model is obtained, I switch to the conventional phase-amplitude objective function with frequencies 11 to 15 Hz. Under this strategy, the velocity parameters are initially updated using the kinematic features of the waveforms. This helps in mitigating the artifacts arising from strong amplitude variations in the near surface. These amplitude variations are better constrained at later stages since synthetic waveforms more accurately represent the amplitude behavior of observed data, reducing the differences in data residuals, and improving the stability of the inversion.

The layer-stripping approach is supplemented by varying the characteristic decay times (Table 2.3). From stages 21 to 23, when using the phase-amplitude objective function, I return to the lower frequencies used previously, using a longer decay constant ( $\tau = 0.3$  s) that allows inclusion of later portions of the wavefields. Although I tested four different time-damping values (i.e. 0.1 s, 0.2 s, 0.3 s, and 0.4 s), I ultimately obtained optimal results using only two values ( $\tau = 0.2$  s and  $\tau = 0.3$  s, corresponding to 10 and 15 per cent of the maximum time window, respectively). The use of larger  $\tau$  values risks contamination of the inversion because of the inclusion of late arriving surface waves and converted modes, which have only imperfectly been removed by data preconditioning.

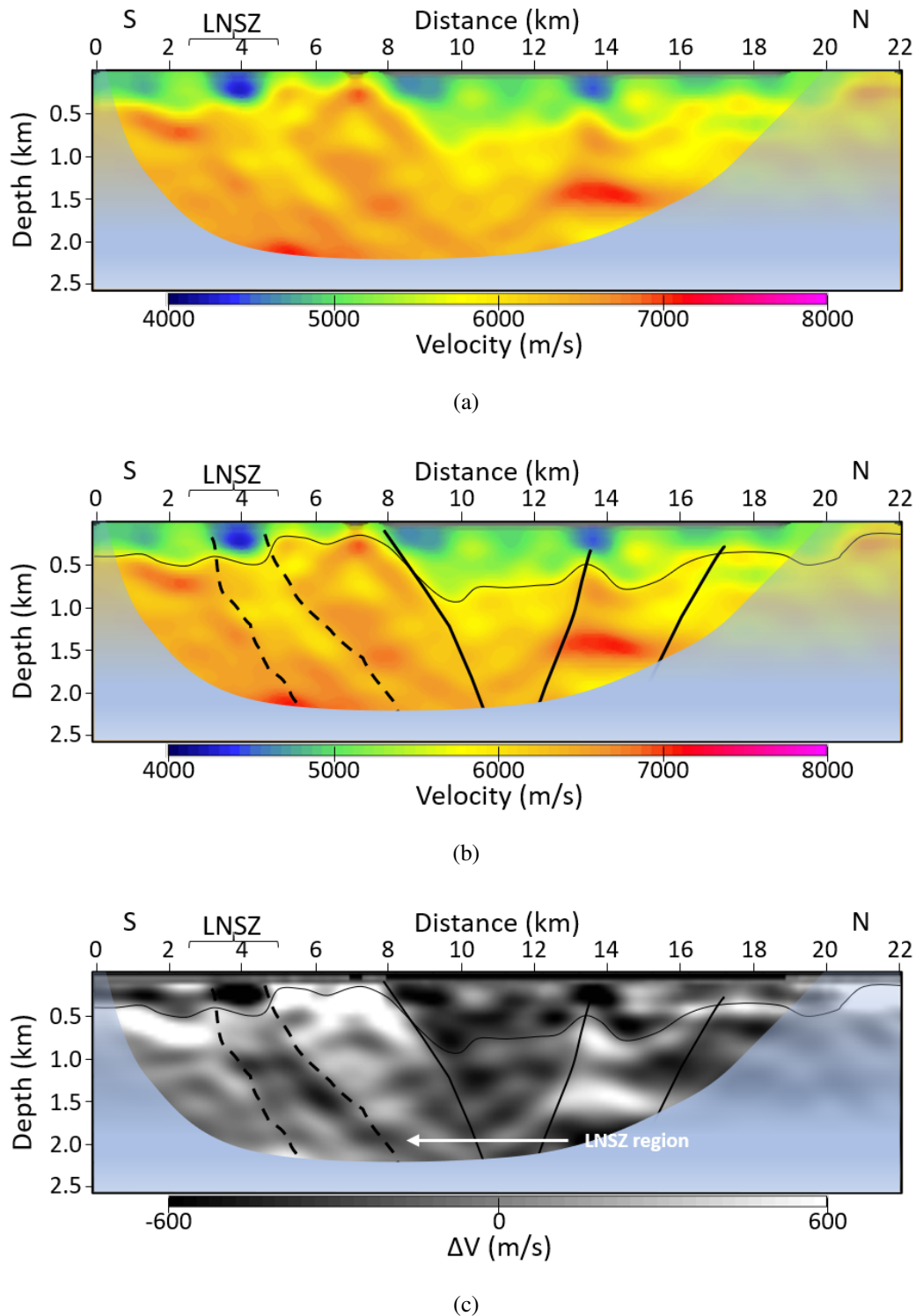


Figure 2.7: Final FWI P-wave FWI results, showing a) the velocity model, b) the velocity model with a preliminary structural interpretation (according to different velocity domains and geological map), and c) the de-trended velocity model. Grey-shaded regions indicate areas with little to no energy penetration. The thin solid black line in b) and c) indicates the sub-horizontal separation of sediments and less competent volcanic units, from the folded and faulted Larder Lake Group (north of the LNSZ, indicated by dashed black lines) and the McElroy assemblage (south of the LNSZ). Principal faults are indicated by thick solid black lines.

In addition to the data preconditioning steps described above, I also precondition the FWI gradients (i.e., the update images) as the inversion proceeds. I implement filters in the spatial and wavenumber domains to reduce common artifacts associated with the gradient image, and to enhance convergence. One such filter uses spatial tapers that are tapered to zero proximal to source and receiver locations, in order to inhibit inherent singularities introduced by the spatial Green's functions. This filter suppresses the gradient within approximately 50-100 m of the surface. To further suppress spatial noise in the gradient images, wavenumber filters are implemented and adjusted on an *ad hoc* basis throughout the inversion stages, guided by the maximum theoretical resolution (as calculated by Wu and Toksöz, 1987). I impose aggressive vertical filtering on the wavenumbers to suppress  $z$ -wavenumbers higher than one-half the maximum expected wavenumber, and horizontal wavenumbers in the gradient higher than one-fifth of the same maximum wavenumber are suppressed. It appears to be crucial to fine-tune the filtering at each inversion stage, which means that corner values might slightly differ by 5 to 10 percent from these criteria.

In the initial inversion runs (stages 1 and 2 in Table 2.3), I assume a source wavelet given by a two-excursion Küpper wavelet (Kupper, 1958; Brenders and Pratt, 2007b) with a dominant frequency equal to 5 Hz. This assumed source signature is a simple approximation that allows to start the inversion. The estimation of source signatures is of great importance, especially when working with explosive sources in onshore seismic data. Inaccurate estimation of source wavelets may lead to erroneous computation of synthetic data, generating higher data misfit and erroneous inversion results. I estimate the true source signatures in the later stages of FWI by solving the equations given by Pratt (1999), in which the current velocity model is assumed to be accurate enough. I then use updated velocity models to re-estimate source signatures in a sequential fashion after each inversion stage. As we proceed we progressively note improvements in the phase and amplitude behavior of the estimated source signatures.

### 2.4.3 Validation

A thorough appraisal and validation of the results is vital due to the non-unique nature of seismic waveform inversion. To this end, I carry out extensive assessments by qualitatively evaluating waveform fit in the time domain, estimating and comparing *a posteriori* source wavelets for all shot gathers, and by performing checkerboard tests.

Waveform fit for a representative shot gather is depicted in Figure 2.8 and Figure 2.9. The observed data in Figure 2.8a are from a vibroseis source located approximately 15 km along the projected geometry, Figure 2.8b exhibits an equivalent synthetic gather generated with the FATT velocity model, and Figure 2.8c shows the synthetic waveforms resulting from the final FWI velocity model. Waveforms in both Figure 2.8b and 2.8c match the picked first-arrival times within one

half cycle, complying with the cycle-skipping criterion (Virieux and Operto, 2009). The synthetic data in Figure 2.8b appear to be limited to first-arrival energy, whereas later phases are observed in the synthetic data of Figure 2.8c. It is evident that the synthetic gather resulting from the final P-wave velocity model correlates better with the field data in terms of waveform shape, amplitude, and phase. This highlights the reliability of the velocity model, as later arrivals are successfully reproduced.

A better evaluation of the similarities between observed and forward-modeled data is depicted in Figure 2.9, in which I provide a zoom-in of a 500-ms long window of the waveforms from Figure 2.8. Figure 2.9a reveals the complex behavior of observed late phases, whereas Figure 2.9b displays the same data but with a bandpass frequency filter (0-10-20-35), re-sampled to 10 ms, and trace-decimated. We perform this filtering to get a more meaningful visual comparison with the synthetic data. As expected, the forward-modeled data from the FATT starting model (Figure 2.9c) fail to reproduce the detailed waveforms in the observed arrivals. In contrast, almost all arrivals are well represented in the forward-modeled data from the FWI result (Figure 2.9d). The phase and amplitude behavior of the observed waveforms are remarkably well replicated in this synthetic shot gather, confirming the high-confidence we may assign to the inverted model.

Figure 2.10 depicts the time-domain source signatures inverted by using the approach of Pratt (1999), described in Section 2.2.2. Figures 2.10a and 2.10b show the estimated source wavelets from using the initial FATT model and the final FWI model, respectively. Source signatures inverted from the initial FATT model show poor coherency and low repeatability. In contrast, the coherency and consistency of source signatures inverted using the final visco-acoustic FWI model are significantly better, confirming the validity and quality of our final velocity structure.

As a final validation step, I perform checkerboard tests to verify the resolving strength of our inversion results. To do this, I add checkered velocity perturbations of +/- 5 per cent to the starting velocity model from FATT, with two different dimensional settings: 1000x500 m and 500x250 m. I select the spatial dimensions of the perturbations based on the upper resolution limit of FWI, which depends on the maximum vertical and horizontal wavenumber allowed into the model reconstruction. The resolution of the model is on the order of 833x333 m (i.e., approximately one wavelength). The 1000x500 m patterns should be reconstructed in most portions of the model, whereas resolving 500x250 m perturbations will be more challenging because this size is near the theoretical resolution limit of FWI (i.e. half the seismic wavelength). The synthetic data for the perturbed models are generated by employing the same finite-difference forward-modeling algorithm described in Section 2.4.2. Likewise, the checkerboard pattern is retrieved by using the same multiscale layer-stripping strategy displayed in Table 2.3.

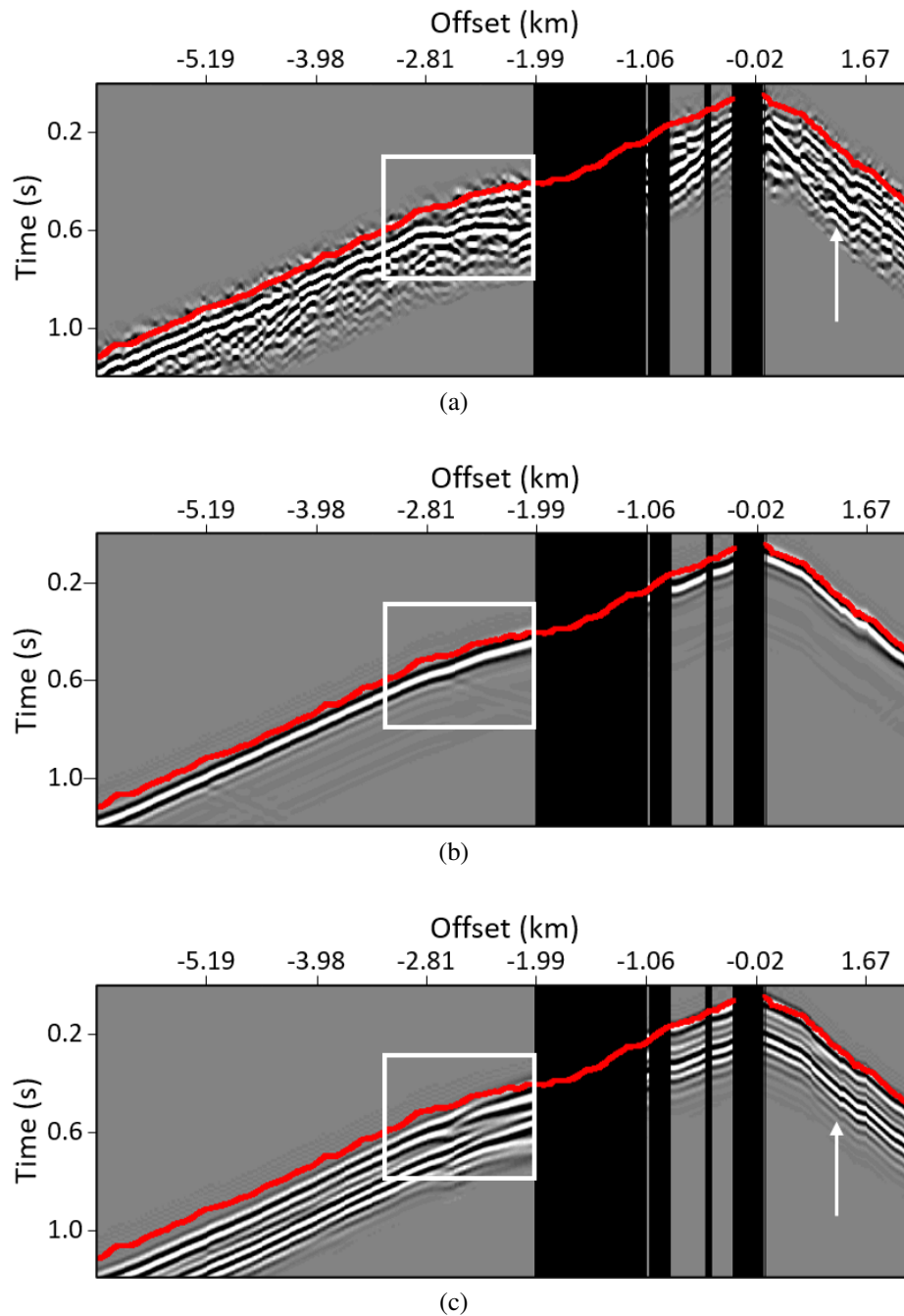


Figure 2.8: Comparison of a) observed waveforms of a shot gather located at approximately 15 km along the projected line, b) visco-acoustic synthetic waveforms using the FATT velocity model, and c) visco-acoustic synthetic waveforms using the final FWI velocity model. The red line in all panels represents the manually picked first-arrival times on the observed data. The white arrows indicate areas of good agreement between observed and final predicted waveforms. The white rectangles represent a zoomed-in area to be discussed in the next figure. Waveforms discarded due to noise or out-of-plane errors are indicated by the black regions.

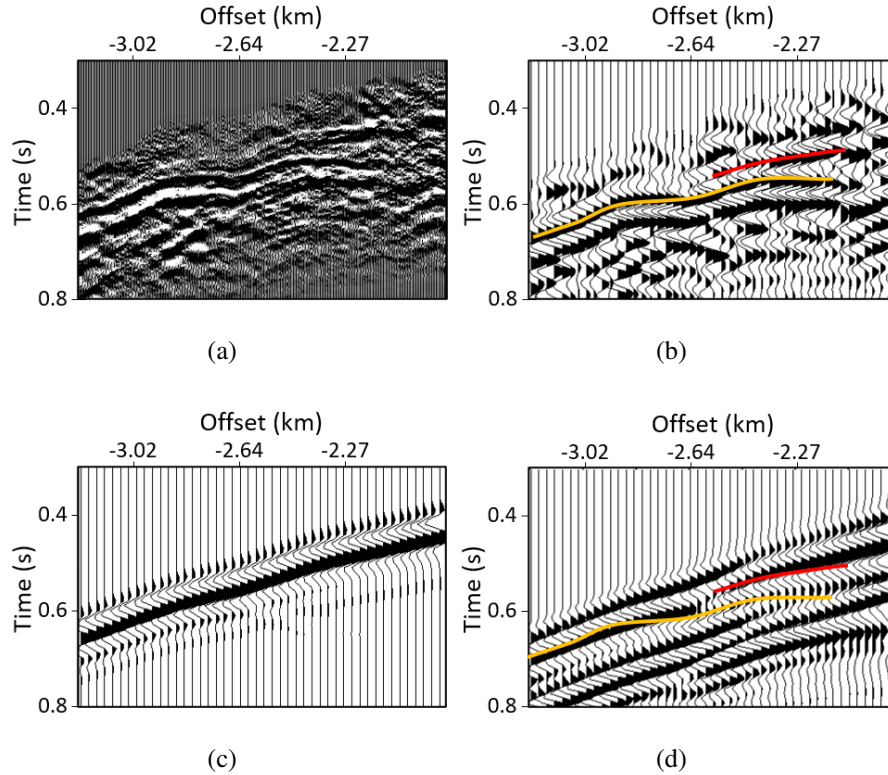


Figure 2.9: Zoom-in on the rectangles displayed in Figure 5.12 showing a) the original observed waveforms, b) observed waveforms after bandpass filtering, re-sampling, and trace decimation, c) synthetic waveforms from the FATT velocity model, and d) synthetic waveforms from the final FWI velocity model. Colored lines in (b) and (d) are indicative of the same seismic phases.

The results of the checkerboard tests are depicted in Figure 2.11. We observe the inversion succeeds in retrieving the perturbations associated with the larger (1000x500 m) checkerboard features (Figure 2.11a), and also correctly reconstructs most of the smaller patterns (Figure 2.11b). It is noticeable, though, that the reconstruction of the 500x250 m anomalies is degraded around the edges of the model and the shapes of the elements are not as well reconstructed as for the spatially-larger counterpart. This is because the smaller pattern is very close to the resolution limit of FWI. The region of highest confidence is the southern section of the model due to better source coverage and, hence, wavepath coverage (Figure 2.11). The checkerboard elements are poorly retrieved in the northern portion of the model (beyond 18 km) mainly due to the lack of sources, which are located between 2 and 16 km.

#### 2.4.4 FWI on explosive/vibroseis vs. vibroseis-only data

One of the purposes of this chapter is to evaluate the effectiveness of utilizing the very low frequencies available from the sparsely distributed explosive sources, as a supplement to the much

denser vibroseis sources. The premise is that the incorporation of the long-wavelength features recoverable from the low-frequency components of impulsive sources would lead to an improvement in subsequent higher frequency FWI from the vibroseis source data.

Such sources may allow a 3- or 4-Hz starting frequency for FWI. In complex hardrock environments inversions are extremely susceptible to cycle-skipping due to lateral changes in physical properties of rock units (e.g. contact zones and layer boundaries). Incorporating lower wavelength updates by utilizing the explosive sources should improve the replication of complicated seismic phases associated with first arrival energy. This, in turn, potentially results in more accurate modeled seismograms, mitigating the cycle-skipping phenomenon during FWI.

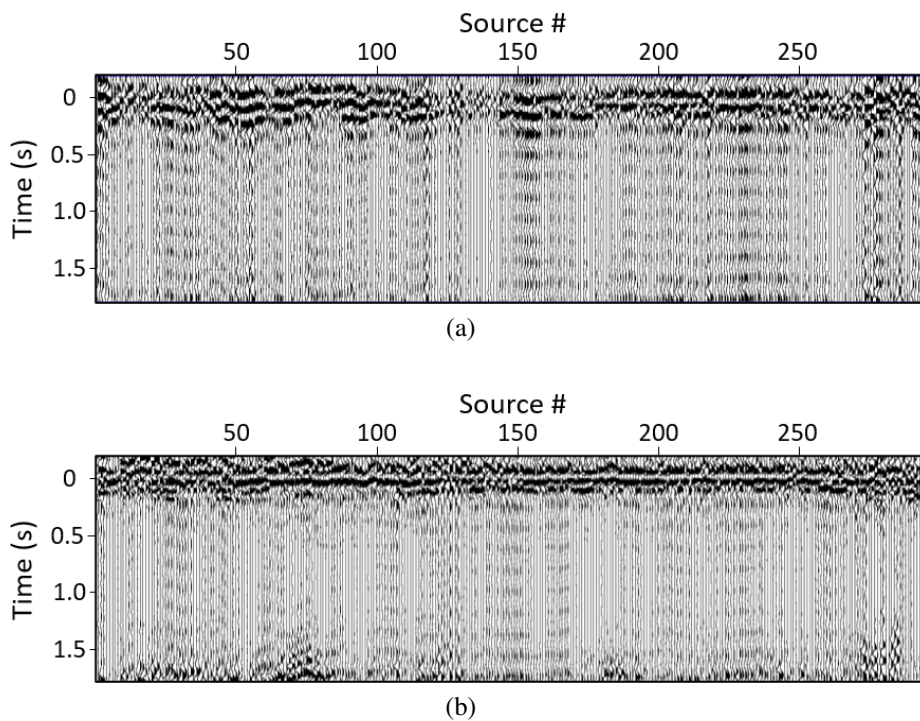


Figure 2.10: Time-domain source signature for each shot in our dataset. These signatures are estimated using (a) the initial FATT model, and (b) the final FWI model.

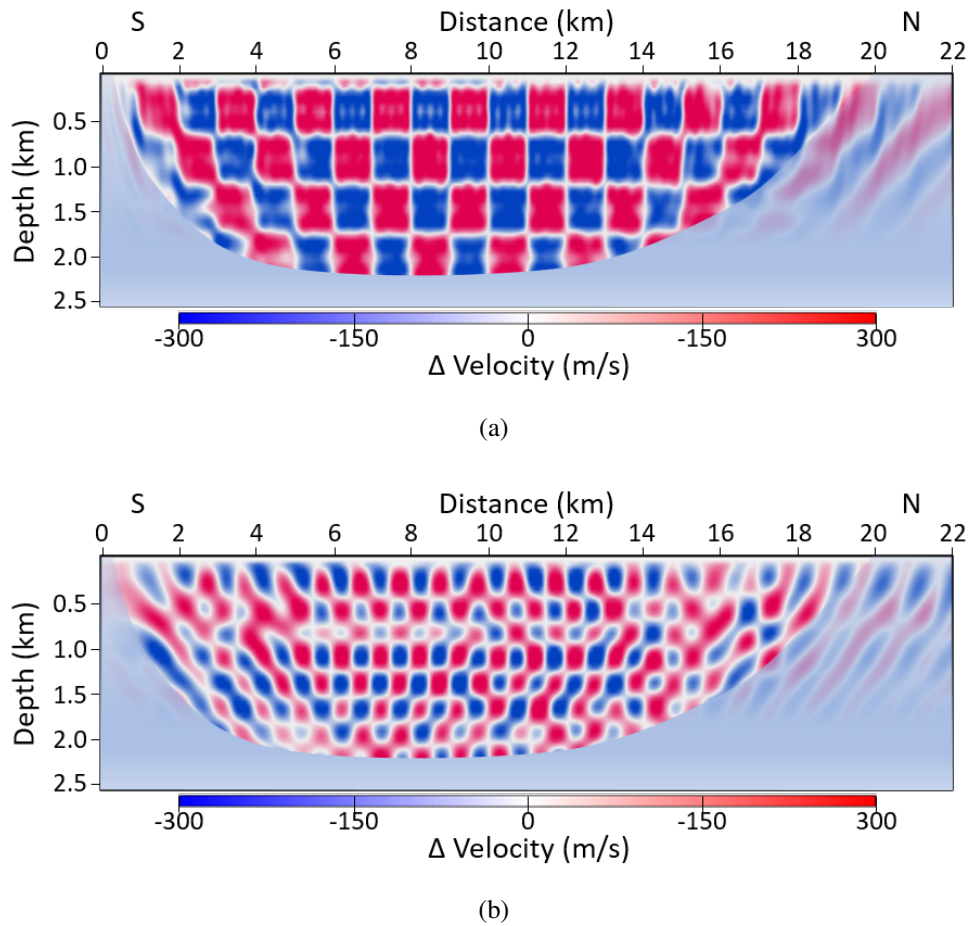


Figure 2.11: Resolution analysis by checkerboard tests, with +/- 5 per cent velocity anomalies superimposed on the starting FATT model. Checkered pattern dimensions are a) 1000x500 m and b) 500x250 m.

Under the scheme of Table 2.3, the explosive/vibroseis inversion stream is characterized by the continuation of the explosive source FWI velocity inversions into the vibroseis stream, whereas the vibroseis-only stream begins without the benefit of the explosive source FWI. In order to evaluate the two results, I qualitatively compare the resulting velocity structures, and I compare the estimated source signatures. Figure 2.12a shows the velocity result after the inversion of the 13th frequency stage using the vibroseis-only approach, whereas Figure 2.12b depicts the P-wave velocity model after implementing the explosive/vibroseis approach.

CHAPTER 2. FULL-WAVEFORM INVERSION IN A CRYSTALLINE TERRAIN USING COMBINED EXPLOSIVE AND VIBROSEIS SOURCES

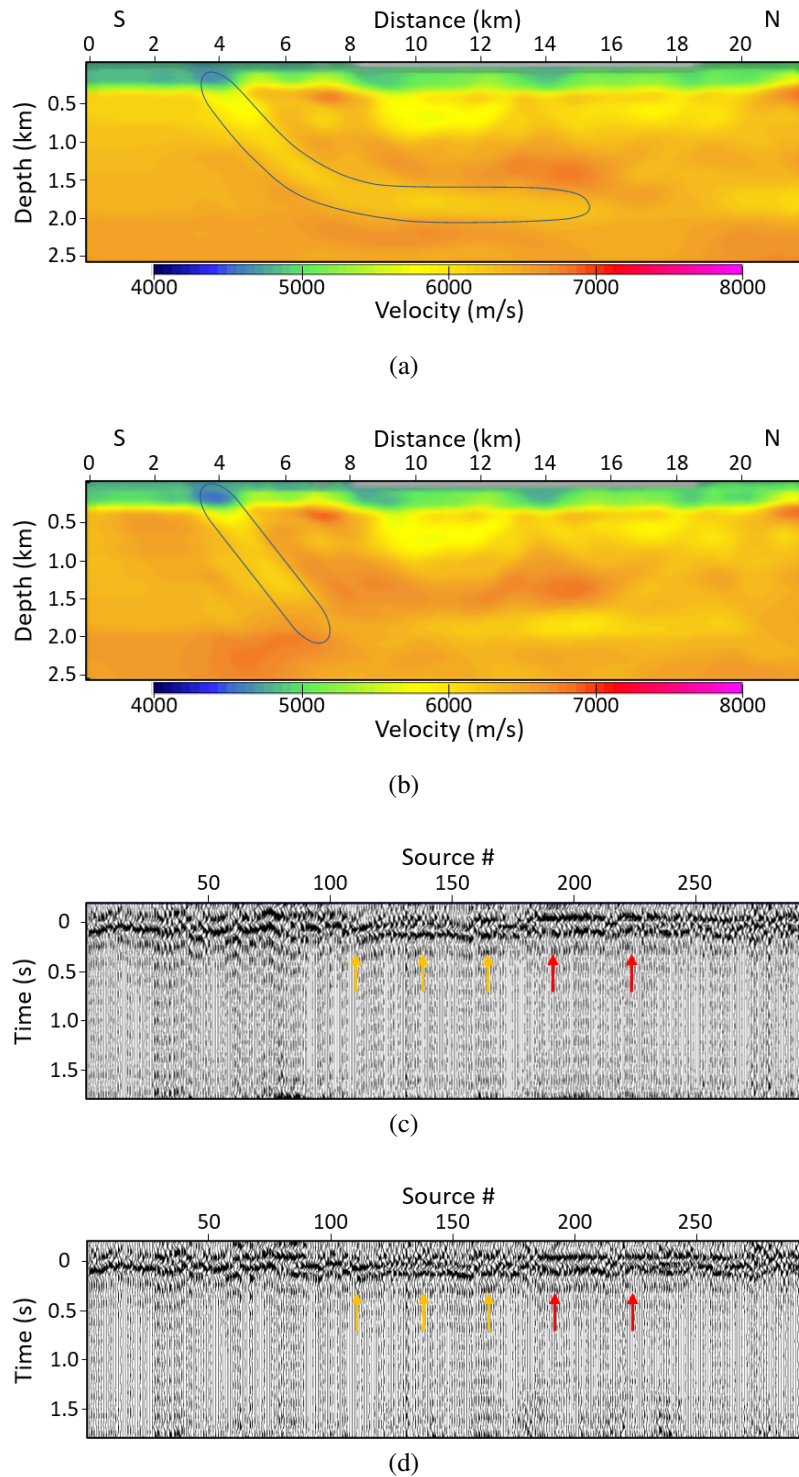


Figure 2.12: Explosive/vibroiseis FWI results vs. vibroseis-only results, showing results after the 13th inversion stage (see Table 5.1). Velocity models obtained by starting the FWI at a) starting at 7 Hz (without explosive sources), and b) 4 Hz (with explosive sources). Grey-shaded regions indicate areas with little to no energy penetration. The blue outline identifies the shape of the low velocity anomaly referred to in the text. Source signature inversions are depicted c) using the velocity model in a), and d) using the velocity model in b). Key features are identified in c) that suggest a more reliable velocity reconstruction (e.g. orange and red arrows showing flatter events and enhanced continuity/coherency, respectively).

Both results reveal a low-velocity anomaly associated with the LNSZ and, at first sight, both images appear to be similar. However, several key features suggest the information from explosive sources is valuable. For instance, the vibroseis-only result shows an apparent horizontal continuation of the low-velocity anomaly at approximately 1.8 km depth between 6 and 8 km along the model (Figure 2.12a), which appears to be an artifact. This horizontal continuation is not observed on the explosive/vibroseis result (Figure 2.12b), which shows the structure continuing vertically to a greater depth; this correlates more closely with the known geology around the LNSZ. There is a horizontal feature along the southern end of both profiles at approximately 2 km depth, which seems to be more apparent in Figure 2.12b. It can be observed, however, that such a feature is separated by the vertical low-velocity anomaly, and does not continue towards the north portion of the profile. Similarly, Figure 2.12c and 2.12d display the inverted source signatures for each shot gather employing the velocity model in Figure 2.12a and 2.12b, respectively. We observe a more consistent and focused appearance in Figure 2.12d (orange arrows), and sections with greater coherency between inverted source wavelets (red arrows). Because these are partial results at the 13th frequency stage, the cumulative improvements introduced by the long- and intermediate-wavelength components from the explosive sources (unavailable on the vibroseis-only inversions) will further enhance results at later stages. These features support the initial use of the data from the sparsely positioned explosive sources, before continuing FWI using the full vibroseis geometry.

## 2.5 Results and discussion

### 2.5.1 Representative sensitivity kernels

As described in the introduction, it is informative to assess the behavior of representative “wavepaths” with a single representative source-receiver pair (Woodward, 1992). Figure 2.13 displays two such monochromatic wavepaths at 7 and 15 Hz for a single source-receiver pair with an offset of about 7 km (approximately two-thirds the maximum useful offset in the full dataset); I use the final FWI P-wave velocity model for the construction of the sensitivity kernels. The vibroseis source for both numerical kernels is located at 11.8 km along the projected geometry and the receiver at 19 km. We observe that the resolution in the wavepath at the lowest vibroseis frequency (Figure 2.13a) is naturally broad and penetrates deeply into the section. The apparent wavepath coverage is similar to the raypath coverage that would be expected from the FATT, but it is notably richer in low-wavenumber information. Finer-scale features are seen on the 15-Hz wavepath (Figure 2.13b), especially around the near-surface region. These images demonstrate that FWI is capable of reaching deeper portions of the model than traveltimes tomography, significantly adding to the geological information that can be retrieved from the survey data. This is especially true when

low frequencies are available.

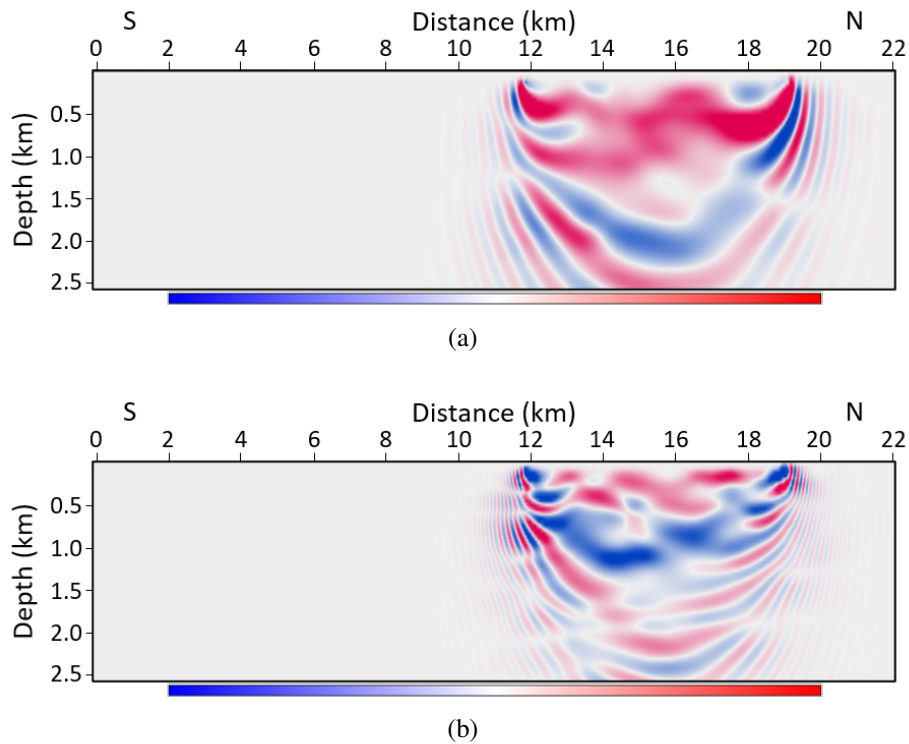


Figure 2.13: Wavepath images, depicting the model update response for a monofrequency source-receiver pair at a) the minimum frequency of 7 Hz and b) the maximum frequency of 15 Hz. The source is located at 11.8 km along the projected line and the receiver is located at 19 km.

## 2.5.2 Full-waveform inversion results

The final P-wave velocity image from the southern part of the Larder Lake transect using explosive and vibroseis sources, with frequencies from 4 to 15 Hz is depicted in Figure 2.7a. Note that the 295 vibroseis sources are positioned with approximately even spacing between 2 and 16 km, which explains the reduced coverage at the northern end of the model. The final velocity image in Figure 2.7a displays significantly improved structural information over that seen in the FATT model (Figure 2.6). I add some interpreted structural information in Figure 2.7b. In order to better assess structural features, especially around the LNSZ, following Kamei et al. (2012) I remove the dominant 1D vertical velocity “background” trend from the FWI result. I estimate this trend by fitting a third-degree depth-dependent polynomial  $V_0(z) = az^3 + bz^2 + cz + d$  to the 2D FATT velocity image, and the de-trended velocity model is defined as  $\Delta V = V(x, z) - V_0(z)$  (Figure 2.7c). This allows to adequately adapt the 1D vertical trend to the rapid vertical velocity variations seen within the near-surface zones. This variation arises primarily from lithological contacts between rock units (e.g. thin sedimentary layers and volcanic units).

All panels in Figure 2.7 show an increased structural complexity north of the LNSZ, as exhibited by the level of lateral and vertical velocity fluctuations. A primary feature of the inverted P-wave velocity model on Figure 2.7a is the pattern of moderate lateral velocity variations, highlighted by complex sub-vertical structures visible on panel 2.7b. Another primary feature is the pronounced separation of the sub-horizontal low-velocity, mostly “weathering-like” region from the more competent rock units, around 200-300 m from the surface (as indicated by the thin near-horizontal black line in Figure 2.7b). A sub-vertical low-velocity anomaly is observed at about 4 km along the projected geometry (identified by dashed vertical black lines), spatially coincident with the surface exposure of the LNSZ. This anomaly is related to a steep shear zone extending from the surface to the bottom of the section, displaying a near-vertical configuration in the first 300-400 m to then transition to a less steeper structure - with an apparent dip of about 35-40 degrees from the horizontal. Structures near this zone are dominated by prominent lateral velocity contrasts, whereas vertical velocity changes are not as apparent as in the north range of the section. These sub-vertical velocity domains are better seen on the de-trended model in Figure 2.7c, where the boundaries are more evident. The de-trended model thus helps in defining our preliminary structural interpretation, especially near the LNSZ.

In reality, the velocity within a shear zone is governed by a combination of different rock types, and by geomechanical and geochemical processes that modify the elastic properties of the structure, resulting in local velocity variations within the shear zone. Therefore, the dimensions and apparent dip of the sub-vertical anomaly do not necessarily represent the full geometry of the LNSZ. The velocity structure in Figures 2.7a, 2.7b, and 2.7c may, for example, reflect the degree of rock alteration/deformation within the shear zone.

In addition to geological heterogeneity, significant cross-line structural features (oblique to our profile) may be misrepresented or not represented at all because the survey geometry does not properly illuminate the subsurface. If the imaging plane (i.e., the vertical plane beneath the projected geometry line, see Figure 5.1), does not coincide with the dip-line direction of the subsurface geological structure, the recorded waveforms would not be responding to velocity variations exactly beneath the geometry line. Rather these variations may be projections of cross-line or out-of-plane variations onto the imaging plane. Under such a scenario, the apparent dip of inclined structures will be less than their true dip. Thus, the LNSZ might actually have a steeper dip than its apparent dip seen on Figure 2.7, due to this relationship between the imaging plane and the true structure.

### 2.5.3 Geological discussion

Although a full geological discussion is beyond the scope of this paper, it is worth highlighting some key aspects of the inverted velocity structure, and relating these to the known geology of the

area. Brace et al. (2018) described the volcanic succession present south of the LNSZ as comprising the McElroy and the Skead assemblages, whereas north of the LNSZ the rock units are part of the older, more competent Larder Lake group. The Larder Lake group is overlain by sedimentary rocks of the Hearst assemblage. Figures 2.7a and 2.7b exhibit a velocity cross-section that correlates well with this geology; within the results, significant lateral velocity contrasts around the LNSZ are observed, revealing a high-velocity rock body between 4.5 and 8 km and thereafter a basin-like low-velocity structure between 8 and 20 km along the profile. See the geological map in Figure 2.1 between the dashed yellow lines (major faults). These velocity changes respond to rock units of varying age groups, and their associated degree of metamorphism. The velocity ranges recovered by the inversion are in agreement with velocity estimations on core samples from the Blake River Group, which are representative of our study area (see Grandjean et al. 1995). This difference in structural domains north and south of the LNSZ may be explained by complex fold geometries and fault planes seen north of the shear zone but unrecognized to the south, as pointed out by Brace and Sherlock (2017), Brace et al. (2018), and St-Jean et al. (2019).

A particular example is seen on the footwall of the fault plane north of the LNSZ in Figure 2.7b (assuming such a plane is associated with a compressional regime). Here the hanging wall exhibits a lower velocity compared to the footwall, suggesting the lower-velocity materials in the hanging wall are weakly consolidated sediments or strongly deformed volcanic units (or, most likely, the combination of both). This velocity behavior is consistent with the findings of St-Jean et al. (2019) who reported that the sedimentary section north of the LNSZ is dominated by metamorphosed sedimentary rocks (originally related to mudstone and sandstone units), which may explain the low-velocity basin-like development. Furthermore, this indicates that the clastic column thickens northwards (at least locally, with velocities of approximately 5-5.5 km/s). See Grandjean et al. (1995) for representative examples of velocity variations in the region.

The complex geology of the Larder Lake area and the limitations of the acquisition geometry have complicated the inversion of fine structural details. Nonetheless, the steep, north-facing architecture seen in the inverted velocity model around the LNSZ also correlates with the structural description given by Jackson et al. (1995), who defined the area as hosting moderate to steeply north-dipping inclined fabric. In addition, the results shown in this chapter are consistent with the structural interpretation of Nedimović (2000) who worked with the Lithoprobe Abitibi line 23, also crossing the LNSZ along almost the same geometry as our survey. Nedimović (2000) processed several seismic cross-sections to identify structural features around the LNSZ, suggesting the LNSZ is north-dipping with a sub-vertical angle equivalent to that shown in Figure 2.7c.

### Synthetic experiment - LNSZ

Determining the structural architecture of a potentially gold-bearing area, such as the LNSZ, is key for developing efficient mining exploration strategies. There is no widespread consensus even on the most generic structural features of the LNSZ, such as its dipping direction. This shear zone has been reported in the literature as a reverse fault dipping both south (Jackson et al., 1990a) and north (Corfu et al., 1989; Nedimović, 2000). Additionally, mafic to felsic alkaline mineralization and gold prospects associated to the LNSZ (St-Jean et al., 2019), has generated interest in this area in recent years.

In order to assess the capability of the inversion technique of retrieving LNSZ-like structures, I conduct a synthetic experiment by introducing a north-dipping slab into the starting FATT model, and evaluating the ability of the inversion to recover an image of this slab. The dip angle of the structure is based on the near-surface low-velocity anomaly observed in the final P-wave velocity model around 4 km along the profile. The width of the slab is 1.5 km, which represents roughly two wavelengths at the maximum lateral wavenumber allowed in the reconstruction. Figure 2.14a shows the velocity model used to generate synthetic data; this is the same model as the FATT model in Figure 2.6, but with a low-velocity slab with a 1D linear increase in velocity from 5 km/s at the top to about 6 km/s at the bottom. Figure 2.14b shows the resulting velocity reconstruction. The true velocity anomaly is accurately reproduced only at the near-surface, down to about 1 km in depth. Deeper portions

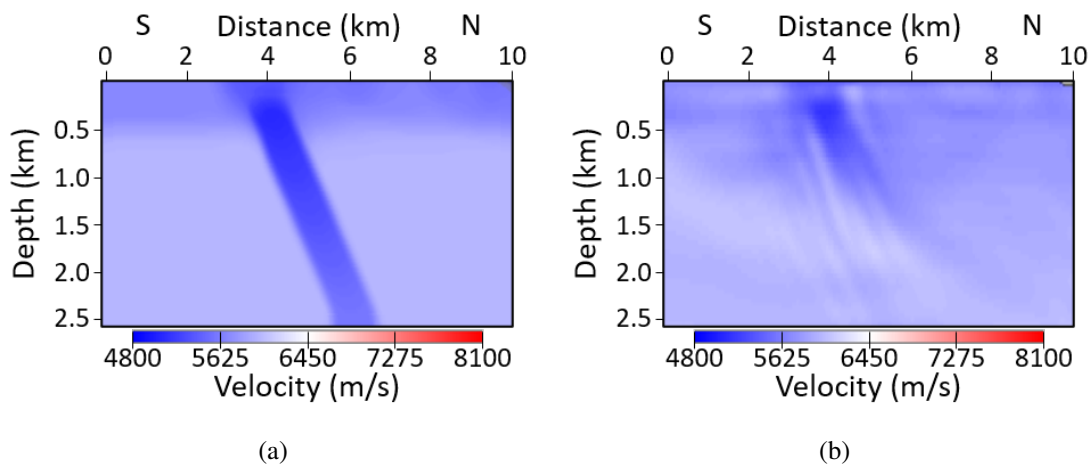


Figure 2.14: Synthetic FWI experiment for a steeply dipping slab inserted into the FATT velocity model. a) True velocity model containing the low-velocity slab, and b) FWI result using the inversion strategy described in Table 5.1. Here we only show the first 10 km of the profile.

I implement the same nonlinear iterative FWI strategy described in Table 2.3 to solve for the velocities, again using the initial FATT model as the starting model (without the low velocity slab). Figure 2.14b displays the resulting velocity reconstruction. The true velocity anomaly is accurately reproduced only at the near-surface, down to about 1 km in depth. Deeper portions

of the low-velocity slab are difficult to retrieve, to the point that only the edges of the slab are correctly inverted for up to a maximum depth of approximately 2 km. The inversion results of our steeply dipping zone are very similar to those obtained by Mora (1989) who inverted for a low-velocity circular anomaly within a homogeneous half-space (Figure 9c in his article). He found that the results of this particular experiment lack the contribution of low-wavenumber components, as inversions are limited to using back-scattered wavefields. Mora termed these reconstructions “migration-like”. This is consistent with Pratt et al. (1996), who also indicated that inversions at depth create migration-like inversion results. This is because deeper parts of the anomaly are illuminated only by the outer, high-wavenumber lobes of the wavepaths; under these conditions inner low-wavenumber lobes (within the first-Fresnel zone) do not contribute to the reconstruction. Consequently, image boundaries and their polarities are well defined, whereas the quantitative velocity reconstructions are missing. Readers should refer to Wu and Toksöz (1987); Mora (1989); Pratt et al. (1996); Kazei et al. (2013) for a thorough explanation on resolvable wavenumbers in seismic inversion.

While I recognize that velocity reconstructions are always more readily accomplished on synthetic experiments, these synthetic tests nevertheless allow to understand the limitations of the inversion technique as well as its capabilities on resolving a given structural setting, such as the one shown in Figure 2.14. Significant correlation is found between the synthetic results in Figure 2.14b, and the reconstruction of the LNSZ in Figure 2.7c. As predicted by the experiment, deeper portions of the model are retrieved through a migration-like reconstruction. The edges of the anomaly are recovered up to approximately 2 km depth. While we may not be able to image the exact boundaries of the structurally complex LNSZ, this synthetic (albeit noise-free) study demonstrates there is a potential to gain a general understating on its apparent dip, width, and orientation.

## 2.6 Conclusions

In this chapter, I present results of visco-acoustic full-waveform tomography as applied to the southern portion of the crooked 2D-1C Larder Lake seismic transect. I have successfully demonstrated that low-frequency components available from a sparse set of explosive sources allow more accurate reconstructions of the velocity structure over those using vibroseis data alone. This is because frequencies as low as 4 Hz are available from the explosive data, helping to mitigate cycle-skipping issues, and making use of long-wavelength structures that are sensitive to these low-frequency wavefields. Furthermore, I find our inversions to be more stable when initially inverting only the kinematic (phase-only) components of the observed wavefields, before introducing amplitude information.

The resulting final FWI velocity image enhances the geological understanding of the area, especially in the region of the poorly exposed LNSZ. The limited documentation on this potentially gold-bearing zone is ambiguous regarding its structural architecture. The inverted velocity images indicate that the LNSZ is a north-dipping structure, with a near-vertical dipping angle in the first 300-400 m, becoming less steep thereafter. Moreover, a complex structural configuration is observed north of the LNSZ exhibiting prominent velocity changes. This configuration is consistent with the known geology of the area. Likewise, sub-horizontal, less competent and weakly consolidated near-surface layers are evident on the FWI results within the few first hundred meters of the near surface. These near-surface layers are characterized by velocities between 5000 and 5500 m/s.

# Chapter 3

## Seismic imaging of crystalline structures: 2D and 2.5D visco-acoustic full-waveform inversion

### 3.1 Introduction

Superficial ore deposits (with depths less than 1 km) are being depleted worldwide, and the mining industry is rapidly steering towards deeper exploration of mineral endowments (Xie et al., 2019; Matthews, 2002). This is especially true in the southern Abitibi region of Canada, where post-orogenic uplift has placed potential mineral deposits within a mineable depth of approximately 1 to 3 km (Bleeker, 2015). The imaging of subsurface structures in crystalline environments is usually characterized by regional sections where local and near-surface structures are poorly imaged. Therefore, the gap between surface geology and the crustal-scale architecture interpreted in seismic sections must be addressed, so near-surface ore deposits can be exploited.

Standard seismic processing techniques are adversely affected by the heterogeneity of the weathering layer and the complexity of shallow structures, limiting the imaging of structures at depth. The estimation of a velocity field is one of the main controlling aspects in the success of seismic processing. However, in strongly heterogeneous near-surface regions, limited accuracy and resolution generally compromises the quality of the imaging of deeper structures through seismic migration (Cheraghi et al., 2019; Saffarzadeh et al., 2018; Khoshnavaz et al., 2016).

Full-waveform inversion (FWI) is an imaging technique that potentially retrieves high-quality velocity models of the subsurface (Brunod et al., 2019; Liu, Z., & Zhang, 2017; Brenders and Pratt, 2007b), and is optimal for near-surface velocity reconstruction. FWI is a nonlinear inverse technique that relies on the combination of ray- and wave-based methods (Smithyman and Clowes,

2013). The former is employed for the generation of an initial macro-velocity model, assumed to represent the low-wavenumber properties of the velocity field. Wave-based methods are then implemented for the reconstruction of the medium-to-high-wavenumber components. The approach seeks to minimize data residuals (i.e., the differences between synthetic and measured wavefields), by iteratively updating the underlying model parameter. Often, FWI is implemented using a 2D modeling scheme because of its affordable computational cost and generally high-quality inversion results (Borisov et al., 2020; Adamczyk et al., 2015). In complex geological settings and severely crooked geometries, a full three-dimensional (3D) numerical solution of the wave propagation phenomenon is desired (Wang et al., 2019b; Operto et al., 2013). However, such solutions are computationally prohibitive, mainly due to the burden of multisource seismic modeling (Virieux and Operto, 2009).

Two-and-half-dimensional (2.5D) modeling and inversion is an approach that is more accurate than a purely 2D strategy, but that uses much less computational resources than fully 3D simulations (Pratt, 1989; Smithyman and Clowes, 2013; Kamei et al., 2015). In the 2.5D scheme, we abandon the line-source assumption inherent to a 2D formulation, and instead we accurately solve for the amplitude and phase characteristics of true 3D wave propagation by simulating point sources, while still considering a 2D subsurface velocity model. By using a 2.5D strategy, the predicted geometrical spreading of the wavefields are properly accounted for. In contrast, the more limited 2D approach requires corrections be applied to the observed data in terms of geometrical spreading effects in order to match the 2D nature of the predicted wavefield calculations. The 2.5D modeling approach assumes no velocity variations exist in the cross-line direction, but it may be applied in situations where these out-of-plane variations are negligible. The method involves transforming the frequency-domain wave equation into the transverse wavenumber ( $k_y$ ) domain, computing solutions in the frequency-wavenumber domain for each transverse wavenumber component, and then transforming back to the spatial domain (Song and Williamson, 1995). I employ the approach of Zhou and Greenhalgh (2006) to efficiently discretize the out-of-plane wavenumber spectrum for the inverse Fourier transform.

I follow a similar inversion strategy to that used in Chapter 2 in which I performed 2D visco-acoustic frequency-domain FWI on the southern portion of the Larder Lake dataset. While that chapter was successful in delineating a prominent shear zone (i.e., the Lincoln-Nipissing Shear Zone - LNSZ), the results suffered from data rejection due to the crookedness of the profile, and the 2D nature of the forward-modeling scheme. In this chapter, I implement both 2D and 2.5D FWI in order to assess the improvement in imaging near-surface structures when out-of-plane components are used in crooked geometries. I start by minimizing logarithmic phase-only residuals (Shin and Min, 2006), in an attempt to fit the phase of the forward-scattered waveforms, which may be considered to be the most linear aspect of the wavefield. In later inversion stages, I switch and

instead minimize conventional phase-amplitude residuals, fitting both the kinematic and dynamic components of the observed wavefields. This allows for a more stable velocity reconstruction since FWI is highly sensitive to amplitude variations in the observed wavefields. I further address the severe nonlinearity of waveform tomography by the hierarchical introduction of the low-frequency spectrum of explosive and vibratory sources into the inversion scheme.

I demonstrate that by employing 2.5D modeling and inversion, finer geological features are retrieved. Direct quantitative and qualitative interpretations are performed on the inverted velocity model. Prominent structures in the area, such as the LNSZ and the Larder Lake Cadillac Deformation Zone (LLCDZ), are well imaged and in agreement with the known geology of the area. In addition, semi-regional fault planes associated with the main breaks that can be related to mineralization pathways in the area are identified.

In the first section of this chapter, I present a brief description of the theoretical framework of 2D and 2.5D FWI. In the second section, I implement 2D and 2.5D full-waveform inversion to the crooked Larder Lake dataset. This section is divided into several subsections. In the first, second, and third part, I describe the geological aspects of the study area, the acquisition geometry, and the data preconditioning prior to FWI, respectively. In the fourth part, I introduce the application of both 2D and 2.5D FWI, including modeling and inversion strategies, FWI P-wave velocity models, and model appraisal using checkerboard tests, synthetic waveforms, and source wavelet inversion. I then provide a general structural interpretation of the results in the fifth part of this section. Finally, relevant conclusions are drawn in the last section of the chapter paper.

## **3.2 Method**

The tomographic process involves the treatment of the inverse and forward problem as a coupled system, connected through principles of physics. To implement seismic tomography, one needs to first establish a framework to solve the forward problem.

### **3.2.1 Forward problem**

Two-dimensional seismic profiles are usually processed with 2D FWI (Malinowski et al., 2011; Kamei et al., 2012; Gray et al., 2019); however, complex geology and severely crooked profiles requires of a more accurate solution, such as 2.5D FWI (Smithyman and Clowes, 2013; Xiong et al., 2013).

## 2D case

If both the survey geometry and the subsurface model were perfectly two-dimensional, I could make use of the 2D, isotropic, visco-acoustic wave equation

$$\nabla \cdot \left( \frac{1}{\rho(x, z)} \nabla u(x, z; \omega) \right) + \frac{\omega^2}{\kappa(x, z)} u(x, z; \omega) = f(x, z; \omega), \quad (3.1)$$

where  $\rho$  is the bulk density,  $\kappa$  is the bulk modulus,  $\omega$  is the angular frequency,  $u$  is the pressure field, and  $f$  is a generalized source term. Indeed, this is the approach I used in Chapter 2, in which a finite-difference approach was adopted to solve this wave equation as I worked through an appropriate selection of data frequencies.

## 2.5D case

Equation (3.1) implies that point sources (and point receivers) extend infinitely in the direction perpendicular to the shooting line, effectively forming a line source in 3D space. This means that the dynamics of geometrical spreading (and the kinetics to a lesser extent) will be incorrect. For fully 2D inverse problems this implies a correction must be applied to the observed data to make them compliant with the modeling used in equation (3.1) (Williamson and Pratt, 1995).

For cases in which the survey geometry is significantly deviated from a straight line, the 2D equation is limited due to the errors it creates in source-receiver offsets. However, as described by Song and Williamson (1995); Song et al. (1995); Zhou and Greenhalgh (2006), the propagation of visco-acoustic wavefields can be better modeled by the 2.5D wave equation,

$$\begin{aligned} \left( \nabla \cdot \left( \frac{1}{\rho(x, z)} \nabla \right) + \frac{\omega^2}{\kappa(x, z)} - \frac{k_y^2}{\rho(x, z)} \right) u(x, k_y, z; \omega) \\ = f(x, k_y, z; \omega), \end{aligned} \quad (3.2)$$

where  $k_y$  is the transverse wavenumber component. In this approach the model itself (i.e., the geology) is assumed to be 2D (invariant in the strike direction), but the wave propagation is fully 3D. The 2.5D equation has the benefit of modeling point sources and point receivers as true (3D) points, and these points may occupy any location in 3D space. The final 3D wavefield response,  $u(x, y, z; \omega)$ , is calculated by the inverse wavenumber transform with respect to  $k_y$ ,

$$u(x, y, z; \omega) = \int_{-\infty}^{\infty} u(x, k_y, z; \omega) e^{-ik_y y} dk_y, \quad (3.3)$$

for a range of out-of-plane wavenumbers determined by a maximum wavenumber cutoff called

*critical value of the medium,  $k_c$* . This *critical value of the medium* highlights the separation between wave propagation and evanescent fields (Zhou and Greenhalgh, 2006).

The range of out-of-plane wavenumbers over which the wave equation is solved can be expressed as,

$$k_{y\text{range}} = [0, \min(k_c)]. \quad (3.4)$$

Once the range of transverse wavenumbers is established, the sampling,  $\Delta k_y$ , is defined. This sampling is required for the reconstruction of the cross-profile components. An insufficient number of out-of-plane components,  $N_{k_y}$ , may increase the effect of “ghost” sources, which arise as numerical artifacts from the double inverse Fourier transform and appear as wrapped unwanted signal in time-domain seismograms. Ghost sources are an indication of undersampling, and may be mitigated by using a smaller  $\Delta k_y$ . However, because equation (3.2) must be solved  $N_{k_y}$  times, the use of a small  $k_y$  interval may result in an unfeasible increase of computational cost. Song and Williamson (1995) and Zhou and Greenhalgh (2006) discussed alternative approaches to address the phenomenon. I adopt the strategy introduced by Zhou and Greenhalgh (2006) based on the dominant seismic wavelength and the maximum source-receiver offset. This is an irregular sampling strategy, which has proven to be more efficient and numerically more stable than regular sampling techniques (Smithyman and Clowes, 2013). The range of transverse wavenumber components is derived so that  $k_y < k_c$ . This implies that we are working with the portion of the function representing propagating waves, and we ignore evanescent waves.

The 2.5D approach has a high computational cost, which depends on the  $k_y$  sampling points required for the reconstruction. To reduce the computational burden, I implement a programming code that parallelizes calculations over frequencies,  $\Omega$ , and out-of-plane wavenumbers,  $k_y$ . This is possible because the wave equation, equation (3.2), solves sets of  $\Omega$  and  $k_y$  independently.

### **Laplace-Fourier domain modeling and inelastic attenuation**

An important distinction regarding our forward and inverse approach in the frequency domain is that real-valued frequencies are implicit in previous equations, i.e., solutions exist within the Fourier domain. However, the forward and inverse problem is in fact solved in the Laplace-Fourier domain in this work, in which frequencies are taken on complex values. In this domain, one can control the amount of information to include during modeling and inversion, mitigating nonlinearity and cycle-skipping issues by only allowing the early part of the seismograms into the reconstruction. This feature is introduced by considering complex-valued,  $\Omega$ , instead of real-valued,  $\omega$ , frequencies. Complex frequencies are defined as  $\Omega = \omega - i\sigma$ , where  $\sigma = \frac{1}{\tau}$  is a real-valued Laplace constant. Readers are referred to Chapter 2 and references therein for further details on

the time-damping capability of the Laplace-Fourier framework.

Similarly, the introduction of a complex-valued velocity field,  $c$ , readily allows attenuation,  $Q^{-1}$ , to be implemented in the frequency domain by introducing an imaginary component such that,

$$Q^{-1}(x, z) = -\frac{\Im [c(x, z; \omega)]}{2\Re [c(x, z; \omega)]}, \quad (3.5)$$

(Song et al., 1995), where  $Q^{-1}$  is the inverse of the seismic quality factor,  $c$  represents a complex-valued quantity,  $\Im [c(x, z; \omega)]$ , and  $\Re [c(x, z; \omega)]$  indicate the imaginary and real parts of the complex-valued velocity field.

### 3.2.2 Inverse problem

Prior to executing FWI, a starting estimate of the velocity model is required. This initial approximation is usually found by implementing high-frequency asymptotic ray methods, e.g., traveltome tomography (Cerveny, 2001; Chapman, 2004). Full-waveform inversion then uses the resulting low-wavenumber velocity field to iteratively estimate the model perturbations not accounted for in the starting model. As the iteration proceeds, model perturbations are calculated by minimizing the “misfit” function  $E(\mathbf{m})$  (usually the  $L_2$  norm of the data residuals) through nonlinear local descent methods (Pratt et al., 1996; Adamczyk et al., 2014; Florez et al., 2016). In this study, I implement a steepest-descent gradient algorithm. The simple gradient of the data residuals,  $\nabla_m E(\mathbf{m})$ , may be mapped onto model perturbations using

$$\delta\mathbf{m} = -\alpha\nabla_m E(\mathbf{m}), \quad (3.6)$$

(see Pratt et al. 1998), where  $\delta\mathbf{m}$  indicates the model update,  $\alpha$  is the step length. Instead of using the simple gradient in equation (3.6), I use the preconditioned conjugate gradient in a similar fashion. Two different data residuals are optimized in this chapter: conventional phase-amplitude, and logarithmic phase-only residuals (readers are referred to Chapter 2 and references therein for a detail description on this matter).

During the inversion the source waveform is continuously estimated and updated. I employ a linear method introduced by Pratt (1999) to estimate source signatures after every inversion stage, using the most recently updated velocity model. Because the source signature is not known *a priori*, this iterative estimation renders a more accurate approximation of the amplitude and phase components of the “true” source wavelet (especially as the velocity model is updated and improved).

### **3.3 Case study in 2D and 2.5D FWI - Larder Lake**

#### **3.3.1 Local geology**

The study area is located within the Abitibi greenstone belt of the Superior Province in Canada. The belt is an east-west-trending greenschist-facies metavolcanic unit, divided into seven major volcanic stratigraphic episodes from pre-2750 to 2695 Ma (Ayer et al., 2005; Thurston et al., 2008). The Larder Lake seismic survey is a 2D crooked line that extends through several geological assemblages from the Skead assemblage to the south, the Larder Lake assemblage in the center, and the Blake River assemblage to the north (Figure 3.1). These assemblages are composed of volcanic sequences that have been intruded by syntectonic and significant mafic to felsic batholiths. The intrusions are coeval with the deposition of two sedimentary basins, the Timiskaming-type clastic sequences and the Porcupine-type turbiditic sequences.

Bleeker (2015) suggested that prominent structural events in the area (e.g., the LLCZ) may have been initiated as crustal-scale extensional faults during the development of the sedimentary units. Because economic concentrations of mineral endowments in the area are in the form of lode gold, dominated by structurally controlled gold-bearing quartz-carbonate veins, detailed seismic imaging of such structural components is vital. Two important structural features are present in the geological map shown in Figure 3.1: the LNSZ to the south, and the LLCZ to the north. Current research (Brace and Sherlock, 2017; St-Jean et al., 2019) is focused towards determining the relationship between the gold-bearing LLCZ, and the poorly documented and barely exposed LNSZ. For instance, in Chapter 2 I suggested the LNSZ has a north-dipping structural inclination, contrary to previous descriptions of the shear zone (e.g., Jackson et al. 1990b). However, my previous analysis covered only the southern portion of the Larder Lake transect. Imaging the entire Larder Lake survey is necessary to describe both deformation zones (i.e., LNSZ and LLCZ). These zones are dominated by multiple steeply dipping structures, especially along the Larder Lake assemblage where folded and faulted structures complicate the geological scenario.

#### **3.3.2 Acquisition geometry**

The acquisition parameters of the (southern) Larder Lake survey are described in Chapter 2 and references therein. Here, I present a brief summary of the entire (approximately 45-km long) crooked 2D geometry. Two types of sources are used: six explosive sources and 840 vibroseis sources. Vibroseis sources have a spacing of 50 m and use frequency sweeps from 2 to 150 Hz, whereas the explosive sources have a much wider spacing (between 5 and 7 km), and are rich in low-frequency components.

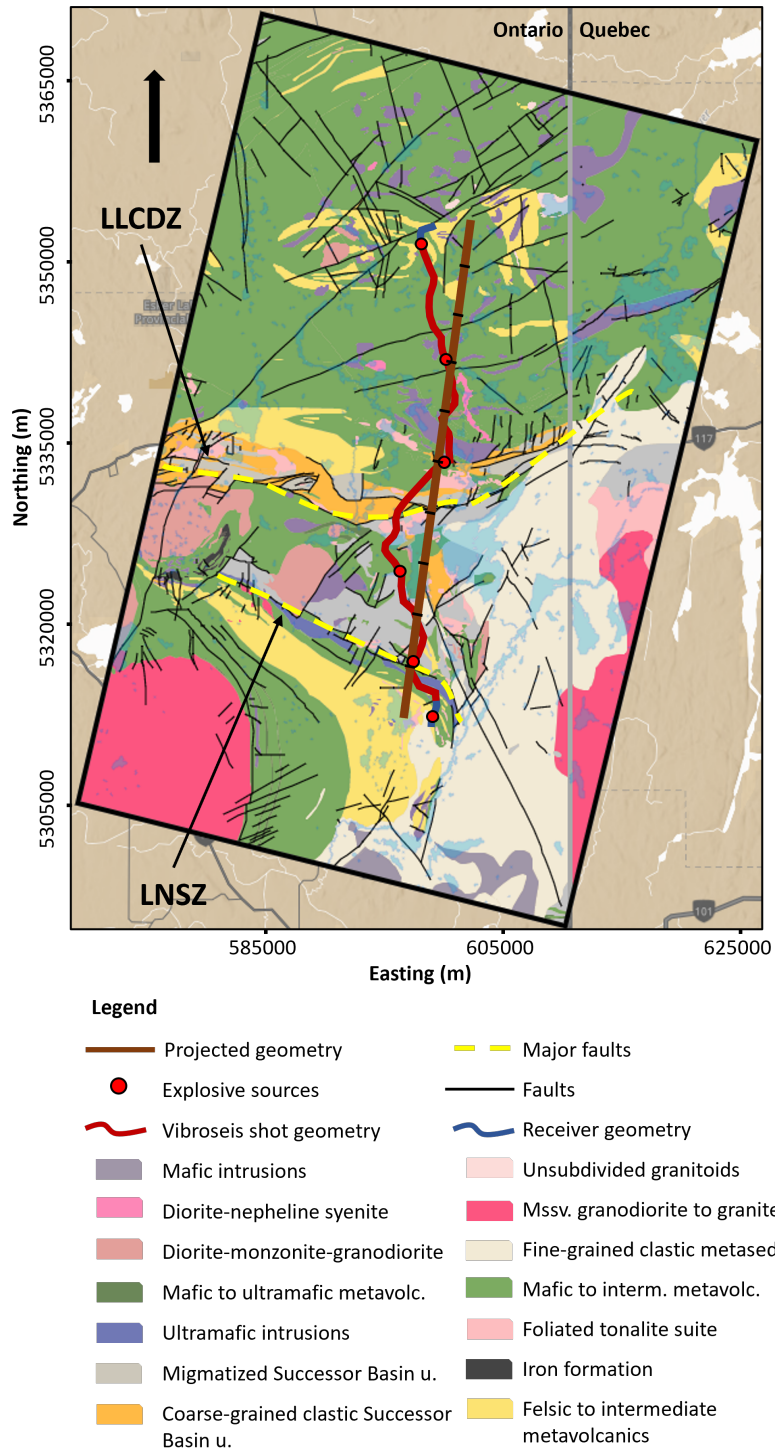


Figure 3.1: Relevant geological units and the 2D seismic acquisition geometry at the Larder Lake area. The original (crooked) geometry is shown by the red solid line (receivers and vibroseis sources). Explosive sources are highlighted by red dots. The projected geometry is identified by the solid brown line. Key structural features are depicted by the two dashed yellow lines: the Larder Lake-Cadillac Deformation Zone (to the north) and the Lincoln-Nipissing Shear Zone (to the south). Black lines on the projected geometry indicate 4 km intervals, which correlate with the horizontal axis of the models shown here. Grey line indicates the Ontario and Quebec border. Modified after Metal Earth - Geology map of Larder Lake area (2019).

The sensors are 2,426 vertical-component 5-Hz geophones with a spacing of 12.5 m. A high signal-to-noise ratio is observed in most vibroseis sources up to a maximum offset of approximately 8 km, although for some sources acceptable data may be observed at offsets up to approximately 15 km. In contrast, the explosive sources exhibit arrivals with a high signal-to-noise ratio at offsets as long as 30 km.

Under the 2D-modeling and inversion approach, the sources and receivers are projected onto the 2D plane depicted in Figure 3.1. This projection introduces travelttime errors, since the true offsets differ considerably from the projected offsets. I avoid introducing these errors by removing non-compliant data, defined as having offset errors above 6 per cent. This approach has proven effective in several case studies, see for instance Kamei et al. (2015), Consolvo et al. (2017), and Chapter 2 of this thesis. Different approaches to handle the offset differences after source and receiver projection onto a 2D plane have been established (see Chapter 2 and references therein); however, these approaches tend to introduce further complications into the data (Smithyman and Clowes, 2013). The advantage of the 2.5D-modeling and inversion approach is that this rejection of data traces is not required, since there are no offset errors present.

### 3.3.3 Data preconditioning

Prior to initiating FWI, the observed data must undergo a set of preconditioning steps to improve the signal-to-noise ratios, and to remove seismic phases not accounted for in the visco-acoustic modeling method. I implement filtering in the frequency-wavenumber domain to guide the removal of unwanted arrivals, I compensate for station-ground coupling effects by applying surface-consistent amplitude corrections, and I use shot-to-shot amplitude balancing. See Chapter 2 for a more in-detail description of the pre-processing approach. The data for performing 2D and 2.5D FWI undergo the same preprocessing steps (except for the rejection of traces due to offset errors, which only occurs in the 2D case).

As a frequency-domain FWI scheme is used, it is informative to evaluate the processed and unprocessed waveforms in the frequency domain. Figure 3.2 displays the real part of monochromatic data for each source and receiver pair at 7 Hz (i.e., the lowest frequency used on vibroseis sources). Figure 3.2a depicts data before any preconditioning, and the data appear incoherent, due to contamination by air waves, ground roll, elastic modes, and random noise (especially at near-offsets). In contrast, Figures 3.2b and 3.2c, showing the same data after preconditioning, exhibit a significant improvement in energy coherency and continuity due to the removal of these phases. Full-waveform inversion is highly sensitive to such seismic arrivals, and their removal is crucial for the inversion to succeed. The preconditioned data shown in Figures 3.2b and 3.2c include filtering in the Laplace-Fourier domain. The filtering strategy in this domain facilitates the selective damp-

ing of dynamic components prior to performing FWI, which allows the reconstruction to focus on early arriving phases. Figures 3.2b and 3.2c shows that a considerable amount of late arriving energy has been eliminated, further mitigating nonlinear effects.

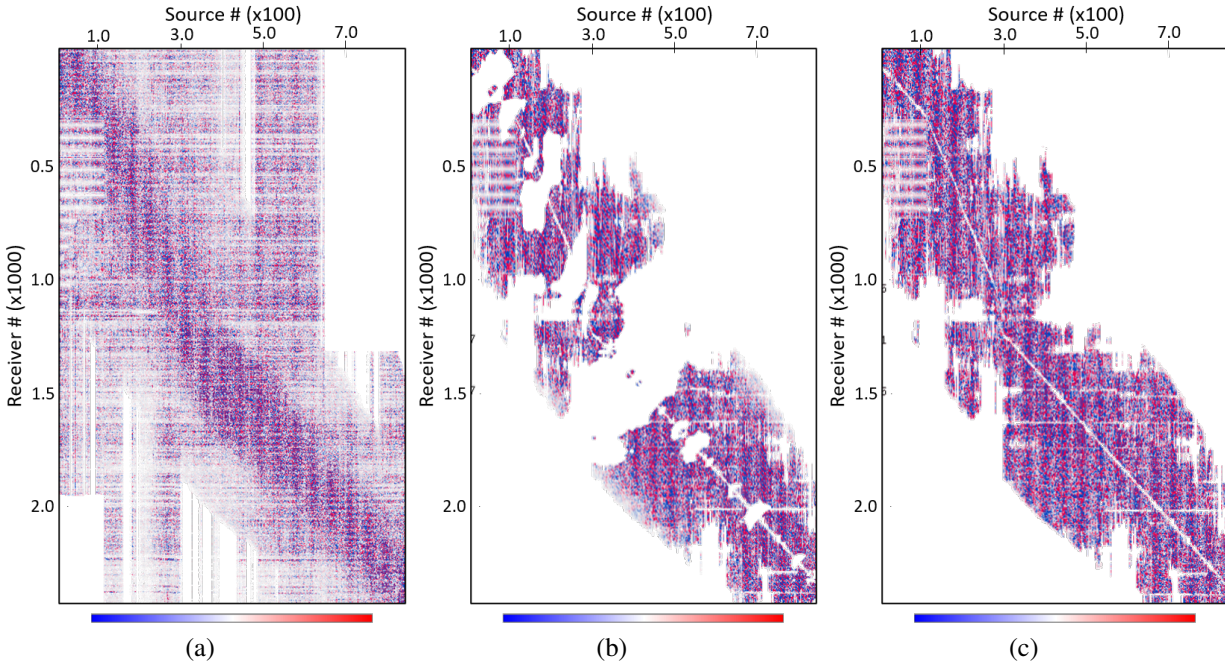


Figure 3.2: Monochromatic data images showing the real part of frequency-domain wavefields at 7 Hz (a) before and (b, c) after data preconditioning. Data in (b) is used for 2D FWI (includes rejection of traces due to offset errors), whereas data in (c) is used for 2.5D FWI. A more coherent and continuous pattern is observed after the removal of contaminating phases in (b, c) (e.g., elastic modes, surface waves, etc.). Blank areas indicate seismograms without traveltimes because of (b) rejection due to offset errors and noise, and (c) noise. Notice that under a 2.5D scheme, no data rejection due to offset errors is required.

Blank regions in Figure 3.2b and Figure 3.2c represent unavailable data partly due to noise. For instance, a considerable amount of noise is observed between receivers 500 and 700 for the southernmost sources. One can also see that the average available offset is about 8 km, except for the six explosive sources that exhibit longer offsets (e.g., sources 450 and 831 in the middle and end of the array, respectively). As mentioned above, under the 2D experiment it is necessary to reject data that suffer from large offset errors. This is reflected by the differences in data preconditioning between Figure 3.2b and Figure 3.2c. The former exhibits data rejection of non-compliant traces due to offset errors. Around 13 per cent of seismic traces are removed from the dataset, most of them concentrated within near-to-medium-offset ranges. These data may prove crucial for the retrieval of medium-to-high wavenumber components during FWI, especially at late stages when longer  $\tau$  values are introduced along with shorter offsets. The rejection of waveforms due to the profile crookedness further motivates me to adopt a 2.5D FWI approach, which accounts for the

true (3D) locations of the sources and receivers thereby avoiding any offset errors.

### 3.3.4 Full-waveform inversion

#### Initial velocity model

As mentioned in Section 3.2.2, full-waveform inversion requires the construction of a smooth velocity model, describing the intermediate- and long-wavelength characteristics of the medium. Three-dimensional non-linear refraction traveltime tomography is performed following the approach introduced by Zhang and Toksöz (1998) and used in Chapter 2. I manually pick first arrivals on 846 shot gathers up to 30- and 15-km offsets on explosive and vibroseis sources, respectively. On average, vibroseis shots have useful source-receiver offsets up to 8-10 km, whereas explosive sources exhibit useful data to their full offset extent (i.e., 30 km). In vibroseis sources, the identification of first-arrival phases on offsets longer than 10 km is equivocal due to the decay in signal-to-noise ratio and high-frequency noise. After 10 iterations of the 3D traveltime inversion, the algorithm is able to reduce the root-mean-square (RMS) misfit between synthetic and observed traveltimes to within one-sixth the dominant period at 7 Hz, well within the one-half-cycle criterion. This criterion states the differences between predicted and observed traveltimes must lie within half a dominant period, so that cycle skips during data fitting are avoided (Sirgue and Pratt, 2004).

I generate an initial velocity model for both 2D and 2.5D scheme. During 3D traveltime tomography, I set velocity updates in the cross-line direction to be performed in cells twice the size of those in the in-line direction. This acts as a regularization constraint, whereby velocity updates in the  $y$ -direction are less prompt to converge to local high-velocity changes. Because the initial model is obtained through 3D traveltime tomography, a 2D slice is extracted along the projected geometry (Figure 3.1). The 2.5D equivalent section is set along the in-line axis with strong smoothing in the cross-line direction, effectively assuming the properties of the medium do not considerably vary in the cross-line direction. This is generally true for acquisition geometries that are parallel to the strike. Nevertheless, the obliqueness of crooked geometries with respect to local strike may introduce traveltime errors because the velocity field is not exactly homogeneous in the cross-line direction. Figure 3.3a depicts the starting velocity model from traveltime inversion.

#### Model building

I adopt a visco-acoustic, and isotropic approximation for the execution of the forward modeling stage in the frequency domain. I perform the model discretization using a regular mesh with 50x50 m cells, selected because this is approximately a quarter of the minimum propagating wavelength at 20 Hz and a minimum velocity of 4 km/s. This level of discretization is used to

avoid numerical dispersion (Jo et al., 1996). The physical dimensions of the model are  $42 \times 2.5$  km. I add 15 grid points at the corner and edges of the numerical model to properly implement perfectly matched-layer boundary conditions, after Berenger (1994).

Following a similar approach used by Kamei et al. (2015), a free surface is not modeled, but rather a non-reflective “implicit” free-surface condition is implemented (Bleibinhaus and Rondey, 2009). I impose strong attenuation in the air layer above sources and receivers, effectively suppressing the generation of near-surface reflective phases due to the high-impedance contrast. This “implicit” free-surface condition at the top of the model significantly helps mitigating the effect of reflective energy near the surface. I use a constant seismic quality factor,  $Q$ , equal to 1 above the surface, and equal to 500 in the subsurface, which simulates a mildly attenuative geology.

Because the study area is located within a hard-rock environment, several experiments for estimating the density distribution within our model are performed. Readers are referred to Brocher (2005) for a thorough revision of velocity and density relationships. I use density models derived from i) the Nafe-Drake curve (Ludwig et al., 1970), ii) an empirical relationship introduced by Christensen and Mooney (1995) for crystalline rocks, valid for depths less than 10 km, and iii) the Gardner’s relationship (Gardner et al., 1974). I find that only the dynamic part of the gradient response is altered by switching among the different density functions, resulting in gradient updates with velocity differences of less than 2 per cent. Therefore, the Gardner’s relationship is used, trusting the iterative process will correct gradient artifacts derived from the chosen density approximation.

### **Synthetic modeling**

I use discretized Laplace-Fourier frequencies to solve for the visco-acoustic wave equation. I follow a similar approach used in Chapter 2, discretizing frequencies in 0.5 Hz intervals to a maximum frequency of 20 Hz. Forward modeling is performed for 846 sources, with 2,426 receivers per source. When time-domain seismograms (for visual comparisons) is required, the synthetic waveforms are transformed from the frequency domain to the time domain by using the inverse Laplace-Fourier Discrete Fourier Transformation.

### **Transverse wavenumber approach**

Due to the severe crookedness of the Larder Lake transect, I am particularly motivated in performing 2.5D full-waveform inversion to include the cross-line components into the model reconstruction, despite the computational cost. Table 3.1 lists the sequential out-of-plane wavenumber sampling scheme for forward modeling and inversion (after Zhou and Greenhalgh 2006). The column denoted as “stage” refers to the inversion stages that are listed in Table 3.2. The number of

transverse wavenumbers,  $N_{k_y}$ , are also given in the table.

Table 3.1: Transverse wavenumber components per inversion group. See Table 3.2 for further details on the stages of FWI we use.

Stage	$N_{k_y}$	Stage	$N_{k_y}$
1	62	7	288
2	115	8	330
3	178	9	374
4	212	10	420
5	249	⋮	⋮
6	249	20	1008

### Inversion

The inversion scheme is based on a multiscale approach in which low-wavenumber information is resolved prior to the inversion of finer structural features. In Chapter 2, I demonstrated that the low-frequency components available in explosive sources benefit the retrieval of long-wavelength characteristics of the velocity field during early stages of the inversion. Thus, I start by inverting the lowest useful frequencies in explosive sources before introducing the information from vibroseis sources. Table 3.2 lists relevant parameters adopted during the inversion, both 2D and 2.5D FWI follow the same inversion scheme.

To further mitigate the cycle-skipping phenomenon, progressive offsets are introduced as the inversion strategy advances. At early stages, frequencies between 4 Hz and 7.5 Hz are available from the explosive sources. I begin using this limited set of low frequency data. At later stages, frequencies between 7 Hz and 15 Hz from the vibroseis sources are used. A frequency overlap between explosive and vibroseis sources is included to ensure the continuity and stability of the inversion. A total of 23 discrete frequency components from 4 Hz to 15 Hz are inverted. The frequency content of the Larder Lake dataset extends well beyond 15 Hz. The inversion of these higher frequencies might have rendered an improved tomographic image in terms of spatial resolution, although cycle skip errors become progressively more difficult to suppress at high frequencies. However, I stopped the FWI at 15 Hz in favor of inversion stability, and to mitigate the computational burden of regridding using smaller grid cells.

In Chapter 2, I included later arrivals by relaxing the constraints on the time-damping constant as the inversion progressed, effectively reconstructing higher-wavenumber components. Unfortunately, testing reveals that this layer-stripping approach is detrimental when inverting for the full Larder Lake dataset. Instead, I use only a single time-damping factor equal to 10 per cent of the maximum time window (i.e.,  $\tau = 0.2$  s). This outcome is likely due to the increased non-linearity of the later seismic arrivals in the more geologically-complex northern portion of the Larder Lake seismic transect. Gradient updates are more sensitive to these later arrivals and inversion stability is compromised, requiring the implementation of a single and aggressive time-damping factor.

Table 3.2: Multiscale inversion strategy.

Inversion Strategy	Stage	Frequencies (Hz)	Iter.	Offset corners (km)	Residuals	Time-damping constant (s)
Explosive sources	1	4 4.5 5	1	1-1-8-10	Log. phase-only	0.2
	2	4.5 5 5.5 6	5			
	3	5 5.5 6 6.5 7				
	4	5.5 6 6.5 7 7.5				
Vibroseis sources	5	7 7.5 8	1	1-1-10-12		
	6	7 7.5 8	3			
	7	7 7.5 8 8.5				
	8	7 7.5 8 8.5 9				
	9	7.5 8 8.5 9 9.5	5	1-1-12-15	Conventional phase-amplitude	
	10	8 8.5 9 9.5 10				
	⋮	⋮				
	20	13 13.5 14 14.5 15				

The multiscale strategy also includes the hierarchical combination of phase and amplitude residuals (Kamei and Pratt, 2013; Kamei et al., 2015). When attempting to minimize conventional phase-amplitude residuals at early stages, large data errors are generated, causing the contamination of the gradient updates. I therefore first perform FWI by using a logarithmic phase-only objective function from 4 Hz to 11 Hz in order to update the model using only the kinematic components of the observed data. At a later stage I include the dynamic components of the observed wavefield by using a conventional phase-amplitude objective function from 11 Hz to 15 Hz. This approach improves convergence by alleviating the sensitivity of the inversion strategy to strong amplitude variations in the observed waveforms.

Figure 3.3 displays the inversion results. Figure 3.3a depicts the initial velocity model from traveltome tomography, and Figures 3.3b and 3.3c depicts the P-wave velocity models from 2D and 2.5D FWI, respectively. Figures 3.3d and 3.3e show the differences between the initial velocity model and the final 2D and 2.5D FWI model, respectively. In all displays, grey-shaded regions

represent areas with little to no energy penetration (e.g., the grey-shaded area in Figure 3.3a depicts the portion of the model not sampled by the ray-tracing technique).

Although the general velocity trend is very similar for both the 2D and the 2.5D FWI results, the details of the velocity structures are different. For instance, the low velocity anomalies observed in the very near surface between 4 and 18 km along the profile are more clearly imaged on the 2.5D FWI result. These near-surface features likely represent contrasts within metasedimentary, highly-weathered material. Similarly, the basin-like low-velocity anomaly between 8 and 18 km along the 2.5D profile better illustrates the contact between two different velocity domains than the 2D profile. The model appraisal shown below further supports the improvements brought by 2.5D modeling and inversion. The velocity discrepancies between Figure 3.3b and Figure 3.3c are due to the failure of the 2D approach in modeling the contribution from cross-line energy components. This is especially true in the Larder Lake seismic transect because of its severe crookedness, which has CMP traces scattered from as far as 4 km away from the profile. Only when performing 2.5D FWI can we appreciate the actual impact data removal has on the velocity inversion (approximately 13 per cent of the data are removed under the 2D approach).

By evaluating Figures 3.3d and 3.3e, it appears that 2.5D FWI retrieves more information than its 2D counterpart. The 2.5D FWI result shows larger velocity differences with respect to the initial velocity model, meaning a larger range of velocity variations are captured. These differences are more apparent in near-surface areas - with depths less than 1 km - and become less apparent at deeper portions of the model, where the velocity field behaves more uniformly. We observe how the strong signature from the competent/less-competent rock interface, seen in Figure 3.3a at around 300 m, is clearly removed by the 2.5D FWI strategy. This effect is depicted in Figure 3.3e by the sub-horizontal anomaly at 300 m, which supports the premise that the 2.5D P-wave model better represents the “true” velocity variations of the subsurface.

### **Model appraisal**

A model appraisal is a vital step to validate the inversion results. This is because convergence, per se, is not a direct indicator of the accuracy of the inverted model due to the non-uniqueness of the inverse approach. I assess the validity of the final FWI P-wave model by considering three approaches: checkerboard resolution tests, time-domain finite-difference seismograms, and source signature inversion. The model validity is further supported by the geological interpretation given below.

**Resolution tests:** I perform resolution analysis by executing checkerboard tests. I add +/- 5 per cent checkered velocity perturbations to the initial velocity model (Figure 3.3a) and generate synthetic data for this perturbed model.

CHAPTER 3. SEISMIC IMAGING OF CRYSTALLINE STRUCTURES: 2D AND 2.5D VISCO-ACOUSTIC FULL-WAVEFORM INVERSION

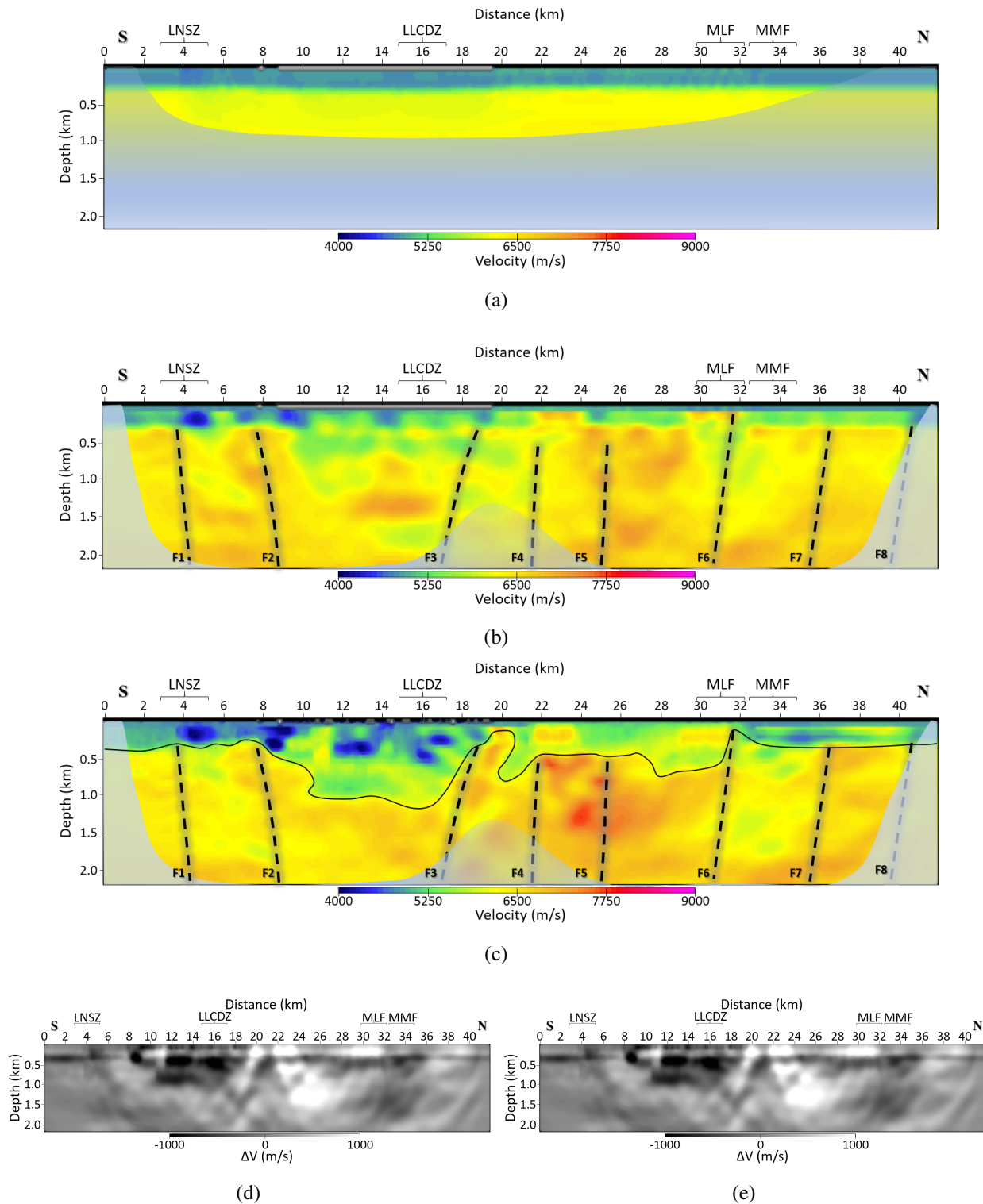


Figure 3.3: Full-waveform inversion results. (a) initial velocity model from traveltim tomography, (b) 2D and (c) 2.5D final FWI model, velocity difference of initial velocity model from (d) 2D (i.e., Figure 3.3b minus 3.3a) and (e) 2.5D (i.e., Figure 3.3c minus 3.3a) FWI model. Dashed black lines represent a preliminary structural interpretation, which is associated with several interpreted fault planes as indicated at the bottom of (b, c). The solid black line in (c) represents an interpreted separation between sedimentary material/deformed volcanic rocks, and more competent volcanic successions at depth.

Then, the same 2.5D multiscale-hierarchical inversion scheme described in Table 3.2 is implemented, initiating the reconstruction with the starting and unperturbed velocity model. I consider two different checkerboard settings: 1000x500 m and 500x250 m based on the upper-resolution limit of FWI, which is in the order of  $625 \times 312$  m in this case (using one-eighth and one-quarter the maximum expected wavenumber at 15 Hz and 4.5 km/s). Figure 3.4a shows the results of the checkerboard inversion. It is evident that the checkerboard elements are very well defined when inverting for the 1000x500 pattern (Figure 3.4a).

However, the recovery of the finer pattern (Figure 3.4b) is not as successful and distortions of the elements are noticeable. The inversion approach is powerful enough to resolve features above the theoretical resolution of FWI, but structural features at the theoretical resolution indicated above, may not be fully recovered. Figure 3.4b exhibits encouraging results based on the amplitude and shape of the recovered elements. Most areas within the model exhibit velocity variations resolved to within 5 per cent of their actual values. The low-confidence area 19 km along the profile at approximately 1.5 km depth is the result of the pronounced velocity difference immediately north of the LLCDDZ. In addition, a lack of seismic sources south of the LLCDDZ may preclude the inversion from accurately retrieving subsurface information, degrading the model resolution.

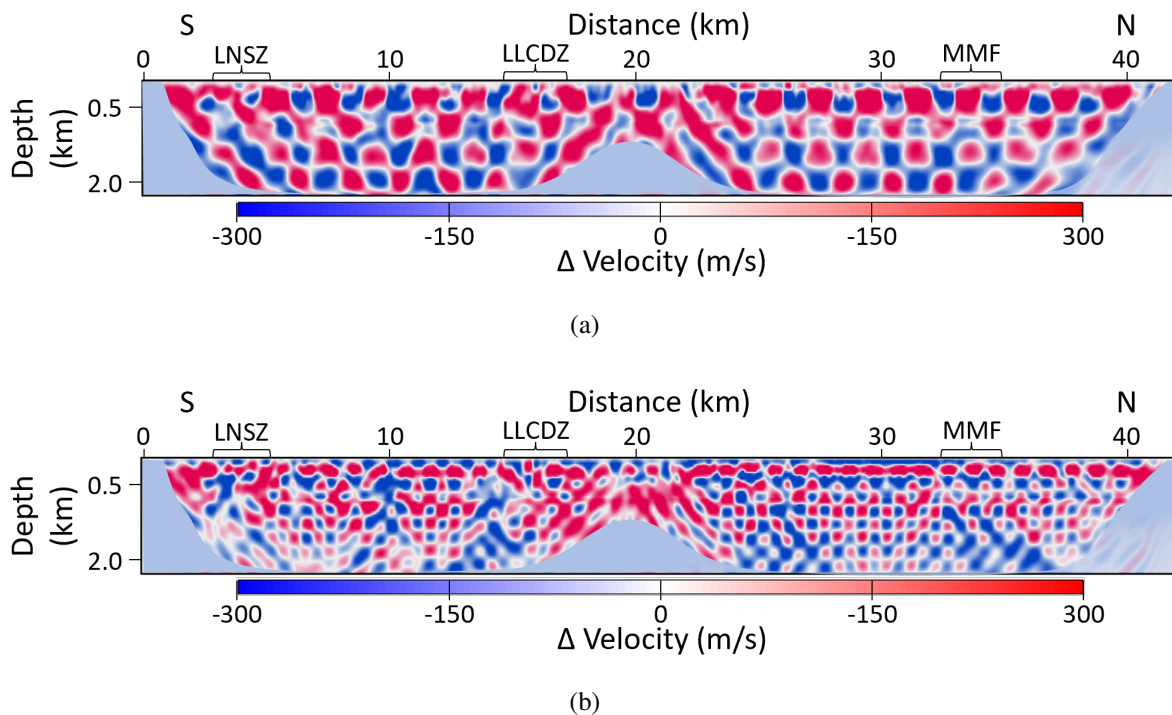


Figure 3.4: Resolution analysis by checkerboard tests, with +/- 5 per cent velocity anomalies superimposed on the initial FATT model. Checkered pattern dimensions are a) 1000x500 m and b) 500x250 m.

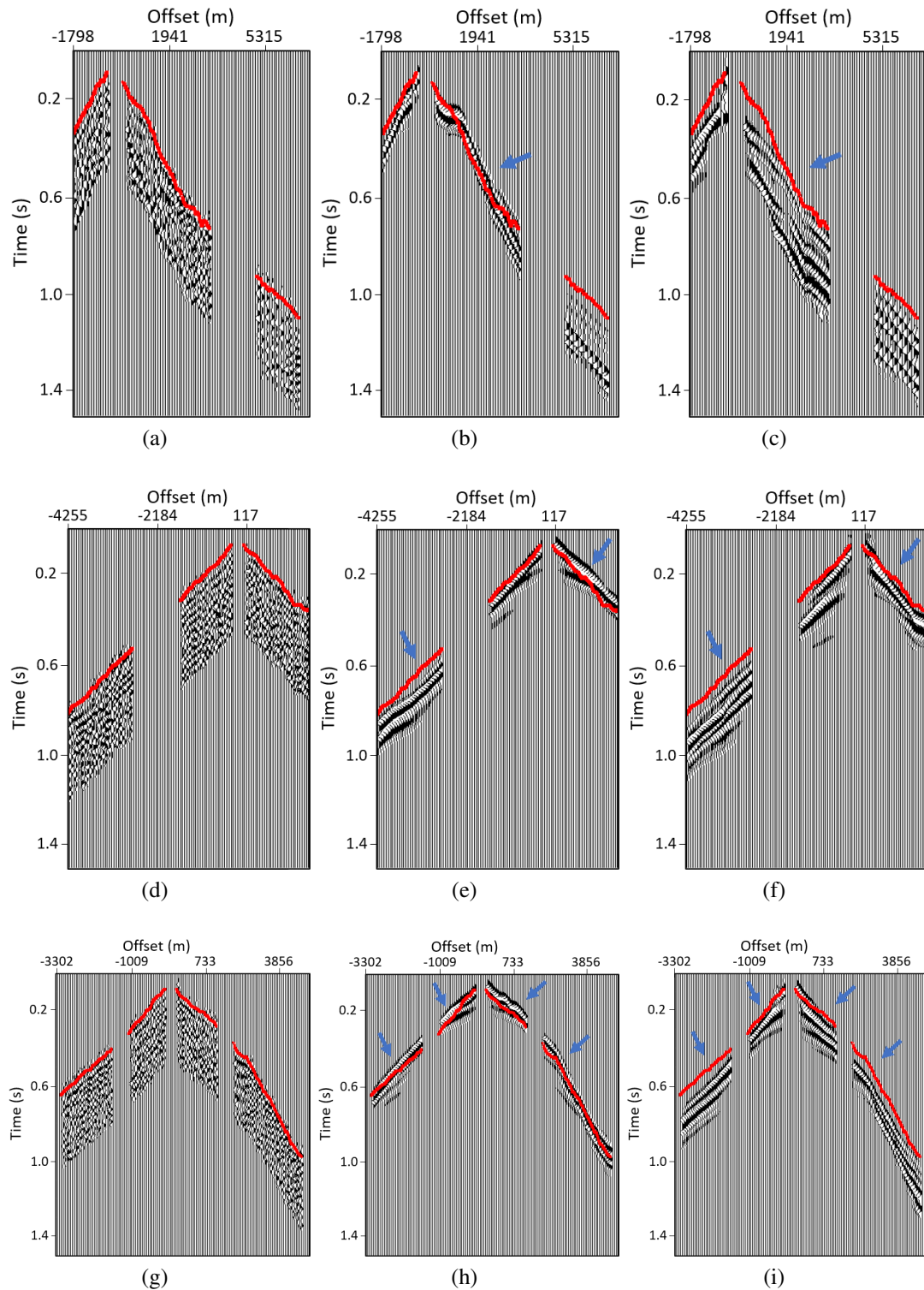


Figure 3.5: Observed (a, d, g) and synthetic waveforms generated with 2D approach (b, e, h) and the 2.5D approach (c, f, i), and using the respective FWI velocity models. The red line in all panels represents the manually picked first-arrival times on the observed data. The blue arrows indicate severe mismatch areas on the 2D modeled waveforms as well; this same area exhibits a good match on the 2.5D modeled waveforms.

**Time-domain finite-difference modeled seismograms:** I perform visco-acoustic modeling to assess the ability of these two approaches to predict the effect of line crookedness on the resulting synthetic seismograms. The final 2D, (Figure 3.3b), and 2.5D (Figure 3.3c), P-wave velocity models are used to perform 2D and 2.5D forward modeling, respectively. We follow an identical numerical solution of the wave equation as the one described in Chapter 2. Figure 3.5 exhibits the results from the 2D and 2.5D finite-difference modeling using a time window of 2 s and 30 discrete frequencies from 0.5 Hz to 15 Hz in 0.5 Hz intervals. I use the 2D and 2.5D FWI velocity models along with their respective inverted source signatures.

Figures 3.5a, 3.5d, and 3.5g are the observed seismograms located at approximately 2, 13, and 15 km along the model. Figures 3.5b, 3.5e, and 3.5h represent forward modeled shot gathers using the velocity model from 2D FWI, and Figures 3.5c, 3.5f, and 3.5i display synthetic shot gathers using the velocity model from 2.5D FWI. By preserving the 3D nature of the survey, out-of-plane components are much better accounted for, as demonstrated by the excellent fit of the 2.5D modeled data.

The fit seen in Figure 3.5 is a prime example of the difference between 2D v. 2.5D schemes, the latter includes offline wavenumber components providing a more accurate mathematical approximation of the wavefields. The kinematics of the 2D wavefield are clearly affected by the severe crookedness of the survey, causing significant traveltimes errors. In contrast, both the kinematic and dynamic components are better represented on the 2.5D results, as portrayed by the almost-perfect traveltimes fit and the amplitude and phase similarities in the coda of the 2.5D seismograms. Although 3D spreading effects are correctly handled by the 2.5D approach, additional unconstrained effects may degrade the reproducibility of observed data, even with the 2.5D framework in place. Some of these additional effects include seismic phases not simulated by the acoustic approximation, unknown station coupling effects, and complex, fine-scale geological variations not recovered by the inversion.

**A *posteriori* source wavelets:** in order to better assess the quality of our FWI inversions, I carry out source signature inversion following Pratt (1999). Figure 3.6 depicts the inverted source signatures using the initial traveltimes velocity model (Figure 3.6a), the final 2D (Figure 3.6b), and 2.5D (Figure 3.6c) FWI models. Improvements in terms of continuity and consistency of the FWI results over that of the traveltimes tomography result are observed. In some portions of the profile, the inverted source using the 2D FWI approach seems to perform slightly better than the 2.5D counterpart. The fact that we are using much more data in the 2.5D approach might explain the slight quality degradation of the 2.5D inverted signatures. In addition, factors involving station-coupling conditions and abrupt topographic variations would further degrade the quality of both signature groups (i.e., 2D and 2.5D schemes).

### 3.3.5 Interpretation

Because the kinematics of the wavefield are sensitive to variations in geological architecture, velocity images in Figure 3.3 are accurate qualitative representations of geological structures. The interpretation shown in the images is performed on the 2.5D FWI velocity model (Figure 3.3c) since it is deemed to be more accurate than the 2D model (Figure 3.3b). Structures identified on the 2.5D FWI model (i.e., F1-F8 - fault planes) are positioned on the 2D FWI model (Figure 3.3). Note that the interpretation of the final 2.5D FWI model given here slightly differs from that given in Chapter 2 for the FWI model of southern Larder Lake. The main reasons for the discrepancies are the use of more sources when inverting for the entire Larder Lake profile, and the implementation of subtle but important modifications to the inversion strategy (for instance, differences in time-damping factors, offset scheduling, and frequency scheduling).

To facilitate the interpretation, Figure 3.7 shows the final 2.5D FWI model with a portion of the geological map and the main assemblages. Major structures around the Larder Lake transect are well resolved in both 2D and 2.5D FWI models, such as the LNSZ, the LLCDDZ, the Mulven fault (MLF), and the Misema-Mist fault (MMF). The boundaries of these structures are evidenced by velocity anomalies corresponding to different velocity domains. For instance, the LNSZ is delineated by a low-velocity contrast approximately 5 km along the profile between F1 and F2. The LNSZ might have a steeper dipping character than the one shown in Figure 3.3c. Although the inversion should properly handle the crooked line geometry for a simple 2D geology, the Larder Lake transect shows a high degree of obliqueness with respect to the strike of the LNSZ, as can be seen in Figure 3.1. Therefore, the apparent dipping character of the LNSZ may be an underestimation of its true dip.

The northern boundary of the main break - LLCDDZ - is clearly highlighted by a high-velocity contrast extending towards the surface, as indicated by F3. The low-velocity basin-like region between the northern portion of the LNSZ and F3 (black solid line between 7 and 18 km) is indicative of a more complex lithological and structural transition towards the trace of the LLCDDZ. This velocity behavior correlates with the geological units identified from surface geology in terms of a thicker and less competent metasedimentary column. This metasedimentary material is associated with Hearst- and Timiskaming-like sediments overlaying the Larder Lake group (Jackson et al., 1995).

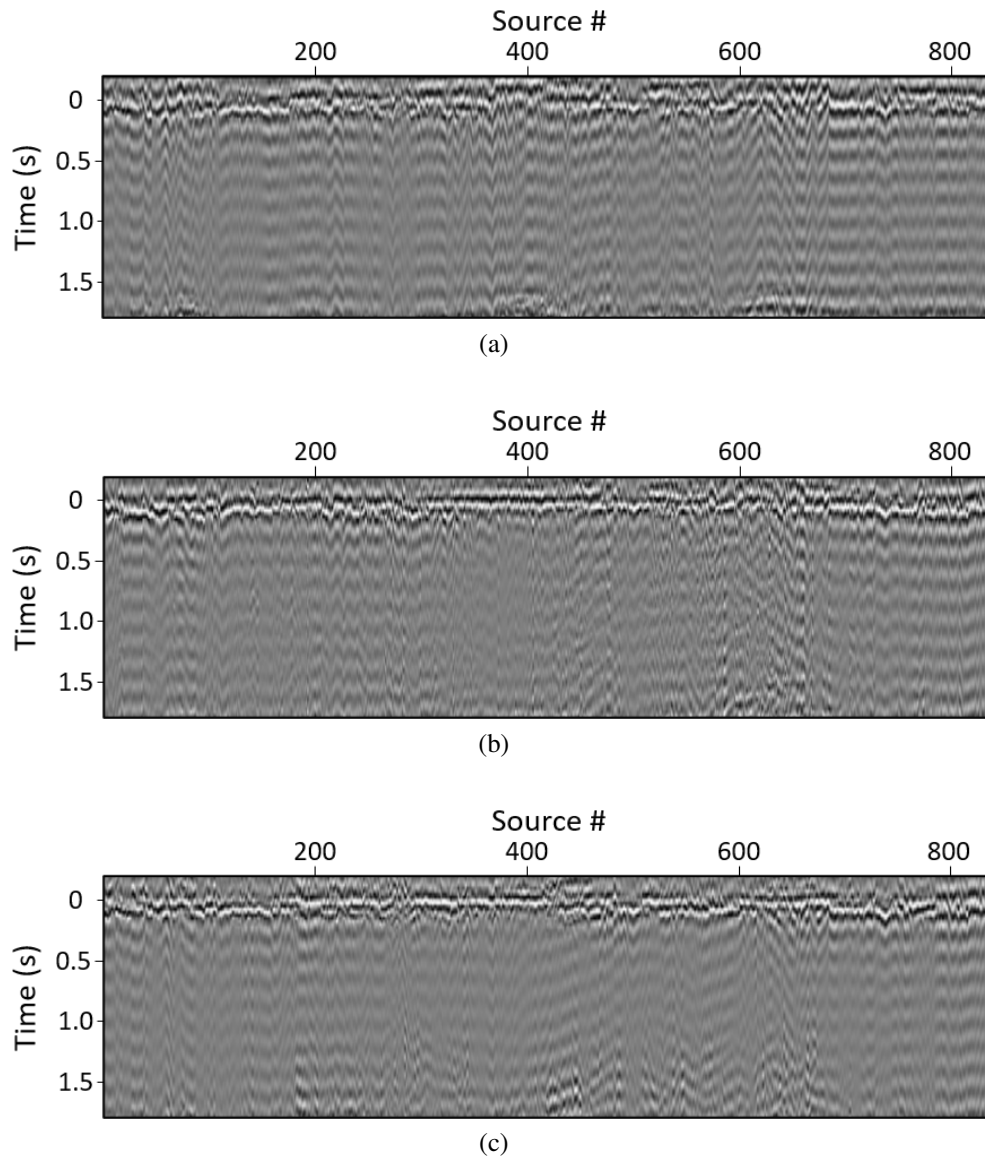


Figure 3.6: Source inversion using the a) initial, b) 2D FWI, and c) 2.5D FWI velocity models, respectively.

The velocities retrieved by 2.5D FWI correlate with known velocity variations in the area. Grandjean et al. (1995) presented a compilation of density and velocity measurements on core samples from the Blake River Group of the Abitibi belt. Although core samples were not extracted along the Larder Lake reflection profile, their velocity measurements are representative of the different rock types in the region. The northern portion of the Larder Lake transect overlays rocks of the Blake River assemblage, as observed in Figure 3.7. The velocity model exhibits higher velocities north of the LLCDDZ, with an average range of 6.6 - 7.0 km/s, which is consistent with the higher mafic content of the pillowed to massive metabasalt and metavolcanic rocks of the Kinojevis and Blake River assemblages. To the south of the LLCDDZ, the presence of metasedimentary units

and reworked volcanic rocks of the Timmiskaming and Hearst assemblages, is evidenced by the basin-like low-velocity anomaly between the structures F2 and F3. The velocities in the first few meters (up to 1 km in the center of the basin-like anomaly) are consistent with what would be expected from metasedimentary and highly-weathered material in the area, with velocities varying between 4.5 km/s (very-near-surface metasediments, conglomerates, graded to massive sandstone units) and 6.1 km/s (metavolcaniclastic rocks, conglomerate/breccia units composed by basalt). The rocks within the Larder Lake Group (underlying the Hearst and Timmiskaming assemblages) include pillowed to massive metabasalt, subvolcanic mafic and ultramafic intrusions with velocities varying between 6.1 km/s and 6.7 km/s (Grandjean et al., 1995; Jackson, 1995; Jackson et al., 1995).

Structures F4 and F5 (between the LLCDDZ and the MLF) are interpreted as semi-regional fault planes separated by different velocity domains. The geological units between F4 and F5 in Figure 3.7 exhibit an evident higher velocity behavior than the surrounding rocks, indicating a substantial difference in material composition and/or physical properties. These two structural features are not recognized at the surface, but their existence (and that of F8) is rather inferred by the strong velocity variations delineating their boundaries. These faults do not seem to extend beyond the black solid line, revealing that the tectonic activity associated with their formation might have ceased prior to the deposition of the Hearst and Larder Lake metasedimentary column. The region corresponding to the MLF and the MMF - identified from outcrops - matches an expected decrease in velocity. The steeply dipping boundaries of the MLF and MMF are delineated by the low-velocity F6 and F7 structures.

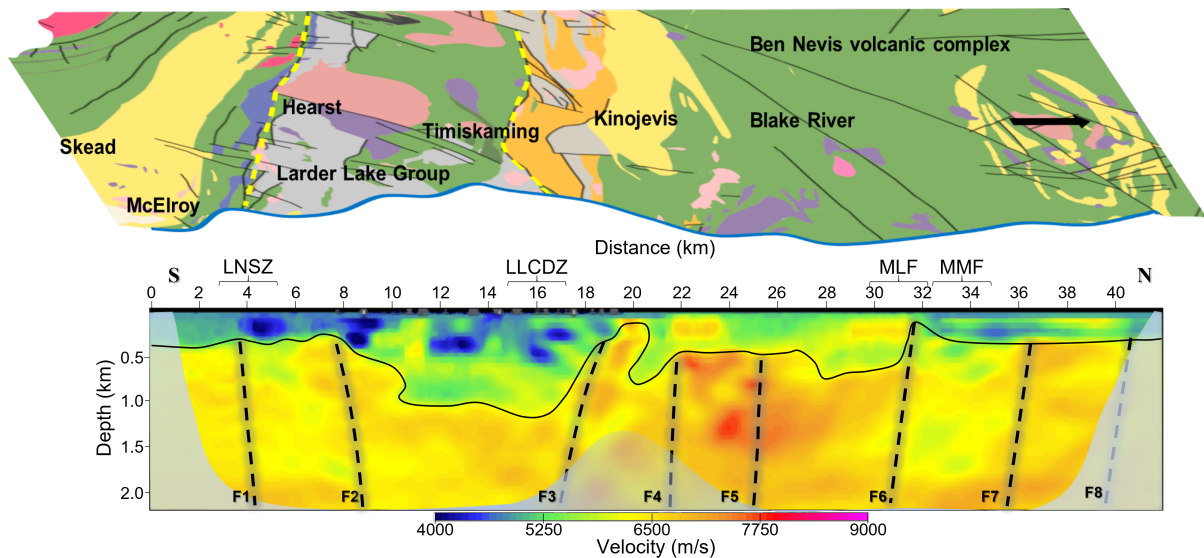


Figure 3.7: Final 2.D FWI velocity model overlaid by a portion of the local geological map of Larder Lake.

The velocity field below the black solid line in Figure 3.7 displays smooth lateral and verti-

cal velocity variations (except along the main breaks, such as the LNSZ and the LLCZ). This uniformity poses a challenge for conventional seismic migration imaging techniques. Subsurface regions with low impedance contrasts are usually transparent for imaging techniques relying on conventional migration methods. This is one of the reasons most seismic images of the Superior Province, including Larder Lake, lack coherent and continuous reflections (coupled with the irregular shape of igneous and metamorphosed rock bodies that scatter seismic energy in all directions, reducing the amount of coherent reflected energy). These conditions make it impossible to reliably interpret structures in the first few kilometers on migrated sections. Thus, the imaging provided here through full-waveform inversion is crucial in order to successfully correlate surface geology with crustal-scale structures. This more accurate near-surface structural information will allow for a better understanding of the geological architecture associated with mineralization pathways.

### 3.4 Conclusions

Two- and two-and-half-dimensional first-arrival FWI are implemented on a crooked seismic dataset in a geologically complex crystalline environment. The seismic profile severely deviates from an ideal 2D line by up to 4 km at its sharpest bend. The 2D FWI approach requires the rejection of data traces to avoid introducing traveltimes errors. In severely crooked geometries such as these, the 2D approach exceeds acceptable values, and the overall quality and accuracy of the inverted velocity image will be significantly degraded. I demonstrate that the implementation of 2.5D FWI on the Larder Lake geometry is vital for retrieving a velocity field containing fine structural details. I find that although the 2D FWI model accurately reconstructs major structural features, it fails to provide high-resolution details within different velocity domains. In contrast, the 2.5D FWI result exhibits a higher degree of detail and velocity structures that correlate closely with surface geology. These results highlight the significance of accounting for the 3D nature of wave propagation not only in the computation of the initial velocity model but also in the execution of the full-waveform inversion strategy.

Both 2D and 2.5D FWI methods benefit from the hierarchical incorporation of low-frequency information. I combine explosive and vibroseis sources in order to retrieve the low-wavenumber components of the Larder Lake velocity structure, starting at 4 Hz. This allows us to address cycle-skipping problems, and further allows to better delineate the long-wavelength characteristics of the major breaks. Appraisal tests in terms of time-domain waveform modeling, resolution, and source signature inversions demonstrate the velocity results are reliable. The velocity structures derived from 2D and 2.5D FWI can be used for direct quantitative analysis and interpretation of the geological units in the area, filling the gap between surface geology and crustal-scale structures.

# Chapter 4

## Seismic imaging of crystalline structures: improving energy focusing and signal alignment with azimuthal binning

### 4.1 Introduction

Seismic reflection processing is crucial in imaging subsurface structural features. Claerbout (1971) suggested that the typical hyperbolic amplitude summation in reflection processing provides detail and reliable information of the subsurface, after some kinematic corrections. These corrections are commonly based on normal moveout (NMO), and in-line dip moveout (DMO) corrections (Hale, 1983; Yilmaz and Claerbout, 1984). In simple geological settings where the acquisition line is straight and perpendicular to the main strike of the reflectors (i.e., structural variations are confined to the in-line plane), such corrections yield accurate seismic images. The acquisition of crooked profiles is commonplace in exploration campaigns along crystalline settings partly because the mining industry and academic efforts are not willing to fund expensive three-dimensional (3D) acquisition geometries. However, the implementation of reflection processing in crystalline terrains along severely crooked lines is more complicated (Spencer, 1993; Garabito, 2018). In complex settings, such as in Larder Lake, crooked-line profiling complicates the stacking process due to energy defocusing resulting from the contribution of out-of-plane reflections. These reflections do not have a hyperbolic moveout and, therefore, cause hyperbolic corrections to underperform (Yilmaz, 2001). Amplitude smearing is a key diagnostic of such an under-performance, degrading the quality of stacked and migrated seismic sections.

Seismic reflection imaging of 3D structures using 2D-crooked datasets in crystalline terrains requires careful design of nonstandard strategies to enhance energy focusing and signal alignment.

Several studies have been carried out on this topic. Du Bois et al. (1990), Nedimović and West (2003), and Beckel and Juhlin (2019) introduced reflection time corrections to compensate for cross-dip components. Tsumura et al. (2009), Kashubin et al. (2009), and Lundberg and Juhlin (2011) optimized the binning method to reduce the effect of cross-profile dip. Reflection time corrections are not attempted in this work, instead, we consider the optimized binning approach. (Nedimović and West, 2003) found that cross-dip analysis in the Larder Lake area was unfeasible; however, in a more recent study, Mancuso and Naghizadeh (2021) illustrated that the implementation of a generalized cross dip moveout correction on crooked transects enhanced energy focusing in the same area.

Steeply dipping structures are better imaged by shooting in the direction of maximum structural inclination, in which case no out-of-plane dip is perceived. This is generally true under the assumption of a 2D geological setting where cross-line structural variation is minimal. In crooked geometries, remnant cross-profile energy not accounted for during NMO/DMO persist, which worsen with the obliqueness between the profile and the geological strike. If untreated, cross-profile energy will have a detrimental effect on the quality of the resulting reflectivity image.

Optimizing the strategy used to bin data traces is a potential solution to mitigate out-of-plane energy (Sheriff and Geldart, 1995). I generate an effective local pseudo-processing line in the direction of maximum dip by collecting seismic traces along the dominant geological strike. Judicious and geologically-driven azimuthal binning can be implemented to diminish the contribution of cross-dip components and improve signal alignment before stack. Readers are referred to Kashubin and Juhlin (2010), Kim et al. (2014), and references therein for further insights on the effectiveness of the azimuthal binning technique. These authors performed thorough synthetic experiments on optimum binning strategies.

In this chapter, I devise a strategic seismic processing workflow to account for the complexities of crooked seismic profiles acquired on hardrock terrains inspired by the success of the azimuthal binning strategies reviewed above. The strategy includes an optimized binning approach and an enhanced migration velocity field. I initiate seismic reflection processing on the Larder Lake dataset by finding and implementing locally optimum bin azimuths. Then, the migration velocity field is improved by using the near-surface full-waveform inversion (FWI) velocity model generated in Chapter 3, in conjunction with conventional velocity analysis (CVA). I find that this combination renders more accurate results than those from only using conventional velocity analysis. This is because the heterogeneity of shallow layers is correctly solved for when using the high-quality FWI model.

## 4.2 Energy focusing and signal alignment

Reflection processing of 2D acquisition arrays often results in high-quality reflectivity images when the geometry is that of a straight line, and when the subsurface is characterized by simple geology, such as that encountered in layered sedimentary environments. However, seismic processing becomes challenging when data are acquired along crooked geometries over metamorphosed, deformed, and folded structures. The intricate geometry of rock units and their properties in crystalline environments gives rise to complex seismic energy scattering. Focusing problems arise when the 3D character of such energy scattering is ignored, and when crooked lines are treated as straight lines. Straight-line processing implies standard binning, which disregards the energy radiation patterns captured by crooked geometries. In this conventional approach, reflection points are deemed to lie below the midpoint of a given source-receiver pair along the processing line. Hence, the actual offline moveout of reflection points at depth is not corrected during the data processing stream. Neglecting this correction may result in severe signal ill-alignment. To enhance energy focusing and the alignment of reflections, we must introduce corrections for the out-of-line energy and/or devise a geologically-driven binning strategy.

### 4.2.1 Standard binning

The conventional CMP method assumes there are no CMP reflection points scattered in the direction perpendicular to the profile, which implies straight-line acquisitions and a perfectly 2D Earth (with no variations in the third dimension). In such a case, the processing line may be divided into CMP bins, whose length is commonly half the group interval (Yilmaz, 2001). Traces that fall within this in-line spatial dimension are collected to form a CMP gather. In crooked profiles, however, this in-line spatial dimension becomes a CMP region that surrounds the acquisition geometry and covers an area tens to hundreds of meters wide. Here, the processing (or “slalom”) line is divided into CMP bins that are conventionally oriented perpendicular to the line. This standard binning method fails to consider geometrical complexity due to local geological variations. The conventional processing of crooked profiles often yields suboptimal seismic images in hardrock settings due to the destructive interference of out-of-plane reflections, which lead to out-of-plane energy stacking (Nedimović and West, 2003; Beckel and Juhlin, 2019). More sophisticated solutions are required to deal with the swath distribution effect of midpoint traces in a crooked geometry.

### 4.2.2 Cross-profile dip effects

Cross-dip analyses have been successfully employed to correct for out-of-plane energy stacking in severely crooked transects (Ahmadi et al., 2014; Beckel and Juhlin, 2019). In crooked surveys, reflection times within each CMP gather are affected by cross-dip components. These components stem from the obliqueness between the effective stacking line and the geological strike. Uncorrected offline traveltimes hinder adequate signal alignment as they do not obey the ideal hyperbolic trajectory of in-line reflection times. As a result, reflections are seriously defocused and amplitude smearing occurs during stacking. The smearing effect of ill-aligned signal varies according to different factors such as the cross-profile offset, the velocity variation around the CMP scattering region, and the in-line and cross-line dip component of the subsurface structures (Nedimović and West, 2003). Accounting for these factors and performing appropriate time corrections does not always yield satisfactory results. Nedimović and West (2003) unsuccessfully attempted to implement cross-dip analysis along the Lithoprobe's Abitibi line 23 profile, which geometry coincides with the Larder Lake survey (both surveys acquired over the same road). They found that cross-dip analysis failed to provide reliable information of transverse dip components. I speculate that cross-offset distribution, the complex interaction of reflection events, as well as the profile crookedness, and the high variability of local strike might have been the culprit.

### 4.2.3 Azimuthal binning

I now turn my attention towards an approach that has proven to enhance energy focusing: azimuthal binning. A cloud of scattered midpoint traces is expected in crooked seismic geometries (e.g., Figure 4.1) with a cross-profile offset that generally increases with the crookedness of the acquisition. As mentioned above, bins are used to collect CMP traces along the processing line. Cross-dip effects are introduced by assuming geological structures and lateral velocity variations remain constant in the direction perpendicular to the slalom line (same direction along which the bin's width increases). The gravity of this assumption intensifies as the cross-profile offset and the bin width increases. Data traces reflected off different structural domains might be grouped within the same bin, causing reflected energy to destructively interfere during stacking due to their out-of-phase nature.

Locally optimizing the orientation of bins along the slalom line improves energy focusing and mitigates the aforementioned cross-dip effects. Kashubin and Juhlin (2010), among others, demonstrated that by orienting bins parallel to the local geological strike, seismic traces collected within each CMP gather exhibit enhanced focusing of reflection events. The improvement of energy focusing within each CMP gather has a direct effect on signal coherency. The signature of reflected energy contained within the data traces are stacked in phase and, therefore coherent

reflections are preserved. The azimuthal binning method sets the appropriate conditions for the success of processes like NMO and DMO. This is because CMP gathers are less contaminated by cross-dip components, which increases the accuracy of hyperbolic corrections.

In this chapter, I use surface geologic data (including geological maps, and geological reports) from the Larder Lake area to extract strike information (Pyke et al., 1973; Jackson, 1995; Jackson et al., 1995; Brace and Sherlock, 2017; Brace et al., 2018; St-Jean et al., 2019). I use this information to characterize the direction of prominent structures, such as the Lincoln-Nipissing Shear Zone (LNSZ) and the Larder Lake-Cadillac Deformation Zone (LLCDZ), which control the overall subsurface architecture in the area. The extracted geological strikes are used to perform azimuthal binning. The process involves testing a variety of azimuthal bins at different intervals along the processing line, to find the optimal local directions. Stack sections are produced for each of the tested intervals, the optimum (i.e., azimuthal) directions are found by qualitatively assessing these stacked sections, and subjectively selecting the azimuth exhibiting optimal reflection continuity and amplitude strength. These attributes are a proxy for energy focusing and signal alignment.

### 4.3 Seismic reflection processing in Larder Lake

I follow a conventional imaging strategy for the reflection processing of the Larder Lake dataset. I incorporate the FWI velocity model generated in Chapter 3 within this strategy to improve migration velocity fields, as well as the optimized binning method described in Section 4.2.3. The reflected energy in crystalline datasets is usually masked by stronger arrivals, such as surface waves and conversion modes. Preserving and enhancing reflective phases is crucial in the reflection processing workflow of the Larder Lake dataset. I consider different slalom lines onto which the CMP traces are projected, namely a straight line, a three-segment line, and a smooth line following the acquisition geometry. The quality of the resulting CMP gathers on each of the slalom lines is assessed in terms of signal alignment and the subsequent reflectivity stacked image. Figure 4.1 depicts these three processing lines over the cloud of midpoint traces.

The first step in the analysis is to determine the optimum bin size. Routinely, the stacking line is discretized by assigning a bin size equivalent to half the group interval. However, for crooked lines a bin width must be assigned as well. In general, small bins limit CMP fold coverage, and therefore negatively impacts the noise attenuation capability of the stacking process and producing unsatisfactory images. On the other hand, large bins potentially collect CMP traces with large cross-dip moveout due to the increase in CMP cross-offset, fostering signal ill-alignment, and generating suboptimal stacked images. After testing different bin sizes (not shown here), I find the optimum bin geometry to be that of rectangular bins with an in-line dimension equal to half the group interval (i.e., 6.25 m), and a cross-line dimension equal to 200 m. These tests indicated that

a 6.25x200 m bin geometry could be used without severe degradation.

After determining the CMP bin geometry, I implement a processing sequence following that used by Naghizadeh et al. (2019). I use a conventional post-stack time migration algorithm which has proved to render good results in crystalline environments (Yilmaz, 2001; Schmelzbach et al., 2007; Cheraghi et al., 2019).

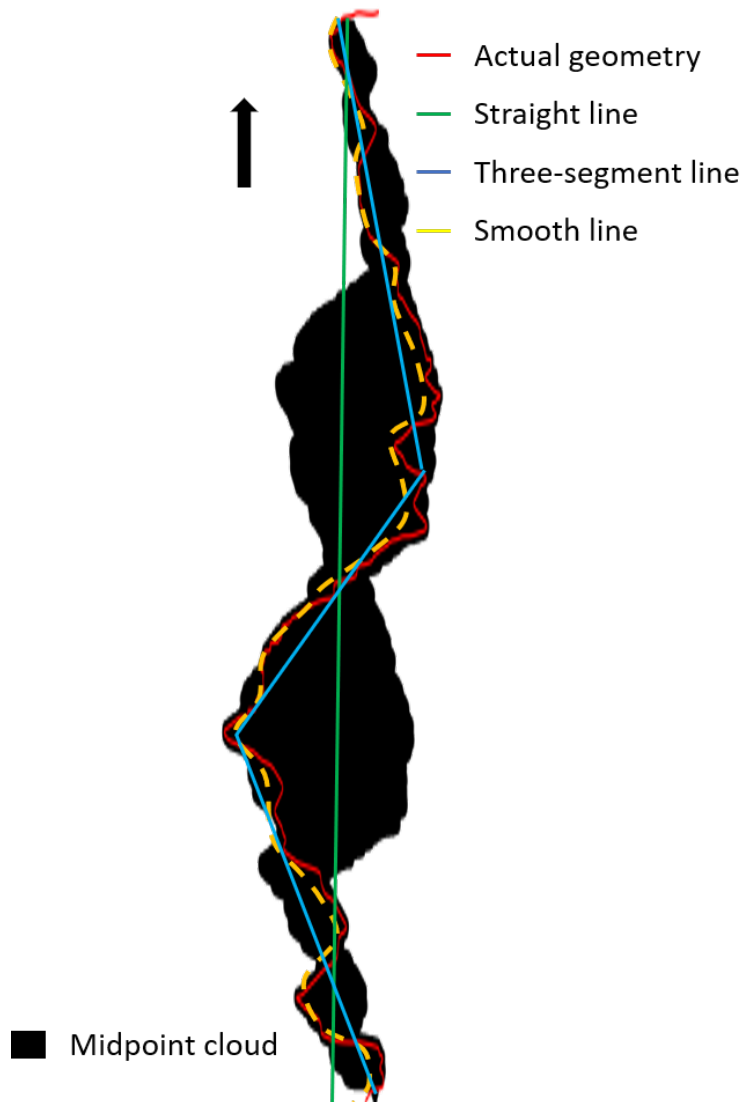


Figure 4.1: Three different processing line geometries considered for reflection processing. Note, in spite of the apparent width of this cloud, the maximum cross-line dimension was limited to 0.2 km.

Some of the main processes in the processing workflow implemented in this chapter include (1) static corrections - elevation and refraction statics are applied, however, residual statics are not considered in the final processing sequence because they did not significantly improve the stack. Refraction statics are calculated by using the first arrival energy picks described in Chapter 2 and

3. (2) Frequency filters - bandpass filters and F-K filters to remove elastic modes, air waves, and ground-roll. (3) Amplitude enhancement - shot-to-shot balancing, amplitude recovery, surgically-designed spectral whitening (avoiding the introduction of high-frequency noise), etc. (4) Velocity analysis - I use semblance analysis and perform velocity picking at 1000 m intervals for the first pass, and 500 m intervals for the second and third pass. (5) NMO and DMO corrections. (6) Stacking and migration. Table 4.1 lists in more detail the processes we use in arriving at a final migration image.

Table 4.1: Processing sequence of Larder Lake.

Item	Process	Comments
1	Import SEG-Y data	-
2	Build geometry data	Bin size (6.25x200 m), standard v. azimuthal binning
3	Manual first-break picking	Full offset range
4	Trace editing and muting	First-arrival muting and rejection of noisy traces
5	Frequency filters	Band-pass and F-K filtering
6	Ensemble balance	-
7	Amplitude recovery	Time-power constant: 1.5
8	Spectral equalization	Time-variant gains / range: 5-80 Hz
9	Surface consistent decon.	Operator: 160 ms / Prewhitening: 0.1%
10	Elevation statics	Datum: 500 m / Replacement velocity: 5600 m/s
11	Refraction statics	Traveltime tomography
12	Velocity analysis	1000 m first and 500 m second and third pass
13	NMO correction	30% stretch mute
14	DMO correction	Common offset F-K DMO
15	CDP stack	-
16	AGC	Operator length: 1024
17	F-X Decon.	Wiener-Levinson deconvolution
18	Post-stack time migration	Stolt F-K migration
19	Trace equalization	-

### 4.3.1 Enhanced binning

The conventional CMP approach, where traces illuminating the same point at depth are collected together to increase signal-to-noise ratio, becomes an oversimplification on crooked line surveys. I emphasize the importance of energy focusing by employing locally optimized bin orientations along a smooth slalom-line, which follows the crooked geometry.

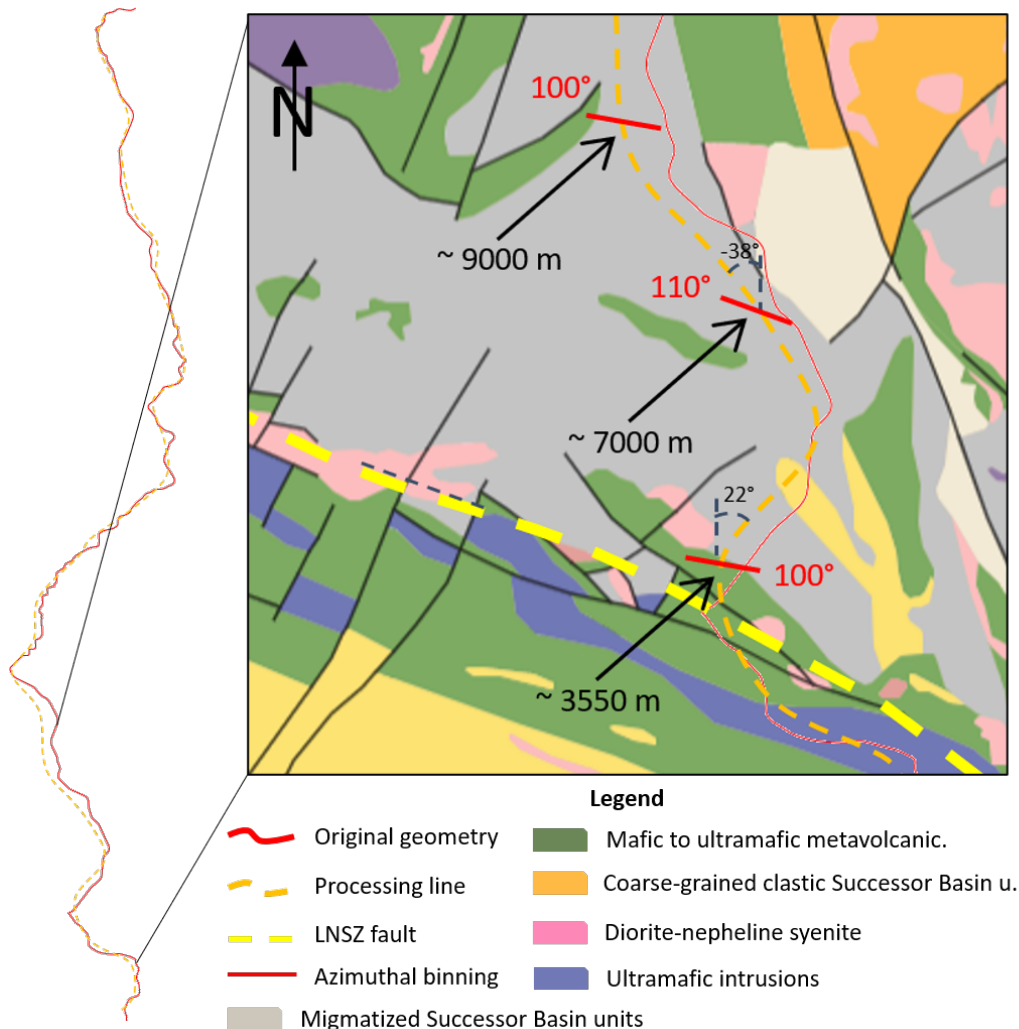


Figure 4.2: Southern portion of the Larder Lake transect around the LNSZ. Locally optimized bins are shown in red at three different positions along the slalom line.

**CMP binning** The optimized azimuth method creates a pseudo-processing line locally parallel to the direction of maximum inclination (i.e., locally perpendicular to the strike). To illustrate the azimuthal binning procedure, Figure 4.2 displays the southern portion of the Larder Lake transect superimposed on the local geological map. I pick this region because it is representative of the structural complications in the study area. These complications arise because (i) local struc-

tural variability in terms of strike is more prominent between the LNSZ and LLCDZ, and (ii) the crookedness of the acquisition line is more severe between these two structural breaks. Therefore, finding locally optimum bin azimuths within this region represents a double challenge.

Figure 4.2 depicts the area around the LNSZ where, over the span of approximately 8 km along the slalom line, the azimuthal binning method proved to be critical to overcome image distortions due to the profile crookedness. Table 4.2 lists the most relevant changes in bin direction along the slalom line, including the portion of the transect shown in Figure 4.2. In this table, the *local coordinates* tab refers to the model coordinates. The *UTM northing* tab represents the actual UTM northing coordinates of the Larder Lake transect referred to datum NAD83 UTM 17N. The standard binning azimuth, the locally optimized azimuth, and the strike of local geology are also listed on Table 4.2.

Table 4.2: Standard (std) v. optimized (opt) binning azimuths for Larder Lake. Bin direction in the standard CMP method is perpendicular to the processing line. In the optimized method, bin direction is determined according to local geological strike.

ID	Local coord. (m)	UTM northing <sup>†</sup>	Std. binning azimuth	Opt. binning azimuth	Local geological strike <sup>‡</sup>
1	2000	5314913	44°	100°	WNW
2	3550	5316463	112°	100°	<b>WNW</b> ↔W-E
3	7000	5319913	52°	110°	WNW↔W-E
4	9000	5321913	80°	100°	<b>WNW</b> ↔ <b>W-E</b>
5	18000	5330913	117°	110°	W-E↔ENE
6	23000	5335913	84°	100°	W-E↔ENE
7	29000	5341913	79°	80°	ENE
8	37087	5350000	77°	80°	ENE

<sup>†</sup> UTM northing denotes UTM northing coordinates intercepting the acquisition geometry

<sup>‡</sup> Cardinal directions, instead of azimuths, are given for geological strike because they represent estimations from surface geology. Left-right arrows indicate transition zones, and bolded directions indicate the dominant strike in a given transition zone.

Several experiments are performed to assess signal alignment and energy coherency by gathering midpoint traces using different bin orientations. As described above, the direction assigned to the bins are in accordance with the dominant strike of different sub-regions, which bearings are estimated using surface geology information. The method is performed in two passes: first using 5° intervals with a +/- 50° deviation range from the extracted strike, and then using 3° intervals with a +/- 20° deviation range from the extracted strike. I select a +/- 50° deviation range as the coarsest search range because of the significant change in strike observed between the southern and

northern portions of the profile. A WNW geological trend is observed towards the south, whereas a ENE trend is observed towards the central and northern parts of the transect (Table 4.2), which represents a change in direction of approximately  $60^\circ$ .

Three sub-regions with different slalom-line bearings are shown at 3550 m, 7000 m, and 9000 m distance along the processing line in Figure 4.2. From south to north, the bearings of the effective processing line are approximately  $22^\circ$ ,  $-38^\circ$ , and  $0^\circ$ , which represent standard binning azimuths of  $112^\circ$ ,  $52^\circ$ , and  $90^\circ$ , respectively. Since the success of the standard binning approach is based on straight-line processing, and sub-horizontal subsurface layers (i.e., effectively ignoring local variations in geology), these binning azimuths increase the contribution of laterally dipping structures. Gathering CMP traces in an oblique direction, with respect to the strike, increases the risk of concentrating cross-dip energy within a given CMP gather, which generates anomalous reflection traveltimes. These traveltimes degrade signal alignment, and cause amplitude smearing during stacking (see Figure 4.3 and Figure 4.4).

Instead of the standard binning method, the geologically-driven strategy for optimal azimuthal binning described in Section 4.2.3 is implemented, resulting in a selection of optimum binning azimuths. From south to north, these azimuths are  $100^\circ$ ,  $110^\circ$ , and  $100^\circ$ , as depicted by the red bins in Figure 4.2. This represents a difference of  $12^\circ$ ,  $58^\circ$ , and  $10^\circ$ , respectively, with reference to the azimuths that would be used with the standard approach.

The significance of binning optimization is illustrated in Figure 4.3, where five CMP gathers at two different positions along the slalom line are compared in terms of standard and azimuthal binning. A 400-ms window of the gathers, between 2.1 and 2.5 s, is shown. The first location, north of the LNSZ, corresponds to bins centered at 6785 m, 6790 m, 6795 m, 6800 m, and 6805 m (Figure 4.3a and 4.3b). The second location, north of the LLCZ, corresponds to bins centered at 18457 m, 18461 m, 18465 m, 18470 m, and 18475 m (Figure 4.3c and 4.3d). Absolute offsets within the CMP gathers vary between 0 m and 1640 m.

Reflected energy across these CMP gathers is scarce, at best, which is not uncommon in crystalline environments. The deficiency in reflected phases, coupled with poor signal-to-noise ratio, unveils the importance of mitigating signal ill-alignment. The resulting dataset from both standard and azimuthal binning methods are subjected to the same processing before stack, which includes the application of F-K filters, muting, static corrections, NMO, and DMO corrections to the CMP gathers in Figure 4.3. Red arrows indicate areas within the CMPs with evident improvements; for instance, the two prominent reflections around 2.25 s and 2.4 s in Figure 4.3a show much better alignment when azimuthal binning is implemented (Figure 4.3b). These two reflection events would be stacked out of phase under the standard binning framework, degrading signal-to-noise ratio, and increasing amplitude smearing. In contrast, an improvement on amplitude strength and reflection continuity would be expected by stacking the traces in Figure 4.3b, thanks to the evident

enhancement in energy focusing. Given that the same processing sequence is applied to both standard and azimuthal approaches, improvements are assumed to only stem from geologically-driven modifications to the data collection method.

North of the LLCZ, CMPs collected by the optimum binning approach depict better signal alignment than their standard binning counterpart, Figure 4.3d and 4.3c, respectively. The blue arrows indicate the static-like effect of waveforms, which appears as three different noisy reflections in Figure 4.3c. These signal artifacts are due to out-of-plane events that are not surface consistent and deviate from hyperbolic moveouts. This causes standard processing techniques such as statics, NMO, or/and DMO corrections to improperly function. The figures show that the azimuthal binning scheme addresses the strong energy defocusing highlighted by the blue arrows, placing reflection times into a more coherent and in-phase trend.

### **CMP stacking**

I further operate on the traces displayed in Figures 4.3c and 4.3d by stacking them, and assessing the result in terms of energy strength and continuity. I perform stacking on each of the five CMP bins depicted in Figures 4.3c and 4.3d, generating one single stacked trace per bin (i.e., 5 CMP traces per binning method). Figure 4.4 depicts the five CMP stacked traces corresponding to standard (Figure 4.4a) and azimuthal (Figure 4.4b) binning methods. Only the later portions of the waveforms are displayed for better visualization. The arrows highlight the most prominent reflections along the 500-ms window. Blue arrows indicate reflections that are stacked in phase using both conventional and azimuthal binning methods, i.e., both binning strategies perform well. Red arrows, in contrast, denote reflections that are successfully stacked only by the azimuthal method, but not by the standard method. The absence of these red arrows in Figure 4.4a reveals reflection signals have been lost to amplitude smearing under the conventional binning approach. In Figure 4.4b, red arrows highlight the capability of the optimum binning approach in enhancing energy focusing, and preserving reflective signal in severely crooked profiles.

### **4.3.2 Azimuthal v. standard stacked sections**

After implementing both conventional and optimum binning, I proceed to stack the Larder Lake data following the information in Table 4.2, and processing steps in Table 4.1 (up to the 14<sup>th</sup> step). Figure 4.5 shows three sections representing a portion of the Larder Lake transect. Figure 4.5a was processed by a commercial contractor, whereas Figure 4.5b and Figure 4.5c are the results from the in-house processing. The north-dipping reflection package observed within the dashed ellipse is located in the vicinity of the LNSZ (about 3 km north of the deformation zone).

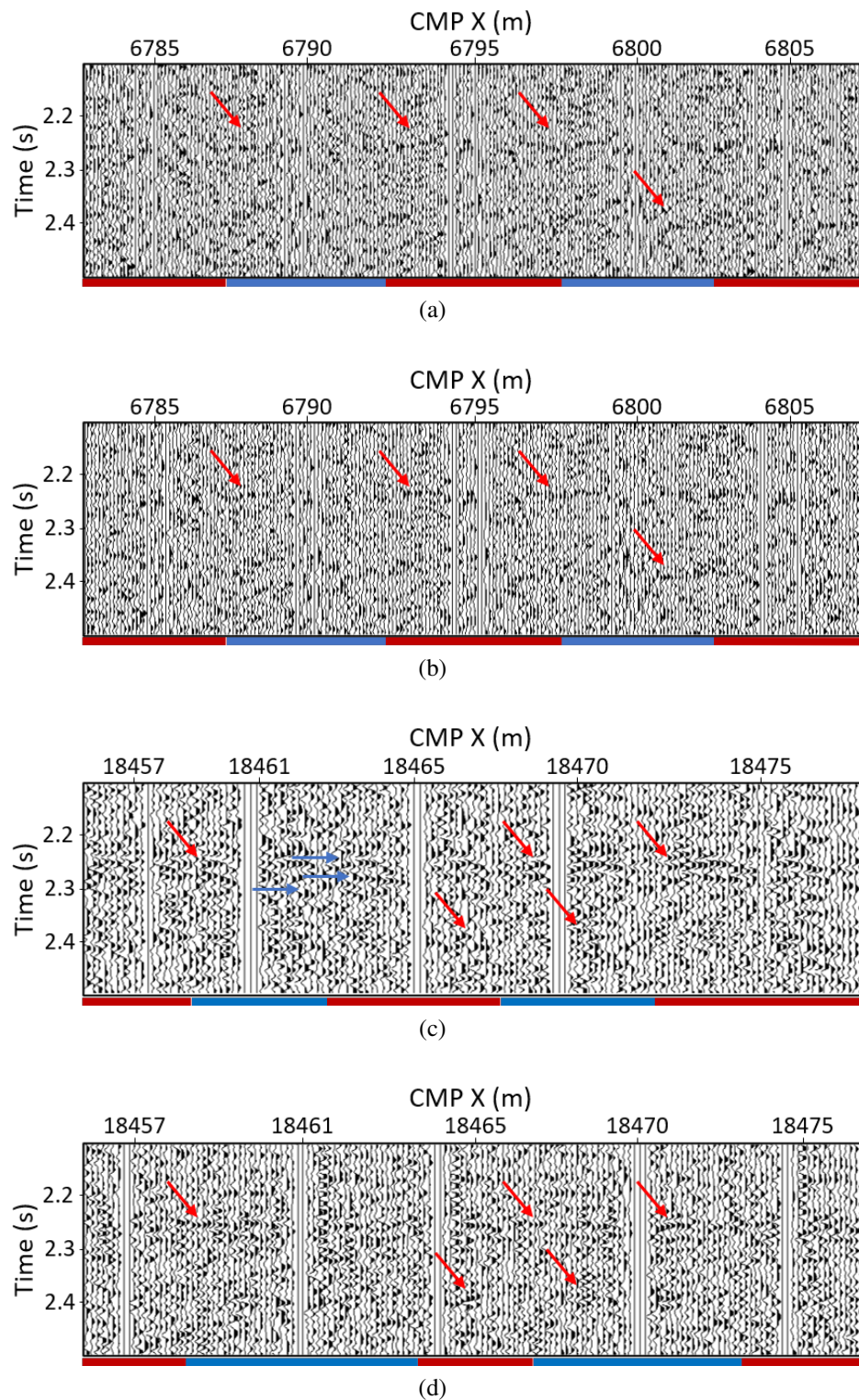


Figure 4.3: CMP gathers using (a, c) the standard binning method, and the (b, d) azimuthal binning method. CMP gathers are located (a, b) north of the LNSZ, and (c, d) north of the LLCZDZ. The horizontal axis indicates the distance along the slalom line, and the alternating red-blue bands indicate CMP fold (i.e., the limits of each color-coded band indicates the amount of traces within that specific bin). Red arrows indicate enhanced signal alignment in (b, d). Blue arrows indicate strong defocusing in (c), caused by reflection time delays from out-of-plane events.

These reflections are better imaged by the in-house optimized binning approach (Figure 4.5c), whereas the commercial processing fails to clearly resolve them (Figure 4.5a).

The main differences between the commercially processed image (Figure 4.5a), and the in-house processed images (Figure 4.5b and 4.5c) are based on (i) careful trace data rejection, (ii) amplitude treatment, and (iii) the use of a refraction-based near-surface velocity model. The near-surface velocity model is more thorough in the in-house processing than in the commercial processing because in the previous chapter a high-quality near-surface velocity model was generated prior to initiating FWI. I performed traveltimes picking on refraction arrivals using the full useful offset extent of vibroseis sources (approximately 15 km) to compute the near-surface velocity model through traveltimes tomography. In contrast, the commercial processing only used offsets up to 5 km for the construction of the initial velocity model.

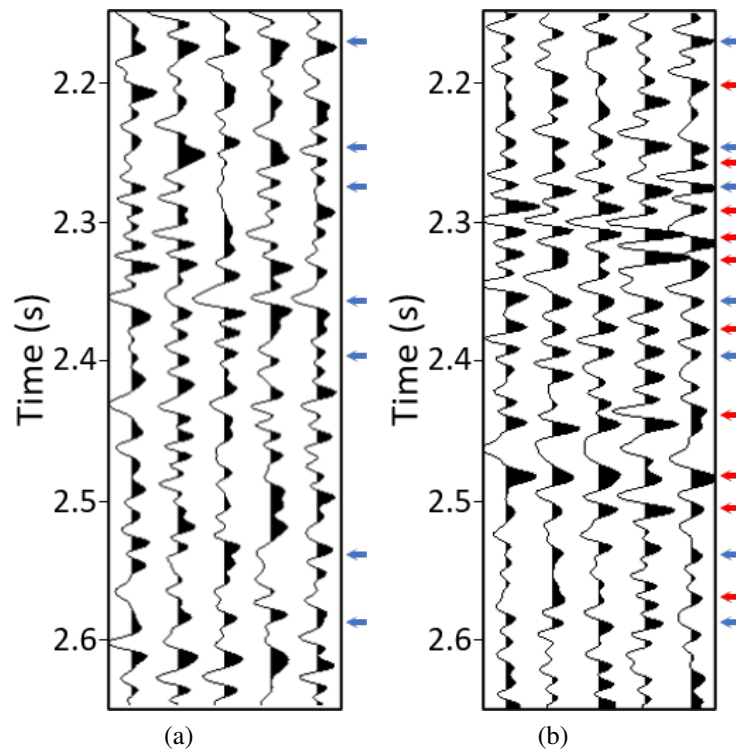


Figure 4.4: Stacked CMP traces under the (a) standard (Figure 4.3c), and (b) azimuthal (Figure 4.3d) approaches. There are 5 CMP traces in (a) and (b), corresponding to the 5 CMP bins depicted in Figures 4.3c and 4.3d. Arrows highlight most prominent reflections, blue arrows indicate reflections stacked in-phase by both binning approaches, whereas red arrows indicate reflections preserved only by the azimuthal method. The improvements in (b) indicate the merits of this approach in spite of the slight decrease in fold.

This is because long offset components are not typically required to accommodate conventional reflection processing based on migration techniques, and traveltimes errors may be introduced where first-arrival picking is ambiguous due to noise (prevalent at long offsets).

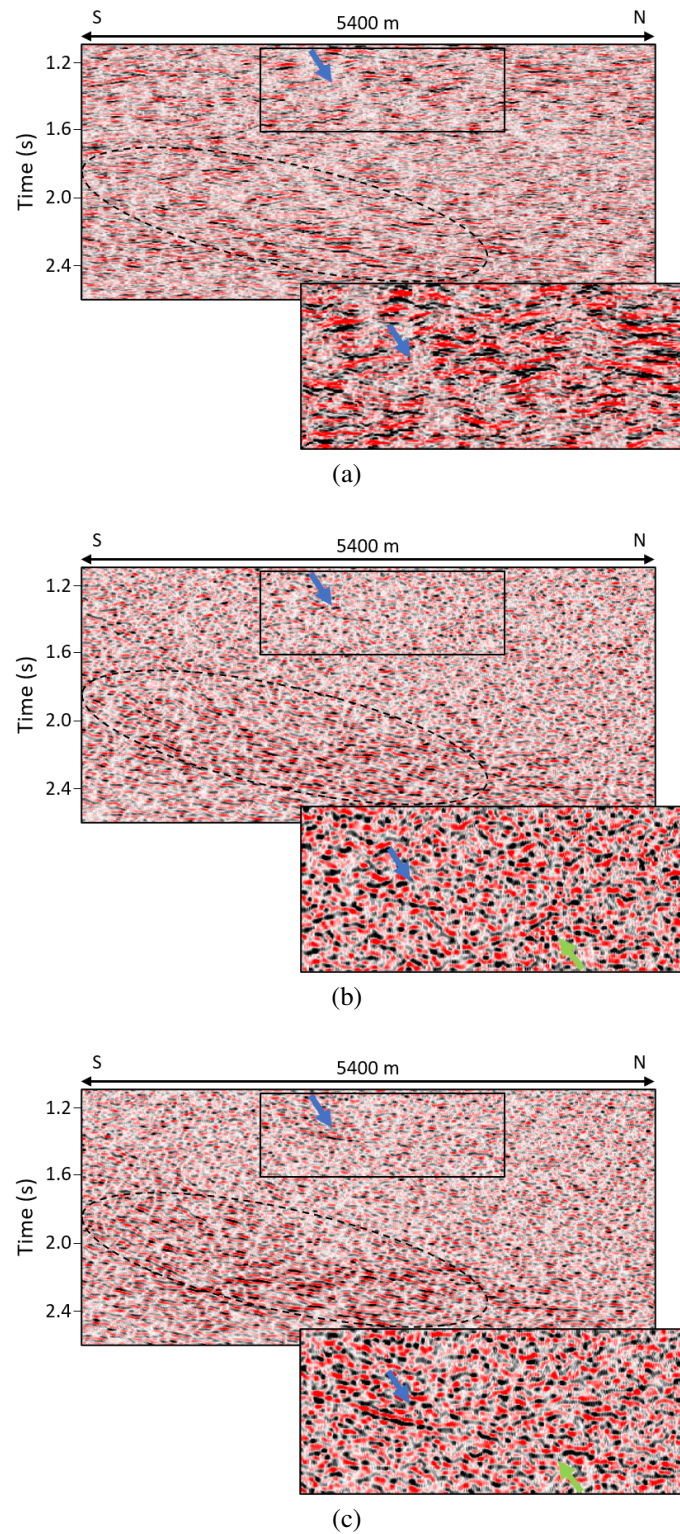


Figure 4.5: A portion of the Larder Lake dataset after stacking using the (a) commercially processed stacked section, (b) standard, and (c) azimuthal binning method. The blue arrows indicate a dipping reflector imaged by the in-house processing (b, c), but not by the commercial processing (a). The smaller image at the bottom of each section represents the zoomed-in of the black rectangle. Within the rectangle, cross-dip effects are mitigated by the optimized binning azimuthal binning, as highlighted by the green arrows.

Refraction static corrections are key in areas with complex weathering layers, such as those in crystalline settings like Larder Lake, and degrade spatial and temporal resolution when not properly applied (Marsden, 1993).

The green arrows indicate the presence of a reflection artifact appearing as a crossing reflection in the standard binning section (Figure 4.5b). This artifact is eliminated in the optimized binning image, resulting in a continuous reflector expanding for about 2 km (Figure 4.5c). This confirms such an artifact is generated by the contribution of out-of-plane energy that is stacked in phase. The amplitude strength of the reflections within this sub-window is enhanced by adopting a locally optimum binning strategy.

### Stacking response to varying azimuths

I evaluate the sensitivity of the stacked image to amplitude smearing caused by signal ill-alignment. This is accomplished by varying bin orientations before stacking. Figure 4.6 illustrates 800-ms x 6-km stacked sections near the southern domain of the LLCDDZ.

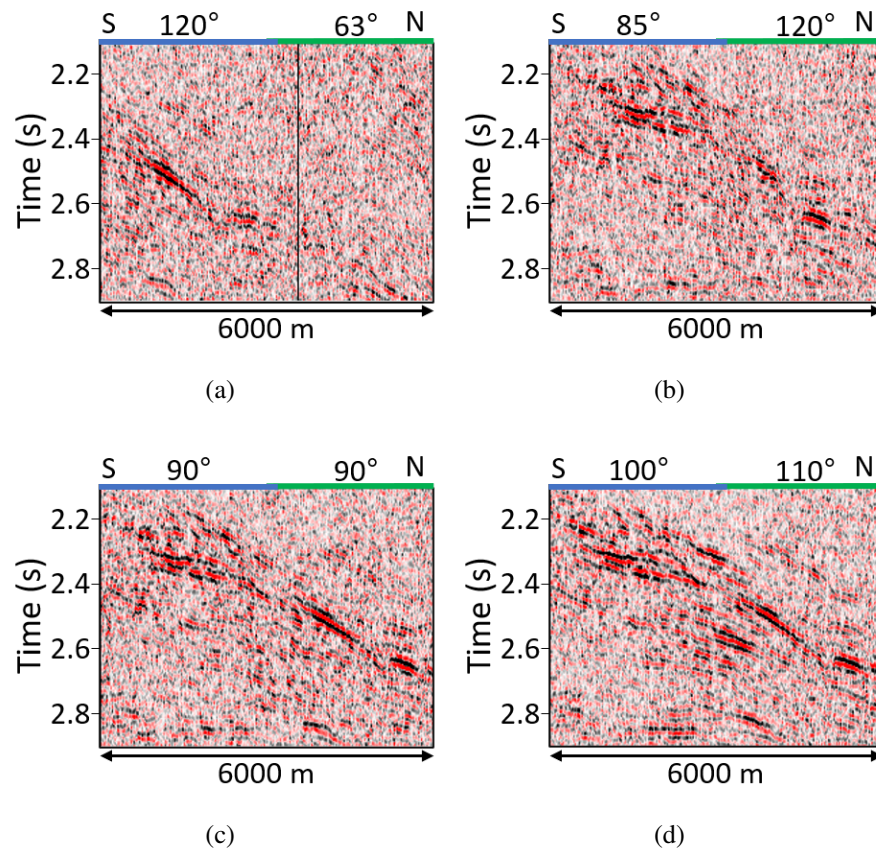


Figure 4.6: Stacked sections with varying azimuths (top blue/green header) near the southern domain of the LLCDDZ. Stacks with (a) arbitrary binning, (b) standard binning, (c) binning according to surface geology information, and (d) optimum binning. The binning of (a) and (b) is not geologically-driven.

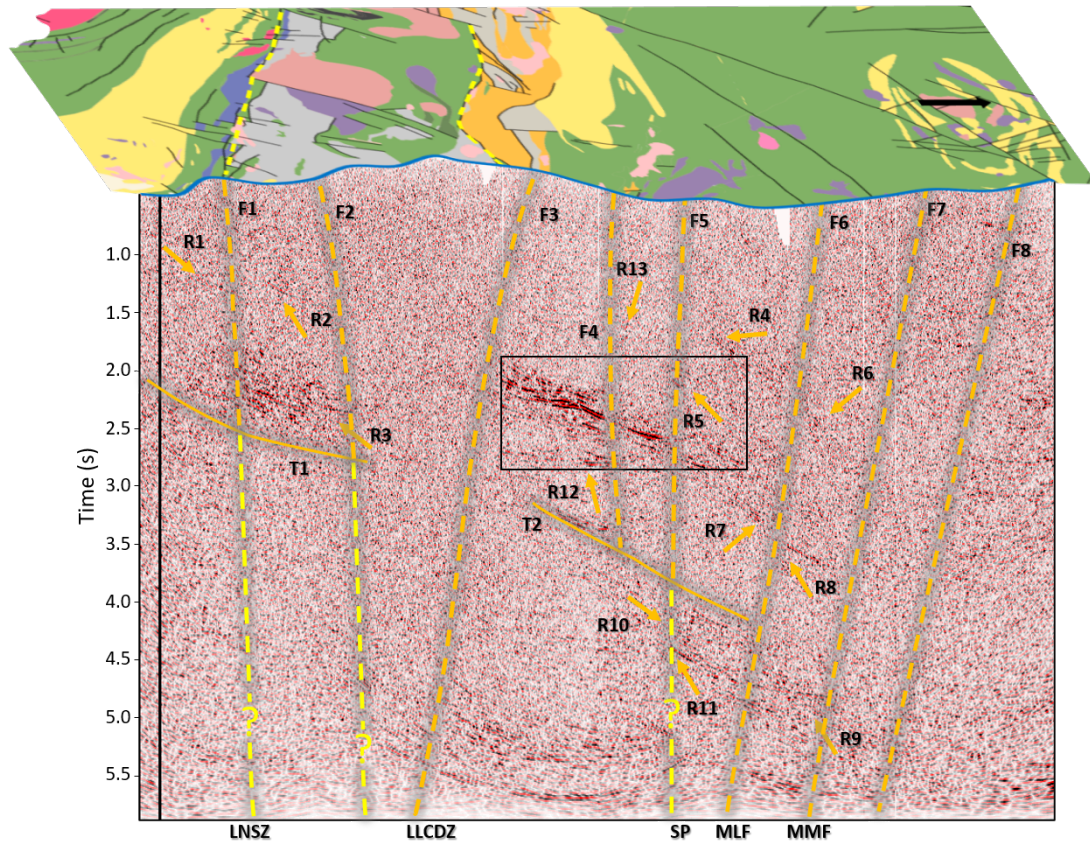
Four different sets of azimuth binning stacks are shown in Figure 4.6. Figure 4.6a displays arbitrarily selected bearings, Figure 4.6b displays the approximate azimuths under the standard approach (perpendicular to the slalom line), Figure 4.6c displays a W-E azimuth, complying with surface geology information (Table 4.2), and Figure 4.6d displays the final optimum azimuth for the area.

The introduction of anomalous traveltimes is problematic when collecting traces in highly variable azimuths, without regard to geometrical or geological information. This is indicated by the lack of coherent reflections in Figure 4.6a. This figure not only depicts poor reflection continuity, but it also portrays severe kinematic problems as observed by the position in time of the strongest reflection, as well as by its shape. This behavior may be expected along the sharpest bends of the profile, and is partly due to the influence of non-hyperbolic traveltimes from out-of-plane events. The image degradation caused by the standard binning approach is readily observed in Figure 4.6b. Anomalous reflection traveltimes are stacked out of phase by ignoring the local geology beneath the processing line, and collecting midpoint traces from different structural domains. Hence, the geometry of dipping reflections is misrepresented, and the overall quality of the image is degraded.

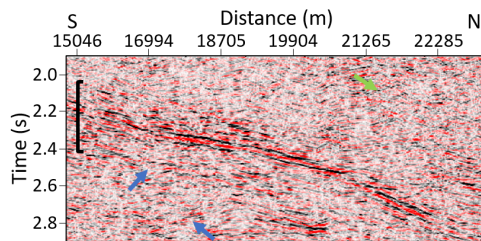
The dominant strike of the area is known from surface geology to be approximately W-E. Binning along the reported dominant strike enhances images in terms of reflection continuity and strength (Figure 4.6c). Nonetheless, better continuity is achieved by rotating the bins towards a slightly more WNW trend (Figure 4.6d). The reflections at the bottom of the section (between approximately 2.6 and 2.8 s) are absent from Figure 4.6c, but are noticeable in Figure 4.6d. This result indicates that the configuration of structures at depth, near the southern portion of the LL-CDZ, are most likely transitioning from a WNW to a W-E trend, and are not necessarily aligned along a dominant W-E strike of the prominent structures observed in outcrops. This final optimum azimuth image is found upon a qualitative evaluation of reflection strength, coherency, and continuity after a detailed comparison of stacking results using a range of different azimuthal binning configurations as described in Section 4.3.1.

### 4.3.3 Azimuthal v. standard migrated sections

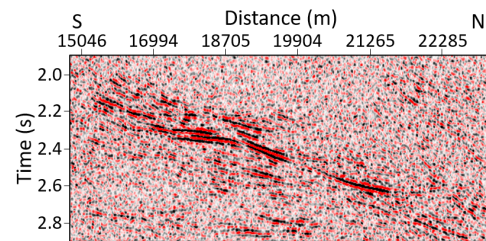
To correctly position dipping reflections, which are enhanced by the optimized binning approach, I perform Stolt F-K post-stack time seismic migration. Figure 4.7a displays the final migrated section intersecting the local geological map along the effective processing line. Two main reflection packages separated by the LLCDZ (F3) fault, both at approximately 2 s, are observed. The rectangle in Figure 4.7a indicates part of the northernmost reflection package, which terminates against the F3 fault. The structural interpretation of the final migrated section will be discussed below.



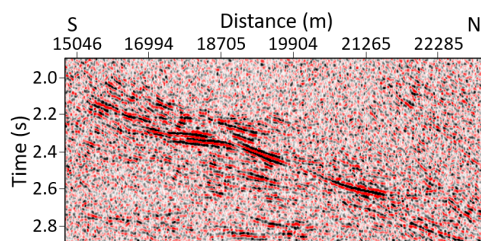
(a)



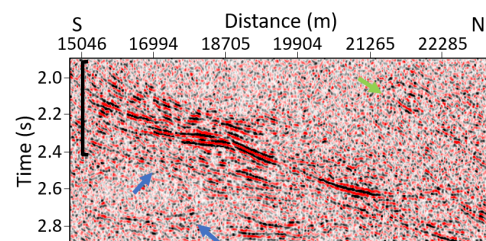
(b)



(c)



(d)



(e)

Figure 4.7: (a) Final post-stack migrated section from azimuthal binning. A zoomed-in window of the migrated section near the LLCZ is shown from using the (b) commercial processing, (c) CVA model, (d) FATT+CVA model, and (e) FWI+CVA model. The blue and green arrows highlight reflections appearing in the in-house section, but lost in the commercial section. The solid black line in (b) and (e) indicates the vertical extent of the reflection package. Letter F - faults, letter T - truncation surface, SP - splay fault, MLF - Mulven fault, MMF - Misema-Mist fault.

Several tests are performed to assess the effectiveness of different migration velocity fields. The FATT and FWI velocity models represent more accurate approximations of near-surface velocity variations. I use them to complement the CVA model at shallow depths after applying proper smoothing. The CVA model is generated by picking velocity functions using semblance analysis on CMP gathers. The FATT and FWI velocity models only extend to a depth of approximately 0.8 km and 2.5 km, respectively. In the time domain, this is equivalent to an investigation depth of approximately 0.8 s for the FWI model. Because this is only a fraction of the full time section (up to 6 s as shown in Figure 4.7a), the smoothed FATT and FWI models are not shown. Instead, the assessment of their contribution is performed by implementing seismic migration.

Three different migrated sections are produced by using the velocity model from CVA, the FATT+CVA model, and the FWI+CVA model. I carry out a depth-to-time conversion of the FWI velocity model implementing  $t(x, z) = \int dt = \int s(x, z') dz'$ , where  $t(x, z)$  is the time and  $s(x, z')$  is the slowness. Figures 4.7b to 4.7e depict migrated images using the (i) commercially processed section (Figure 4.7b), (ii) CVA model (Figure 4.7c), (iii) FATT+CVA model (Figure 4.7d), and (iv) FWI+CVA model (Figure 4.7e). All these images correspond to the area within the rectangle in Figure 4.7a. Note that the full migrated section in Figure 4.7a was obtained by using the FWI+CVA velocity field.

The most striking aspect of the commercially migrated section (Figure 4.7b) is the lower frequency content and, therefore, the lower resolution in comparison with the in-house results. We can observe that the reflection character in Figure 4.7e is better defined than in Figure 4.7b. Clearer morphological features are observed in the former, whereas the geometry of the reflection package associated with the commercially processed section seems to be a continuous, single contact due in part to the lack of high frequency information. A continuous reflector of over 8 km in length is not likely in this highly metamorphosed and tectonically altered region. The reflector package within the black rectangle exhibits stronger amplitude strength as well as clearer reflections in the in-house processed image. This is highlighted by the blue arrows in Figure 4.7e. This may be contrasted with Figure 4.7b, which shows an absence of reflective energy. The commercially processed section does not exhibit the dipping reflections observed at the top right-hand corner of the in-house sections (green arrows). This feature might be related to important local structural variations (e.g., subordinate fracture system, splay fault, etc.). Moreover, the vertical extent of the main reflection package is delineated by the black square bracket in Figure 4.7b and 4.7e. The in-house image resolves a longer vertical section of the reflections, approximately twice the extent observed on the image from the commercially processed section. Overall, the in-house processing successfully retrieves finer structural details.

Reflection continuity is improved at depth by incorporating the P-wave FWI velocity model into the migration velocity field. This improvement is observed by the remarkable refinement of

the section resulting from the FWI+CVA model (Figure 4.7e). The poor performance of migrating with the CVA model only (Figure 4.7c), is likely due to near-surface residual dip moveout effects, which are not completely addressed by the locally optimum binning strategy and/or DMO corrections. The results shown in Figure 4.7 demonstrate that shallow velocity variations play a significant role in imaging structures at depth. Therefore, improving the accuracy of near-surface velocity models can render superior seismic images, especially in crystalline environments suffering from heterogeneous weathering layers.

## 4.4 CMP gathering on slalom lines

Although the CMP method was originally designed for straight-line processing, I find that using a smooth line that follows the real survey trajectory yields better results when implementing azimuthal binning (Figure 4.1). The straight- and three-segment- binning-line processing approaches rendered suboptimal stacked sections (not shown here). As expected, the least optimal zones are related to sharp bends in the geometry, away from the effective processing line. In contrast, the smooth-line processing approach eases the task of locally orienting bins under the azimuthal binning method. We use the crookedness of the profile to our advantage by locally optimizing bin orientation along the predominant geological strike. If a smooth slalom line is to be discarded to simplify data processing and interpretation, the next best option would be the multiple straight-segment processing lines. This is due to the severe crookedness of our survey, where processing over a single straight line is likely to yield poor images. This result also correlates with the findings of Mancuso and Naghizadeh (2021), who, upon performing cross-dip analysis in severely crooked datasets, concluded that a curved line geometry was more effective than the typical straight-line geometry. The consequences of collecting and stacking traces by conventional binning along these smooth slalom lines are major signal losses. This is evidenced by the much lower amplitude strength in the traces shown in Figure 4.4a.

## 4.5 Structural interpretation of migrated reflections

The relationship between reflection patterns and local structural features has been documented by Ayer et al. (2005); Thurston et al. (2008); Brace et al. (2018), who provide an in-depth geotectonic description of the Larder Lake area. Despite the efforts in reducing the contribution of out-of-plane events, the interpretation of 2D profiles illuminating inherently complex 3D structures is subject to a certain degree of inaccuracy.

The reflections observed in the migrated section (Figure 4.7a) appear to consistently dip northwards in an otherwise weak reflective environment. Major structural features are highlighted in the

Figure by dashed orange lines (i.e., the LNSZ, LLCDDZ, SP-splay fault, MLF-Mulven fault, and the MMF-Misema-Mist fault). Dashed yellow lines indicate potential (but not certain) scenarios of the actual fault plane, F refers to fault plane(s), R refers to reflector package(s), and T refers to potential truncation surfaces. Note that, in this chapter, I adopt the terminology from seismic reflection terminations (Cross and Lessenger, 1988) for an easier structural description. This terminology should not be mistaken for discontinuities of depositional sequences/system tracts.

In addition, although not shown in this work, the *post-stack* migrated section in Figure 4.7a exhibits a similar reflection character as the commercially processed *pre-stack* time migrated (PSTM) image. The approach of post-stack migration with azimuthal binning presented in this study is not intended to represent a generalized statement of improvement over a PSTM processing workflow in crystalline environments (by any means). However, the computational cost associated with PSTM makes the implementation of a post-stack technique attractive. The azimuthal binning method mitigates cross-dip effects, which addresses the problem of non-hyperbolic arrivals (for which PSTM or PSDM are preferred). If the condition of hyperbolic traveltimes is met, partial migration techniques such as DMO are more effective in correcting the moveout caused by steeply dipping structures, without the need for a PSTM scheme.

Because the LLCDDZ is the dominant gold-bearing geological feature in the area, I separate the description given below into two domains, southern and northern domains of the LLCDDZ.

### 4.5.1 Southern domain

Reliable seismic interpretation is challenging due to the lack of reflected energy. Nonetheless, the poorly documented LNSZ located approximately 10 km south of the LLCDDZ is successfully imaged. As observed in Figure 4.7a, and suggested in Chapters 2 and 3, the LNSZ is a sub-vertical north-dipping reverse fault (southern boundary defined by F1). Although reflectors R1 and R2 are more coherent and continuous in the unmitigated section, we can still identify them on the migrated image in Figure 4.7a. They appear as a diagnostic feature of the north-dipping behavior of the LNSZ. The truncation pattern between R1, R2, and the LNSZ boundaries (F1-F2), emphasizes the reverse nature of the fault, at least around shallow areas. I interpret R2 (around 1.25 s) as being the result of strong impedance contrasts in the vicinity of the LNSZ, and can be better visualized in Figure 4.5c. This feature can be compared to an onlap reflection termination, which exhibits a similar degree of inclination as the deeper R3 reflection package, suggesting they belong to the same structural domain. The high-amplitude feature, spatially correlates with the north dipping LNSZ anomaly observed in the FWI model presented in Chapters 2 and 3.

A genetic relationship between the LNSZ and the LLCDDZ, in terms of mineralization mechanisms has been suggested by reports of the shear zone hosting mafic to felsic intrusions associated

with gold prospects (Brace et al., 2018). The high-amplitude feature mentioned above may be indicative of a mineralized contact at approximately 3.5 km depth (approximately 1.25 s) near the LNSZ. Malehmir et al. (2017b) found a similar scenario in the Halfmile lake case study in the Bathurst mining camp. A strong high-amplitude feature led them to discover a deep mineralized zone. Although the mineral endowment associated to the Bathurst mining camp is a volcanogenic massive sulfide (VMS) deposit, different to the structurally-controlled lode gold deposits associated to the Larder Lake area, the amplitude response to varying rock types (e.g., a felsic intrusion in an otherwise mafic or ultramafic environment in Larder Lake) would produce a high-amplitude signature. This signature would be similar to a high-amplitude signature produced in a VMS deposit, although the response is sensitive to different rock types/conditions. Note that the commercially processed section in Figure 4.5a shows a lack of reflected energy, not portraying the presence of the high-amplitude feature.

The LNSZ has been reported to extend to a depth of 6 km (Nedimović, 2000). I establish the LNSZ extends to a depth of approximately 8 km (around 2.5 s), as displayed by the truncation surface T1. The characteristics of the R3 terminations support this observation because reflectors truncate the LNSZ trace in an *en-echelon* pattern. That is to say, the reflector at the top of the R3 package extends farther south than its equivalent at the bottom, delineating the LNSZ trace around that region. Nonetheless, given that the 2.5-s estimate is mainly based on the identification of morphological variations in reflection geometry, the LNSZ might extend even deeper. Areas that are seismically transparent, due to weak reflective energy or scattering, might not generate recognizable and coherent patterns for structural interpretation. However, the failure of the seismic method in transparent zones does not mean the structure disappears. This is plausible around the LNSZ, where weakly reflective material precludes the imaging of deeper portions of the structure. The dashed yellow line represents the continuation of the shear zone at depth, opening the possibility to a genetic relationship between the LNSZ and the main break (LLCDZ).

No meaningful geological information can be extracted from the area between F2 and F3 due to the lack of reflections. However, key near-surface features are encountered in shallow intervals as demonstrated in the FWI velocity structure presented in Chapter 3. For instance, the low-velocity basin-like anomaly observed in Figure 4.8 between 8 and 17 km along the model at approximately 0.4 s (1.2 km depth), which marks the transition from the LNSZ to a more structurally complex LLCDZ (Figure 4.8).

### 4.5.2 Northern domain

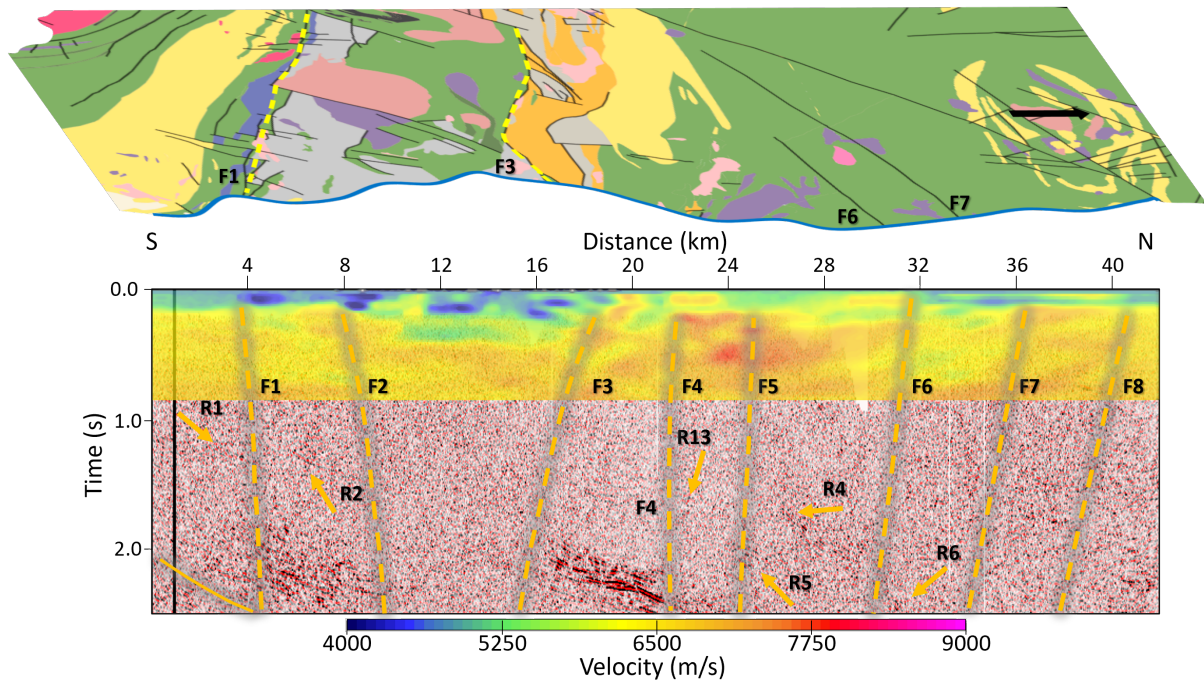


Figure 4.8: P-wave velocity model overlying the final migrated seismic section. Remarkable correlation between the different velocity domains in the FWI model and the spatial position of the main breaks on the reflectivity section is observed.

Evidence of locally strong impedance contrasts and multi-fractured rock units is demonstrated by the reflection package north of the LLCZ, in Figure 4.7a. The intensively faulted zone limits the imaging of continuous reflections in areas with significant impedance contrasts (e.g., between LLCZ and MMF). It seems most of the transect illuminates a seismically transparent geological setting, caused by low reflectivity material. An example of this is the F4 fracture defined by reflections R12 and R13. This structure is truncated by the T2 surface and crosses the most reflective zone of the profile at about 2.4 s.

Prominent reflections (R4 to R11), define the trace of the MLF, MMF, and a potential branch/splay of the MLF - the SP fault (F5). The SP trace is also truncated by the T2 surface, which appears as a moderately strong, laterally continuous reflection. Note, however, that the geometry of R10 and R11 may suggest the SP fault reaches deeper zones and might be related to the MLF (dashed yellow line near R11). It is not clear whether the faults between the LLCZ and the MLF were formed coincidentally with the formation of the larger breaks during extensional periods or by the action of compressive forces. Further analysis is required to reveal the genesis of these structures, and to better map the potential channelways of mineralized solutions and subsequent precipitation of precious metals around the Larder Lake-Cadillac trace.

### 4.5.3 Surface geology and structures at depth

It is evident that reflective signals are virtually absent shallower than 1 s in time in Figure 4.7a, which makes seismic data interpretation ambiguous in the first few kilometers. However, structural features that appear transparent in the reflectivity section can be identified on the FWI velocity structure presented in Chapter 3. Figure 4.8 depicts the first 2.5 s of the seismic section overlaid by the 2.5D FWI model. The combined analysis allows to fill the structural gap between surface geology and crustal-scale seismic images in the region. The main breaks interpreted at depth on migrated sections can be directly correlated with near-surface velocity structures identified using this FWI model.

The southern shear zone in the FWI model correlates with the definition of F1 and F2 on the seismic migrated section, as does the northern boundary of the LLCZ (F3). Strong reflections in the vicinity of the SP (F5) around R4, R5, and R13 match the pronounced velocity anomaly at approximately 22-25 km along the P-wave velocity model. The continuity of the reflections in this area (R4, R5, R13) is compromised by this high-velocity rock body that seems to act as a truncation unit. The transition zone associated with this unit is interpreted as F5. This scenario explains the sudden discontinuity indicated by the reflections south of the SP structure (F5). Reflections R4, R5, and R13 are most likely truncated by the high-velocity anomaly. This explanation would not have been possible without the near-surface FWI velocity model.

The identification of the F4 fault on the migrated section correlates with a change in rock conditions. This is inferred by the contrasting velocity domains around its trace. The velocity structure at approximately 21 km along the profile demonstrates significant velocity contrasts, marking a transition from a low-velocity to a high-velocity domain (moving north of the LLCZ). Reflections within the black rectangle (Figure 4.7a), along with R13, suggest F4 extends up to at least 3.5 s (approximately 11.2 km depth). The migrated section does not exhibit clear evidence of the F4 trace extending towards shallower depths. Nevertheless, the difference in velocity domains in the P-wave model in Figure 4.8 supports the idea of F4 cutting through shallower volcanic rock successions. This structure might be the result of intrusive rocks reaching superficial layers. This highlights the importance of combining quantitative near-surface imaging with regional seismic migrated sections.

## 4.6 Conclusions

In this chapter, I demonstrate that the implementation of locally optimized bin azimuths renders superior seismic images, as illustrated by the results on the severely crooked Larder Lake transect. The azimuthal binning strategy effectively mitigates signal ill-alignment by reducing the

effect of out-of-plane energy. The mitigation of such an effect reduces traveltimes anomalies and energy defocusing. Hence, seismic phases are stacked in-phase, avoiding amplitude smearing during hyperbolic amplitude summation. In contrast, conventional binning strategies yield suboptimal images in highly crooked reflection profiles.

Although the migration approach implemented here is post-stack, the final optimized section is almost equivalent to a pre-stack time migrated image. Carrying out azimuthal binning proves to render optimal results without the computational burden of pre-stack migration techniques. In addition, this study suggests that enhancing migration velocities with high-quality shallow models yields better results than exclusively employing conventional velocity analysis. This is demonstrated by incorporating near-surface FWI velocity models.

Structures at depth are more confidently interpreted by simultaneously analyzing crustal-scale migrated sections and the FWI P-wave velocity model. Based on this combined analysis we introduce new fault planes that help to explain the architecture of reflections in the Larder Lake area. I show major breaks are in good agreement on regional migrated sections and shallow velocity structures (e.g., LNSZ and MMF).

## **Chapter 5**

# **Imaging the northeast lobe of the Sudbury Structure through 2D and 2.5D visco-acoustic full-waveform inversion**

### **5.1 Introduction**

The 1.85 Ga Sudbury Structure hosts the world's largest nickel-copper deposits, playing a major role in the Canadian mining industry. This structure is located in the southern Canadian Precambrian Shield, with its northern boundary straddling granitoid and gneissic rocks of the Archean Superior Province, and its southern boundary comprising metasedimentary and metavolcanic rocks of the Paleoproterozoic Huronian Supergroup (Lenauer and Riller, 2017). Over a 100-year period, intensive research has been conducted to better understand the origin as well as the structural and stratigraphic architecture of the Sudbury Structure. Before the 1960's, endogenic processes explaining the origin of the Sudbury Structure dominated the scientific arena. It was not until Dietz (1964) introduced evidence of shatter cones in the vicinity of Sudbury, that the exogenic hypothesis involving extraterrestrial impact started gaining momentum. Most researchers today have adopted the high-energy impact theory (Peredery and Morrison, 1984; Dressler et al., 1987; Naldrett, 2005; Ames and Farrow, 2007), over that of endogenic origins (Muir, 1984; Norman, 1994; Cowan et al., 1999; Long, 2004). The components of the Sudbury Structure can be divided into three major zones: the Whitewater Group, the Sudbury Igneous Complex (SIC), and the outer shocked and brecciated country rocks known as Sudbury Breccia (Simony, 1964).

The Ni-Cu mineral production from the Sudbury Structure is an important part of the Canadian economy, which relies on the identification and development of new mineral endowments. New discoveries have typically resulted from surface prospecting, and the use of indirect geophysical

methods (e.g., magnetic and electric methods). The need for deeper and more reliable exploration has driven the acquisition of seismic reflection profiles in crystalline environments (Milkereit et al., 2000; Malehmir and Bellefleur, 2009; Kennett and Saygin, 2015; Malehmir et al., 2017c). The reflection method can penetrate kilometer-scale depths while preserving its resolution power.

It is within this context that the structural configuration at depth of the South Range and north-west lobe of the Sudbury Structure has been imaged using seismic reflection data. This history includes the work of Wu et al. (1995); Adam et al. (2000); Milkereit et al. (2000). These authors utilized reflection data surveyed by the Lithoprobe initiative in the late 1980's and early 1990's, predominantly around the South Range. However, the northeast lobe of the Structure remained poorly imaged. In 2017, the Metal Earth project acquired over 900 line-km deep seismic reflection profiles in the Superior Province, including line LN182 located in the northeast lobe of the Sudbury Structure (Naghizadeh, 2019). As I show in this chapter, conventional seismic reflection profiling requires improved near-surface information in order to image the subsurface structures beneath the LN182 transect. The lack of reflected signal prevents the generation of a coherent reflectivity image. The scarcity of reflected phases in the data is likely due to intrinsic low signal-to-noise ratio, complex high-energy seismic scattering from irregularly-shaped geological bodies, poor energy focusing due to out-of-line structures, and amplitude smearing due to signal ill-alignment.

In an attempt to bridge the imaging difficulties, I investigate a non-conventional seismic imaging technique (for hard rock environments) to reveal the architecture of the northeast section of the Sudbury Structure: I utilize 2D and 2.5D full-waveform inversion (FWI). FWI is a non-linear inverse technique that potentially uses the full information contained within the seismic waveforms to iteratively update a subsurface parameter model. Successful FWI requires carefully-designed strategies, especially in hard rock environments where geological structures are complex, and amplitude variations may be significant (Bohlen, 2003; Schreiter et al., 2015). I implement a hierarchical optimization strategy where kinematic components of the waveforms are prioritized, prior to the reconstruction of the dynamic components. Smithyman and Clowes (2013) highlighted that contamination of the inversion due to large data residuals is mitigated by using the logarithmic  $L_2$  objective function at early stages, which improves the stability of the inversion. The strategy implemented here follows the work of Kamei et al. (2015) and the one described in Chapters 2 and 3, where I suggested that large amplitude variations in the observed waveforms may be detrimental to the minimization process especially at the early stages of the inversion, suggesting the use of phase-only residuals.

In this chapter, I demonstrate that FWI is successful in retrieving a quantitative velocity model along a 10-km long transect in the the North Range of the Sudbury Structure. The FWI model is recovered to approximately 1.5 km in depth. Although some authors have indicated that 2.5D FWI methods are critical for crooked line surveys (Smithyman and Clowes, 2013; Xiong et al.,

2013; Boddupalli et al., 2021), others have suggested that 2D methods suffice (Brossier et al., 2009; Kamei et al., 2015; Gras et al., 2019). I illustrate that in this example in which the survey is only mildly crooked, 2.5D FWI is not strictly necessary. Despite the inherent challenges of hard rock data, the inverted velocity structure exhibits clear evidence of the major lithological contacts comprising the Sudbury mining district: the Onaping Formation/SIC contact, the granophyre/norite contact, and the SIC/brecciated-country-rocks contact (Sudbury Breccia). In the first section of this chapter, I briefly introduce the theoretical background of 2D and 2.5D modeling and inversion. In the second and third section, geological aspects of the study area as well as acquisition parameters of the LN182 profile are discussed. I then introduce the implementation of 2D and 2.5D FWI to the LN182 profile in the fourth section. Finally a discussion about the geological significance of FWI results is provided in the fifth section of this chapter, finishing with relevant conclusions.

## 5.2 Method

Full-waveform inversion is an iterative inverse technique used to reconstruct subsurface parameter models by fitting synthetic waveforms to observed waveforms. The method employed here is based on the work of Pratt (1999) and Song and Williamson (1995).

### 5.2.1 Forward modeling

I model visco-acoustic wave propagation using both the 2D and 2.5D wave equation in the frequency domain (Song and Williamson, 1995; Song et al., 1995; Pratt, 1999),

$$\nabla \cdot \left( \frac{1}{\rho(x, z)} \nabla u(x, z; \omega) \right) + \frac{\omega^2}{\kappa(x, z)} u(x, z; \omega) = f(x, z; \omega), \quad (5.1)$$

$$\left( \nabla \cdot \left( \frac{1}{\rho(x, z)} \nabla \right) + \frac{\omega^2}{\kappa(x, z)} - \frac{k_y^2}{\rho(x, z)} \right) u(x, k_y, z; \omega) = f(x, k_y, z; \omega), \quad (5.2)$$

respectively; where  $\rho$  is the bulk density,  $\kappa$  is the bulk modulus (assumed to be complex-valued to accommodate viscous effects),  $\omega$  is the angular frequency,  $u$  is the pressure field,  $k_y$  is the transverse wavenumber component, and  $f$  is a generalized source term. The use of the asymptotic high-frequency ray approximation is avoided, instead I implement finite-difference methods to discretize equations (5.1) and (5.2). The main advantage of solving the 2.5D over the 2D wave equation

is that the 3D nature of wave propagation is captured at any arbitrary location within the model, while still taking numerical advantage of the 2D nature of the subsurface model. This makes 2.5D modeling appealing for severely crooked profiles, provided the geology is approximately 2D. This approach avoids the line-source assumption of 2D profiles, as true (3D) point sources are successfully modeled. Nonetheless, the 2.5D approach has a high computational cost, since equation (5.2) must be solved for every transverse wavenumber and every discrete frequency.

The equations shown above, equation (5.1) and (5.2), are posed in the Fourier domain, where  $\omega$  is a real-valued frequency. Brenders and Pratt (2007b) suggested that the nonlinearity of the inverse problem can be mitigated by adopting an exponential time-damping approach, allowing the reconstruction to focus on the early portion of the waveforms. Shin and Ho Cha (2009) expanded this concept by replacing real-valued frequencies,  $\omega$ , with complex-valued frequencies,  $\Omega = \omega - \frac{i}{\tau}$ , where  $\tau$  is a real-valued Laplace constant. Shin and Ho Cha (2009) termed this technique a ‘‘Laplace-Fourier’’ domain approach, where the iterative data-fitting strategy may only fit the early parts of the waveforms if desired.

### Transverse wavenumbers

The 3D nature of the 2.5D framework in equation (5.2) is captured by applying an inverse spatial Fourier transform with respect to  $k_y$ ,

$$u(x, y, z; \omega) = \int_{-\infty}^{\infty} u(x, k_y, z; \omega) e^{(-ik_y y)} dk_y, \quad (5.3)$$

where  $u(x, y, z)$  is the 3D wavefield response.

The forward problem in equation (5.2) is solved by calculating the out-of-plane wavenumber components following the method introduced by Zhou and Greenhalgh (2006). To define the integration axis in equation (5.3), two main factors are taken into account: the range of transverse wavenumbers, and the sampling interval within that range. The range of transverse wavenumbers is defined as  $k_{y\text{range}} = [0, \min(k_c)]$ , where  $k_c$  is the *critical value* of the medium, which sets the integration range of the wavenumber  $k_y$ , and depends on the frequency,  $\omega$ , and on the velocity of the medium,  $c$ . The sampling interval is chosen so as to minimize the number of wavenumbers to be inverted while preserving numerical accuracy, complying with the criterion  $k_y < k_c$ , following the strategy indicated in Chapter 3 (after Zhou and Greenhalgh 2006).

### 5.2.2 Inversion

The waveform inversion implemented in this chapter is based on the steepest-descent algorithm of Pratt et al. (1998); Pratt (1999), where an  $L_2$ -norm objective function is minimized, iteratively

updating the model parameter by searching along the topography of the sign-reversed gradient image.

The solution to the inverse problem minimizes the sum of the squared residuals,

$$E(\mathbf{m}) = \frac{1}{2} \delta \mathbf{d}' \delta \mathbf{d}, \quad (5.4)$$

where  $E(\mathbf{m})$  is the  $L_2$ -norm objective function,  $\delta \mathbf{d}$  represents data residuals, and  $t$  represents the conjugate transpose. This optimization is performed by employing a gradient method in which model parameters,  $\mathbf{m}$ , are iteratively updated following,

$$\mathbf{m}^{(k+1)} = \mathbf{m}^{(k)} - \alpha^{(k)} \nabla_{\mathbf{m}} E^{(k)}, \quad (5.5)$$

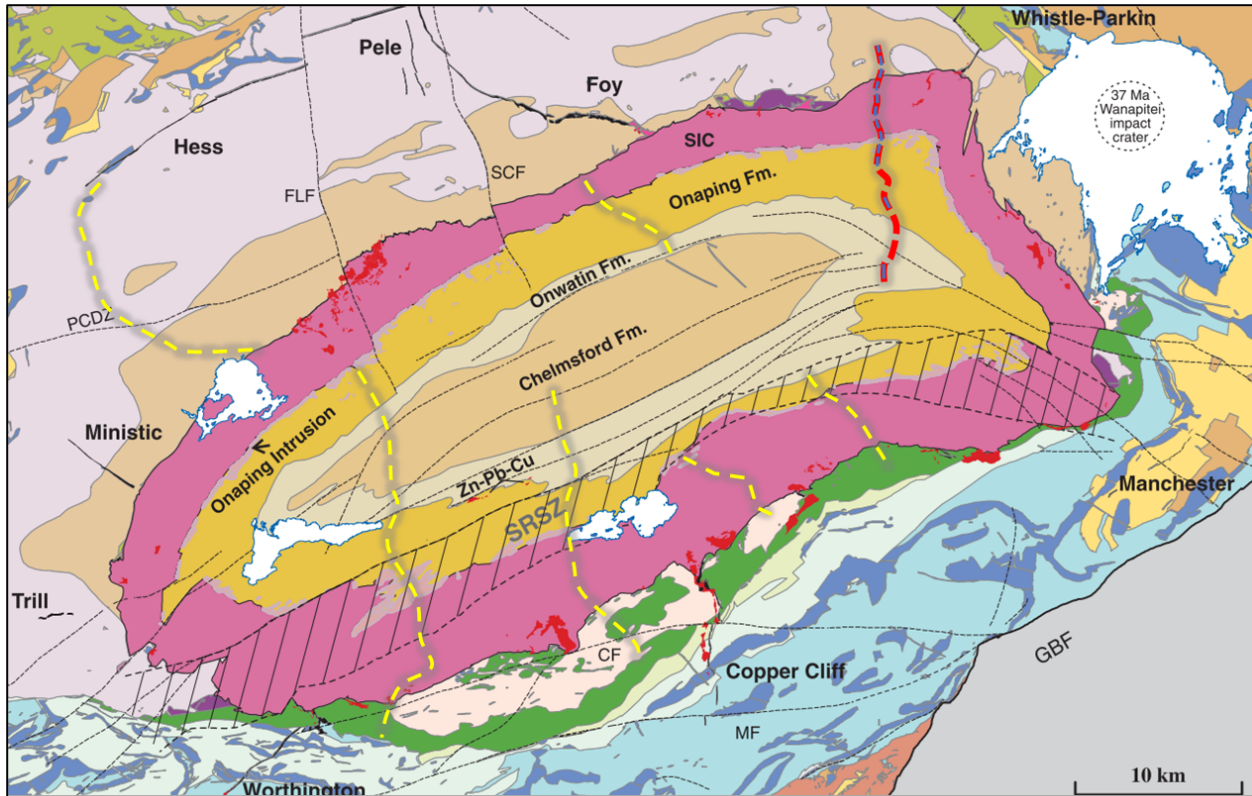
where  $k$  is the iteration number,  $\alpha$  is the step length of the model update (usually computed by linear estimates or line search methods), and  $\nabla_{\mathbf{m}} E$  is the gradient of the objective function. For a full description of the inverse algorithm in the frequency domain, readers are referred to Pratt et al. (1998) and Pratt (1999). In this chapter I minimize two different least squares objective functions, the “logarithmic phase-only” and the “conventional phase-amplitude” objective function. The latter incorporate kinematic (phase) and dynamic (amplitude) components of the wavefields, whereas the former only considers phase information (Shin and Min, 2006).

### 5.3 Geological background

The Sudbury Structure has been the focus of geological mapping due to its economic importance. The structure is divided into three main components: the 8- 10-km wide Whitewater Group (Wu et al., 1995), the 60x30-km SIC (Brocoum and Dalziel, 1974; Klimczak et al., 2007), and the 20 to 80-km long Sudbury Breccia (Dence et al., 1972; Peredery and Morrison, 1984). Figure 5.1 exhibits the geologic map of the Sudbury Structure. The Whitewater Group comprises four conformable formations in a 2.9 km sedimentary column: the Onaping Fm., the Vermilion Fm., the Onwatin Fm., and the Chelmsford Fm.

Because Ni-Cu ore deposits are emplaced near the base of the SIC, this component of the Sudbury Structure is of great relevance. Although there is still debate about the origin of the internal architecture of the SIC (Latypov et al., 2019), the complex is widely accepted as a crustal melt sheet resulting from a high-energy impact event on Archean and Paleoproterozoic rocks within which the Ni-Cu deposits formed. The impact theory is supported by the presence of shock-induced fabrics including shatter cones, planar deformations, pseudotachylitic breccia, etc., (Dressler, 1984a; Spray and Thompson, 1995). Subsequent to the meteorite impact, the melt sheet formed a large area of molten rock from which the main SIC layers crystallized.

CHAPTER 5. IMAGING THE NORTHEAST LOBE OF THE SUDBURY STRUCTURE THROUGH 2D AND 2.5D VISCO-ACOUSTIC FULL-WAVEFORM INVERSION



Legend

- |  |   |
|--|---|
| LN182 - Receiver geometry  | Lithoprobes's transects                           |
| LN182 - Shot geometry  | Faults  |
| Undifferentiated   | Sudbury Igneous Complex and related igneous rocks |
| Chief Lake Igneous Complex   | Nipissing diabase                                 |
| Whitewater Group: postimpact sediments                               | Granite   |
| Ni-Cu-Co-Pt-Pd-Au mineralization                                     | Cobalt Group                                      |
| Whitewater Group: fallback, hydroclastic and plume collapse breccias | Quirke Lake Group                                 |
| Cartier Batholith  | Hough Lake Group                                  |
| East Bull Lake igneous suite   | Upper Elliot Lake Group: metasedimentary rocks    |
| Mafic metavolcanic, metasedimentary rocks                            | Lower Elliot Lake Group: metavolcanic rocks       |
|  | Levack Gneiss Complex                             |

Figure 5.1: Geologic map of the Sudbury Structure. Dashed yellow lines indicate the position of Lithoprobe seismic transects; the dashed red line towards the northeast represents the LN182. The receiver and shot geometries of LN182 are shown by the dashed red line and the dashed blue line, respectively. Modified after Ames et al. (2008).

The cooling and solidification process of the magma occurred in different stages where mafic minerals crystallized first (norite and gabbro rocks), followed by felsic minerals, forming the

granitic rocks of the SIC (Clowes, 2017). Based on these different crystallization stages, four different rock types characterize the Sudbury Igneous Complex, moving outwards from the White-water Group: the granophyre, the quartz-gabbro, the norite, and the Sublayer. Due to the density of sulphide ore minerals, they descended towards the base of the Sublayer, in the contact zone with footwall rocks, which now represents one of the most economically-attractive zones within the SIC (Ames et al., 2007). The contact at depth between the different layers composing the SIC is inferred from analyzing seismic reflection data. Wu et al. (1995) suggested most lithologic units in the North Range of the SIC dip  $20^{\circ}$  -  $30^{\circ}$  south, and are in accordance with borehole logging information and surface geology. Similarly, Milkereit and Green (1992) concluded that the igneous complex dips  $25^{\circ}$  -  $45^{\circ}$  south in the South Range.

The most distal features of the Sudbury Structure are the fractured rocks of the footwall unit corresponding to the Footwall Breccia (proximal to the SIC contact), and the Sudbury Breccia, which is found around the SIC. These two so-called “breccias” are very different rock units. The Footwall Breccia is composed by shattered and crushed country rocks occurring in four settings, discontinuous sheets, “megabreccia”, offset dikes, and intrusions in felsic norite (Dressler, 1984b). The Sudbury Breccia is characterized by the presence of dikes or irregular-shaped bodies having sharp contact with the country rock (Long, 2009). Both the Footwall and Sudbury Breccia have important concentrations of Ni-Cu-PGE mineralization. In general, ore bodies within the Sudbury Structure are hosted by the basal Sublayer, the Footwall Breccia, the Sudbury Breccia, and various footwall rocks (Dressler et al., 1992; Naldrett, 2005). For detailed geological mapping and extensive information of the area, readers are referred to Dressler 1984b; Lenauer and Riller 2012; Lightfoot 2016, and references therein.

## 5.4 Seismic reflection survey

The Sudbury Structure has been the subject of several seismic reflection acquisition campaigns. The Lithoprobe project, a national multidisciplinary Earth science project in Canada (Hammer et al., 2010), incorporated several high-resolution and crustal-scale reflection profiles around the Sudbury impact area as part of the Abitibi-Grenville transect (Ludden and Hynes, 2000). Figure 5.1 depicts some of the Lithoprobe’s seismic transects in dashed yellow lines overlaying the local geology surrounding the Sudbury Structure. Most of the profiles are located around the South Range and towards the center-northwest lobe of the North Range. Lithoprobe data have been processed and interpreted by Milkereit et al. (1994), Wu et al. (1995), Milkereit et al. (2000), among others, and these authors have proposed models describing the architecture of the South Range and the NW portion of the North Range. Nonetheless, the NE lobe of the Sudbury structure remained without an example of seismic reflection profiling until the Metal Earth R&D project

carried out seismic surveying in the area. The Metal earth project acquired several high-resolution seismic transects in 2017, including transect LN182, which is used in this study (Naghizadeh et al., 2019).

Figure 5.1 exhibits the geometry of the LN182 seismic line, showing the source and receiver geometry. Vibroseis sources and single wireless vertical-component 5-Hz geophones were used to acquire LN182 with 6.25 m and 12.5 m spacing, respectively. A linear upsweep of 5-120 Hz was generated by four vibroseis trucks forming the vibroseis source system. Vibroseis sources were sparingly used only on the northern half of the profile and very small sections in the center and southern part. Due to the low source coverage in the southern part of LN182, I decide to disregard this zone and work only with the denser northern portion, which resulted in an approximately 10-km long section. Over 1,500 vibroseis sources are available, however, I decimate them to 330 sources with a 25 m spacing to alleviate the computational burden of multisource inversion. The LN182 transect comprises over 1,300 receivers; I use 935 receivers after disregarding the southern portion of the profile.

The data are characterized by sources with clear refraction arrivals up to a maximum offset limited to 6-8 km, with a strong presence of elastic modes and surface waves. Far-offset components are dominated by low signal-to-noise waveforms, which may compromise the investigation depth of both traveltimes and waveform tomography. For the initial portion of this study I implement 2D forward modeling and inversion, for which a 2D geometry is required. I follow an approach similar to that we used earlier in Chapters 2 and 3, in which the 3D coordinates of source and receiver stations are projected onto a 2D line. This projection generates offset errors in source-receiver pairs for which the true offset differs from the projected offset. To avoid the introduction of excessive traveltimes errors, I remove data traces that exceed a given offset error threshold. In general, the maximum acceptable offset error depends on the maximum traveltimes error produced. Smithyman and Clowes (2012) suggested such a traveltimes error must comply with the half-cycle criterion (i.e., traveltimes residuals are within half the period at the highest frequency of interest). This criteria was used to establish a 6 per cent threshold for non-compliance. Figure 5.2 depicts source-receiver pairs of data, where black regions indicate available data traces, whereas white regions indicate no available waveforms. Figure 5.2a depicts the source-receiver-pair chart with the rejection of non-compliant traces due to offset errors. Mainly near-offset regions are removed, with less than 4 per cent of the data being discarded because of projection errors. This outcome is anticipated due to the mild line crookedness observed on Figure 5.1. The reflection profile mildly deviates from a straight path, with a maximum distance of approximately 700 m towards the east and 400 m towards the west. Figure 5.2a depicts the available seismic waveforms after the removal of noisy traces, but no data removal due to offset errors (i.e, these are the ideal data that would be used for a 2.5D approach). We can observe that predominantly very near-offset traces, and far-offset

traces are removed due to noise. This is expected as near-offset regions are contaminated by elastic modes (primarily surface waves), whereas far-offset traces are contaminated by high-frequency noise obscuring weaker refracted arrivals. Based on the results in Figure 5.2, I speculate that the implementation of a 2D technique is likely to provide an acceptable solution. The mildly-crooked nature of the seismic profile requires only minor data removal due to offset errors (Figure 5.2a). In other words, the effect of ignoring out-of-plane wavenumbers may be negligible (provided, of course that the geological variations perpendicular to strike are also mild).

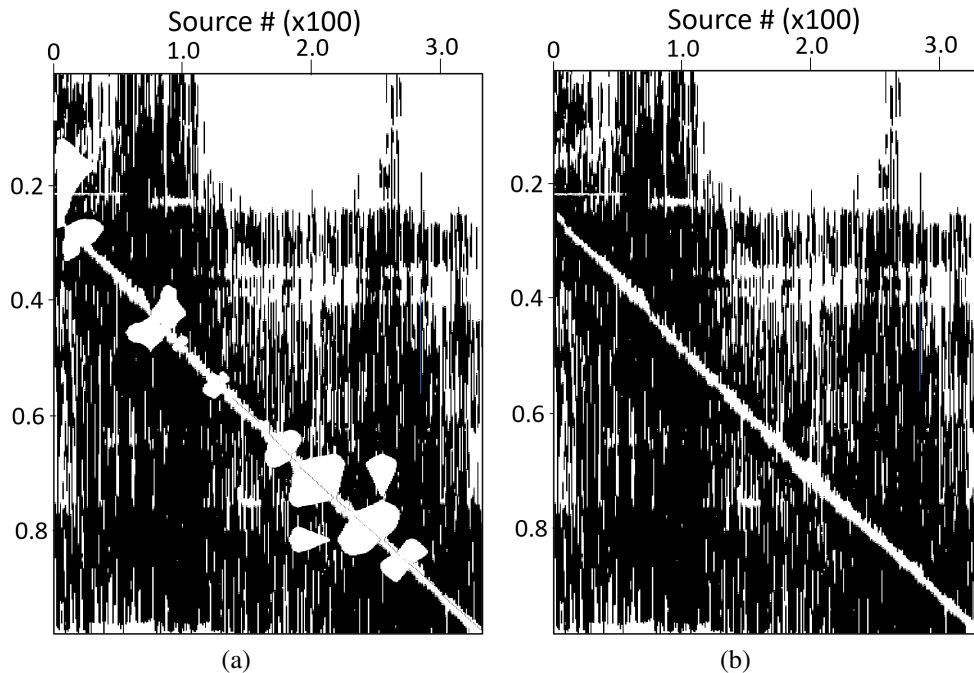


Figure 5.2: Source-receiver pairs of data. Black regions indicate available data, whereas white regions indicate unavailable data. (a) after removing non-compliant traces not meeting the offset error criteria (required for a 2D approach), and (b) before removing non-compliant waveforms (ideal for a 2.5D approach).

## 5.5 Laplace-Fourier-domain FWI

The frequency domain provides the ideal framework for key operations during full-waveform inversion. Advantages include highly efficient use of multi-processing parallel computational resources (especially in 2D and 2.5D), the implementation of a multiscale approach based on frequency continuation, and the introduction of viscous effects by the use of complex-valued velocities. To these advantages we may add the ability to choose what portion of the waveform is included in the reconstruction by implementing a time-damping factor, which is enabled in by using complex-valued frequencies. I implement FWI in the frequency domain after Pratt et al. (1998)

and Pratt (1999), and I extend this implementation into the Laplace-Fourier domain after Shin and Ho Cha (2009).

### 5.5.1 Data preconditioning

The visco-acoustic approximation has proven to yield optimal results in complex geological environments provided an appropriate level of data preconditioning is applied (Ravaut et al., 2004; Brenders and Pratt, 2007a; Malinowski and Operto, 2008). Following a similar approach I used earlier in Chapter 3, I focus on early-arriving waveforms, and remove seismic phases not included in the acoustic finite-difference approximation such as mode conversions, S-waves, surface waves etc. I implement frequency-wavenumber filters in the F-K domain to isolate and reject some of these arrivals; prior to designing the F-K filters, I implement residual statics to shots and receivers. The application of residual statics performs a phase correction of the undesired signal, making them more coherent and easier to remove. I reject noisy traces based on the ability to manually pick first arrival times; data traces lacking picked traveltimes are considered to have low signal-to-noise ratio. I window time waveforms to within 2.5 s following the picked first breaks. I apply surface-consistent amplitude corrections, and shot-to-shot amplitude balancing to alleviate the effect of source radiation patterns and ground coupling. I apply low-pass frequency filters (corners 0-0-22-28 Hz), and time damping in the Laplace-Fourier domain (with time-decay constants of  $\tau = 0.1$  s,  $\tau = 0.25$  s,  $\tau = 0.5$  s; equivalent to 4, 10, and 20 per cent of the maximum time window).

I find significant differences in the dynamic range contained within observed waveforms versus that of modeled waveforms. The observed amplitudes are one order of magnitude higher than the synthetic amplitudes, both portraying a typical amplitude decay with offset but with significant relative amplitude differences between near- and far-offset traces. This disparity is partly due to the limitations of the finite-difference forward modeling scheme and may cause large data residuals during the inversion. To avoid this, I estimate correction factors to scale the observed amplitudes to those present in the forward-modeled data in order to minimize those amplitude residuals that stem from the oversimplification of the visco-acoustic approximation. I follow the approach introduced by Brenders and Pratt (2007b), who used an exponential-decay function to parameterize the decay of RMS amplitudes with offset. They computed the amplitude correction factors using a least squares linear regression of the logarithms of the RMS amplitudes as a function of offset. Brenders and Pratt (2007b) used these correction factors to scale the observed data so the amplitude versus offset (AVO) behavior matches that of the forward-modeled data. Brenders and Pratt (2007b) refer to this as “AVO” behavior, although this differs from Zoeppritz-based AVO analysis commonly used in reflection seismology. I sorted data traces into 50 equally-spaced offset bins between 0.5 and 10 km. Figure 5.3 depicts the logarithmic RMS amplitude of synthetic (5.3a), observed (5.3b),

and amplitude-corrected observed data (5.3c). The observed waveforms are low-pass filtered to 28 Hz, and the synthetic data are forward modeled to 30 Hz before performing the correction, both datasets are time-windowed to 2.5 s. We observe in Figure 5.3c that the observed amplitudes have been successfully matched to the same order of magnitude of the synthetic data. This correction enhances inversion stability from all offsets as large data residuals are mitigated.

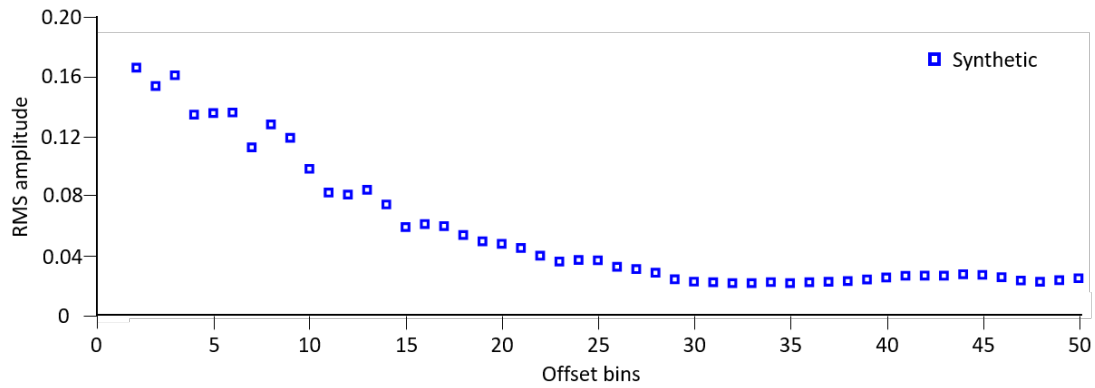
Figure 5.4 depicts a seismic gather located at a distance of 2 km along the transect, before and after data preconditioning. Figure 5.4a, representing the raw gather without any preconditioning, displays strong near-offset secondary arrivals in the form of air waves, surface waves, and other elastic modes. In addition to the preconditioning steps described above, I mitigate the effect of these strong near-offset phases on the data residuals by implementing an offset-dependent cosine taper to the residuals. The black regions in Figure 5.4b and 5.4c, depict zones with waveforms precluded from the inversion due to noise. Figure 5.4b depicts the result from implementing filters in the F-K domain, rejection of data traces, time windowing, and amplitude corrections. Improvements are observed in the signal-to-noise ratio and coherency of first arrivals. The reduction of noise is noticeable, for instance, around 5 km offset where a high-frequency artifact indicated by the white arrow in Figure 5.4a has been successfully mitigated by the data preconditioning steps (Figure 5.4b). Waveforms after applying low-pass filtering and time-damping are depicted in Figure 5.4c. Time damping is implemented using  $\tau = 0.1$  s in the Laplace-Fourier domain. This procedure focuses the inversion on first-arriving seismic energy by damping the amplitudes of later phases.

## 5.5.2 Starting velocity model

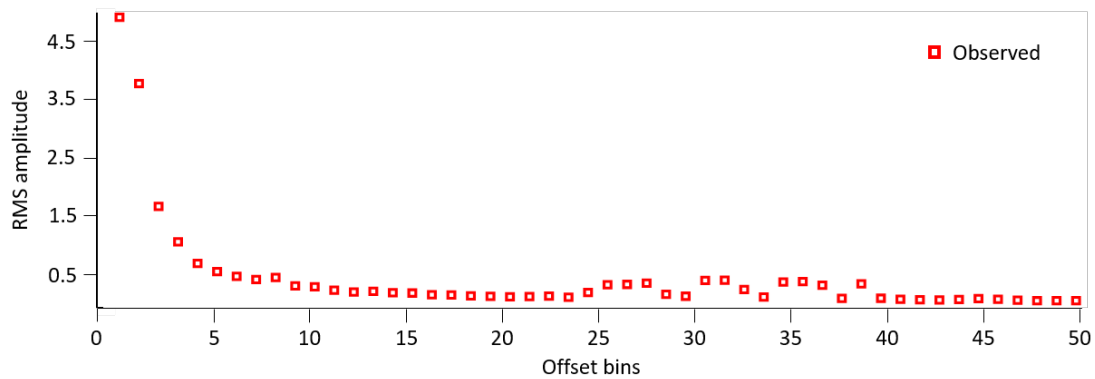
Full-waveform inversion requires an initial velocity model, which I generate by implementing 3D nonlinear first arrival traveltimes tomography (FATT) (after Zhang and Toksöz, 1998). The FATT is a reconstruction of the long wavelength characteristics of the velocity model, and it is a prerequisite in descent-based optimization methods to mitigate the risk of converging to local minima. First-break traveltimes picking is performed on 330 shot gathers with 935 receivers per gather. The interpretation of first arrivals is ambiguous for offsets larger than approximately 8 km, where low signal-to-noise ratio and high-frequency noise significantly affects the dataset.

I implement 3D nonlinear refraction traveltimes tomography using a grid interval equal to 25 m in all directions. The traveltimes tomography process first involves the generation of a layered velocity model using the traveltimes picks of the earliest arrivals. Ray tracing is implemented to compute synthetic traveltimes associated with this initial layered velocity-depth model. This initial prediction is then refined through nonlinear traveltimes tomography, iteratively perturbing the velocity model while minimizing the difference between picked and predicted traveltimes in a

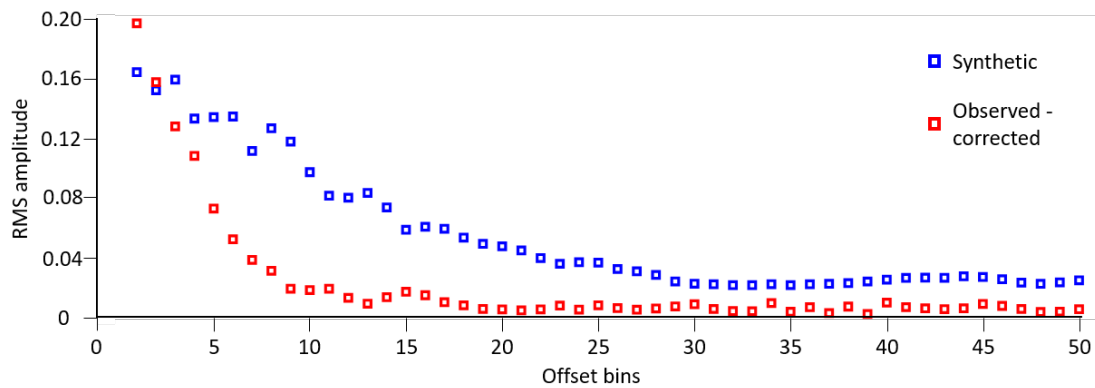
least-square fashion.



(a)



(b)

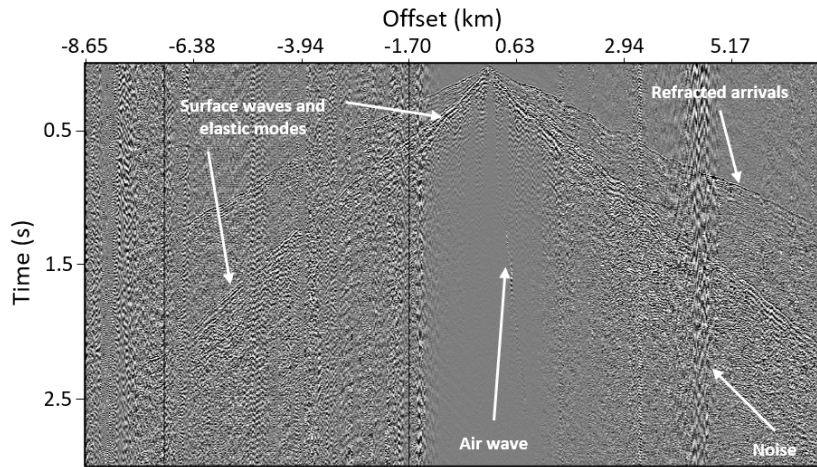


(c)

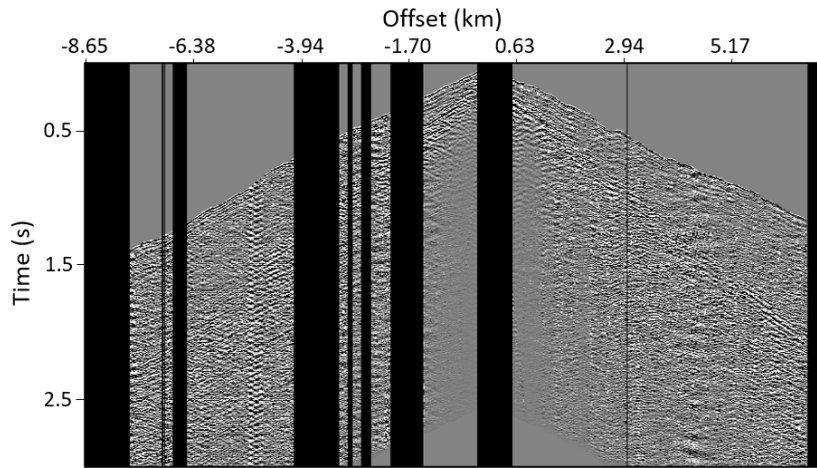
Figure 5.3: Amplitude versus offset bins of (a) forward modeled data, (b) observed data, (c) forward modeled, and observed data after amplitude correction. The observed data are scaled to the synthetic data, mitigating the minimization of large data residuals during the inversion.

Figure 5.5 depicts the root-mean-square (RMS) travelt ime misfit for all data traces used in the 3D tomography.

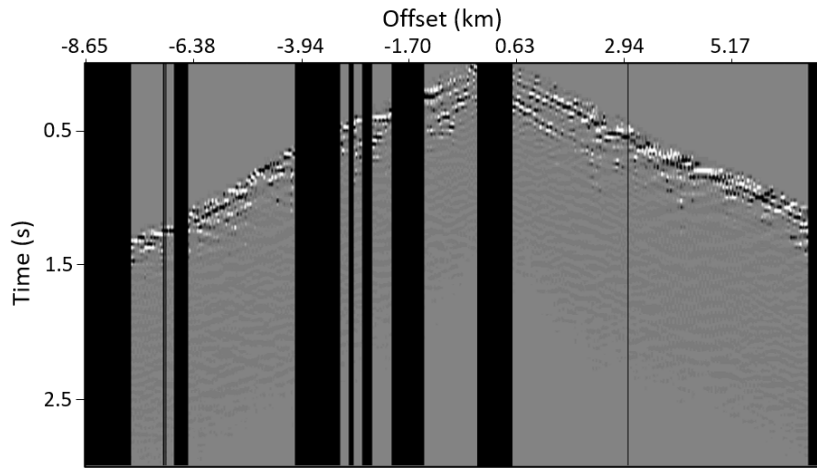
CHAPTER 5. IMAGING THE NORTHEAST LOBE OF THE SUDBURY STRUCTURE THROUGH 2D AND 2.5D VISCO-ACOUSTIC FULL-WAVEFORM INVERSION



(a)



(b)



(c)

Figure 5.4: Vibroseis gather at approximately 2 km along the survey geometry. The data are presented (a) prior to preconditioning, with no time windowing or muting; (b) with windowing, muting, F-K filtering, surface-consistent and shot-to-shot amplitude balancing, and with observed-to-synthetic amplitude scaling; (c) with all preconditioning, including low pass filtering and time-damping (with  $\tau = 0.1$  s).

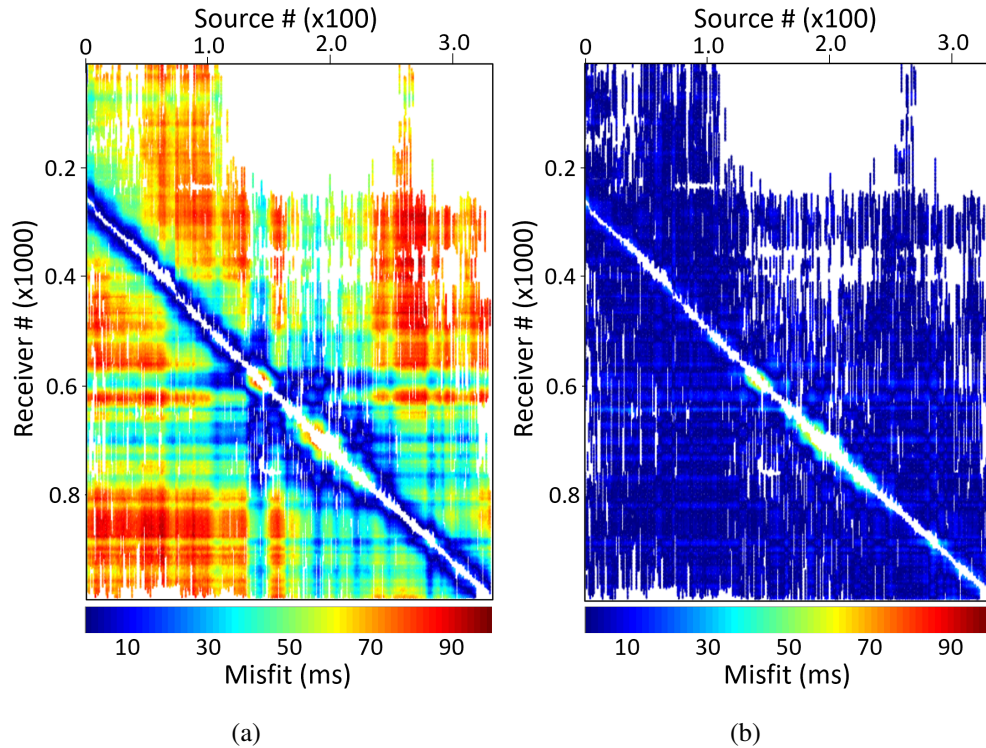
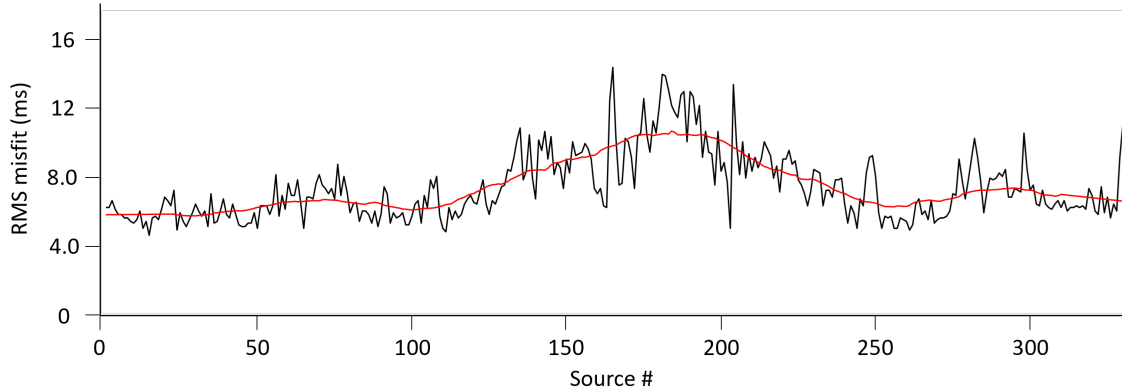


Figure 5.5: Traveltime residuals mapped onto source and receiver indices, computed using the velocity model (a) before, and (b) after 3D traveltimes tomography.

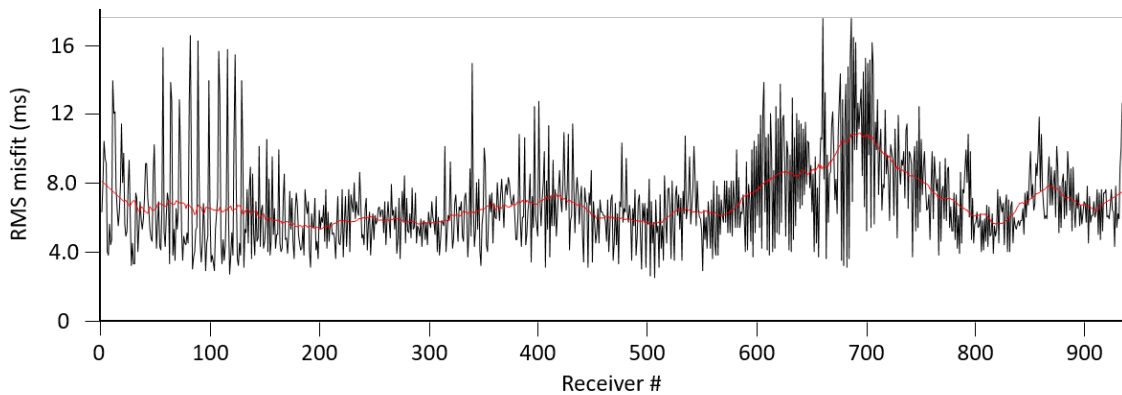
Blank areas indicate regions without waveforms due to the presence of noise. Figure 5.5a depicts the RMS residual associated with the initial velocity model, and Figure 5.5b depicts the RMS residual of the final traveltimes tomography model. The initial velocity model poorly predicts traveltimes, especially on near-to-medium offset traces.

After the 10th iteration, the overall RMS residuals between predicted and observed traveltimes is reduced to approximately 8 ms, which is well within the half-cycle criterion (i.e., traveltimes prediction are within half the period of the lowest frequency used for the inversion). This very low RMS residual achieved partly by neglecting large offset traces where the manual picking is ambiguous, reducing the impact on data misfit (see, for instance, region between source #100 and #330 in Figure 5.5). Figure 5.6 depicts the final data misfit in a common i) shot array (5.6a), and ii) receiver array (5.6b). The red lines on both graphs represent a Savitzky–Golay smoothing filter applied to the RMS traveltimes residuals using local polynomial approximation. The implementation of the filter allows us to obtain an RMS misfit value for both sources and receivers without distorting the general tendency of the data. The RMS traveltimes misfit observed in sources and receivers is of 7.6 ms and 7.0 ms, respectively. The highest traveltimes misfit is observed around the source # 180 in Figure 5.6a, which roughly correlates with the increase in traveltimes residuals observed in Figure 5.6b, around receiver # 700. These results are in agreement with the available

data shown in Figure 5.2, we observe an absent of medium-to-far-offset data traces around source # 200, which is associated with a systematic low signal-to-noise ratio in these gathers.



(a)



(b)

Figure 5.6: Final traveltimes misfit observed in (a) common shot array, and (b) common receiver array. The red line represents a Savitzky–Golay smoothing filter, indicating the RMS misfit trend of the full array.

I display the final traveltimes tomography model in Figure 5.7. The investigation depth of the traveltimes method is limited to near-surface areas, with reliable velocities estimations extending to less than 500 m depth. The northernmost section of the velocity model displays a larger near-surface area of low confidence as depicted by the grey shading on the image. This reflects an absence of ray coverage, reflecting the sparsity of traveltimes picks due to the quality of gathers along this portion of the transect. The starting velocity model is suitable for FWI based on two key results. First, the velocity variations in Figure 5.7 are sufficiently smooth, and represent the long-scale features of the background structure. This avoids the introduction of spurious short-wavelength artifacts into the subsequent FWI process. Second, the FATT model fits observed and predicted traveltimes to within 8 ms, which is approximately one-fifteenth of the dominant period

at the lowest FWI frequency (i.e., 125 ms at 8 Hz). This indicates that cycle skipping is unlikely to occur at the initial stage of FWI. I generate a starting velocity model in accordance with both 2D and 2.5D FWI schemes, following the approach explained in Chapter 3.

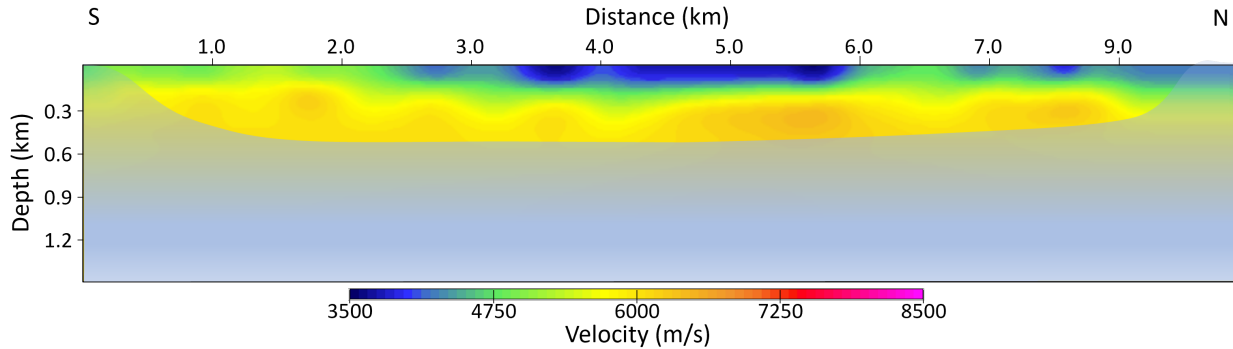


Figure 5.7: Final traveltim tomography (starting velocity model for FWI). The grey-shaded region indicates areas in which no raypaths are observed.

### 5.5.3 Modeling

I perform visco-acoustic finite-difference forward modeling in the frequency domain by solving equation (5.1) and (5.2). Forward modeling is carried out for all 330 vibroseis sources using a constant frequency increment of 0.4 Hz, from 0.4 Hz to 30 Hz (75 discrete frequencies). The starting velocity model used for forward modeling and FWI is 10 km long and 1.5 km deep. I use a cell size equal to 25 m to avoid numerical dispersion at a maximum frequency of 30 Hz. This is to comply with the criterion of sampling the smallest propagating wavelength using at least four grid points (Jo et al., 1996). I use a maximum modeling frequency equal to 30 Hz in order to have more freedom in later stages of FWI to move to higher frequencies. This decision is made taking into account the relatively small size of our geometry, which allows this without creating a significant computational burden.

The perfectly matched-layer absorbing boundary condition (Berenger, 1994) is used at every corner and edge of the numerical model. I impose an “implicit free-surface” (Bleibinhaus and Rondenay, 2009) absorbing boundary condition above the surface to deal with free-surface multiples. Under the visco-acoustic scheme, I implement high attenuation above the surface with  $Q = 1$ , and a constant subsurface attenuation with  $Q = 500$ . Albeit an oversimplification, the use of a homogeneous subsurface attenuation has proven to yield acceptable FWI results when  $Q$  is considered as a passive modeling parameter (rather than being considered an inversion parameter; see Kurzmann et al. (2013); Operto and Miniussi (2018)). I derive and update the density model after the inversion of each frequency stage by using Gardner’s relationship (Gardner et al., 1974).

### 5.5.4 Full-waveform inversion

I perform 2D and 2.5D FWI following the scheme described in Table 5.1. The main approach is based on the hierarchical implementation of two different objective functions, the progressive inclusion of later seismic phases using variable time-damping in the Laplace-Fourier domain, and the implementation of multiscale frequency continuation.

Sirgue and Pratt (2004) demonstrated that optimal FWI results may be obtained by only inverting for a carefully-chosen subset of frequencies; they termed this approach “efficient full-waveform inversion”. However, with the advent of multiprocessor computational resources this is more selective than is required. Due to the complex geological setting in hardrock environments, which generates complex scattering of the forward propagated wavefield, I use a much finer frequency sampling interval. Instead, I comply with the Nyquist criterion by adopting the sampling criterion,  $\Delta f = 1/T_{max}$ , where  $\Delta f$  is the frequency interval, and  $T_{max}$  is the time window used to select the data. I use frequency sampling intervals of 0.4 Hz from 8 Hz to 22 Hz, and 8 Hz to 15.2 Hz for the 2D and 2.5D inversion schemes, respectively (Table 5.1). Five sequential frequencies in each inversion stage are used, overlapping frequency components to guarantee a stable transition between low- and high- frequency information as the inversion advances. I maintain the total number of frequencies per stage constant in order to preserve the computational efficiency of the strategy.

To reduce the introduction of amplitude artifacts to gradient updates, I start the velocity inversion by fitting only the kinematic (phase) components of the observed wavefields. This approach proved to be necessary even after the implementation of amplitude scaling of the observed waveforms. Table 5.1 lists parameters for stages 1 to 35 from 8 Hz to 22 Hz, for which the logarithmic phase-only residuals are minimized. Once the velocity model is updated with this kinematic information, I proceed to minimize conventional phase-amplitude residuals, thereby adding amplitude information into the reconstruction. The conventional phase-amplitude objective function is minimized using frequencies between 8 Hz and 22 Hz. Wavenumber filters are also introduced to constrain the gradient before velocity updates are implemented. The filters mitigate the introduction of spatial noise by only allowing a portion of the expected maximum wavenumber into the reconstruction.

Table 5.1: Multiscale inversion strategy.

Stage	Frequencies (Hz)	Iter.	Laplace constant (s)	2D	2.5D	Residuals
1	8.0			✓	✓	
2	8.0-8.4-8.8	10	0.1	✓	✓	
3	8.0-8.4-8.8-9.2-9.6			✓	✓	
4	8.4-8.8-9.2-9.6-10.0			✓	✓	
:	:			:	:	:
17	13.6-14.0-14.4-14.8-15.2	10	0.1	✓	✓	
18	14.0-14.4-14.8-15.2-15.6			✓		
:	:	:	:	:	:	Log. phase-only
34	20.4-20.8-21.2-21.6-22.0	10	0.1	✓		
35 - Repeat 2-34	-			0.25	✓	
36 - Repeat 2-34	-	5	0.5	✓		Conventional phase-amplitude

Filter corners are frequency-dependent, and are calculated in an *ad hoc* basis for each frequency stage following the maximum theoretical resolution (as estimated by Wu and Toksöz, 1987).

I complement the multiscale strategy described above (i.e., frequency continuation and hierarchical data residual optimization), by varying the effective time window by increasing the time-damping constant in the Laplace-Fourier domain. This approach allows the progressive investigation of ever-deeper parts of the structure, and hence I refer to this as a “layer-stripping” approach. I start by using a very low Laplace constant equal to 4 per cent of the maximum time window,  $\tau = 0.1$  s. Figure 5.4c depicts the application of this time-damping factor in the time domain. The use of such a small value allows us to enhance refracted arrivals while damping the contribution of later phases, reducing the risk of cycle skipping. I continue the inversion strategy by using larger time-damping constants after the 34th stage, as indicated in Table 5.1. This strategy allows to properly fit the most later portions of the data arising from the relaxation of time damping. By preserving the same offset scheme (i.e., progressively including larger offsets as higher frequencies are inverted), and using larger Laplace constants, I also progressively update the higher wavenumber features of the model, corresponding to short-wavelength structural details. Damping values equal to 10 and 20 per cent of the maximum time window are implemented.

I used the linear method presented by Pratt (1999) to update the source wavelet (amplitude and phase characteristics) after each inversion stage. This allows for a progressively more accurate source signature to be used during the inversion, provided the velocity model converges towards the “true” solution.

## 2D v. 2.5D FWI

As described above, both 2D and 2.5D FWI are performed in this chapter. Both approaches use data with the same preconditioning, except that in the 2.5D case no waveform rejection due to offset errors is required. The different nature of the source physics also requires that amplitude scaling is conducted separately. I iteratively update the 2D and 2.5D velocity models using the same multiscale layer-stripping strategy listed in Table 5.1. Prior to initiating 2.5D FWI, I establish a sequential out-of-plane wavenumber scheme following the approach presented in Chapter 3 (after Zhou and Greenhalgh, 2006). The integration over  $k_y$  in equation (5.3) for the maximum inverted frequency contains a total of 68 components. Note that the total wavenumber components depends on the maximum frequency being inverted for in a given inversion stage. Each of these wavenumbers components are solved for each discrete frequency in 2.5D FWI.

Due to the high computational cost of 2.5D modeling, I only perform 2.5D FWI up to the 17th inversion stage. After this stage, I evaluate the resulting 2D and 2.5D FWI velocity models by comparing synthetic waveforms, velocity residuals, and the inverted velocity structure. I am able to conduct these direct comparisons because the same inversion strategy has been applied to both

models. Figure 5.8 depicts the results of 2D (5.8a) and 2.5D (5.8b) FWI after the 17th inversion stage. In Figure 5.8c, I show the velocity differences between these two models. We observe both velocity models still recover nearly identical long-wavelength characteristics of the velocity field. Fine structural details are not expected at this early stage of the inversion scheme since strong time damping is used, and high frequencies are not yet included in the reconstruction. The 2.5D full-waveform inversion model is very similar to its 2D counterpart. Velocity updates are observed in the near-surface, above approximately 1000 m depth in both models, whereas areas at depth remain largely unchanged. This is readily observed in Figure 5.8c, where the velocity residuals are more significant towards the near-surface. However, the RMS velocity residual for the entire model is approximately 16 m/s, which represents a velocity change of less than 0.3 per cent.

To further assess the 2D and 2.5D approaches, I conduct finite-difference forward modeling using both models to solve equations (5.1) and (5.2), respectively. Figure 5.9 depicts 2D (5.9b, 5.9e) and 2.5D (5.9c, 5.9f) synthetic waveforms, and observed waveforms (5.9a, 5.9d), located at 1.5 and 7.5 km along the model. No significant improvements are observed on the 2.5D modeling over the 2D counterpart. The 2.5D modeled shot gather in Figure 5.9f seems to slightly outperform traveltime fitting at near offsets, as indicated by the blue arrow. However, in both cases on the synthetic gathers the traveltime residuals are seen to satisfy the half-cycle criterion at the near- and far- offset zones. In addition, not only do the first-arrival waveforms fit well in both 2D and 2.5D predicted gathers, but also the coda portion of the seismograms exhibits similar characteristics in terms of phase and amplitude strength.

Based on the similarities observed between Figures 5.8a and 5.8b, coupled with the small velocity differences between the inversion models from the two different schemes, as well as the very similar representation of predicted waveforms observed in Figure 5.9, I conclude that the improvements introduced by 2.5D FWI do not justify the associated computational burden. These results illustrate that the out-of-plane effects for these mildly crooked profiles may be neglected, and 2D modeling and inversion may be confidently implemented. Note that "sideswipe" or cross-dip effects as often experienced with reflection processing is less likely to pose a problem for early arrival FWI, since the propagation is largely confined to the vertical plane containing source-receiver pairs. After the 17th stage, we proceed with only 2D full-waveform inversion, as illustrated in Table 5.1.

### **FWI results**

The final full-waveform inversion velocity model is depicted in Figure 5.10a, along with our structural interpretation. The resolving power of the FWI velocity model is significantly higher than that observed in the starting velocity model (Figure 5.7). The structural overlay follows the general trends observed within the different subsurface domains. These domains are predominantly

represented by south-dipping structures, which correlates with the known geology of the area. We discuss this further in section 6 below.

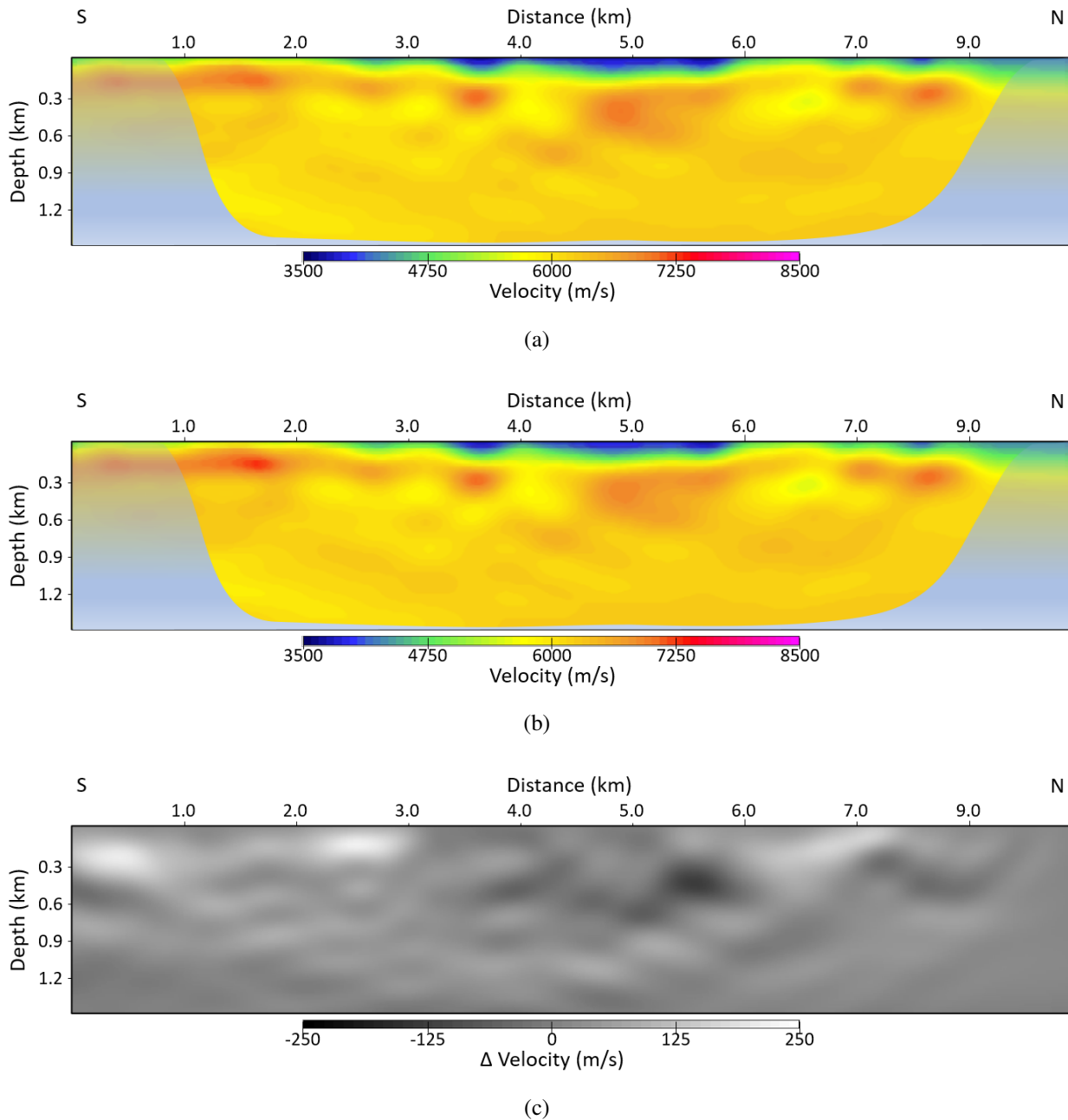


Figure 5.8: Full-waveform tomography results after stage 17 using the (a) 2D and (b) 2.5D modeling approach. (c) the velocity differences between the model in panel (a) and the model in panel (b).

I also compute a detrended velocity model to improve the visualization of prominent velocity variations (see Figure 5.10b). I remove the 1D background trend from the starting velocity model following the strategy used by Kamei et al. (2012). A fourth-degree polynomial is fit to the starting two-dimensional velocity image. I then subtract the resulting depth-dependent 1D velocity

function from the final FWI model in Figure 5.10a.

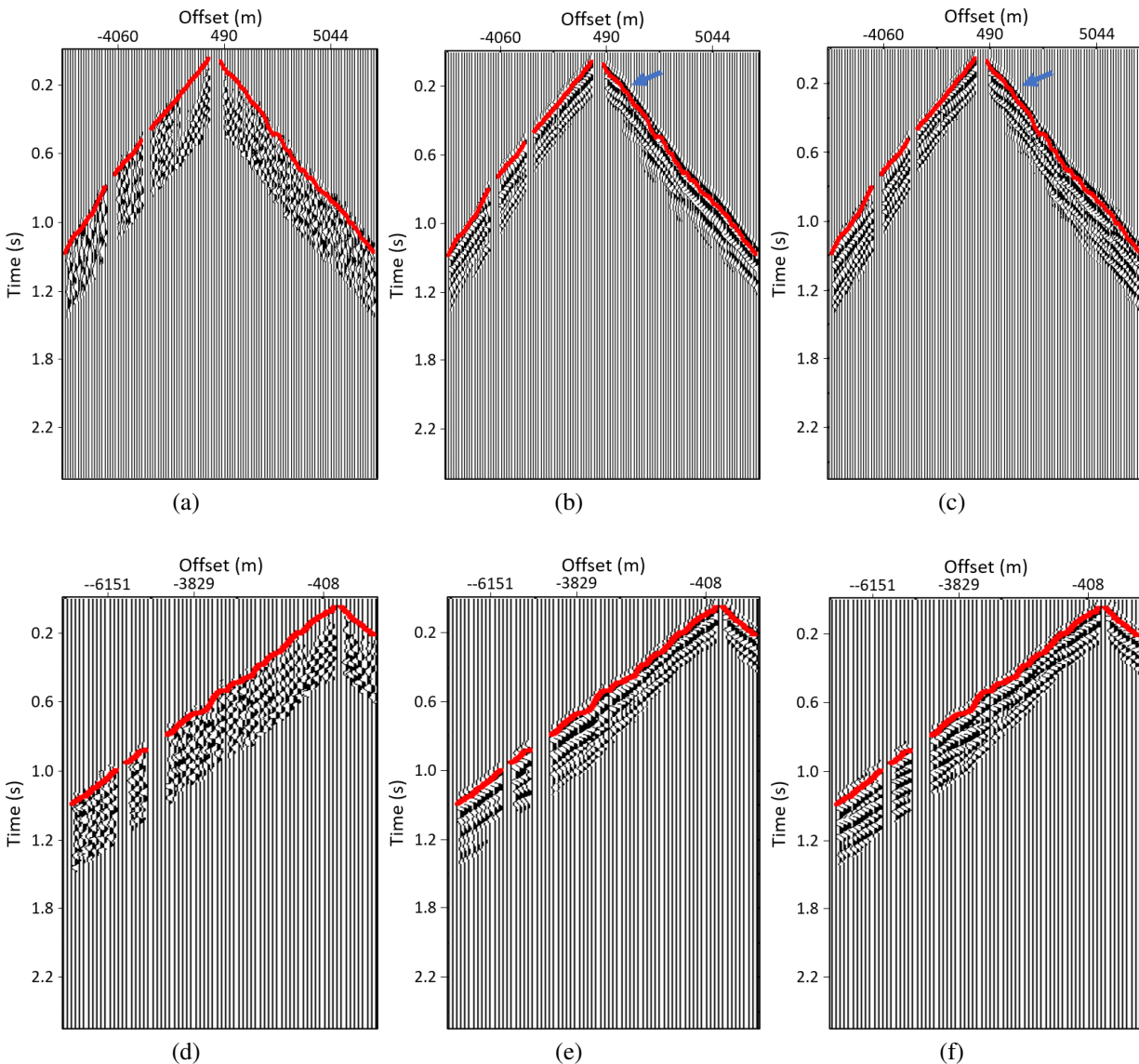


Figure 5.9: Observed (a, d, located at approximately 1.5, and 7.5 km along the model, respectively), and synthetic waveforms generated with the (b, e) 2D and (c, f) 2.5D FWI velocity model. Manually picked first-arrival times are represented by the red line in all panels. The blue arrows indicate a near-offset zone where 2.5D modeling slightly outperforms the 2D modeling in terms of first arrival misfit.

The detrending process enhances the depth continuity of domain “edges”, more clearly characterizing the transition between these velocity domains. On Figure 5.10b we observe that the lateral velocity variations are more apparent than vertical velocity variations. This is an expected structural trend due to the sub-horizontally-layered configuration of the metamorphic and sedimentary rock units in the northeastern portion of the Sudbury Structure.

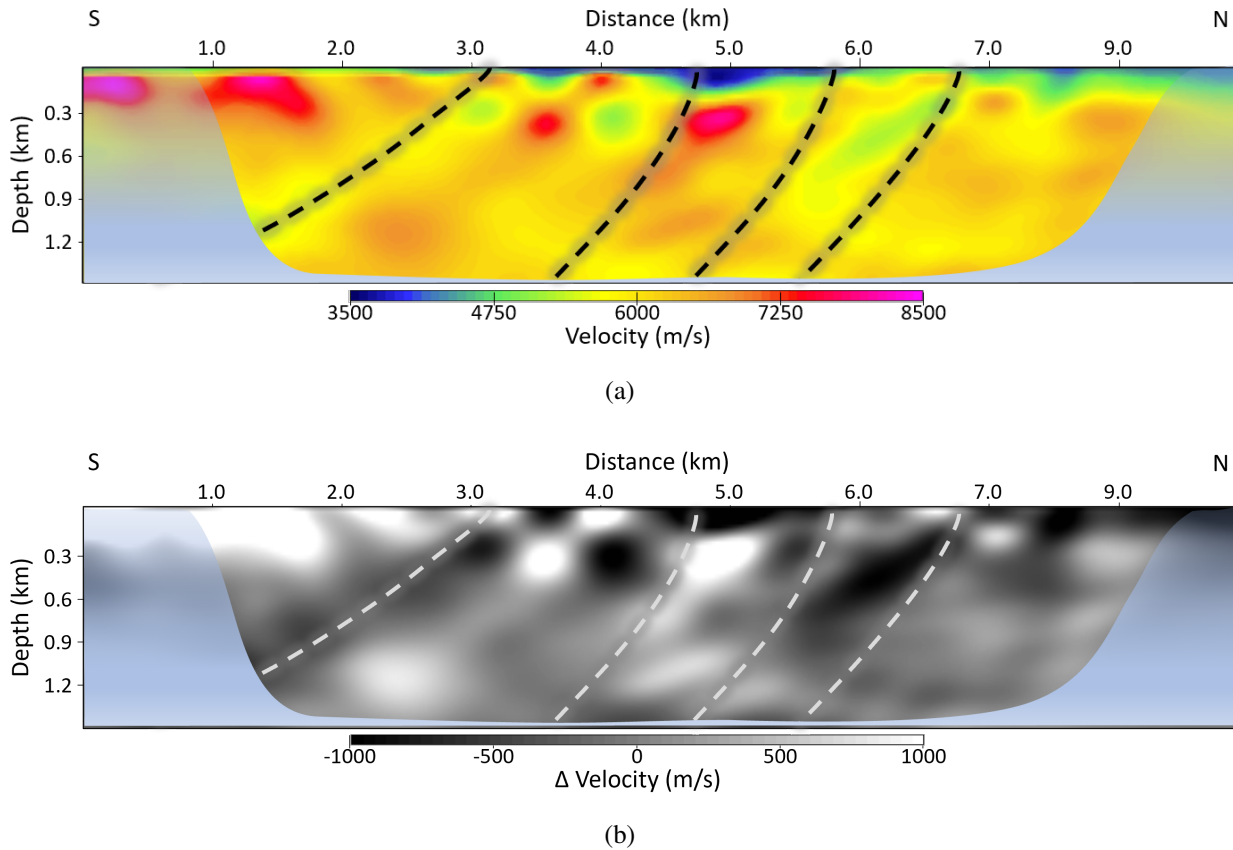


Figure 5.10: Final FWI P-wave results, showing a) the velocity model, and b) the detrended velocity model. Both models depict a structural overlay, which correlates with the known geology of the area. Grey-shaded regions indicate areas with little to no energy penetration.

### FWI appraisal

Inversion results require thorough validation, and I accomplish this by using three different approaches. First, I conduct source signature inversion by using the starting velocity model and the final FWI model, evaluating the resulting time-domain wavelets in terms of coherency and continuity. Second, I perform finite-difference forward modeling, and generate synthetic waveforms in the time domain. I evaluate these results based on their similarities with respect to observed data. Third, I assess the resolution power of the inversion strategy by conducting checkerboard tests.

Source signature inversion is an excellent tool to assess the accuracy of the velocity model because the linear method required for wavelet inversion assumes that the velocity model is known *a priori* (Pratt, 1999). Therefore, quality degradation in terms of consistency and repeatability among the wavelets will be apparent if the velocity model does not represent the actual velocity variations in the subsurface. Figure 5.11 depicts the inverted wavelets. Significant improvements in the general appearance of the wavelets inverted with the FWI model (Figure 5.11b) over those inverted using the starting velocity model (Figure 5.11a) are observed. Although there are distortions

tions in the wavelets along the south end of the profile in Figure 5.11b, the rest of the profile reveals excellent coherency among the estimated source wavelets.

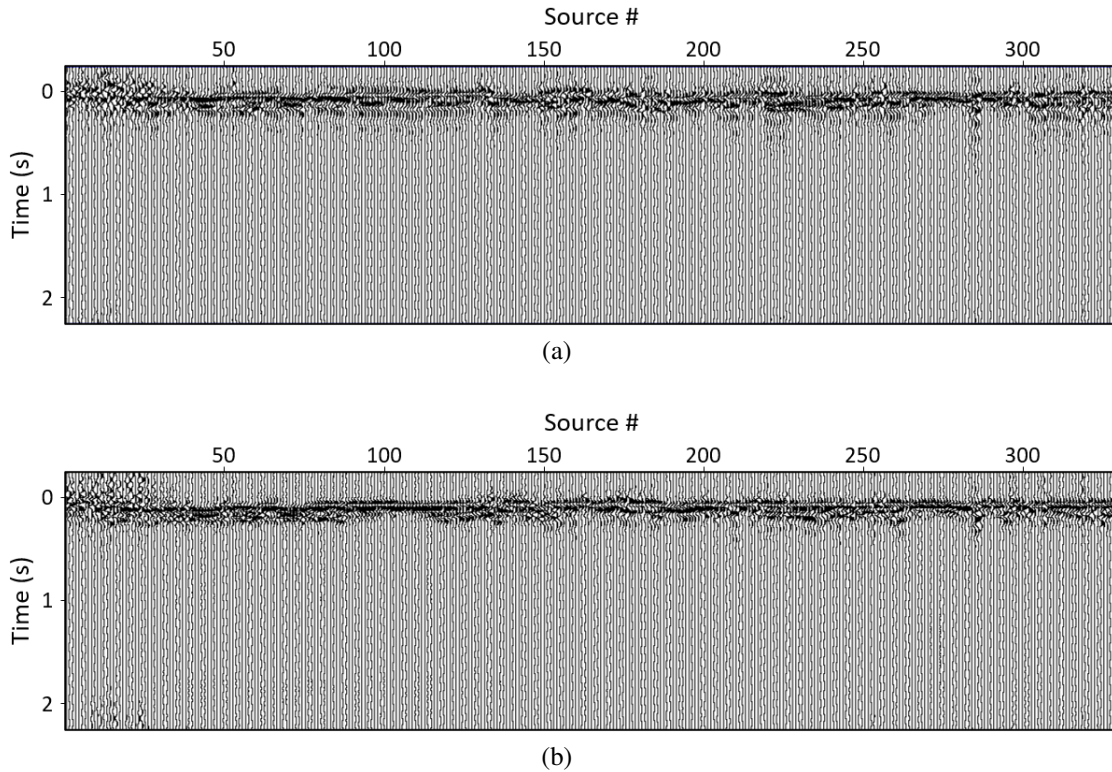


Figure 5.11: Time-domain wavelets recovered for each source. These signatures are estimated using (a) the starting FATT model, and (b) the final 2D FWI model.

Figure 5.12 depicts the time-domain results after performing frequency-domain forward modeling followed by Fourier synthesis. These results are for a shot gather located at 2 km along the profile. Figure 5.12a depicts the observed waveforms. I avoid displaying later portions of the gather because it is our intent to compare the data using the same time window used during the inversion. As depicted in Figure 5.4a and 5.4b, only surface waves and elastic modes are present below refracted arrivals. These phases are not modeled by the visco-acoustic approximation. Figure 5.12b and Figure 5.12c depict synthetic gathers generated using the starting and final FWI velocity models, respectively. Although both synthetic gathers show excellent agreement with respect to the picked refracted traveltimes, significant differences in terms of the morphology of later seismic phases are evident. Synthetic waveforms modeled with starting velocity estimates fail to reproduce the complexity of secondary arrivals observed in the field data (Figure 5.12a). In contrast, the synthetic waveforms obtained through the final FWI model (Figure 5.12c), depict a high degree of reproducibility. For instance, it can be observed that within the white rectangle, the coda of the synthetic waveforms is very similar to that of the measured waveforms.

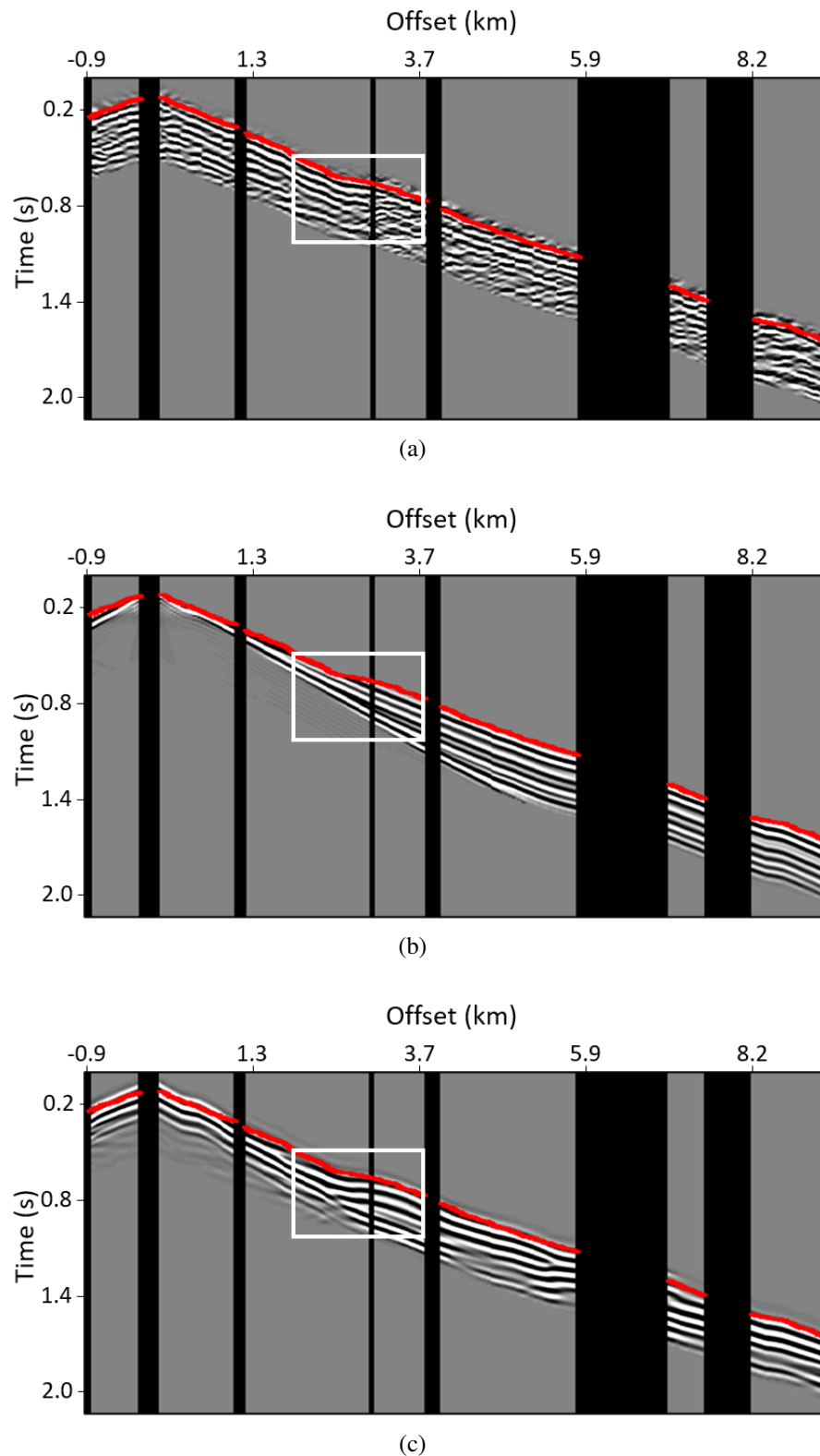


Figure 5.12: (a) observed shot gather located at 2 km along the model. Forward-modeled gather using the (b) starting velocity model, and (c) final FWI velocity model. The red line in all panels indicates the manually picked refracted arrivals. The white rectangle represent a zoomed-in area described below. Black zones highlight waveforms discarded due to low signal-to-noise ratio and/or offset errors.

To better assess the character of these later arrivals, Figure 5.13 shows a 700-ms zoomed-in area corresponding to the white rectangles in Figure 5.12. Figure 5.13a depicts the observed waveforms without any preconditioning in a wiggle display. In order to perform a direct comparison with the synthetic waveforms, I implement the same preconditioning steps used on the observed waveforms: a bandpass frequency filter (corners 0-0-28-30 Hz), and trace decimation (Figure 5.13b). Forward-modeled waveforms are shown in Figure 5.13c and 5.13d, obtained using the starting and final FWI velocity models, respectively. Figure 5.13d more closely represent the characteristics of the observed waveforms, as may be seen by using the colored lines as a visual guide. These colored lines are consistent with those used on Figure 5.13b, where the shape of early arrivals is slightly warped, whereas the shape of later arrivals is not. This is reproduced by the synthetic waveforms in Figure 5.13d.

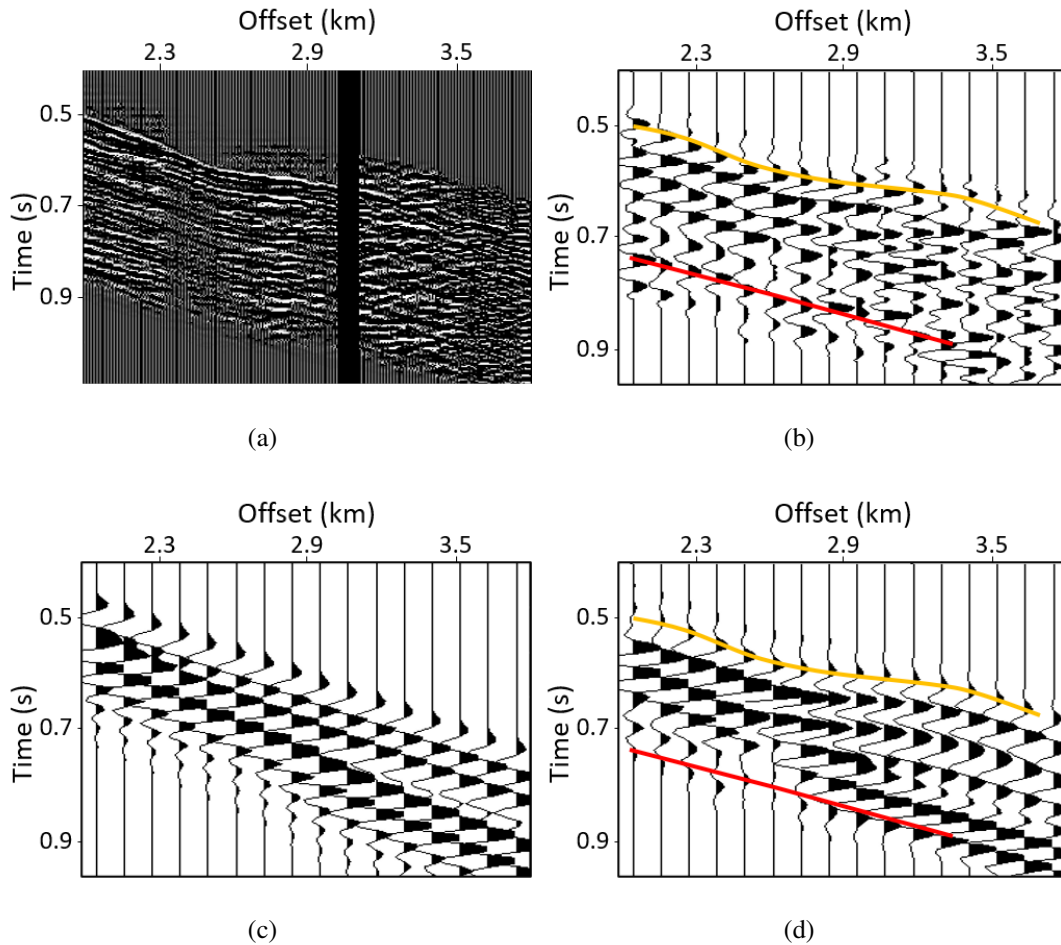


Figure 5.13: Zoom-in on the rectangles displayed in Figure 5.12 showing a) original observed waveforms with no preconditioning, b) observed waveforms after bandpass filtering, re-sampling, and trace decimation, c) synthetic waveforms from the FATT velocity model, and d) synthetic waveforms from the final FWI velocity model. Colored lines in (b) and (d) are indicative of the same seismic phases.

No elastic arrivals are observed in Figures 5.12 and 5.13, nor are they modeled by our finite difference approximation. Nonetheless, complex phases appearing just below first-arriving waveforms in the field data, are effectively reproduced by using the FWI velocity model (e.g., within the white rectangle). These phases may be related to geologically-induced scattering and/or diffraction.

I perform a resolution analysis through checkerboard tests. I design a checkerboard pattern with rectangular anomalies of dimensions 335x165 m, consistent with the half-wavelength resolution of FWI (Wu and Toksöz, 1987). These dimensions are chosen according to the upper resolution limit of FWI, consistent with the wavenumber filters explained earlier in this section. I use 10 and 20 per cent of the maximum expected wavenumber to filter  $x$ - and  $z$ -wavenumbers, respectively. This translates into  $x$ - and  $z$ -wavelengths of approximately 670 and 330 m, respectively, using a minimum propagating velocity of 3 km/s and the maximum inverted frequency. Perturbations of +/- 5 per cent are applied using the checkerboard pattern, and are then added to the starting velocity model. This perturbed velocity model is used to generate synthetic waveforms by performing finite-difference forward modeling. I then implement the same multiscale inversion strategy described in Table 5.1, using the synthetic data and the starting velocity model (without the checkerboard perturbations). Finally I subtract the original model to recover the effect of the checkerboard perturbations.

Figure 5.14 depicts the result of the checkerboard test. The results demonstrate that half-wavelength patterns are successfully recovered down as far as 1.5 km depth. Checkerboard patterns towards the north end of the profile exhibit less coherency, indicating the resolution in this region may be lower than the theoretical half-wavelength criterion.

## 5.6 Discussion

The different rock units comprising the Sudbury Structure may be identified on the velocity model in Figure 5.10. South dipping velocity contrasts spatially correlate with major geological components, such as a portion of the Whitewater Group to the south (between 0 and 3 km along the profile) and the SIC to the north (between 3 and 7 km along the profile). I display the migrated seismic section of the LN182 transect with an overlay of the final FWI velocity model in Figure 5.15. Unlike the reflectivity images from the South Range and the northwest lobe of the North Range interpreted by Wu et al. (1995); Adam et al. (2000); Milkereit et al. (2000), among others, the migrated image shown here lacks of coherent reflections. Only a handful of reflection terminations, highlighted by the blue arrows, are indicative of the structural transition among the different domains within the northeast lobe of the Sudbury Structure.

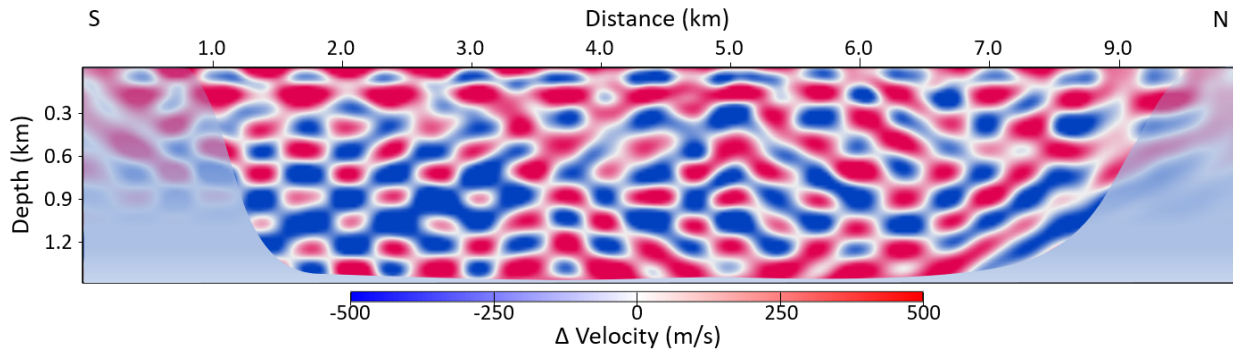


Figure 5.14: Recovery of 335x165 m checkerboard patterns, with +/- 5 per cent velocity anomalies superimposed on the starting FATT model.

The interpretation given here of the major components of the Structure would not have been possible without the FWI results. In the following I briefly discuss the geological significance of the inverted velocity model and reflectivity image based on two zones: the Whitewater Group and the SIC.

### 5.6.1 Whitewater Group

The Vermilion, Onwatin, and Chelmsford Formations, which comprise the inner portion of the Whitewater Group, are not imaged by the velocity structure recovered from the LN182 profile data. However, part of the Onaping Formation in the northeast lobe of the Sudbury Structure is illuminated by the velocity model and the reflectivity image in Figure 5.15. The northern limit of the Onaping Formation is visibly identifiable on the velocity structure in Figure 5.10, as indicated by the overlaid interpretation (dashed black lines) at 3 km along the model. The separation is highlighted by a low-velocity south-dipping structure with an apparent dip of approximately  $25^\circ$  (after properly accounting for the vertical exaggeration). High velocity contrasts are identified in the near surface within the Onaping Formation as observed in Figure 5.15 (200-300 m depth). These localized high-velocity anomalies are located towards the southern areas of the model where the checkerboard tests indicate low confidence. This suggests the actual velocities may vary from those recovered in the image (they may be lower than what it is retrieved by the inversion). This may be due to the algorithm iteratively converging towards local minima, perhaps because the influence of high-velocity localized zones in the upper portion of the Onaping Formation. Figure 5.11b, also indicates relatively low confidence in this area where source signatures exhibit distortions towards the south end of the profile.

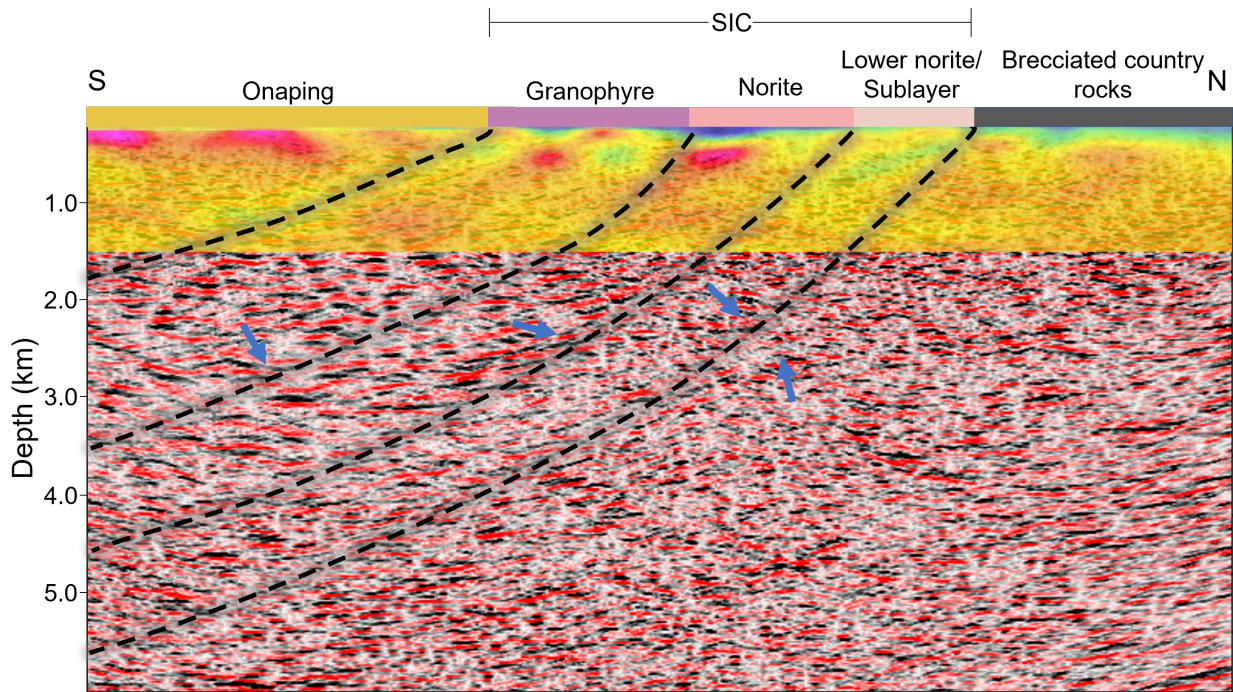


Figure 5.15: Migrated seismic section along the LN182 overlying the final FWI P-wave velocity model. Dashed black lines delineate the trace of transition zones. Blue arrows indicate potential reflection termination patterns.

Although unrealistically high, the velocities observed in Figure 5.15 around the top of the Onaping Formation, are consistent with high-velocity rock bodies. These high-velocity areas may be associated with overconsolidated fall-back breccia units. Another possible scenario for these prominent velocity contrasts in the roof of the Onaping Formation, relates to melanoritic sequences from the felsic norite unit of the SIC, which is immediately overlain by the quartz-gabbro transitional phase. Latypov et al. (2019) concluded that discrete bodies of melanorites occur throughout the entire SIC, locally developed over its roof. They found a large melanorite body (400 to 700 m thick) emplaced within the quartz-gabbro transitional zone, and another melanorite body located between overlaying Onaping Fm and underlying granophyre (i.e., along the very roof of the SIC). Latypov et al. (2019) indicated that these bodies have not been identified in over a century of research because difficulties in visually distinguishing them from the host rocks. This opens the possibility of discrete melanorite bodies located elsewhere in the Sudbury Structure, as suggested by Latypov et al. (2019). Clowes (2017) illustrated the velocity of rock units within the felsic norite are higher than those in the granophyre and Onaping successions. In addition, melanorites have a higher content of orthopyroxene (Latypov et al., 2019), which is associated with a higher P-wave velocity as indicated by White et al. (1994) (approximately 7.2 km/s). The melanorites would likely exhibit significant velocity contrasts if emplaced within a less competent or less consolidated host rock, as it might be the case on shallow areas of the Onaping Formation.

## 5.6.2 Sudbury Igneous Complex

The Sudbury Igneous Complex consists of four main units as observed in Figure 5.15, the granophyre, the quartz-gabbro transitional phase, the norite, and the Sublayer (Pye et al., 1984). The quartz-gabbro phase is a thin unit that marks a compositional break between the granophyre and the norite (Chai and Eckstrand, 1994), however it is not evident in the inverted velocity model. The velocity estimations obtained through full-waveform inversion may be compared with *in situ* borehole velocity measurements in the North Range of the Sudbury Structure. White et al. (1994), Salisbury et al. (1994), and Clowes (2017) indicated that the velocity within the granophyre unit is lower than that in the norite unit, which matches the results presented here as average velocities between 5.7 and 6.2 km/s within the granophyre, and 6.2 and 6.5 km/s within the norite are observed. Note that the high velocities observed within the norite corresponds to the upper felsic norite unit, whereas a decrease in seismic velocities is observed in the lower norite unit, near the contact with the Sublayer, as portrayed by the low velocity area around 7 km along the model in Figure 5.10a. This near-surface slab-like low-velocity zone may be interpreted as a complex transition between the lower norite/Sublayer and the footwall breccia rocks. Within the footwall breccia prominent variations in physical properties occur, as observed earlier by White et al. (1994). The low velocity area underlying the felsic norite correlates with the findings of Clowes (2017), who described this unit as having the lowest seismic velocities, despite showing an increase in bulk density. Eaton et al. (2010) indicated that the brecciated country rocks that underlay the SIC exhibit more prominent velocity and density variations. This is observed on the velocity image, where the footwall breccia displays a higher velocity trend than the overlaying norite unit. For instance, the lower norite unit and the contact Sublayer are associated with low seismic velocities ranging between 5.7 and 6.2 km/s as presented by White et al. (1994). This velocity range is portrayed by the FWI P-wave model in Figure 5.10a, between approximately 5.5 and 7 km along the profile. A higher velocity trend is observed in the inverted model below the contact Sublayer, towards the brecciated country rock, varying between 5.8 and 6.8 km/s, which correlates with values presented by White et al. (1994) for the footwall breccia (between 6.0 and 6.9 km/s).

The interpretation at depth of the SIC units is performed by carefully evaluating reflection terminations on the migrated section along the same structural path identified on the velocity image. The blue arrows in Figure 5.15 reveal reflection termination patterns indicative of a change in amplitude behavior in terms of continuity, likely representing a change in structural domain. Although a reliable structural interpretation at depth is limited due to the lack of reflected energy, I am able to infer the architecture of the SIC by combining the FWI model with previous interpretations of the North Range of the Sudbury Structure (see, for instance, Milkereit and Green (1992); Milkereit et al. (1994); Adam et al. (2000); Clowes (2017)).

The thickness of SIC layers appears to be variable on the migrated section, with the granophyre

thickening at depth. Lenauer and Riller (2017) found along-strike thickness variations of the SIC as well as thicknesses variability within individual SIC layers, mostly reporting changes in plan-view thicknesses. Variations on intra-SIC thickness were also reported by Milkereit et al. (1994), who suggested, for instance, that the combined total thickness between the Onaping Formation and the granophyre layer is approximately 2.5 km at the center of the Whitewater Group. However, the thickness estimation given here of the granophyre unit alone is of approximately 2 km, which would imply a thicker succession towards the center of the Whitewater Group. This thickness is consistent with that reported by Wu et al. (1995) through the analysis of reflection images. In addition, a thick norite unit is reported in this study, in which the combined upper and lower sections is somewhat thicker than those units reported in previous studies (e.g. Milkereit and Green, 1992). The asymmetry of the Sudbury Structure is illustrated by the considerable variation in dip angles along the entire Structure, as observed by Dreuse et al. (2010). They proposed that, in general, a systematic angular difference between upper and lower SIC contacts is distinguishable, and that the top of the SIC exhibits consistently shallower dips. In the images presented in this chapter, the structure in Figure 5.10a and 5.15 depicts the upper units of SIC having slightly shallower dips than its basal units. These differences range from approximately  $25^\circ$  (Onaping Formation/SIC) to  $35^\circ$  (SIC/brecciated country rocks). These shallow dips are typical of the North Range of the Sudbury Structure, as highlighted by Milkereit and Green (1992), in contrast with the steeper units of the South Range.

## 5.7 Conclusions

I perform visco-acoustic full-waveform inversion in the frequency domain to retrieve the velocity structure of the poorly imaged northeast lobe of the Sudbury Structure. I demonstrate that the computationally expensive two-and-half-dimensional FWI in the LN182 profile is unnecessary. This is due to the fact that the profile is only mildly crooked. The influence of out-of-plane wavenumbers in gradient updates and inversion results is not significant when less than 4 per cent of the data are non-compliant with our offset error threshold criteria in a 10-km-long seismic transect.

The final FWI model along the LN182 seismic transect is a high-quality quantitative representation of the structural architecture of the northeast lobe. This velocity model describes the position and extension at depth of prominent structural features associated with the Sudbury high-energy-impact Structure, such as the Onaping formation, the granophyre/norite units, and the brecciated footwall rocks. The combination of full-waveform inversion and reflection imaging allows us to describe key structural characteristics of the main SIC layers in the northeast lobe, including its variable layer thicknesses and dips. Results are in good agreement with known geology and borehole measurements.

# Chapter 6

## General conclusions

### 6.1 Seismic imaging of hard rock environments

Throughout this project, I presented the implementation of seismic imaging methods to data surveyed over crystalline terrains of Archean age in the Superior Province in Canada. In Chapters 2 to 4, I presented results from a 2D dataset located in the Larder Lake mining district in the Abitibi greenstone belt, whereas Chapter 5 presents results from a 2D dataset located in the northeast lobe of the Sudbury Structure, towards the southern limits of the Superior Province. The Larder Lake seismic transect is a highly crooked dataset with a length of approximately 45 km, and the Sudbury seismic transect is a mildly crooked dataset with a length of approximately 15 km. Using these surveys, I explored the feasibility of performing visco-acoustic two- and two-and-half - dimensional full-waveform inversion in the frequency domain, with the purpose of retrieving high-confidence velocity structures of the near surface. I also implemented advanced seismic reflection processing strategies to enhance the imaging at depth of prominent structures, associated with mineralization pathways. I unraveled the shallow structural architecture of these important mining zones, and their continuation at depth by combining the results from 2D and 2.5D FWI, with those from seismic migration. The joint analysis of shallow and deep structural domains resulted in robust interpretations of the areas under study.

#### 6.1.1 Low-frequency components of explosive sources

In Chapters 2 and 3, I used sparsely distributed explosive sources in conjunction with densely distributed vibroseis sources, primarily because of the very low frequencies available in the explosive sources. One of the main challenges of FWI is its inherent nonlinearity, which increases when inverting for higher frequencies and/or late arriving seismic phases. In these chapters, I addressed the nonlinearity of the inversion by using very low frequencies from explosive sources, before intro-

ducing the higher frequencies of vibroseis sources. The experiment demonstrated that frequencies as low as 4 Hz can be utilized to update the low-wavenumber features of the gradient image. This resulted in early-stage long-wavelength velocity updates that mitigated the risk of cycle skipping during the later stages of the inversion.

I assessed the FWI results, with and without the contribution of the low frequencies in explosive sources, based on a comparative analysis of the inverted velocity structures, and inverted source signatures. Although only a few explosive sources were used, structural improvements were identified in the P-wave velocity model that combined both explosive and vibroseis sources. The experiment illustrated that the incorporation of low-frequency components is important to update the smoothest elements of the velocity structure, avoiding convergence to local minima. The velocity model inverted using only vibroseis sources, with a starting frequency of 7 Hz instead of 4 Hz, exhibited velocity irregularities in the expected structural trend. These irregularities are associated with convergence to local minima, and their influence continued to harm the inversion at later stages. The availability of low frequency content in the observed explosive data proved beneficial for the quality of the final inverted model. This availability also relaxes the constraints on the starting velocity model by allowing the dominant period in the data to be larger, which implies the half-cycle criterion (to avoid cycle skipping) is more easily met. This relaxation may be important in crystalline environments where the computation of velocity models is prone to be affected by strong shallow velocity variations.

### **6.1.2 Dynamic variations in the observed wavefield**

In Chapters 2, 3, and 5, I minimized two different data residuals, namely “logarithmic phase-only” and “conventional phase-amplitude” data residuals. During gradient optimization, the hierarchical implementation of these objective functions improved both inversion stability and convergence rate. When implemented in hard rock environments, the conventional phase-amplitude data residuals are inherently large due to complex energy scattering, which causes strong amplitude variations within the observed waveforms. These dynamic variations significantly influence the performance of the inversion at early stages. This phenomenon persists even after applying proper preconditioning steps to the dataset, such as surface-consistent amplitude corrections, and observed-to-synthetic amplitude scaling. Due to the sensitivity of FWI to large data residuals, I start the inversion process by minimizing only the kinematics of the observed wavefields.

Fitting the phase components of seismograms effectively reduced the difficulty caused by large data residuals associated with the amplitude difference between modeled and observed data. Logarithmic phase-only residuals are associated with data fitting based on the time positioning of the events, which neglects any influence from amplitude components. This results in a more sta-

ble inversion, in which the starting velocity model guarantees that, at least, the initial kinematics are correct. Therefore, the algorithm matches correct phases between the modeled and observed waveforms, iteratively updating the underlying velocity model. Once this model more closely represents “true” velocity variations, synthetic data are more accurately reproduced, and large amplitude residuals are alleviated. I used conventional residuals during late inversion stages, when the dynamic components of observed waveforms were better represented by our synthetic approximations.

### 6.1.3 Progressive strategy on offsets and later seismic phases

In Chapters 2, 3, and 5, I applied a multiscale layer-stripping FWI strategy based on the progressive inclusion of the increasingly nonlinear portions of the wavefield. It is well-known that conventional seismic imaging is poorly sensitive to intermediate- and long- wavelength features, due to short-offset geometries, and limited frequency bandwidth. In contrast, these features are key for FWI to succeed, and they can be updated within the target model by progressively increasing offsets and including later arrivals. Because FWI is particularly non-linear if the number of propagating wavelengths in the data are large. FWI is thus increasingly nonlinear as the late arrivals are included. We therefore limit large offsets and secondary seismic phases during the early stages. Relaxing these constrains, allows for short-wavelength structural features to be progressively reconstructed without driving the inversion to erroneous solutions.

I applied relatively strong constraints on the offset continuation strategy, and on the time-domain damping schedule, in order to avoid convergence to local minima. The strategy was vital in Larder Lake and Sudbury because of their complex geology, which includes steeply dipping interfaces and fault-bend folds, that contain smaller nonlinear wavelength characteristics. In Chapter 2, I presented a synthetic experiment which demonstrated that this multiscale strategy is successful in retrieving the small  $x$ -horizontal and  $z$ -vertical wavenumbers of a south-dipping structure. This result validated the inversion strategy that I then applied in Chapter 3 on the long-offset Larder Lake dataset, and in the following chapter. For instance, in Chapter 5, I illustrated the benefits of this inversion approach by circling back to lower frequencies, and updating the model with a second- and third- pass inversion schedule, in which I relaxed the time damping in the Laplace-Fourier domain. This second- and third- pass inversion schedule resulted in the introduction of finer structural features. The layer-stripping approach implemented in these chapters effectively yielded short-wavelength structural details, and indicated a natural transition between low- and high- wavenumber components of the wavefields.

#### 6.1.4 2D v. 2.5D full-waveform inversion

I implemented both 2D and 2.5D FWI in Chapters 3, and 5. Although the seismic surveys I used in this project were both two dimensional, they have a certain crookedness associated with them. The modeling and inversion of 2D seismic data assumes a line-source geometry, in which 3D wave propagation effects such as spherical spreading are not accounted for. This may lead to wrong solutions as the media are inherently embedded within a heterogeneous 3D space. In some cases, depending on the profile crookedness and local geology, the line-source assumption may be adequate. For instance, when the structure in which waves propagate is heterogeneous in only two directions in 3D space, and the source geometry is constant perpendicular to the strike of the structure. Under this scenario, two-dimensional modeling is adequate due to the symmetry of wave propagation generated by the source geometry and the predominant direction of geological structures. However, even when the seismic profile is predominantly perpendicular to the structure, but severely crooked, the line-source assumption fails, and 3D wave propagation effects are more significant. In these cases, two-dimensional forward solvers are an oversimplification, and should be avoided. This is not only because of the limitations of the numerical solver itself, but also because of the consequences these limitations have on the data. For example, when 2D modeling is implemented on crooked seismic profiles, a significant number of data traces must be removed in order to preclude the introduction of traveltimes errors. These errors stem from the projection of source and receiver stations onto a 2D plane, which might cause significant differences between original and projected source-receiver distances.

The 2.5D modeling approach represents a compromise between oversimplified 2D solutions, and computationally limiting 3D solutions for the data considered in this thesis. I demonstrated this using a 2.5D scheme by abandoning the line-source assumption, and simulating point sources in 3D space, is necessary to retrieve accurate velocity models when surveys suffer from a high degree of crookedness. In Chapter 3, I implemented 2D and 2.5D FWI to the severely crooked Larder Lake seismic profile. I identified significant differences between the resulting 2D and 2.5D P-wave velocity model, especially in terms of near-surface high-wavenumber information, which was only reconstructed by the 2.5D model. In contrast, the execution of 2.5D FWI proved not to be necessary for the mildly crooked Sudbury seismic transect in Chapter 5. I presented 2D and 2.5D time-domain forward modeled waveforms that were virtually identical. Velocity differences between the inverted 2D and 2.5D FWI P-wave models in Chapter 5 were also negligible, with an average of approximately 16 m/s. This represents a difference of less than a 0.3 per cent velocity variation in the area. Based on the results from Chapters 3 and 5, I concluded that two-and-half-dimensional FWI is required for these data only when the crookedness of the seismic survey is significant. Otherwise, the computationally efficient two-dimensional approach is recommended.

### 6.1.5 Advanced seismic reflection processing

In Chapter 4, an advanced seismic reflection processing method was applied to the Larder Lake dataset in order to improve the imaging at depth of the reflectivity section. I presented an effective methodology to mitigate the effect of out-of-plane energy components captured by the severely crooked profile. Likewise, I introduced an enhanced migration velocity model, which combines the high-quality FWI P-wave velocity structure derived in Chapter 3, with conventional velocity analysis.

The crookedness of the Larder Lake survey generates severe scattering of CMP locations, resulting in a swath of data distribution covering an area of over 4 km wide around the transect. This, coupled with the complex geological configuration of the area, causes the signal from out-of-plane structures (with a dip direction oblique to the processing line) to interfere with the signal from in-line structures. CMP gathers containing a mixture of these seismic phases in the Larder Lake area displayed significant signal ill-alignment, which resulted in amplitude smearing, and reduced the quality of stacked images. I mitigated the influence of cross-dip components by implementing azimuthal binning in Chapter 4. I used information from surface geology, and the interpreted geology at depth, to devise a locally optimum binning strategy, in accordance with the predominant geological strike of the area. The method generates pseudo-processing lines that are locally parallel to the direction of maximum inclination, which enhances the imaging of steeply dipping structures, and reduces the effect of cross-profile structural components. This is because CMP bins collect traces reflected from the same structure, improving energy focusing within these optimum bin gathers. Hyperbolic corrections are then more effective in aligning the reflected signals, which ultimately are stacked in phase. I demonstrated that ignoring out-of-plane energy has a pronounced harmful effect on the final migrated image, especially on the imaging of structures at depth. This binning strategy worked remarkably well in the challenging Larder Lake area, where rapidly changing dip directions and lateral changing profile directions, occur. The interpretability of the seismic section increases when the optimum binning method is implemented.

In Chapter 4, I also evaluated the performance of different migration velocity fields. I used conventional velocity analysis by carefully selecting velocity functions from semblance analysis on CMP gathers, in order to derive a velocity model for migration. I complemented the resulting conventional velocity field, with the near-surface velocity estimations from the nonlinear travel-time tomography model, and the full-waveform inversion model, both obtained in Chapter 3. This experiment illustrated that well-controlled near-surface velocity variations have an impact on the migration of structures at depth. The combined use of the conventional and FWI velocity model, yielded more coherent and continuous reflections. In crystalline environments in Larder Lake, near-surface layers present significant velocity variations, which stem from the complex relationship between metasedimentary materials, and shallow volcanic units. I found it vital to incorporate

well-constrained shallow velocity variations into the migration velocity field, in order to account for the heterogeneity of the near-surface in these hard rock terrains.

### **6.1.6 Geological significance of seismic imaging**

Archean cratons have been intensively reworked throughout their history. The mainly granite-greenstone rocks of the Archean crust of the Superior Province provide evidence of this, and significant metamorphism processes have shaped its current architecture. In this thesis, I have tried to delineate and untangle the main structural domains of two mining areas within the Superior Province, Larder Lake and Sudbury, through the use of seismic imaging methods. I uncovered several key structural features in the near surface, and at depth, within these two mining districts. One of the most important outcomes of seismic imaging, as implemented in this thesis, is that I introduced the missing link between the structural development at depth, and the shallow structural configuration (with depths less than 3 km) of prominent mineralization conduits. I combined quantitative seismic images from FWI with reflectivity images from reflection processing in order to illuminate and better interpret shallow and deep portions of the subsurface, respectively. This is a significant outcome as the imaging of crystalline environments in the Superior Province has usually been constrained using regional seismic sections, with little to no information on the near surface.

In Chapter 2 through 4, I described the geological significance of both the inverted P-wave velocity structure, and the migrated seismic section in the Larder Lake area. The approximate size of the FWI velocity model is 45x2.5 km, and the maximum depth of the migrated section is approximately 18 km. I demonstrated that structural interpretations above 3 km are only possible through the analysis of the FWI P-wave model. This is because the migrated section lacked coherent reflections in the near surface. I presented new structural information by separating the area into two domains: south and north of the LLCZ. The long-standing debate regarding the architecture of the LNSZ, which is located south of the LLCZ, is further elucidated by my results. I illustrated that the LNSZ is predominantly a north-dipping structure, which dips steeply in the very near surface (with depths less than 500 m), and exhibits a shallower dip at deeper zones. Due to the high degree of obliqueness of the Larder Lake transect with respect to local geology, the observed structural dip is in reality an apparent dip, meaning the true inclination of the structure is likely steeper. I interpreted the extension at depth of this structural break to be approximately 8 km, based on the combined analysis of the velocity field and the migrated section. Several reflection terminations patterns around the LNSZ indicated its presence at depth. Nevertheless, although not interpreted in the seismic section, a structural-genetic relationship between the LLCZ and the LNSZ may exist, meaning the LNSZ extends further at depth, and may be of economic importance

due to its similarities with the world-class gold-bearing LLCZ. These similarities are based on the presence of mafic to felsic intrusions within the LNSZ, analogous to mineralized structures in the LLCZ. The northern margin of the LLCZ is well imaged by the velocity structure, and by reflection terminations at depth in the reflectivity section. The LLCZ represents the main structural break in the Larder Lake area, and prominent reflections at depth delineate its trace. However, the truncation of important reflection packages between the LLCZ and the MLF to the north, are difficult to interpret with the migrated image alone. I demonstrated that this truncation is related to surface-reaching structures, identified in the FWI velocity model, and termed in this thesis “SP” - a splay fault system associated with the MLF. This splay fault system correlates with mapped surface geology of ultramafic intrusions. The connection between the sudden disappearance of reflections at depth as observed in the migrated section, with seismically-transparent ultramafic structures, would not have been possible without the near-surface FWI velocity structure.

In Chapter 5, I imaged the architecture of internal SIC layers to a depth of approximately 1.5 km. The velocity model retrieved in the northeast lobe of the Sudbury Structure revealed important structural characteristics of the units conforming the SIC, including the granophyre, the norite, and the Sublayer. I confirmed that the overall inclination of these rock units is shallower, compared to the South Range of the Sudbury Structure. Internal thickness and dip variations were also identified, which closely correlated with previous studies in the North Range of the Structure. The inverted P-wave velocity structure agrees with borehole velocity measurements, confirming the validity of velocity estimations throughout the model. However, the migrated seismic section corresponding to our survey, lacked of reflected phases, and where they were reflections available, they were relatively short. For this reason, the structural interpretation at depth in the northeast lobe of the Sudbury Structure was somewhat ambiguous, and had to rely on previous interpretations on the northwest area of the Structure (Milkereit and Green 1992; Milkereit et al. 1994; Wu et al. 1995; among others). In Chapters 2 to 5, the general architecture character of the identified geological structures are best observed by assessing the velocity model in the near surface. This is mainly because reflectivity images lacked continuous and coherent reflective phases, which not uncommon in crystalline settings.

## 6.2 Future considerations

Throughout the realization of this project, I identified some areas in which future practical improvements could be achieved. These include

- Simultaneous inversion of explosive and vibroseis sources by using separate source wavelets.
- Traveltime correction of projected 2D geometries in crooked surveys in order to avoid the

rejection of data traces.

- Combination of azimuthal binning and cross-profile dip analysis for enhanced imaging.

In Chapters 2 and 3, I used explosive and vibroseis sources to update the underlying velocity model with the lowest available frequency. This allowed the inversion process to be more stable, mitigating divergence. The inversion of explosive and vibroseis sources was not carried out simultaneously, however. I first used the explosive sources, and then abandoned them to continue the inversion with the vibroseis sources alone. Although this strategy performed well in updating the long-wavelength characteristics of the velocity background, it precluded later inversion stages to benefit from the frequency content of explosive sources, because they were no longer used. The main reason for not using both types of sources simultaneously, was because I did not estimate individual and separate source signatures. Simultaneously inverting with these two types of sources, implies I must invert for suitable source wavelets after each inversion stage, which is a non-trivial process and their manipulation may introduce further complexity into the reconstruction. However, calculating separate source wavelets and simultaneously inverting with them, may provide better inversion results and should be further investigated. This is because low frequencies contained in explosive sources will continue to update the model, potentially resulting in a more natural transition to higher frequencies.

Waveforms were discarded in Chapters 2, 3, and 5 due to offset errors arising from the projection onto a 2D plane of sources and receivers of crooked profiles. These offset errors may introduced anomalous traveltimes, potentially degrading inversion results, as highlighted by Kamei et al. (2015). Nonetheless, alternatives to completely disregarding seismic traces should be further evaluated, so that potentially all data could be used in the inversion. For instance, Zelt (1999) fitted a straight line to source and receiver positions, and projected the sources perpendicularly onto the straight line. He then projected the receiver stations onto the straight line, while preserving their original source-receiver offset, and further applying static time corrections to account for topographic changes at the original position of receivers. Smithyman and Clowes (2012), performed FWI on a 2D projected geometry. Their projection was complemented by corrections derived from traveltimes residuals between projected and actual source and receiver coordinates. Kashubin et al. (2009); Zhang and Juhlin (2013), separately projected sources and receivers in a methodology somewhat similar to that used by Zelt (1999). They placed sources on a straight line by means of orthogonal projection, and then receivers were positioned on the straight line preserving their original source-receiver offsets. In all these cases, authors did not have to reject data traces, performing waveform inversion using the full dataset. These all provide alternatives to the strategy I applied in this thesis. These strategies may be necessary for extremely crooked profiles, where the rejection of waveforms is severe.

In Chapter 4, I performed azimuthal binning, ultimately improving energy focusing and mitigating the signal ill-alignment of reflected phases. However, remnant static artifacts may be further corrected by jointly performing azimuthal binning and cross-dip analysis. Several cross-dip correction methods have been established, such as the pseudo-3D technique introduced by Du Bois et al. (1990), who concluded that the harming effects of lateral dips were corrected, yielding an optimum stacked section. Kim et al. (1992) reprocessed Lithoprobe reflection data and implemented “dynamic cross-dip corrections”, improving the imaging of near-surface, shallowly dipping reflectors in the Kapuskasing zone. Nedimović and West (2003), introduced the cross-dip-moveout (CDMO) correction in order to complement standard moveout corrections, such as NMO and DMO. A combination of azimuthal binning and cross-dip analysis was presented by Lundberg and Juhlin (2011). They extracted geological strike and dip information from a crooked seismic transect acquired over the Ullared Deformation Zone in Sweden. The combination of optimum binning and cross-profile dip corrections may proved important in regions where large azimuthal distribution and variable inclination degrees of geological bodies occur.

### 6.2.1 FWI developments on the horizon

The full-waveform inversion approach implemented in this thesis using data from two different mining districts (Larder Lake and Sudbury) can possibly be improved for future imaging campaigns in crystalline terrains. The main areas for improvements are associated with the the acquisition (i.e., the seismic experiment set up), and algorithm development (i.e., the FWI engine). On the acquisition side, wide-angle data and low frequencies have traditionally been two of the most important characteristics of the seismic experiment for FWI. I demonstrated in this thesis that the use of explosive sources (particularly in the Larder Lake area) provides both very low frequencies and excellent signal-to-noise ratio at long offsets. These source attributes help in solving cycle skipping problems, since the data fitting process is first performed using the long-wavelength features of the wavefield, thereby reducing the risk of fitting wrong phases. The long-wavelength information available in explosive sources also helps reconstructing the low-wavenumber components of the velocity background, improving the kinematic accuracy of the model. Using explosive sources, with a much improved spatial separation within the limits of the Nyquist criterion, would therefore be beneficial for FWI in areas such as Larder Lake. An example of adapting acquisition systems to FWI requirements is the development of Wolfspär, a 2015 BP-designed- and built-ultra-low-frequency marine-seismic source (Dellinger et al., 2016). Their motivation was based on recording frequencies capable of penetrating complex overburden structures, improving their imaging, and to enhance the generation of starting velocity models so as to deal with cycle skips. Dellinger et al. (2016) recorded frequencies as low as 1.6 Hz over a field tests in the Gulf of Mexico

with high signal-to-noise ratio of up to 30 km in offsets.

Another important aspect of the acquisition geometry are 2D vs 3D seismic experiments. In this study, the seismic experiment is based on 2D crooked line reflection profiles. At Larder Lake, this allowed me to take advantage of the swath distribution area covered by the severely crooked geometry to perform 2.5D FWI. However, would 3D FWI based on a 3D seismic experiment have added significant information? Considering the benefit/cost ratio associated with a three-dimensional acquisition, I would not think so. This is especially true when in complex geological environments, such as Sudbury and Larder Lake, the geology is predominantly controlled by major structural trends. For instance, in the southern Abitibi subprovince, lithological sequences are dominated by east-trending structural features such as the LLCZ and the Destor-Porcupine deformation zone (Corfu, 1993; Montsion et al., 2021). In such areas, 3D acquisition campaigns are unlikely to add the value that justifies the acquisition costs. Instead, 2D geometries perpendicular to the geological strike might suffice, provided the subsurface is evenly illuminated and spatially sampled by the seismic experiment. The same conclusion applies when using severely crooked profiles, as demonstrated in this work. Boddupalli et al. (2021) implemented 2D, 2.5D, and 3D FWI to a wide-angle seismic dataset from the Deep Galicia Margin west of Iberia. Although they found that 3D FWI outperforms the 2D FWI results, the 2.5D and 3D FWI velocity models do not exhibit significant differences (see Figure 9 in their article). In addition, Boddupalli et al. (2021) illustrated that average velocities with distance for each of the FWI models resulted in significant correlation only between the 2.5D and 3D FWI models. They also showed that during the recovery of checkerboard patterns, the 2.5D and 3D FWI performed better than the 2D FWI reconstruction. This suggests that 2.5D FWI, as implemented here, may provide a low-cost and economically viable solution. I would go as far as suggesting 2D FWI would still be a plausible solution if straight-line geometries and low-frequency data are available, coupled with comprehensive data preprocessing. Kalinicheva et al. (2017) proposed the use of 2D FWI over that of 3D FWI to optimize imaging-based exploration and experiments for optimum FWI parameter selection. Of course, if turnaround times and budget are not to be considered, 3D FWI is a better option than simplifying the problem with 2D or 2.5D approximations (Bentham et al., 2018; Teodor et al., 2021; Kamath et al., 2021).

On the algorithm development side, an isotropic-based acoustic algorithm was implemented in this study. Nonetheless, accounting for anisotropy may prove beneficial in future work, especially if dealing with steeply dipping structures. Extensions of FWI to anisotropic media have been accomplished in an acoustic framework to reduce potential artifacts on the inverted model parameters (such as overestimation or underestimation of velocities) (Gholami et al., 2011; Ramos-Martinez et al., 2017; Masmoudi and Alkhalifah, 2018; Le, 2020; Shin et al., 2021). These extensions have a challenge in common: the definition of the parameter classes to be considered in the inversion (Virieux and Operto, 2009; Plessix and Cao, 2011). Gholami et al. (2011) demonstrated

that both monoparameter anisotropic FWI (e.g., reconstruction of the NMO velocity in a vertical transversely isotropic - VTI - media) and multiparameter anisotropic FWI (e.g., simultaneous reconstruction of the vertical and horizontal velocities), can be successfully implemented by properly parameterizing the subsurface model, constrained by the acquisition geometry. For instance, they showed that by constraining the inversion with one wave velocity (either the vertical, the horizontal, or the NMO velocity), and with smooth background models of the Thomsen's parameters  $\delta$  and  $\varepsilon$ , one can quantitatively image either of the aforementioned velocities. Alkhalifah and Plessix (2014) arrived to a similar conclusion of that in the work of Gholami et al. (2011), anisotropic FWI is viable if the problem is properly parameterized. Masmoudi and Alkhalifah (2018) illustrated that a successful multistage inversion strategy can be implemented by updating higher symmetry anisotropy parameters first, and then lower symmetry anisotropy parameters, in a hierarchical approach (starting by optimizing the isotropic, then the VTI, and then the orthorhombic parameters).

The full-waveform inversion approach taken in this study involved the use of a visco-acoustic mathematical approximation in the frequency domain as a forward modeling engine (viscous effects are passively accounted for by using a constant attenuation model). This approach, although suitable for the problem at hand due to judicious data pre-processing and preconditioning methods applied during inversion, may be improved. More realistic forward modeling approaches are required to take advantage of the full set of seismic phases available in the seismic experiment, and to effectively invert for elastic parameter classes such as density, S-wave velocity, and anisotropy. Using the full anisotropic solution to the elastic wave equation is perhaps still prohibitive in industrial settings due to computational burden and turnaround times (Brittan and Jones, 2019). However, elastic modeling better approximates the dynamics of seismic wavefields and, hence, should become part of the standard FWI workflow as subsurface media is more appropriately described by elasticity theory. Successful attempts at elastic modeling and inversion have already been implemented (Yuan et al., 2015; Kamath and Tsvankin, 2016; Trinh et al., 2017b; Teodor et al., 2021).

# Bibliography

- Adam, E., Perron, G., Milkereit, B., Wu, J., Calvert, A. J., Salisbury, M., Verpaelst, P., and Dion, D.-J. (2000). A review of high-resolution seismic profiling across the Sudbury, Selbaie, Noranda, and Matagami mining camps. *Canadian Journal of Earth Sciences*, 37(2-3):503–516.
- Adamczyk, A., Malinowski, M., and Górszczyk, A. (2015). Full-waveform inversion of conventional Vibroseis data recorded along a regional profile from southeast Poland. *Geophysical Journal International*, 203(1):351–365.
- Adamczyk, A., Malinowski, M., and Malehmir, A. (2014). High resolution near surface velocity model building using full waveform inversion a case study from southwest Sweden. *Geophysical Journal International*, 197(3):1693–1704.
- Ahmadi, O., Juhlin, C., Proceida, K. G. E., and 2014, U. (2014). New Insights from Seismic Imaging over the Youanmi Terrane, Yilgarn Craton, Western Australia. *Elsevier*, 59:113–119.
- Aki, K. and Richards, P. (1980). *Quantitative Seismology: Theory and Methods*.
- Aki, K. and Richards, P. (2002). *Quantitative seismology*. University Science Books, 2nd edition.
- Alkhalifah, T. and Plessix, R.-É. (2014). A recipe for practical full-waveform inversion in anisotropic media: An analytical parameter resolution study. <http://dx.doi.org/10.1190/geo2013-0366.1>, 79(3):R91–R101.
- Ames, D. and Farrow, C. (2007). Metallogeny of the Sudbury Mining Camp, Ontario. *Geological Association of Canada, Mineral Deposits Division*, 5:329–350.
- Ames, D. E., Davidson, A., and Wodicka, N. (2008). Geology of the giant Sudbury polymetallic mining camp, Ontario, Canada. *Economic Geology*, 103(5):1057–1077.
- Ames, D. E., Farrow, C. E. G., and Goodfellow, W. D. (2007). Metallogeny of the Sudbury mining camp, Ontario. Mineral deposits of Canada: A synthesis of major deposit-types, district metallogeny, the evolution of geological provinces, and exploration methods. *Geological Association of Canada, Mineral Deposits Division*, 5:329–350.

## BIBLIOGRAPHY

- Angus, D. A., Thomson, C. J., and Pratt, R. G. (2004). A one way wave equation for modelling variations in seismic waveforms due to elastic anisotropy. *Geophysical Journal International*, 156(3):595–614.
- Aster, R. C., Borchers, B., and Thurber, C. H. (2004). *Parameter estimation and inverse problems*.
- Ayer, J. A., Thurston, P., Bateman, R., Dubé, B., Gibson, H., Hamilton, M., Hathway, B., Hocker, S., Houlié, M., Hudak, G., Ispolatov, V., Lafrance, B., Lesher, C., Péloquin, A., Piercey, S., Reed, L., Thompson, P., and MacDonald, P. (2005). Overview of Results from the Greenstone Architecture Project: Discover Abitibi Initiative. Technical report, Ontario Geological Survey, Open File Report 6154.
- Beckel, R. A. and Juhlin, C. (2019). The cross-dip correction as a tool to improve imaging of crooked-line seismic data: A case study from the post-glacial Burträsk fault, Sweden. In *Solid Earth*, volume 10, pages 581–598. Copernicus GmbH.
- Bednar, J. B., Shin, C., and Pyun, S. (2007). Comparison of waveform inversion, part 2: Phase approach. *Geophysical Prospecting*, 55(4):465–475.
- Bentham, H., Morgan, J., and Angus, D. (2018). Investigating the use of 3-D full-waveform inversion to characterize the host rock at a geological disposal site. *Geophysical Journal International*, 215(3):2035–2046.
- Berenger, J. P. (1994). A perfectly matched layer for the absorption of electromagnetic waves. *Journal of Computational Physics*, 114:185–200.
- Bergslid, T. S., Raknes, E. B., and Arntsen, B. (2015). The influence of anisotropy on elastic full-waveform inversion. *SEG Technical Program Expanded Abstracts*, 34:1425–1429.
- Bevis, J. (1757). The History and Philosophy of Earthquakes, from the Remotest to the Present Times: Collected from the Best Writers on the Subject. With a Particular Account of the Phænomena of the Great One of November the 1st, 1755, in Various Parts of the Globe. *Royal Academy of Berlin*, page 351.
- Bigot, L. and Jébrak, M. (2015). Gold mineralization at the syenite-hosted Beattie gold deposit, Duparquet, Neoproterozoic Abitibi belt, Canada. *Economic Geology*, 110(2):315–335.
- Bleeker, W. (2015). Synorogenic gold mineralization in granite-greenstone terranes: the deep connection between extension, major faults, synorogenic clastic basins, magmatism, thrust inversion, and long-term preservation. *Targeted Geoscience Initiative*, 4:25–47.

## BIBLIOGRAPHY

- Bleibinhaus, F. and Rondenay, S. (2009). Effects of surface scattering in full-waveform inversion. *Geophysics*, 74(6).
- Boddupalli, B., Minshull, T. A., Morgan, J., Bayrakci, G., and Klaeschen, D. (2021). Comparison of 2-D and 3-D full waveform inversion imaging using wide-angle seismic data from the Deep Galicia Margin. *Geophysical Journal International*, 227(1):228–256.
- Bohlen, T. (2003). Elastic Seismic-Wave Scattering from Massive Sulfide Orebodies: On the Role of Composition and Shape. In *Book on Hardrock Seismic Exploration, SEG Developments in Geophysics series, No. 10*.
- Borisov, D., Gao, F., Williamson, P., and Tromp, J. (2020). Application of 2D full-waveform inversion on exploration land data. *Geophysics*, 85(2):R75–R86.
- Brace, B. and Sherlock, R. (2017). Preliminary Results from Detailed Geological Mapping of Syenite-Associated Gold Mineralization Along the Lincoln-Nipissing Fault, Larder Lake, Ontario. Technical report, Ontario Geological Survey, Open File Report 6333, p.36-1 to 36-6.
- Brace, S., Kontak, D. J., Rubingh, K. E., and Jugo, P. (2018). Geological mapping of Timiskaming-age intrusions along the Lincoln-Nipissing shear zone, Larder Lake, Ontario. Technical report, Ontario Geological Survey.
- Brenders, A. J. and Pratt, R. G. (2007a). Efficient waveform tomography for lithospheric imaging: Implications for realistic, two-dimensional acquisition geometries and low-frequency data. *Geophysical Journal International*, 168(1):152–170.
- Brenders, A. J. and Pratt, R. G. (2007b). Full waveform tomography for lithospheric imaging: results from a blind test in a realistic crustal model. *Geophysical Journal International*, 168(1):133–151.
- Brittan, J. and Jones, I. (2019). FWI evolution-From a monolith to a toolkit. *The Leading Edge*, 38(3):179–184.
- Brocher, T. M. (2005). Empirical relations between elastic wavespeeds and density in the Earth's crust. *Bulletin of the Seismological Society of America*, 95(6):2081–2092.
- Brocoum, S. J. and Dalziel, I. W. D. (1974). The Sudbury Basin, the Southern Province, the Grenville Front, and the Penokean Orogeny. Technical report.
- Brossier, R., Operto, S., and Virieux, J. (2009). Seismic imaging of complex onshore structures by 2D elastic frequency-domain full-waveform inversion. *Geophysics*, 74(6).

## BIBLIOGRAPHY

- Brunod, J., Pierini, S., Tognarelli, A., and Stucchi, E. (2019). Acoustic global FWI for shallow P-wave velocity field estimation. In *81st EAGE Conference and Exhibition 2019*, volume 2019, pages 1–5. EAGE Publishing BV.
- Butzer, S. (2015). *3D elastic time-frequency full-waveform inversion*. PhD thesis, Karlsruher Instituts für Technologie (KIT).
- by Ari Ben-Menahem (1995). A Concise History of Mainstream Seismology: Origins, Legacy, and Perspectives. Technical Report 4.
- Cao, S. and Greenhalgh, S. (1994). Finite-difference solution of the eikonal equation using an efficient, first-arrival, wavefront tracking scheme. *Geophysics*, 59(4):632–643.
- Card, K. and Hutchinson, R. (1972). The Sudbury Structure: its regional geological setting. *Spec. Pap. Geol. Assoc. Can.*, 10:67–78.
- Cary, P. and Lorentz, G. A. (1993). Four-component surface-consistent deconvolution. Technical Report 3.
- Cerveny, V. (2001). *Seismic Ray Theory*. Cambridge University Press, Cambridge.
- Chai, G. and Eckstrand, O. R. (1994). Rare earth element characteristics of the Sudbury Igneous Complex and its country rocks: new constraints on genesis. *Chemical Geology*, 113:221–244.
- Chapman, C. (2004). *Fundamentals of seismic wave propagation*. Cambridge University Press.
- Chen, B., Fang, D., and Zhou, B. (1995). Modified Berenger PML absorbing boundary condition for FD-TD meshes. *IEEE Microwave and Guided Wave Letters*, 5(11):399–401.
- Cheraghi, S., Naghizadeh, M., Snyder, D. B., Haugaard, R., and Gemmell, T. (2019). High-resolution seismic imaging of crooked two-dimensional profiles in greenstone belts of the Canadian shield: results from the Swayze area, Ontario, Canada. *Geophysical Prospecting*, 68(1):62–81.
- Christensen, N. I. and Mooney, W. D. (1995). Seismic velocity structure and composition of the continental crust: a global view. *Journal of Geophysical Research*, 100(B6):9761–9788.
- Claerbout, J. F. (1971). Toward a unified theory of reflector mapping. *Geophysics*, 36(3):467–481.
- Clowes, R. M. (2017). An essential combination illustrated by LITHOPROBE interpretations-Part 2, exploration examples. *Geoscience Canada*, 44(4):135–180.

## BIBLIOGRAPHY

- Clowes, R. M., Cook, F., Profile, S., Hajnal, Z., and Hall, J. (1999). Canada's LITHOPROBE Project (Collaborative, multidisciplinary geoscience research leads to new understanding of continental evolution). 22:3–20.
- Clowes, R. M., Hammer, P. T., Fernández-Viejo, G., and Welford, J. K. (2005). Lithospheric structure in northwestern Canada from Lithoprobe seismic refraction and related studies: A synthesis. *Canadian Journal of Earth Sciences*, 42(6):1277–1293.
- Consolvo, B. P. (2018). *Full-Waveform Inversion with Scaled-Sobolev Preconditioning Applied to Vibroseis Field Data*. Thesis, The University of Western Ontario.
- Consolvo, B. P., Zuberi, M. A. H., Pratt, R. G., and Cary, P. (2017). FWI with Scaled-Sobolev Preconditioning Applied to Short-offset Vibroseis Field Data. *79th Annual International Conference and Exhibition, EAGE, Extended Abstracts*, (June 2017):10–15.
- Corfu, F. (1993). The evolution of the southern Abitibi greenstone belt in light of precise U-Pb geochronology. *Economic Geology*, 88(6):1323–1340.
- Corfu, F., Krogh, T. E., Kwok, Y. Y., and Jensen, L. S. (1989). U-Pb zircon geochronology in the southwestern Abitibi greenstone belt, Superior Province. *Can. J. Earth Sci.*, 26:1747–1763.
- Cowan, E., Riller, U., and Schwerdtner, W. (1999). Emplacement geometry of the Sudbury Igneous Complex: structural examination of a proposed impact melt sheet. *Geological Society of America*, (339):399–418.
- Cross, T. A. and Lessenger, M. A. (1988). Seismic stratigraphy. *Earth and Planetary Science*, 16:319–354.
- Dellinger, J., Ross, A., Meaux, D., Brenders, A., Gesoff, G., Etgen, J. T., Naranjo, J., America, B., Openshaw, G., and Harper, M. (2016). Wolfspar ® , an "FWI-friendly" ultra-low-frequency marine seismic source. In *SEG Technical Program Expanded Abstracts*, pages 4891–4895.
- Dence, M. B., Boudette, E. L., and Lucchitta, I. (1972). Guide to the geology of Sudbury Basin, Ontario, Canada (Apollo 17 Training Exercise 5/23/1972-5/25/1972). Technical report, US Geological Survey.
- Dietz, R. S. (1964). Sudbury Structure as an Astrobleme. *The Journal of Geology*, 72(4):412–434.
- Djeffal, A., Pecher, I. A., Singh, S. C., Crutchley, G. J., and Kaipio, J. (2021). Improved imaging of gas hydrate reservoirs and their plumbing system using 2D elastic full-waveform inversion. *Interpretation*, 9(3):T955–T968.

## BIBLIOGRAPHY

- Dokter, E., Köhn, D., Wilken, D., De Nil, D., and Rabbel, W. (2017). Full waveform inversion of SH- and Love-wave data in near-surface prospecting. *Geophysical Prospecting*, 65:216–236.
- Dressler, B., Peredery, W., and Muir, T. (1992). Geology and mineral deposits of the Sudbury Structure. *Geology and mineral deposits of the Sudbury structure*, 8.
- Dressler, B. O. (1984a). Sudbury geological compilation. *Ontario Geological Survey, Precambrian Geology Series*, 2491(1):50.
- Dressler, B. O. (1984b). The effects of the Sudbury event and the intrusion of the Sudbury Igneous Complex on the footwall rocks of the Sudbury Structure. In *The geology and ore deposits of the Sudbury structure*. Technical report, Ontario Geological Survey.
- Dressler, B. O., Morrison, G. G., Peredery, W. V., and Rao, B. V. (1987). The Sudbury Structure, Ontario, Canada - A Review. In *Research in Terrestrial Impact Structures*, pages 39–68. Vieweg+Teubner Verlag.
- Dreuse, R., Doman, D., Santimano, T., and Riller, U. (2010). Crater floor topography and impact melt sheet geometry of the Sudbury impact structure, Canada. *Terra Nova*, 22(6):463–469.
- Du Bois, L., Levato, L., Besnard, J., Escher, A., Marchant, R., Olivier, R., Ouwehand, M., Sellami, S., Steck, A., and Wagner, J. J. (1990). Pseudo-3D study using crooked line processing from the Swiss Alpine western profile-Line 2 (Val d'Anniviers-Valais). *Tectonophysics*, 173(1-4):31–42.
- Duff, D., Hurich, C., and Deemer, S. (2012). Seismic properties of the Voisey's Bay massive sulfide deposit: Insights into approaches to seismic imaging. *Geophysics*, 77(5):15–43.
- Dukhin, A. S. and Goetz, P. J. (2010). Fundamentals of acoustics in homogeneous liquids: Longitudinal rheology. In *Studies in Interface Science*, volume 24, pages 91–125. Elsevier B.V.
- Eaton, D. W., Adam, E., Milkereit, B., Salisbury, M., Roberts, B., White, D., and Wright, J. (2010). Enhancing base-metal exploration with seismic imaging. *Canadian Journal of Earth Sciences*, 47(5):741–760.
- Ebeniro, J., Opara, C., and Adizua, O. F. (2018). Near-surface Seismic Velocity Model Building from First Arrival Travel-times-A Case Study from an Onshore, Niger Delta Field. *Article in Universal Journal of Physics and Application*, 12(1):1–10.
- Egorov, A., Bóna, A., Pevzner, R., and Tertyshnikov, K. (2018). Potential of full waveform inversion of vertical hard rock environment seismic profile data in. *ASEG Extended Abstracts*, 2018(1):1–3.

## BIBLIOGRAPHY

- Ernst, J. R., Green, A. G., Maurer, H., and Holliger, K. (2007). Application of a new 2D time-domain full-waveform inversion scheme to crosshole radar data. *Geophysics*, 72(5).
- Flinchum, B. A., Steven Holbrook, W., Rempe, D., Moon, S., Riebe, C. S., Carr, B. J., Hayes, J. L., Clair, J. S., and Peters, M. P. (2018). Critical zone structure under a granite ridge inferred from drilling and three-dimensional seismic refraction data. *Journal of Geophysical Research: Earth Surface*, 123(6):1317–1343.
- Florez, K. A., Mantilla, J. G., and Ramirez, A. B. (2016). Full waveform inversion (FWI) in time for seismic data acquired using a blended geometry. In *2016 21st Symposium on Signal Processing, Images and Artificial Vision, STSIVA 2016*. Institute of Electrical and Electronics Engineers Inc.
- Garabito, G. (2018). A comparative study of common-reflection-surface prestack time migration and data regularization: Application in crooked-line data. *Geophysics*, 83(4):S355–S364.
- Gardner, G. H., Gardner, L. W., and Gregory, A. R. (1974). Formation velocity and density - the diagnostic basics for stratigraphic traps. *Geophysics*, 39(6):770–780.
- George, A., Liu, J., and Ng, E. (1994). Computer solution of sparse linear systems.
- Gholami, Y., Brossier, R., Operto, S., Prioux, V., Ribodetti, A., and Virieux, J. (2011). Two-dimensional acoustic anisotropic (VTI) full waveform inversion: The Valhall case study. *SEG Technical Program Expanded Abstracts*, 30(1):2543–2548.
- Gillin, E. J. (2020). Seismology's acoustic debt: Robert Mallet, Chladni's figures, and the Victorian science of earthquakes. *Sound Studies*, 6(1):65–82.
- Gobashy, M., Abdelazeem, M., and Abdrabou, M. (2020). Minerals and ore deposits exploration using meta-heuristic based optimization on magnetic data. *Contributions to Geophysics and Geodesy*, 50(2):161–199.
- Goodfellow, W. D., Mccutcheon, S. R., and Peter, J. M. (2003). Massive Sulfide Deposits of the Bathurst Mining Camp, New Brunswick, and Northern Maine: Introduction and Summary of Findings. Technical report.
- Grandjean, G., Wu, H., White, D., Mareschal, M., Hubert, C., Grandjean, G., Wu, H., Mareschal Gknie, M., White, D., and Hubert, C. (1995). Crustal velocity models for the Archean Abitibi greenstone belt from seismic refraction data. *Can. J. Earth Sci*, 32:149–166.

## BIBLIOGRAPHY

- Gras, C., Dagnino, D., Estela Jiménez-Tejero, C., Meléndez, A., Sallarès, V., and Ranero, C. R. (2019). Full-waveform inversion of short-offset, band-limited seismic data in the Alboran Basin (SE Iberia). *Solid Earth*, 10:1833–1855.
- Gray, M., Bell, R. E., Morgan, J. V., Henrys, S., and Barker, D. H. N. (2019). Imaging the Shallow Subsurface Structure of the North Hikurangi Subduction Zone, New Zealand, using 2D full-waveform inversion. *Journal of Geophysical Research: Solid Earth*, 124(8):9049–9074.
- Green, R. (1974). The seismic refraction method—a review. *Geoexploration*, 12(4):259–284.
- Grieve, R. A., Stoffer, D., and Deutsch, A. (1991). The Sudbury Structure: controversial or misunderstood? *Journal of Geophysical Research*, 96(E5).
- Groos, L., Schäfer, M., Forbriger, T., and Bohlen, T. (2017). Application of a complete workflow for 2D elastic full-waveform inversion to recorded shallow-seismic Rayleigh waves. *Geophysics*, 82(2):R109–R117.
- Hagedoorn, J. G. (1954). A process of seismic reflection interpretation. *Geophysical Prospecting*, 2(2):85–127.
- Hale, D. (1983). *Dip moveout by Fourier transform*. PhD thesis, Stanford University.
- Halls, H. (2009). A 100 km-long paleomagnetic traverse radial to the Sudbury Structure, Canada and its bearing on Proterozoic deformation and metamorphism of the surrounding basement. *Tectonophysics*, 474:493–506.
- Hammer, P. T., Clowes, R. M., Cook, F. A., van der Velden, A. J., and Vasudevan, K. (2010). The Lithoprobe trans-continental lithospheric cross sections: Imaging the internal structure of the North American continent. *Canadian Journal of Earth Sciences*, 47(5):821–857.
- Hastings, F. D., Schneider, J. B., and Brochat, S. L. (1996). Application of the perfectly matched layer (PML) absorbing boundary condition to elastic wave propagation. *The Journal of the Acoustical Society of America*, 100(5):3061–3069.
- Hicks, G. J. and Pratt, R. G. (2001). Reflection waveform inversion using local descent methods: Estimating attenuation and velocity over a gas-sand deposit. *Geophysics*, 66(2):598–612.
- Hoffman, P. F. (1991). On accretion of granite-greenstone terranes. *Greenstone, Gold and Crustal Evolution*, pages 32–45.
- Huang, H., Spencer, C., and Green, A. (1986). A method for the inversion of refraction and reflection travel times for laterally varying velocity structures. Technical Report 3.

## BIBLIOGRAPHY

- Huang, Y., Strati, V., Mantovani, F., Shirey, S. B., and McDonough, W. F. (2014). Regional study of the Archean to Proterozoic crust at the Sudbury Neutrino Observatory (SNO+), Ontario: Predicting the geoneutrino flux. *Geochemistry, Geophysics, Geosystems*, 15(10):3925–3944.
- Hubbard, S. S. and Linde, N. (2011). Hydrogeophysics. In *Treatise on Water Science*, volume 2, pages 401–434. Elsevier.
- Ispolatov, V., Lafrance, B., Dubé, B., Creaser, R., and Hamilton, M. (2008). Geologic and structural setting of gold mineralization in the Kirkland Lake-Larder Lake gold belt, Ontario. *Economic Geology*, 103(6):1309–1340.
- Ivansson, S. (1985). A study of methods for tomographic velocity estimation in the presence of low-velocity zones. *Geophysics*, 50(6):969–988.
- Jackson, S. L. (1995). Precambrian geology - Larder Lake area. Ontario Geological Survey. Map 2628, scale: 1:50000. Technical report.
- Jackson, S. L., Cruden, A. R., White, D., and Milkereit, B. (1995). A seismic-reflection-based regional crosssection of the southern Abitibi greenstone belt1. *Can. J. Earth Sci*, 32:135–148.
- Jackson, S. L., Kirrnerly, C., Wilkinson, L., and Xiandong, J. (1990a). Southern Abitibi Greenstone Belt: Structural and stratigraphic studies in the Larder Lake area. Technical report, Ontario Geological Survey.
- Jackson, S. L., Sutcliffe, R. H., Ludden, J. N., Hubert, C., Green, A. G., Milkereit, B., Mayrand, L., West, G. F., and Verpaelst, P. (1990b). Southern Abitibi greenstone belt: Archean crustal structure from seismic-reflection profiles. *Geology*, 18(11):1086.
- Jensen, E. and Barton, M. (2000). Gold deposits related to alkaline magmatism. *Reviews in Economic Geology*, 13:279–314.
- Jiang, W. (2020). 3-D joint inversion of seismic waveform and airborne gravity gradiometry data. *Geophysical Journal International*, 223(2):746–764.
- Jo, C., Shin, C., and Suh, J. H. (1996). An optimal 9 point, finite difference, frequency space, 2-D scalar wave extrapolator. *GEOPHYSICS*, 61(2):529–537.
- Jolly, W. (1976). Metamorphic history of the Archean Abitibi belt. *Geological Survey of Canada*, pages 63–78.

## BIBLIOGRAPHY

- Kalinicheva, T., Warner, M., Ashley, J., and Mancini, F. (2017). Two- vs three-dimensional full-waveform inversion in a 3D world. In *SEG Technical Program Expanded Abstracts*, pages 1383–1387. Society of Exploration Geophysicists.
- Kamath, N., Brossier, R., Métivier, L., Pladys, A., and Yang, P. (2021). Multiparameter full-waveform inversion of 3D ocean-bottom cable data from the Valhall field. *Geophysics*, 86(1):B15–B35.
- Kamath, N. and Tsvankin, I. (2016). Elastic full-waveform inversion for VTI media: Methodology and sensitivity analysis. *Geophysics*, 81(2):C53–C68.
- Kamei, R. (2013). *Strategies for visco-acoustic waveform inversion in the Laplace-Fourier domain, with application to the Nankai subduction zone*. Phd thesis, The University of Western Ontario.
- Kamei, R., Miyoshi, T., Pratt, R. G., Takanashi, M., and Masaya, S. (2015). Application of waveform tomography to a crooked-line 2D land seismic data set. *Geophysics*, 80(5):B115–B129.
- Kamei, R. and Pratt, R. G. (2013). Inversion strategies for visco-acoustic waveform inversion. *Geophysical Journal International*, pages 859–884.
- Kamei, R., Pratt, R. G., and Tsuji, T. (2012). Waveform tomography imaging of a megasplay fault system in the seismogenic Nankai subduction zone. *Earth and Planetary Science Letters*.
- Kamei, R., Pratt, R. G., and Tsuji, T. (2014). Misfit functionals in Laplace-Fourier domain waveform inversion, with application to wide-angle ocean bottom seismograph data. *Geophysical Prospecting*, 62(5):1054–1074.
- Kashubin, A. S. and Juhlin, C. (2010). Mapping of crustal scale tectonic boundaries in the Ossa-Morena Zone using reprocessed IBERSEIS reflection seismic data. *Tectonophysics*, 489(1-4):139–158.
- Kashubin, A. S., Tryggvason, A., Juhlin, C., Rybalka, A. V., Kashubina, T. V., and Shkred, I. G. (2009). The Krasnouralsky profile in the Middle Urals, Russia: A tomographic approach to vintage DSS data. *Tectonophysics*, 472(1-4):249–263.
- Kazei, V. V., Troyan, V. N., Kashtan, B. M., and Mulder, W. A. (2013). On the role of reflections, refractions and diving waves in full-waveform inversion. *Geophysical Prospecting*, 61(6):1252–1263.
- Kennett, B. L. N. and Saygin, E. (2015). The nature of the Moho in Australia from reflection profiling: A review. *Elsevier*, 5:74–91.

## BIBLIOGRAPHY

- Khoshnavaz, M. J., Bona, A., Hossain, M. S., and Urosevic, M. (2016). Interpretation of hard rock seismic data using 3D prestack diffraction imaging. *ASEG Extended Abstracts*, 2016(1):1–5.
- Kim, J., Lee, S., Seo, Y., Geol, H. J. J. E., and 2014, U. (2014). Enhancement of Seismic Stacking Energy with Crossdip Correction for Crooked Survey Lines. *Journal of Engineering Geology*, 24:171–178.
- Kim, J., Moon, W. M., Percival, J. A., and West, F. G. (1992). Seismic imaging of shallow reflectors in the Eastern Kapuskasing Structural Zone, with correction of crossdip attitudes. *Geophysical Research Letters*, 19(20):2035–2038.
- Klimczak, C., Wittek, A., Doman, D., and Riller, U. (2007). Fold origin of the NE-lobe of the Sudbury Basin, Canada: Evidence from heterogeneous fabric development in the Onaping Formation and the Sudbury Igneous Complex. *Journal of Structural Geology*, 29(11):1744–1756.
- Knott, C. G. (1899). Reflection and refraction of elastic waves with seismological applications. *Phil. mag.*, 48(5):64–97.
- Köhn, D., De Nil, D., Kurzmann, A., Przebindowska, A., and Bohlen, T. (2012). On the influence of model parametrization in elastic full waveform tomography. *Geophysical Journal International*, 191(1):325–345.
- Kosloff, D. D. and Baysal, E. (1982). Forward modeling by a Fourier method. *GEOPHYSICS*, 47(10):1402–1412.
- Kupper, F. J. (1958). Theoretische Untersuchung über die Mehrfachaufstellung von Geophonen. *Geophysical Prospecting*, 6(3):194–256.
- Kurzmann, A., Przebindowska, A., Köhn, D., and Bohlen, T. (2013). Acoustic full waveform tomography in the presence of attenuation: a sensitivity analysis. *Geophysical Journal International*, 195(2):985–1000.
- Lailly, P. (1983). The seismic inverse problem as a sequence of before stack migrations. In *Conference on Inverse Scattering, Theory and Application, Society of Industrial and Applied Mathematics*, pages 206–220.
- Latypov, R., Chistyakova, S., Grieve, R., and Huhma, H. (2019). Evidence for igneous differentiation in Sudbury Igneous Complex and impact-driven evolution of terrestrial planet proto-crusts. *Nature Communications*, 10(1):1–13.
- Le, H. (2020). Acoustic anisotropic full waveform inversion: A parameterization study by examples. *SEG Technical Program Expanded Abstracts*, pages 519–523.

## BIBLIOGRAPHY

- Lenauer, I. and Riller, U. (2012). Geometric consequences of ductile fabric development from brittle shear faults in mafic melt sheets: Evidence from the Sudbury Igneous Complex, Canada. *Journal of Structural Geology*, 35:40–50.
- Lenauer, I. and Riller, U. (2017). A trishear model for the deformation of the Sudbury Igneous Complex, Canada. *Journal of Structural Geology*, 97:212–224.
- Levander, A., Zelt, C. A., and Symes, W. (2007). Crust and Lithospheric Structure - Active Source Studies of Crust and Lithospheric Structure. In *Treatise on Geophysics*, pages 479–511. Elsevier.
- Levin, S. A. (1989). Surface-consistent deconvolution. Technical Report 9.
- Li, Y. and Gu, H. (2019). Full waveform inversion for velocity and density with rock physical relationship constraints. *Journal of Applied Geophysics*, 167:106–117.
- Lightfoot, P. C. (2016). *Nickel sulfide ores and impact melts: Origin of the Sudbury Igneous Complex*. Elsevier.
- Liu, Z., & Zhang, J. (2017). Joint travelttime and waveform envelope inversion for near-surface imaging. *Pure and Applied Geophysics*, 174(3):1269–1289.
- Long, D. (2004). The tectonostratigraphic evolution of the Huronian basement and the subsequent basin fill: geological constraints on impact models of the Sudbury event. *Precambrian Research*, 129:203–223.
- Long, D. G. F. (2009). The Huronian Supergroup; in A Field Guide to the Geology of Sudbury, Ontario. Technical report, Ontario Geological Survey.
- Ludden, J. and Hynes, A. (2000). The Abitibi-Grenville Lithoprobe transect part III: introduction. *Canadian Journal of Earth Sciences*, 37:115–516.
- Ludwig, W., Nafe, J., and Drake, C. (1970). Seismic refraction. *The Sea*, 4:53–84.
- Lundberg, E. and Juhlin, C. (2011). High resolution reflection seismic imaging of the Ullared Deformation Zone, southern Sweden. *Precambrian Research*, 190(1-4):25–34.
- Ma, Z. and Qian, R. (2020). Overview of seismic methods for Urban Underground Space. *Interpretation*, 8(4):54–69.
- Makris, J., Abraham, Z. B., Behle, A., Ginzburg, A., Giese, P., Steinmetz, L., Whitmarsh, R. B., and Eleftheriou, S. (1983). Seismic refraction profiles between Cyprus and Israel and their interpretation. *Geophysical Journal International*, 75(3):575–591.

## BIBLIOGRAPHY

- Malehmir, A. and Bellefleur, G. (2009). Case History 3D seismic reflection imaging of volcanic-hosted massive sulfide deposits: Insights from reprocessing Halfmile Lake data, New Brunswick, Canada. *Geophysics*, 74(6):41–62.
- Malehmir, A., Bellefleur, G., Koivisto, E., and Juhlin, C. (2017a). Pros and cons of 2D vs 3D seismic mineral exploration surveys. *First Break*, 35(8):49–55.
- Malehmir, A., Bellefleur, G., Koivisto, E. A.-L., and Juhlin, C. (2017b). Pros and cons of 2D vs. 3D seismic mineral exploration surveys. *First Break*, 35(8):49–55.
- Malehmir, A., Durrheim, R., Bellefleur, G., Urosevic, M., Juhlin, C., White, D. J., Milkereit, B., and Campbell, G. (2012). Seismic methods in mineral exploration and mine planning: A general overview of past and present case histories and a look into the future. *Geophysics*, 77(5):55–71.
- Malehmir, A., Maries, G., Bäckström, E., Schön, M., and Marsden, P. (2017c). Developing cost-effective seismic mineral exploration methods using a landstreamer and a drophammer. *Scientific Reports*, 7(1):1–7.
- Malinowski, M. and Operto, S. (2008). Quantitative imaging of the Permo-Mesozoic complex and its basement by frequency domain waveform tomography of wide-aperture seismic data from the Polish Basin. *Geophysical Prospecting*, 56(6):805–825.
- Malinowski, M., Operto, S., and Ribodetti, A. (2011). High-resolution seismic attenuation imaging from wide-aperture onshore data by visco-acoustic frequency-domain full-waveform inversion. *Geophysical Journal International*, 186(3):1179–1204.
- Mallet, R. (1846). On the Dynamics of Earthquakes; Being an Attempt to Reduce Their Observed Phenomena to the Known Laws of Wave Motion in Solids and Fluids. *The Transactions of the Royal Irish Academy*, 21:51–105.
- Mallet, R. (1862). *Great Neapolitan Earthquake of 1857: The First Principles of Observational Seismology as Developed in the Report to the Royal Society of London*.
- Mancuso, C. and Naghizadeh, M. (2021). Generalized Cross Dip Moveout Correction of Crooked 2D Seismic Surveys. *Geophysics*, page Accepted.
- Margrave, G. F., Ferguson, R. J., and Hogan, C. M. (2011). Full Waveform Inversion Using One-way Migration and Well Calibration. In *Recovery - 2011 CSPG CSEG CWLS Convention*, volume 77, pages 1–4.
- Marsden, D. (1993). Static corrections - a review. *The Leading Edge*, 12(1):43–49.

## BIBLIOGRAPHY

- Martin, T., Yang, Y., Daniel Whitmore, N., Chemingui, N., Alcantara, T., and Frugier, E. (2021). Efficient reflectivity modelling for full wavefield FWI. *First Break*, 39(3):53–58.
- Masmoudi, N. and Alkhalifah, T. (2018). Full-waveform inversion in acoustic orthorhombic media and application to a North Sea data set. <https://doi.org/10.1190/geo2017-0738.1>, 83(5):C179–C193.
- Matthews, L. (2002). Base metal exploration: Looking deeper and adding value with seismic data. *Canadian Society of Exploration Geophysicists Recorder*, 27:37–43.
- Mayne, W. H. (1962). Common reflection point horizontal data stacking techniques. *GEO-PHYSICS*, 27(6):927–938.
- Metal Earth - Geology map of Larder Lake area, P. (2019). Retrieved January 10, 2020, from <https://merc.laurentian.ca/research/activities/transectlarderlake>.
- Michell, J. (1761). Conjectures concerning the cause and observations upon the phenomena of earthquakes. *Phil. Trans. Roy. Soc.*, 60.
- Milkereit, B. (2015). Teck Chair in Exploration Geophysics. Technical report.
- Milkereit, B., Berrer, E. K., King, A. R., Watts, A. H., Roberts, B., Adam, E., Eaton, D. W., Wu, J., and Salisbury, M. (2000). Development of 3-D seismic exploration technology for deep nickel-copper deposits-A case history from the Sudbury basin, Canada. *Geophysics*, 65(6).
- Milkereit, B. and Green, A. (1992). Deep geometry of the Sudbury structure from seismic reflection profiling. *Geology*, 20(9):807–811.
- Milkereit, B., Green, A., Wu, J., White, D., and Adam, E. (1994). Integrated seismic and borehole geophysical study of the Sudbury Igneous Complex. *Geophysical Research Letters*, 21(10):931–934.
- Mo, L. and Harris, J. M. (2002). Finite-difference calculation of direct-arrival traveltimes using the eikonal equation. *Geophysics*, 67(4):1270–1274.
- Monecke, T., Mercier-Langevin, P., Dubé, B., Monecke, T., Mercier-Langevin, P., Dubé, B., and Frieman, B. M. (2019). Geology of the Abitibi Greenstone Belt. In *Archean Base and Precious Metal Deposits, Southern Abitibi Greenstone Belt, Canada*. Society of Economic Geologists.
- Montsion, R. M., Perrouty, S., Lindsay, M. D., Jessell, M. W., and Frieman, B. M. (2021). Mapping structural complexity using geophysics: A new geostatistical approach applied to greenstone belts of the southern Superior Province, Canada. *Tectonophysics*, 812:228889.

## BIBLIOGRAPHY

- Mora, P. (1987). Nonlinear two dimensional elastic inversion of multioffset seismic data. *Geophysics*, 52(9):1211–1228.
- Mora, P. (1989). Inversion = migration + tomography. *Geophysics*, 54(12):1575–1586.
- Moser, T. J. (1991). Shortest path calculation of seismic rays. *Geophysics*, 56(1):59–67.
- Muir, T. (1984). The Sudbury Structure: Consideration and models for an endogenic origin. *Ontario Geological Survey*, 1:449–489.
- Naghizadeh, M. (2019). The Metal Earth project: Crustal scale reflection seismic study of the Archean Superior Province of Canada. *CSEG Recorder*, 44(04).
- Naghizadeh, M., Snyder, D. B., Cheraghi, S., Foster, S., Cilensek, S., Floreani, E., and Mackie, J. (2019). Acquisition and Processing of Wider Bandwidth Seismic Data in Crystalline Crust: Progress with the Metal Earth Project. *Minerals*, 9(3):145.
- Naldrett, A. (2005). Magmatic Sulfide Deposits: Geology, Geochemistry and Exploration. *Springer*, page 727.
- Nedimović, M. R. (2000). *Seismic reflection imaging in crystalline terrains*. PhD thesis, University of Toronto.
- Nedimović, M. R. and West, G. F. (2003). Crooked line 2D seismic reflection imaging in crystalline terrains: Part 1, data processing. *Geophysics*, 68(1):274–285.
- Norman, M. (1994). Sudbury Igneous Complex: impact melt or endogenous magma? Implications for lunar crustal evolution. *Geological Society of America*, (187):331–341.
- Olasunkanmi, N. K., Bamigboye, O. S., and Aina, A. (2017). Exploration for iron ore in Agbado-Okudu, Kogi State, Nigeria. *Arabian Journal of Geosciences*, 10(24):1–12.
- Operto, S., Brossier, R., Combe, L., Métivier, L., Ribodetti, A., and Virieux, J. (2013). Computationally efficient three-dimensional acoustic finite-difference frequency-domain seismic modeling in vertical transversely isotropic media with sparse direct solver. *Geophysics*, 79(5):T257–T275.
- Operto, S. and Miniussi, A. (2018). On the role of density and attenuation in three-dimensional multiparameter viscoacoustic VTI frequency-domain FWI: an OBC case study from the North Sea. *Geophysical Journal International*, 213(3):2037–2059.

## BIBLIOGRAPHY

- Owusu, J. C., Podgornova, O., Charara, M., Leaney, S., Campbell, A., Ali, S., Borodin, I., Nutt, L., and Menkiti, H. (2015). Anisotropic elastic full-waveform inversion of walkaway vertical seismic profiling data from the Arabian Gulf. *Geophysical Prospecting*, 64(1):38–53.
- Peredery, W. and Morrison, G. (1984). Discussion of the origin of the Sudbury Structure; in *The Geology and Ore Deposits of the Sudbury Structure. Ontario Geological Survey*, 1:491–511.
- Phillips, W. S. and Fehler, M. C. (1991). Traveltime tomography: A comparison of popular methods. *Geophysics*, 56(10):1639–1649.
- Plessix, R. E. (2006). A review of the adjoint-state method for computing the gradient of a functional with geophysical applications. *Geophysical Journal International*, 167(2):495–503.
- Plessix, R.-É. and Cao, Q. (2011). A parametrization study for surface seismic full waveform inversion in an acoustic vertical transversely isotropic medium. *Geophysical Journal International*, 185(1):539–556.
- Plessix, R.-É. and Krupovnickas, T. (2021). Low-frequency, long-offset elastic waveform inversion in the context of velocity model building. *The Leading Edge*, 40(5):342–347.
- Podvin, P. and Lecomte, I. (1991). Finite difference computation of traveltimes in very contrasted velocity models: a massively parallel approach and its associated tools. *Geophysical Journal International*, 105(1):271–284.
- Pratt, R. and Smithyman, B. (2018). Full Waveform Inversion for Density: Reciprocity, Divergence, Parameter Resolution, and Other Issues. *80th EAGE Conference and Exhibition 2018: Opportunities Presented by the Energy Transition*, 2018(1):1–5.
- Pratt, R. G. (1989). *Wave equation methods in cross-hole seismic imaging*. PhD thesis.
- Pratt, R. G. (1990). Inverse theory applied to multi source crosshole tomography Part 2 Elastic wave equation method. *Geophysical Prospecting*, 38(3):311–329.
- Pratt, R. G. (1999). Seismic waveform inversion in the frequency domain, Part 1 Theory and verification in a physical scale model. *Geophysics*, 64(3):888–901.
- Pratt, R. G., Shin, C., and Hicks (1998). Gauss-Newton and full Newton methods in frequency-space seismic waveform inversion. *Geophysical Journal International*, 133(2):341–362.
- Pratt, R. G., Song, Z.-M., Williamson, P., and Warner, M. (1996). Two-dimensional velocity models from wide-angle seismic data by wavefield inversion. *Geophysical Journal International*, 124(2):323–340.

## BIBLIOGRAPHY

- Pratt, R. G. and Worthington, M. H. (1988). The application of diffraction tomography to crosshole seismic data. *Geophysics*, 53(10):1284–1294.
- Pratt, R. G. and Worthington, M. H. (1990). Inverse theory applied to multi source crosshole tomography Part 1 Acoustic wave equation method. *Geophysical Prospecting*, 38(3):287–310.
- Prieux, V., Brossier, R., Operto, S., and Virieux, J. (2013). Multiparameter full waveform inversion of multicomponent ocean-bottom-cable data from the Valhall field. Part 1: imaging compressional wave speed, density and attenuation. *Geophysical Journal International*, 194(3):1640–1664.
- Pye, E., Naldrett, A., and Giblin, P. (1984). The geology and ore deposits of the Sudbury Structure. *Ontario Geological Survey*, 1:603.
- Pyke, D., Ayres, L., and Innes, D. (1973). Timmins - Kirkland Lake. Ontario Division of Mines, Map 2205, scale 1:253440. Technical report.
- Qian, J. and Symes, W. W. (2002). Finite-difference quasi-P traveltimes for anisotropic media. *Geophysics*, 67(1):147–155.
- Ramos-Martinez, J., Shi, J., Qiu, L., Valenciano, A., and Chemingui, N. (2017). Multi-Parameter FWI - Long-Wavelength Updates and Leakage Reduction in Acoustic Anisotropic Media. *79th EAGE Conference and Exhibition 2017*, 2017(1):1–5.
- Ravaut, C., Operto, S., Imbrota, L., Virieux, J., Herrero, A., and Dell'Aversana, P. (2004). Multiscale imaging of complex structures from multifold wide-aperture seismic data by frequency-domain full-waveform tomography: application to a thrust belt. *Geophysical Journal International*, 159(3):1032–1056.
- Riller, U. (2005). Structural characteristics of the Sudbury impact structure, Canada: Impact-induced versus orogenic deformation - A review. *Meteoritics and Planetary Science*, 40(11):1723–1740.
- Robert, F. (2001). Syenite associated disseminated gold deposits in the Abitibi greenstone belt, Canada. *Mineralium Deposita*, 39:503–516.
- Rousell, D., Gibson, H., and Jonasson, I. (1997). The tectonic, magmatic and mineralization history of the Sudbury Structure. *Exploration and Mining Geology*, 1(6):1–22.
- Saenger, E. H. and Bohlen, T. (2004). Finite difference modeling of viscoelastic and anisotropic wave propagation using the rotated staggered grid. *Geophysics*, 69(2):583–591.

## BIBLIOGRAPHY

- Saffarzadeh, S., Javaherian, A., Hasani, H., and Talebi, M. A. (2018). Improving fault image by determination of optimum seismic survey parameters using ray-based modeling. *Journal of Geophysics and Engineering*, 15(3):666–680.
- Salisbury, M. H., Iuliucci, R., and Long, C. (1994). Velocity and reflection structure of the Sudbury Structure from laboratory measurements. *Geophysical Research Letters*, 21(10):923–926.
- Sava, P. and Fomel, S. (2006). Time-shift imaging condition in seismic migration. <http://dx.doi.org/10.1190/1.2338824>.
- Savage, W. S. (1964). Mineral resources and mining properties in the Kirkland Lake-Larder Lake area. Technical report, Ontario Department of Mines, Toronto.
- Schmelzbach, C., Juhlin, C., Carbonell, R., and Simancas, J. F. (2007). Prestack and poststack migration of crooked-line seismic reflection data: A case study from the South Portuguese Zone fold belt, southwestern Iberia. *Geophysics*, 72(2).
- Schneider, W. A. (1978). Integral formulation for migration in two and three dimensions. *Geophysics*, 43(1):49–76.
- Schreiter, L., Hloušek, F., Hellwig, O., and Buske, S. (2015). Characterization of seismic reflections from faults in a crystalline environment, Schneeberg, Germany. *Geophysical Prospecting*, 63(4):1015–1032.
- Sheriff, R. and Geldart, L. (1982). *Exploration seismology*. New York: Cambridge University Press.
- Sheriff, R. E. and Geldart, L. P. (1995). *Exploration seismology*. New York: Cambridge University Press.
- Shin, C. and Ho Cha, Y. (2009). Waveform inversion in the Laplace-Fourier domain. *Geophysical Journal International*, 177(3):1067–1079.
- Shin, C. and Min, D. J. (2006). Waveform inversion using a logarithmic wavefield. *Geophysics*, 71(3).
- Shin, Y., Oh, J. W., Kim, S., and Min, D. J. (2019). Mono-component multiparameter acoustic full waveform inversion in vertically transverse isotropic media using converted vector wavefields. *Journal of Applied Geophysics*, 170:103816.

## BIBLIOGRAPHY

- Shin, Y., Oh, J.-W., and Min, D.-J. (2021). An efficient multiparameter acoustic anisotropic full-waveform inversion depending on parameterization. *Acta Geophysica 2021* 69:4, 69(4):1257–1267.
- Silva, R. U., De Basabe, J. D., Sen, M. K., González-Escobar, M., and Gomez-Treviño, E. (2019). Joint acoustic full waveform and gravimetric inversion. *SEG Technical Program Expanded Abstracts*, pages 1053–1057.
- Simony, P. (1964). Northwestern Temagami area. Technical report, Ontario Department of Mines.
- Sirgue, L. and Pratt, R. G. (2004). Efficient waveform inversion and imaging: A strategy for selecting temporal frequencies. *Geophysics*, 69(1):231–248.
- Smithyman, B. R. and Clowes, R. M. (2012). Waveform tomography of field vibroseis data using an approximate 2D geometry leads to improved velocity models. *Geophysics*, 77(1):R33–R43.
- Smithyman, B. R. and Clowes, R. M. (2013). Waveform tomography in 2.5D Parameterization for crooked-line acquisition geometry. *Journal of Geophysical Research: Solid Earth*, 118(5):2119–2137.
- Song, Z. and Williamson, P. (1995). Frequency domain acoustic wave modeling and inversion of crosshole data: Part I 2.5D modeling method. *Geophysics*, 60(3):784–795.
- Song, Z.-M., Williamson, P. R., and Pratt, R. G. (1995). Frequency-domain acoustic-wave modeling and inversion of crosshole data: Part II - inversion method, synthetic experiments and real-data results. *Geophysics*, 60(3):796–809.
- Spencer, C. (1993). A vibroseis reflection seismic survey at the Buchans Mine in central Newfoundland. *Geophysics*, 58(1):154–166.
- Spray, J. G., Butler, H. R., and Thompson, L. M. (2004). Tectonic influences on the morphometry of the Sudbury impact structure: Implications for terrestrial cratering and modeling. *Meteoritics and Planetary Science*, 39(2):287–301.
- Spray, J. G. and Thompson, L. M. (1995). Friction melt distribution in a multi-ring impact basin. *Nature*, 373:130–132.
- St-Jean, N., Hunt, L., and Sherlock, R. L. (2019). Mapping a New Exposure of the Basal Unconformity Between the Hearst and Larder Lake Assemblages, Skead Township, Northeastern Ontario. Technical report.

## BIBLIOGRAPHY

- Stöffler, D., Deutsch, A., Avermann, M., Bischoff, L., Brockmeyer, P., Buhl, D., Lakomv, R., and Müller-Mohr, V. (1992). The formation of the Sudbury structure, Canada: Toward a unified impact model. In *Special Paper of the Geological Society of America*, volume 293, pages 303–318. Geological Society of America.
- Sun, D., Jiao, K., Cheng, X., and Vigh, D. (2016). Reflection based waveform inversion. In *SEG Technical Program Expanded Abstracts*, volume 35, pages 1151–1156. Society of Exploration Geophysicists.
- Sun, D., Jiao, K., Cheng, X., Xu, Z., Zhang, L., and Vigh, D. (2017). Born Modeling based Adjustive Reflection Full Waveform Inversion. In *SEG Technical Program Expanded Abstracts*, pages 1460–1465. Society of Exploration Geophysicists.
- Taner, M. T. and Koehler, F. (1981). Surface consistent. *Geophysics*, 46(I):17–22.
- Tarantola, A. (1984a). Inversion of seismic reflection data in the acoustic approximation. *Geophysics*, 49(8):1259–1266.
- Tarantola, A. (1984b). Linearized inversion of seismic reflection data\*. *Geophysical Prospecting*, 32(6):998–1015.
- Teodor, D., Comina, C., Anjom, F. K., Brossier, R., Socco, L. V., and Virieux, J. (2021). Challenges in shallow target reconstruction by 3D elastic full-waveform inversion - Which initial model? *Geophysics*, 86(4):R433–R446.
- Therriault, A. M., Fowler, A. D., and Grieve, R. A. (2002). The Sudbury Igneous Complex: A differentiated impact melt sheet. *Economic Geology*, 97(7):1521–1540.
- Thurston, P. C., Ayer, J. A., Goutier, J., and Hamilton, M. A. (2008). Depositional gaps in abitibi greenstone belt stratigraphy: A key to exploration for syngenetic mineralization. *Economic Geology*, 103(6):1097–1134.
- Trinh, P., Brossier, R., Métivier, L., Virieux, J., and Wellington, P. (2017a). Bessel smoothing filter for spectral-element mesh. *Geophysical Journal International*, 209(3):1489–1512.
- Trinh, P.-T., Brossier, R., Métivier, L., Tavard, L., Virieux, J., and Wellington, P. (2017b). Efficient 3D elastic FWI using a spectral-element method on Cartesian-based mesh. *SEG Technical Program Expanded Abstracts*, pages 1533–1538.
- Trinh, P. T., Brossier, R., Métivier, L., and Virieux, J. (2019). Data-oriented strategy and  $V_p/V_s$  model-constraint for simultaneous  $V_p$  and  $V_s$  reconstruction in 3D visco-elastic FWI:

## BIBLIOGRAPHY

- Application to the SEAM II Foothill dataset. *SEG Technical Program Expanded Abstracts*, pages 1213–1217.
- Tsumura, N., Komada, N., Sano, J., Kikuchi, S., Yamamoto, S., Ito, T., Sato, T., Miyauchi, T., Kawamura, T., Shishikura, M., Abe, S., Sato, H., Kawanaka, T., Suda, S., Higashinaka, M., and Ikawa, T. (2009). A bump on the upper surface of the Philippine Sea plate beneath the Boso Peninsula, Japan inferred from seismic reflection surveys: A possible asperity of the 1703 Genroku earthquake. *Tectonophysics*, 472(1-4):39–50.
- Ubide, T., Guyett, P. C., Kenny, G. G., O’Sullivan, E. M., Ames, D. E., Petrus, J. A., Riggs, N., and Kamber, B. S. (2017). Protracted volcanism after large impacts: Evidence from the Sudbury impact basin. *Journal of Geophysical Research: Planets*, 122(4):701–728.
- van Vossen, R., Curtis, A., Laake, A., and Trampert, J. (2006). Surface-consistent deconvolution using reciprocity and waveform inversion. *Geophysics*, 71(2):41–56.
- Vidale, J. (1988). Finite-difference calculation of travel times. *Bulletin of the Seismological Society of America*, 78(6):2062–2076.
- Vidale, J. E. (1990). Finite-difference calculation of traveltimes in three dimensions. *Geophysics*, 55(5):521–526.
- Virieux, J. and Operto, S. (2009). An overview of full-waveform inversion in exploration geophysics. *Geophysics*, 74(6):WCC1–WCC26.
- Wang, H., Burtz, O., Routh, P., Wang, D., Violet, J., Lu, R., and Lazaratos, S. (2021). Anisotropic 3D elastic full-wavefield inversion to directly estimate elastic properties and its role in interpretation. *The Leading Edge*, 40(4):277–286.
- Wang, P., Zhang, Z., Wei, Z., and Huang, R. (2019a). A demigration-based reflection full-waveform inversion workflow. In *2018 SEG International Exposition and Annual Meeting, SEG 2018*, pages 1138–1142. Society of Exploration Geophysicists.
- Wang, Z. Y., Huang, J. P., Liu, D. J., Li, Z. C., Yong, P., and Yang, Z. J. (2019b). 3D variable-grid full-waveform inversion on GPU. *Petroleum Science*, 16(5):1001–1014.
- Wapenaar, C. P. A. (1996). Inversion versus migration: A new perspective to an old discussion. *Geophysics*, 61(3):12–65.
- Warner, M., Ratcliffe, A., Nangoo, T., Morgan, J., Umpleby, A., Shah, N., Vinje, V., Štekl, I., Guasch, L., Win, C., Conroy, G., and Bertrand, A. (2013). Anisotropic 3D full-waveform inversion. *Geophysics*, 78(2).

## BIBLIOGRAPHY

- Watremez, L., Prada, M., Chen, C., Minshull, T., O'reilly, B., Reston, T., Wagner, G., Gaw, V., Klaeschen, D., Shannon, P., and Lebedev, S. (2018). Deep structure of the Porcupine Basin from seismic refraction data, offshore western Ireland. *Atlantic Geology*, 54:120–132.
- Whewell, W. (1840). *The philosophy of the inductive sciences: founded upon their histor.* 2nd edition.
- White, D. J., Milkereit, B., Wu, J. J., Salisbury, M. H., Mwenifumbo, J., Berrer, E. K., Moon, W., and Lodha, G. (1994). Seismic reflectivity of the Sudbury Structure North Range from borehole logs. *Geophysical Research Letters*, 21(10):935–938.
- Williamson, P. R. and Pratt, R. G. (1995). A critical review of acoustic wave modeling procedures in 2.5 dimensions. *GEOPHYSICS*, 60(2):591–595.
- Woodward, M. J. (1992). Wave-equation tomography. *Geophysics*, 57(1):15–26.
- Wright, C., Wright, J. A., and Hall, J. (1994). Seismic reflection techniques for base metal exploration in eastern Canada: examples from Buchans, Newfoundland. *Journal of Applied Geophysics*, 32(2-3):105–116.
- Wu, J., Milkereit, B., and Boerner, D. E. (1995). Seismic imaging of the enigmatic Sudbury Structure. *Journal of Geophysical Research: Solid Earth*, 100(B3):4117–4130.
- Wu, R. and Toksöz, M. N. (1987). Diffraction tomography and multisource holography applied to seismic imaging. 52(1):11–25.
- Xie, H., Gao, M., Zhang, R., Peng, G., Wang, W., and Li, A. (2019). Study on the Mechanical Properties and Mechanical Response of Coal Mining at 1000 m or Deeper. *Rock Mechanics and Rock Engineering*, 52(5):1475–1490.
- Xiong, J. L., Lin, Y., Abubakar, A., and Habashy, T. M. (2013). 2.5-D forward and inverse modelling of full-waveform elastic seismic survey. *Geophysical Journal International*, 193(2):938–948.
- Yan, H. and Liu, Y. (2013). Visco-acoustic prestack reverse-time migration based on the time-space domain adaptive high-order finite-difference method. *Geophysical Prospecting*, 61(5):941–954.
- Yilmaz, Ö. (2001). *Seismic Data Analysis*. Society of Exploration Geophysicists.
- Yilmaz, Ö. and Claerbout, J. F. (1984). Prestack partial migration:.. *GEOPHYSICS*, 45:1753–1777.
- Yuan, Y. O., Simons, F. J., and Bozdog, E. (2015). Multiscale adjoint waveform tomography for surface and body waves. *Geophysics*, 80(5):R281–R302.

## BIBLIOGRAPHY

- Zelt, C. A. (1999). Modelling strategies and model assessment for wide-angle seismic traveltime data. *Geophysical Journal International*, 139(1):183–204.
- Zelt, C. A. and Smith, R. B. (1992). Seismic traveltime inversion for 2-D crustal velocity structure. *Geophysical Journal International*, 108(1):16–34.
- Zhang, F. and Juhlin, C. (2013). Full waveform inversion of seismic reflection data from the Forsmark planned repository for spent nuclear fuel, eastern central Sweden. *Geophysical Journal International*, 196(2):1106–1122.
- Zhang, J., Lin, S., Linnen, R., and Martin, R. (2014). Structural setting of the Young-Davidson syenite-hosted gold deposit in the Western Cadillac-Larder Lake Deformation Zone, Abitibi Greenstone Belt, Superior Province, Ontario. *Precambrian Research*, 248:39–59.
- Zhang, J. and Toksöz, M. N. (1998). Nonlinear refraction traveltime tomography. *Geophysics*, 63(5):1726–1737.
- Zhou, B. and Greenhalgh, S. (2006). An adaptive wavenumber sampling strategy for 2.5D seismic-wave modeling in the frequency domain. *Pure and Applied Geophysics*, 163(7):1399–1416.
- Zhou, H. W., Hu, H., Zou, Z., Wo, Y., and Youn, O. (2018). Reverse time migration: A prospect of seismic imaging methodology. *Earth-Science Reviews*, 179:207–227.
- Zieg, M. J. and Marsh, B. D. (2005). The Sudbury Igneous Complex: Viscous emulsion differentiation of a superheated impact melt sheet. *Bulletin of the Geological Society of America*, 117(11-12):1427–1450.

# BRIAN VILLAMIZAR

Geophysicist with 9 years of experience in reservoir characterization. Spec.: full-waveform inversion, seismic processing and interpretation, structural/stratigraphic reservoir modeling, pre/post-stack seismic inversion and attributes analysis for reservoir properties prediction and mapping.

**11/2020 – present**

**Novamera Inc.**

**Senior Geophysicist, Oakville – Canada**

- Coordinate, conduct, and analyze lab- and field- scale technical experiments in order to enhance imaging of narrow veins with the Near-Borehole Imaging Tool (NBIT).
- Develop 3D data positioning algorithm for accurate spatial identification of mineralized contacts based on surveyed NBIT data. Devise optimum signal processing methods adapted to NBIT data.
- Ore geometry 3D modelling based on the integration of core samples, historical production data, and NBIT data.
- Borehole placement and trajectory planning based on the analysis of prospective zones.

**09/2018 – 08/2021**

**Ph.D. Project**

**Western University, London – Canada**

- Devised strategies to mitigate nonlinearity during the implementation of full-waveform inversion (FWI) on reflection profiles in crystalline environments in Canada.
- Near-surface structural imaging in two mining districts, Larder Lake and Sudbury.
- Analyzed effectiveness of 2D v. 2.5D modeling and inversion in severely crooked and mildly crooked geometries.
- Improved reflection imaging by applying optimum binning strategies.
- Improved imaging at depth by combining FWI and conventional velocity analysis before seismic migration.

**01/2018 – 07/2018**

**QITeam International**

**Project Geophysicist, Beijing – China**

- Generated static model – detail stratigraphic and structural seismic interpretation (north of Malay basin).
- Provided G&G support to customers. Technical representative at the 80<sup>th</sup> EAGE Conference – Denmark.

**09/2016 – 12/2017** **Laboratory of Petroleum Resources and Prospecting, China University of Petroleum**  
**Reservoir Geophysicist/Seismic Interpreter**

Tight-Sand Gas Reservoir Description, Sulige Field – China.

- Modeled AVO effects using well data and generated AVO attributes for the interpretation of HC anomalies.
- Provided a 260 km<sup>2</sup> fluid model with an 80%-correlation rate with borehole data, effectively identifying hydrocarbon-bearing zones. Applied AVO seismic inversion, multi-linear analysis, and neural networks.
- Identified gas-related anomalies in thin layers by implementing frequency and multi-attributes analysis.

**11/2011 – 9/2015**

**PDVSA (Venezuelan National Oil and Gas Company)**

**Reservoir Geophysicist/Seismic Interpreter**

Seismic Reservoir Characterization, Static Model, Block Carabobo 1, Orinoco Heavy and Extra-Heavy Oil Belt.

- Delivered 3D structural and stratigraphic models through the analysis and interpretation of well and 2D/3D seismic datasets. Generated structural maps and identified structural and geomorphological features.
- Provided probability litho-fluid volumes (porosity, Vshale, HC occurrence) and facies distribution maps.
- Described sand-channels orientation and dimensions by analyzing multiple seismic attributes.
- Geophysical support to well operations: optimized well placement and trajectories, evaluated new prospects, and provided structural/stratigraphic risk assessments during well drilling operations.
- Operational geophysicist on two 3C-3D seismic acquisition projects. In addition to reflection data, these projects included data surveying and processing of seismic refraction as well as gravity and EM methods.

# BRIAN VILLAMIZAR

10/2010 – 3/2011

PDVSA (Venezuelan National Oil and Gas Company)

**Seismic Interpreter (internship)** - 3D Structural and Velocity Model, Maturin sub-basin, Venezuela.

- Performed seismic-to-well tie analysis, 3D seismic interpretation-compressive regime, velocity and 3D Earth modeling, reservoir delineation, structural maps, and structural and stratigraphic traps identification.

## EDUCATION

University	Dates	Degree	Sponsorship
Western University	09/2018 to 8/2021	Ph.D. in Geophysics	NSERC/Metal Earth - Canada
China University of Petroleum	09/2015 to 07/2018	M.Sc. in Geophysics	Chinese Gov. Spons. - China
Simon Bolivar University	09/2006 to 07/2011	B.Eng. in Geophysics	Venezuela

## COMPETENCES

**Excellent communication skills in both Spanish and English. Basic communication skills in Mandarin.**

**Excellent skills with standard seismic interpretation, modeling, and inversion software:**

**HAMPSON AND RUSSELL – PETREL – GEOTOMO – LANDMARK (PROMAX, OPENWORKS, etc.)**

**PROGRAMMING TOOLS: MATLAB**

## PUBLICATIONS

- Villamizar B., Pratt G., and Naghizadeh M., (2021). *Imaging the northeast lobe of the Sudbury Structure through 2D and 2.5D visco-acoustic full-waveform inversion*. Geophysics (to be submitted for peer review).
- Villamizar B., Pratt G., and Naghizadeh M., (2021). *Seismic imaging of crystalline structures: improving energy focusing and signal alignment with azimuthal binning*. Geophysics (to be submitted for peer review).
- Villamizar B., Pratt G., and Naghizadeh M., (2021). *Seismic imaging of crystalline structures: 2D and 2.5D visco-acoustic full-waveform inversion*. Geophysics (submitted for peer review).
- Villamizar B., Pratt G., and Naghizadeh M., (2021). *Full-waveform inversion of crystalline terrains with combined explosive and vibroseis sources*. Geophysics (submitted for peer review).
- Villamizar B., Sun Y., Liu Y., and *et al.* (2018). *An integrated approach for fluid description in an unconventional reservoir - Sulige gas field, China*: SEG, Expanded Abstracts, Beijing, 2018. Presenter.
- Villamizar B., Hanyang L., Cheng N. *Increasing the value of seismic data with pre-stack spectral blueing*: SEG, Reservoir Geophysics Workshop, DaQing, 2018. Presenter.
- Sun Y., Liu Y., Villamizar B., and *et al.*, (2018). *Nonlinear high order Russell fluid factor AVO inversion based on linear iteration*: 80<sup>th</sup> EAGE Conference and Exhibition. Denmark, 2018.